DEPARTAMENT OF
PHYSICS

MONITORING ADSORPTION DYNAMICS ON THE RUTILE TiO_2(110)-(1×1) SURFACE WITH WFS AND XPS: SURFACE DEFECTS, WATER AND OXYGEN ADSORPTION

JOÃO TRIGUEIRO SANTOS

Master in Physics Engineering

DOCTORATE IN PHYSICS ENGINEERING

NOVA University Lisbon

November, 2021

NOVA SCHOOL OF
SCIENCE & TECHNOLOGY

DEPARTAMENT OF
PHYSICS

MONITORING ADSORPTION DYNAMICS ON THE RUTILE TIO$_2$(110)-(1×1) SURFACE WITH WFS AND XPS: SURFACE DEFECTS, WATER AND OXYGEN ADSORPTION

JOÃO TRIGUEIRO SANTOS

Master in Physics Engineering

Adviser: Orlando Manuel Neves Duarte Teodoro
Associate Professor, NOVA School of Science & Technology

Co-advisers: Nenad Bundaleski
Research Fellow, NOVA School of Science & Technology

Examination Committee:

Chair: José Paulo Moreira dos Santos,
Full Professor, NOVA School of Science & Technology

Rapporteurs: Ana Maria Botelho do Rego,
Associate Professor, Instituto Superior Técnico, University of Lisbon
Jonas Deuermeier,
Research Fellow, NOVA School of Science & Technology

Adviser: Nenad Bundaleski,
Research Fellow, NOVA School of Science & Technology

Members: Reinhard Horst Schwarz,
Associate Professor, Instituto Superior Técnico, University of Lisbon
José Filipe Vilela Vaz,
Associate Professor, University of Minho

DOCTORATE IN PHYSICS ENGINEERING

NOVA University Lisbon
November, 2021

Monitoring Adsorption Dynamics on the Rutile TiO_2(110)-(1×1) Surface with WFS and XPS: Surface Defects, Water and Oxygen Adsorption

Acknowledgements

I first thank my supervisor, Professor Orlando Teodoro, who invited me to the research group and proposed to me the work of this project. For his guidance and support in all matters, and wide experience and knowledge shared in the lab.

A very special thanks to my other supervisor, Nenad Bundaleski, for everything he taught me about all subjects of surface science, as well as countless other scientific and cultural topics. He followed my work closely, providing guidance and solutions to many challenges, was a daily collaborator in this project, the main reviewer of this text and related publications, and a good friend.

I thank the rest of the team in our group. Adérito Santos for his support in the lab in my first year, and his unshakable good mood and willingness to help. Professor Augusto Moutinho, who was always interested in our work and available for discussion and support. Alexander Tolstoguzov, for showing me what rigor and a clean desk can accomplish. Wilson Lima, with whom I shared many lab hours performing the characterization of the Kratos spectrometer, and Ana Fonseca, who managed the neighboring Metrovac lab, whose resources were essential for the maintenance of the UHV systems.

I also thank Fundação para a Ciência e Tecnologia (FCT) for the financial support through the fellowship SFRH/BD/82258/2011

Finally, I thank my partner Marta for making it worth it, and for sharing the load through these years, and my family for giving me the opportunity and motivation to be in this position.

Abstract

In the crystal form of rutile or anatase, the TiO_2 surface is one of the most studied metallic oxide surfaces, due to its potential applications in the catalysis field, in addition to other technological uses. The reactivity of the TiO_2 surface is governed in part by its concentration of defects, such as oxygen vacancies, with its catalytic activity also being affected by the adsorption of atmospheric gases such as water or oxygen. In the preceding work performed by the Applied Surface Science group of CEFITEC, the kinetics of water adsorption on the TiO_2(110)-(1×1) surface were studied by monitoring the time-dependence of the work function change during the adsorption process, by measuring the cut-off position of the secondary electron energy spectra (onset method). This technique has proven to be a very useful tool for the analysis of adsorption dynamics, due to its high sensitivity to adsorbates which modify the surface dipole layer, and short acquisition time requirement. In the work here presented, this study is extended, and the onset method is used as a primary tool, together with XPS, for performing an analysis of the adsorption dynamics of water and oxygen on the rutile TiO_2(110)-(1×1) surface, and how this process is affected by the surface temperature, and the presence of surface defects or contaminants.

First, the physical model behind the onset method was revised, as some of the previous results obtained with this technique could not be explained under the present interpretation of the measurement. In this revision, the electric field between surface regions with different local work functions is considered, and its effect on the onset position is calculated as a function of the surface morphology and external fields.

The TiO_2 related experiments presented in this thesis were performed on a Kratos XSAM 800 system. Before initiating the experimental campaign, the Kratos system was upgraded to the needs of this work. Its control and acquisition hardware system and software was replaced, so that both control and data acquisition tasks could be performed with a modern PC. The spectrometer was recalibrated by measuring its transmission function with two methods, the standard first principles method, and a newly introduced biasing method, which presents clear advantages with respect to the first. Lastly, a method was introduced for the optimization of the transmission function, by a applying the differential evolution search algorithm to the voltages of the spectrometer's electrodes, resulting in an increase of the system's sensitivity in the whole energy range.

Finally, the onset method was used to study the presence of surface defects and the adsorption of water and oxygen on the rutile TiO_2(110)-(1×1) surface. A water adsorption model was introduced which was capable of explaining the results that were previously obtained. The adsorption of hydrocarbon contaminants, accumulated in the UHV system over time, was found to be of substantial importance. It was possible with this model to calculate the constants of the adsorption kinetics and estimate the concentration of water molecules adsorbed on Ti rows and dissociated on bridging oxygen vacancies.

The oxygen adsorption process was monitored both by work function and XPS measurements. The adsorption kinetics were determined for surfaces prepared with different reduction levels. Oxygen adsorption was also associated with a decrease of the Ti^{3+} contribution in the XPS Ti 3p peak, and the magnitude of this decrease was linearly correlated with the increase of the work function following oxygen adsorption. The process of oxygen adsorption were found to be influenced by the presence of both bridging oxygen vacancies and Ti interstitial species.

The onset method was also used as a tool to study the electron stimulated desorption of oxygen and hydrogen species from the TiO_2(110)-(1×1) surface. A Monte-Carlo simulation was used to estimate how the cross-section of oxygen species is affected by the local the presence of oxygen vacancies, and its value was determined for bombardment energies of 40 and 80 eV. The ESD cross-section of hydrogen species for a bombardment energy of 30 eV was measured by first exposing the surface to water, thus introducing surface OH groups, and then initiating the electron bombardment.

Resumo

Nas formas cristalinas de rutilo e anatase, a superfície do TiO_2 é uma das mais estudadas entre as superfícies de óxidos metálicos, devido à sua potencial aplicação no campo da catálise, entre outras aplicações tecnológicas. A reactividade da superfície do TiO_2 é ditada em parte pela sua concentração de defeitos, tais como lacunas de oxigénio, sendo a sua actividade catalítica afectada pela adsorção de gases atmosféricos, tais como água ou oxigénio. Em trabalhos realizados anteriormente pelo grupo de ciência de superfícies do CEFITEC, as dinâmicas da adsorção de água na superfície $TiO_2(110)$-(1×1) de rutilo foram estudadas através da monitorização da função trabalho durante o processo de adsorção, através da medição da posição do limiar do espectro de energia de electrões secundários (método *onset*). Esta técnica revelou-se bastante útil para a analise das dinâmicas de adsorção, devido à sua extrema sensibilidade a modificação da camada de dipolo da superfície provocada por gases adsorvidos, e ao curto intervalo de tempo necessário para a aquisição de dados. No trabalho aqui apresentado, este estudo foi aprofundado, e o método *onset* foi usado como ferramenta principal, juntamente com XPS, para a realização de uma análise detalhada das dinâmicas de adsorção água e oxigénio na superfície $TiO_2(110)$-(1×1), e como este processo é afectado pela temperatura da superfície, e pela presença de defeitos ou contaminantes.

Inicialmente, o modelo físico que descreve o método *onset* foi revisto, uma vez que alguns dos resultados previamente obtidos com esta técnica não se enquadravam com a sua interpretação corrente. Nesta revisão, foi considerado o campo eléctrico presente entre regiões de uma superfície com funções trabalho locais diferentes, e o seu efeito na posição do *onset* foi calculado em função da morfologia da superfície, e da aplicação de campos eléctricos externos.

As experiências relacionadas com o TiO_2 apresentadas neste trabalho foram realizadas num sistema Kratos XSAM 800. Antes da campanha experimental ser iniciada, este sistema foi actualizado de acordo com as necessidades previstas. O sistema de controlo e aquisição foi substituído, de forma a que tanto as tarefas de controlo como de aquisição de dados pudessem ser realizadas por um PC actual. O espectrómetro foi recalibrado, através da medição da sua função de transmissão, com dois métodos distintos, o habitual método dos primeiros princípios, e um novo método aqui introduzido, que revelou apresentar claras vantagens em relação ao primeiro. Por último, introduziu-se também um método de optimização da função de transmissão do espectrómetro, através da aplicação de um algoritmo de evolução diferencial para procura de uma melhor combinação de tensões dos seus eléctrodos, resultando no aumento da sensibilidade do sistema, em toda a sua gama de energias.

O método *onset* foi depois usado para o estudo da presença de defeitos e adsorção de água e oxigénio na superfície de rutilo TiO_2(110)-(1×1). Introduziu-se um modelo para descrever o processo de adsorção de água, capaz de descrever e explicar os resultados previamente obtidos. A adsorção de hidrocarbonetos, contaminantes que se acumulam no sistema de UHV com o tempo e uso, revelou ter uma influência considerável neste processo. Com a introdução deste modelo, foi possível calcular as constantes relacionadas com a cinética de adsorção, e estimar a concentração de moléculas de água adsorvidas nas linhas de Ti, ou dissociadas em lacunas de oxigénio.

O processo de adsorção de oxigénio foi monitorizado pela medição da função trabalho e XPS. A cinética de adsorção foi determinada para superfícies preparadas com diferentes níveis de redução. A adsorção de oxigénio foi associada a um decréscimo da contribuição de Ti^{3+} no pico Ti 3p obtido por XPS, e obteve-se uma relação linear entre a amplitude deste decréscimo e o aumento da função trabalho causada pela adsorção de oxigénio. Concluiu-se ainda que o processo de adsorção do oxigénio é influenciado tanto pela presença de lacunas de oxigénio, como por iões de Ti intersticiais.

Por último, o método *onset* foi também usado como ferramenta de estudo do processo de desorção estimulada por electrões, de oxigénio e hidrogénio, da superfície TiO_2(110)-(1×1). O método de Monte-Carlo foi usado para estimar a alteração da secção eficaz de ESD do oxigénio é afectada pela presença local de lacunas de oxigénio, e o seu valor foi determinado para energias de bombardeamento de 40 e 80 eV. A secção eficaz de ESD do hidrogénio para energias de bombardeamento de 30 eV foi também medida, através da exposição prévia da superfície a vapor de água, introduzindo assim grupos OH na superfície, seguida pelo bombardeamento por electrões.

Contents

List of Acronyms and Abbreviations

AES	Auger electron spectroscopy
AFM	Atomic force microscopy
AO	Analogue output
ARXPS	Angle resolved XPS
BO	Bridging oxygen
BOV	Bridging oxygen vacancy
CCD	Charge-coupled device
CEFITEC	Centro de Física e Investigação Tecnológica
DFT	Density functional theory
DIET	Desorption induced by electronic transitions
EELS	Electron energy loss spectroscopy
EICO	Electron-ion coincidence spectroscopy
ESCA	Electron spectroscopy for chemical analysis
ESD	Electron-stimulated desorption
FAT	Fixed analyser transmission
FCC	Face-centred cubic lattice
FCT-UNL	Faculdade de Ciências e Tecnologia da Universidade Nova de Lisboa
FRR	Fixed retarding ratio
FWHM	Full width half maximum
GIFAD	Grazing incidence fast atom diffraction
GIXRD	Grazing incidence X-ray diffraction
ISS	Ion scattering spectroscopy
KPFM	Kelvin probe force microscopy
LEED	Low energy electron diffraction
LEIS	Low energy ion scattering
PEEM	Photoemission electron microscopy
PES	Photoelectron spectroscopy
RHEED	Reflection high-energy electron diffraction
SAM	Scanning auger microscopy
SEM	Scanning electron microscopy
SFG	Sum-frequency generation
SHG	Second harmonic generation
SIMS	Secondary ion mass spectroscopy
STM	Scanning tunnelling microscopy
TOF-SIMS	Time-of-flight secondary ion mass spectrometry
TPD	Temperature programmed desorption
TPD	Temperature programmed desorption
UHV	Ultra-high vacuum
UPS	Ultraviolet photoelectron spectroscopy

WF	Work function
WFM	Work function microscopy
WFS	Work function spectroscopy
XPEEM	Energy filtered photoemission electron microscopy
XPS	X-ray photoelectron spectroscopy

List of Symbols

E_{des}	Activation energy for desorption
E_{dif}	Activation energy for surface diffusion
P_{ads}	Adsorption probability
R_1	Analyzer inner electrode radius
R_2	Analyzer outer electrode radius
Φ_A	Analyzer work function
γ	Angle between incident X-rays and measured photoelectrons
L	Angular asymmetry of photoemission
A	Area
β	Asymmetry parameter
S	Atomic sensitivity factor
W	Average slit width
E_b	Binding energy
k_B / k	Boltzmann constant
ξ	Correction function
θ	Coverage
η	Coverage of patches
σ	Cross section
CR	Crossover probability
τ	Dead time
α_{H_2O}	Desorption rate of H_2O adsorbed on Ti row
D	Detector efficiency
d	Diameter
F	Differential weight
μ	Dipole moment
λ_{eff}	Effective attenuation length
Φ_0	Electric potential in vacuum
$\bar{\mu}$	Electrochemical potential
φ	Electron flux
U_{ex}	Extraction voltage
E_F	Fermi Energy
ν	Frequency of oscillation

Φ_H	Higher work function (patch)
λ	Inelastic mean free path
I	Intensity
E_k	Kinetic energy
Φ_{loc}	Local work function
Φ_L	Lower work function (patch)
M	Mass
l	Mean free path
R	Measured count rate
NF	Normalization factor
J_N	Number flux of gas particles
ϕ	Particle flux
E_0	Pass energy
F_0	Patch field suppression extraction field
U_0	Patch field suppression voltage
ΔE	Peak width at FWHM
I_{ph}	Photoelectron current
E_p	Photon energy
α	Polarizability/ Acceptance angle
NP	Population size
P	Pressure
τ_w	Pulse width
R_0	Radius of central path / True count rate
τ_r	Recovery time
U	Sample voltage
Φ_s	Sample work function
s_0	sticking coefficient at zero coverage
τ_{dif}	Surface diffusion time constant
z_0	Surface geometry parameter
τ_{res}	Surface residence time
T	Temperature/Transmission
ε_0	Vacuum permittivity
V_{inner}	Voltage of inner electrode
V_{outer}	Voltage of outer electrode
Φ	Work function
J	X-ray flux intensity
I_x	X-ray gun emission current
P_x	X-ray power

1

1 Introduction

1.1 Context and Goals

The work developed through the course of this thesis was performed in the research laboratory of the Applied Surface Science and Vacuum Technology and Metrology group of CEFITEC, located in the Physics department of FCT-UNL. At the beginning of this work, the surface science laboratory was equipped with a custom ultra-high-vacuum setup with the household name of *Multitécnica* system [1], shown in Figure 1.1. It is capable of performing different surface analysis techniques, namely X-ray Photoelectron Spectroscopy (XPS), Auger Electron Spectroscopy (AES), and Low Energy Ion Scattering (LEIS). A second ultra-high vacuum setup for Time-of-Flight Secondary Ion Mass Spectrometry (TOF-SIMS) analysis is also present in the same laboratory.

This thesis follows the work of Marques [1], which was centred on the growth of metallic films on the rutile $TiO_2(110)$-(1×1) surface, with a smaller focus on its reaction with atmospheric gases, namely O_2 and H_2O. The rutile $TiO_2(110)$ surface is one of the most popular surfaces used in surface science studies, as it is suitable for most surface analysis techniques, and it is relatively easy to create a fresh surface *in situ* through sputter-anneal cycles. It is mostly used as a study model for other metal oxides, and for its application in heterogeneous catalysis, whether as the catalyst itself, or as a substrate for the growth of catalytically active films [2].

Heterogeneous catalysis is a form of catalysis in which the catalyst is in a different state of aggregation from the reactants, with the great majority of heterogeneous catalysts being in the solid state. The study of the different physical and chemical reactions occurring on the surface of these solid catalysts is one of the main research fields in surface science. With the advancement of surface analysis techniques in the last 40 years, the understanding of these processes has grown considerably. In this context, extensive research has also been conducted on new catalytic materials, with modern advancements in nanotechnology providing an almost endless source of different compounds and structures for the creation of catalytic surfaces. In theory, the characteristics of such surfaces can be tuned for maximizing the efficiency of specific reactions.

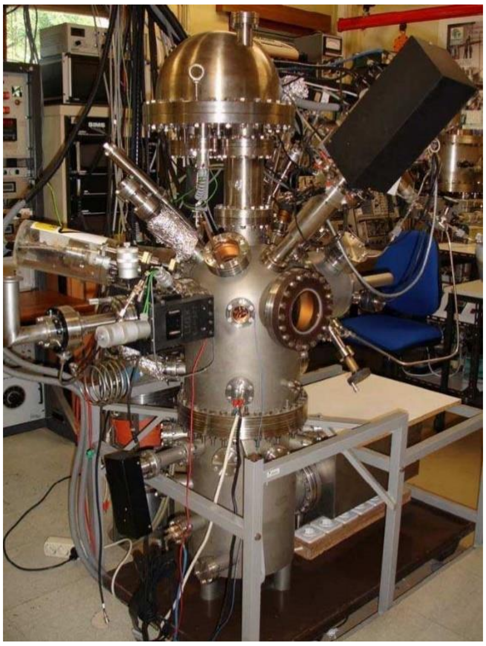

Figure 1.1 - Surface analysis system *Multitécnica*, located in the surface science group of CEFITEC.

The usage of catalysts in the chemical industry is of extreme importance, with up to 90% of chemical processes involving some form of catalysis [3]. With the modern problems related to environmental pollution and climate change, heterogeneous catalysis research has been focused on reducing the emission of harmful gases in various industry processes. Catalytic converters used in the automotive industry are employed to promote the oxidation of CO into CO_2, or the reduction of nitrogen oxides. The rising concern with excessive CO_2 emissions has also lead to a search for heterogeneous catalysts which are able to efficiently promote the hydrogenation of CO_2 to methanol [4,5]. One of the most sought out goals for catalysis is the design of an efficient photocatalyst for water splitting [6]. In this reaction, water would ultimately be converted to hydrogen and oxygen, which could then be used as an energy source without any pollutant by-products. Heterogeneous photocatalysis is a phenomenon which typically occurs on semiconductor materials with a band-gap, such as TiO_2. In this process, as shown in Figure 1.2, the photon energy is used to excite an electron from the valence band to the conduction band, creating an electron-hole pair in the catalyst. If the recombination time of this pair is long enough, it migrates to the surface and drives oxidation and reduction reactions with adsorbed gases [7].

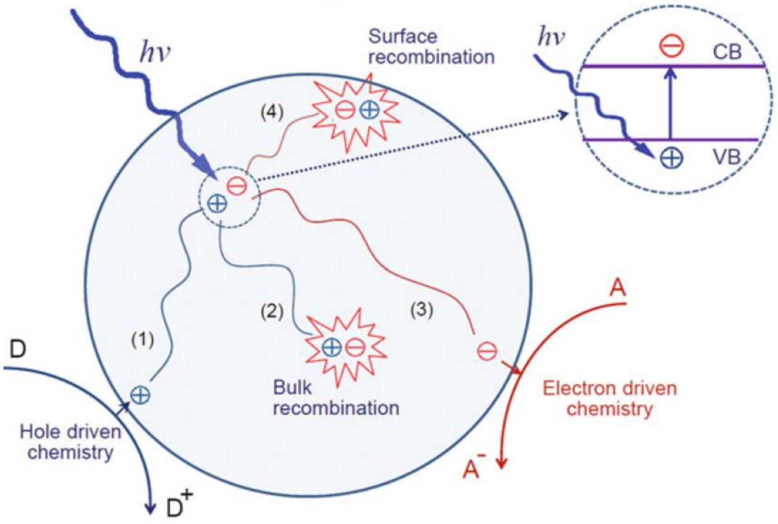

Figure 1.2- Creation of an electron-hole pair by photoexcitation, followed by surface/bulk recombination, or electron/hole (reduction/oxidation) induced surface reactions. Adapted from [7].

The discovery of photocatalytic water splitting on TiO_2 by Fujishima and Honda [8] is responsible for the great interest and modern advancement in the field, with TiO_2 still being the most widely studied photocatalytic material. In either its form of rutile or anatase, TiO_2 has been studied for applications in photo-induced processes related to photovoltaic cells, water and air purification, water splitting, reduction of CO_2 to organic compounds, among others [9]. Of all the different surface crystal planes of rutile and anatase TiO_2, the most widely studied one is the rutile TiO_2(110)-(1×1) surface [2], shown in Figure 1.3, which is also the main focus of study in this work.

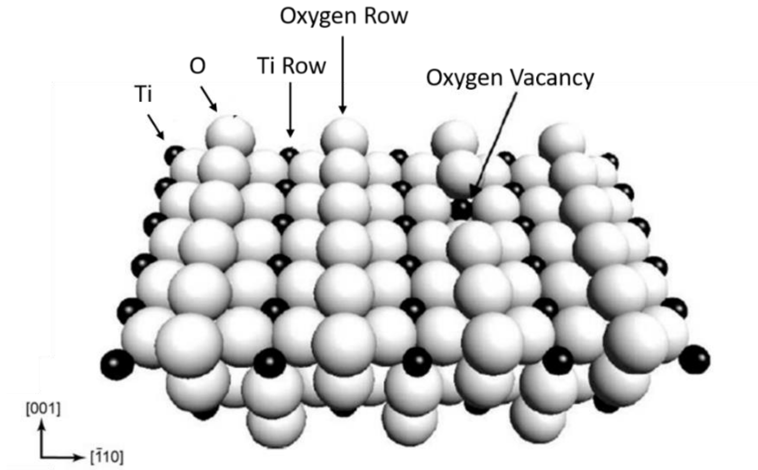

Figure 1.3 – Illustration of the TiO_2(110)-(1×1) surface, showing titanium and oxygen rows, and an oxygen vacancy.

It is established that the reaction of atmospheric gases (O_2 and H_2O) with the TiO_2(110)-(1×1) surface plays an important role in its reactivity, namely in its ability to act as a catalyst. The adsorption of these gases is mainly governed by the defects present on the surface. In the case of the TiO_2 crystal (and other metal oxides [10]), this concentration is generally correlated with the reduction level of the crystal, i.e., its oxygen content levels. The processes used to prepare a fresh surface (sputtering and annealing) lead to a gradual loss of oxygen atoms in the lattice. This in turn generates defects in the surface layers, typically oxygen vacancies, as well as other near-surface defects such as reduced interstitial titanium atoms (Ti^{3+}). Both types of defects are associated with the reactivity of the surface [11–19].

The work of Hugo Marques, performed on the *Multitécnica* system, showed that its instrumentation is not sensitive enough to properly detect and study the adsorption of these gases by XPS. Figure 1.4 shows a set of O 1s XPS spectra taken after a 1 hour exposure to water vapour at a pressure of 1×10^{-9} mbar, with no noticeable shoulder appearing on the H_2O and OH positions.

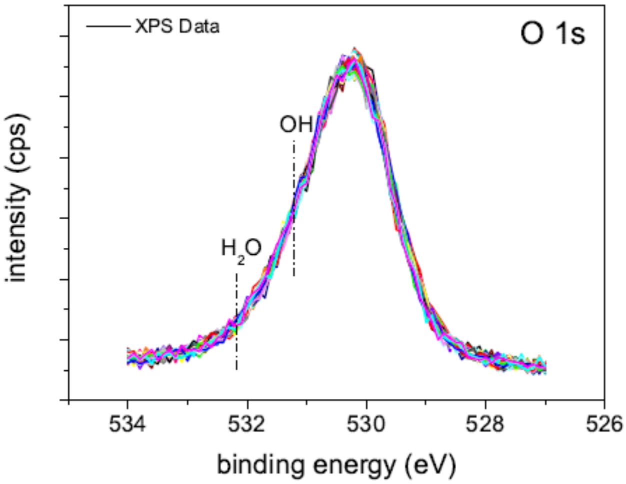

Figure 1.4 – Set of O 1s XPS spectra taken during the surface exposure to water vapour showing no measurable changes in shape [1].

Indeed, the most important fundamental studies of O_2 and H_2O adsorption have mostly been based on Scanning Tunnelling Microscopy (STM) analyses [13,16,20], and modern-day relevant photoelectron emission studies are typically based on Ultraviolet Photoelectron Spectroscopy (UPS), or have either been performed with synchrotron radiation or ambient pressure XPS [21]. However, as significant as STM based studies have been for detailed analysis of adsorption on specific defect sites, they may represent a somewhat limited picture of surface phenomena, due to the fact that these studies are typically focused on analysing flat, wide terrace areas. These may not be representative of the whole sample surface, particularly in the case of a realistic catalyst.

In his work, Marques studied water adsorption by measuring the work function change, based on the low-energy cut-off of the secondary electron energy distribution (designated onset position). It is generally accepted that H_2O is weakly adsorbed on surface Ti rows, and suffers dissociation on bridging oxygen vacancy sites (BOVs), forming two OH groups in the process. A correlation was found between the reduction level of the crystal and the amount of adsorbed water, as the work function change due to water adsorption was more pronounced in highly defective surfaces [22]. Work function decreases when water is adsorbed, due to the vacuum oriented dipole of both the water molecule and the pair of OH groups. Results showing the shift of the work function (low energy cut-off) are shown in Figure 1.5, for a) the new (stoichiometric), and b) the old (reduced) crystal.

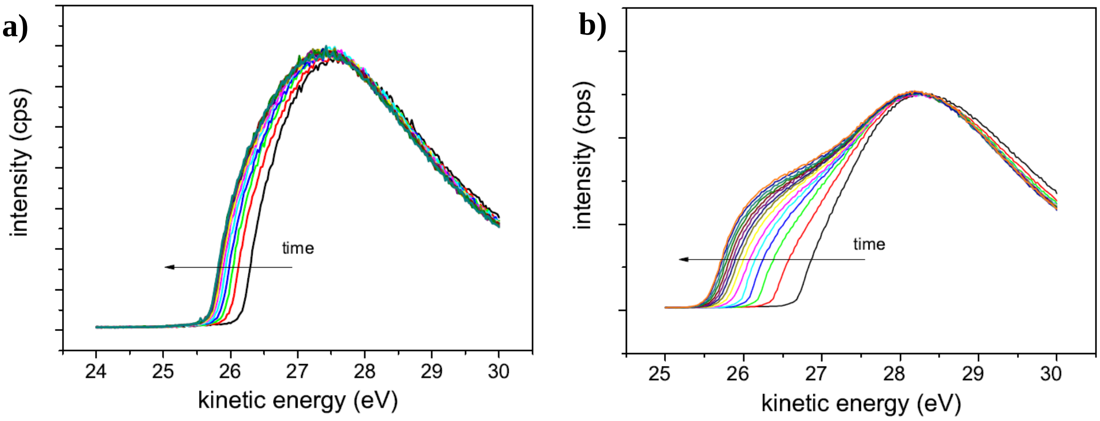

Figure 1.5 – Shift of the low-energy cut-off of the secondary electron distribution during exposure to water, for the stoichiometric (a) and reduced (b) crystals [22].

Further work performed by our group [23–25] continued to demonstrate that the analysis of the work function change is able to provide adsorption information that is not obtainable by XPS analysis. The technique is particularly useful due to its high sensitivity to minor surface changes, and the very low acquisition time required, which allows for a real-time monitoring of the adsorption process. It is possible with this technique to track the adsorption of both H_2O and O_2 gases, as shown in Figure 1.6 a).

Following these studies, some important questions regarding the work function change during the adsorption of water still remain. These questions are related to the nature of the slow, exponential decay of the work function, which appears to always be present in the background, independent of the H_2O pressure. The change of the work function due to the water desorption is also not accurately modelled (when water exposure is interrupted, the work function increases, presumably due to desorption of weakly bound H_2O molecules from Ti rows). Both of these situations are shown in Figure 1.6 b).

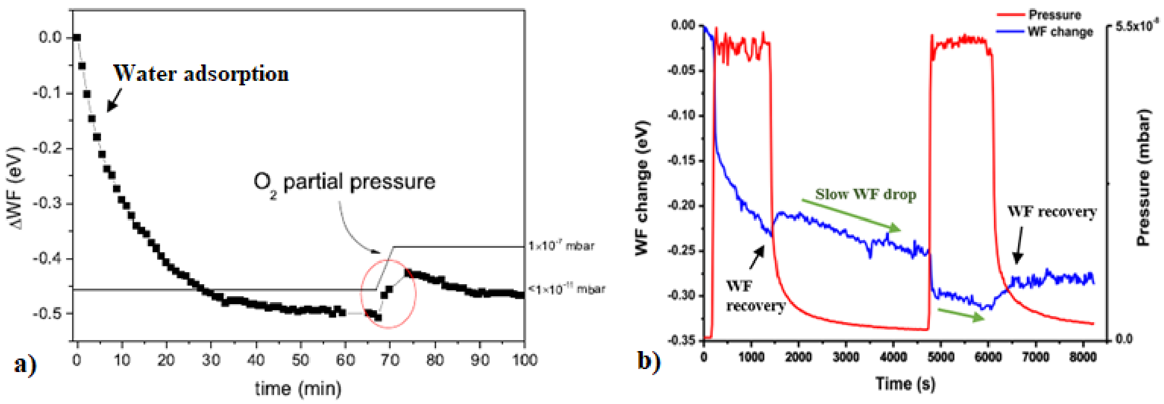

Figure 1.6 – Work function change during a) water and oxygen adsorption [22], and b) water adsorption in cycles[25].

Finally, a fundamental question remains concerning the interpretation of the low energy cut-off shift of the secondary electron energy spectra: how is this shift related to the work function change? In particular, there is a problem with the interpretation of the gradual shift of the low energy cut-off (onset position) as a function of gas exposure or during thin film deposition. If the onset position corresponds to the minimum value of the different local work functions of the analysed area, as previously thought, it should abruptly shift during the deposition/adsorption of a lower work function material for a value equal to the difference between the substrate work function and the work function of the deposit/adsorbate. At the same time, when a material of higher work function material is deposited/adsorbed, there should be no change of the onset position. However, this shift appears experimentally in both directions: towards lower energies when TiO_2 is exposed to water vapour or when silver is deposited, but in the opposite direction during the deposition of gold on TiO_2 or when this surface is exposed to oxygen [1]. In addition, the shift is apparently proportional to the surface coverage of deposited or adsorbed species. These observed problems concerning the interpretation of the onset position imply the need for a revision of the physical model behind this measurement technique.

Before the start of this work, the laboratory acquired a second ultra-high vacuum system capable of performing XPS, the Kratos XSAM 800, which is equipped with better instrumentation than the *Multitécnica* system [26]. This includes an X-ray monochromator, a larger energy analyser, and three channeltron electron multipliers (as opposed to one), which together should produce an XPS signal with a better resolution and higher intensity. Also, it is capable of reaching a lower base pressure, which is essential for avoiding adsorption of contaminants during the planned experiments. This Kratos system was controlled by an outdated computer (PDP-11 series), and a decision was made to upgrade the control and acquisition system, replacing the old computer with a modern PC, allowing easy access to the data in a standard file format, and a programmable control of the system's parameters. Following this upgrade, the system must be properly characterized, which mainly involves measurement of its transmission function (required for accurate XPS quantification analysis). Furthermore, the now fully programmable control of the system can be used to try and perform an optimization of its parameters, further improving the signal-to-noise ratio of the XPS measurement.

The aim of this thesis is to use Work Function Spectroscopy (WFS) based on the onset method, together with XPS, to study the adsorption of O_2 and H_2O gases on the $TiO_2(110)$-(1×1) surface, and how it is influenced by the presence of surface defects. To reach this goal, a series of activities is planned:

- The Kratos XSAM 800 setup will be mounted, the electronics of its control system will be replaced, and new software shall be developed to perform XPS analysis, among other possible functionalities. The XPS system should be characterized, mainly by measuring the transmission function of the charged particle detection system (energy analyser and electron-optics), which is of particular importance following a change of the control system electronics, as minor changes of the control voltages could result in a different transmission function. Finally, an optimization of the charged particle detection system is planned, which could be accomplished by applying an automatic search algorithm to the control voltages in order to experimentally find the optimized system parameters. This should increase the system's sensitivity and thus facilitate the detection of minor surface changes.
- The physical model that is used to describe the onset position will be revised, so that the previously mentioned results can be explained. This should involve a review of the literature concerning the subject, with the goal of better understanding the nature of the onset position, and how it relates to the work function surface distribution. To help with this goal, a set of experiments on samples with a well-controlled work function distribution should be performed, while also running charged particle simulations in parallel to help create a new model to describe the measurement.

A new set of experiments on the $TiO_2(110)$-(1×1) is then planned.

- First, a method to prepare this surface in a reproducible manner should be established, as well as finding a reliable way to measure the surface state, and thus confirm the reproducibility of the surface preparation. Additionally, a way of controlling the amount of surface defects is essential, so that the influence of the concentration of defects such as BOVs on gas adsorption (mainly H_2O and O_2) can be examined. In a first analysis, this could be accomplished by adjusting the sputter-anneal parameters, or by producing defects in a more controllable manner by electron-stimulated desorption (ESD).

- Second, the fundamental nature of the exponential decay of the TiO_2 work function when exposed to residual gas should be investigated. A possible approach is to expose the surface in a controlled way to different sources of work-function change that could possibly be present in the system. These include the individual exposure of different gases that are part of the residual gas at a higher pressure (such as H or H_2), exposure of the surface to different intensities of X-ray radiation, as it is known to create surface defects, or by eliminating possible sources of contamination such as hot filaments.
- Finally the study of the adsorption of H_2O and O_2 (also possibly other small molecules such as CO or H/H_2) on the $TiO_2(110)$-(1×1) surface will be addressed by work function and XPS measurements. This will require following the work function change in real time during the exposure to these gases of surfaces prepared with different defect concentrations. Hopefully, the creation of an adsorption model that describes the adsorption kinetics of these gases can be reached. The detailed plan on the performed experiments depends on the observations that will be made along the course of this work.

1.2 Structure of Thesis

Having in mind the aim and the goals of this work described in the previous section, the structure of this document is described below.

An introduction to basic concepts related to surface science, as well as the principles and instrumentation behind the XPS and work function measurement techniques used throughout this work, are described in chapter 2.

Chapter 3 presents a detailed description of the Kratos XSAM 800, an ultra-high vacuum (UHV) system equipped with XPS instrumentation, which was used to perform all the work related to the TiO_2 surface, including surface preparation, modification (gas exposure, electron/ion bombardment, etc.) and analysis. The details of the upgrades performed to this system, which were essential to operate it and conduct the experiments, are also presented. This includes the update of the data acquisition system (control electronics and software), measurement of the detector non-linearity and spectrometer's transmission function, and finally its optimization.

In chapter 4, the experimental and theoretical investigations aiming to reveal the correct physical interpretation of the work function measurement based on the low energy cut-off of the secondary electron energy spectra are presented, and a new semi-empirical model is established. This includes a review of related literature, and the execution of computer simulations and experimental work, performed with the goal of refining and ultimately confirming this revised model.

The work performed on the rutile $TiO_2(110)$-(1×1) surface, which composes the central part of this thesis, is presented in chapters 5 and 6. In chapter 5, the $TiO_2(110)$-(1×1) surface is described, and a review of the relevant literature related to surface defects and the adsorption of water and oxygen is presented. Additionally, the ESD technique is introduced, and the published works performed on the TiO_2 surface using this method are reviewed. Chapter 6 includes all experimental investigations of the dynamics of different processes taking place on the rutile $TiO_2(110)$-(1×1) surface. These include:

- Surface preparation and related defects
- Adsorption of water and oxygen molecules on surfaces prepared with different concentrations of defects, and its relation with hydrocarbon contamination
- Monitoring the desorption of oxygen and hydrogen species by low energy electron bombardment through the ESD process.

These processes were monitored through XPS and work function measurements, and led to the development of physical models that aim to accurately describe the experimental measurements, allowing the quantification of important magnitudes, such as the adsorption and desorption rates of water and oxygen species, as well as their ESD cross-sections.

Finally, chapter 7 presents the summary and conclusions of the work performed, where the most important activities and findings are reviewed.

2

2 Background

2.1 Surface Science

The early stages of surface science can be dated to the beginning of the 20th century, with the first studies of surface chemical processes in heterogeneous catalysis. Most significantly, it was discovered that some metal surfaces can be used as a catalyst in important chemical processes, such as the hydrogenation of organic compounds (Sabatier process) or the production of ammonia (Haber-Bosch process). Modern surface science emerged in the 1960s, driven in part by the development of the semiconductor industry, in which the surface properties of the semiconductor materials play a critical role. Some of the basic processes linked to particle-surface interactions (sputtering, secondary emission, ion scattering/implantation) were also described, motivated by the research linked to controlled fusion, and the need to describe the plasma-wall interactions inside fusion reactors. Improvements in vacuum technology allowed UHV pressure levels to be reached, which, together with the development of high-speed digital computers, lead to the emergence of a number of new and innovative methods for the analysis of surfaces [27,28].

Fundamental studies of surfaces aim to describe their structure and composition, and how these affect chemical and physical processes that take place on a surface exposed to different environments. In order to minimize the variety of these processes during analysis, and to be able to study each one independently and in a reproducible manner, it is essential that the structure and chemical composition of a surface are well-defined. For this reason, modern surface science studies are typically performed on low index planes of single crystal surfaces, in a UHV environment.

In the case of ideal single crystals, in opposition to polycrystalline or amorphous materials, the whole surface is identical and behaves in the same way, as it is composed of periodic unit cells. Figure 2.1 shows an example of a face-centred cubic lattice (FCC), and the corresponding surface structures and unit cells of the non-reconstructed (100), (110) and (111) planes.

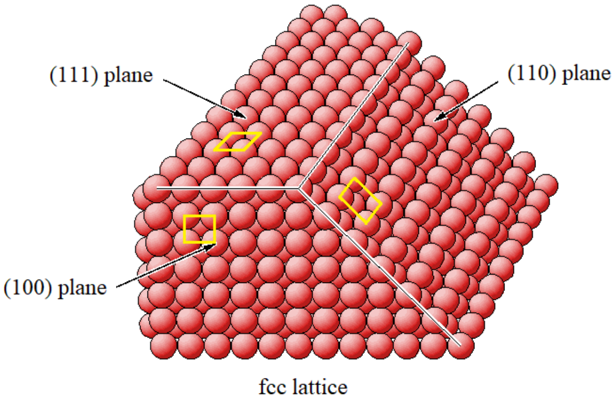

Figure 2.1 – Low index surface planes of FCC lattice. Yellow lines mark the surface unit cells of these planes.

Once ideal crystalline surfaces are well understood and models have been created for the different processes occurring on them, different kinds of irregularities and contaminants can be added in a controlled manner in order to simulate systems of a higher complexity. This way, it is possible to check if the models created are still valid in other, more realistic scenarios. The study of surfaces is of great importance, both in terms of fundamental understanding of materials, and in real world applications. For a surface to be created, the bonds in the solid lattice have to be broken, which requires an energy transfer to the material. Surfaces are thus more energetic than their bulk counterpart, with an energy (surface free energy) that can be understood as half the energy required to divide a solid in two, i.e., breaking the bonds in the bulk to create two identical surfaces.

Inside the bulk of a solid material with crystal structure, electrons travelling along the lattice experience a periodic potential energy. At the surface, the symmetry of the bulk material is broken as the periodicity of the lattice is abruptly interrupted perpendicularly to the interface, leading to a change of the electron wave function. Figure 2.2 a) shows the one-dimensional solution of the Schrödinger equation, when periodicity of the lattice potential is broken at the surface (solid curve), resulting in a surface state (dashed curve). At the interface between the surface and the vacuum, the potential energy of the bulk is modified to that of the vacuum level. An energy barrier originates at the surface due the absence of positive ions above the surface (vacuum potential), and the creation of an electron dipole layer. Figure 2.2 b) shows the distribution of electric charges (electron density) at the surface interface according to the jellium model. In this quantum mechanical model, positive charges are assumed to be uniformly distributed throughout the solid, so that the interacting electrons occupy a flat potential well. It is shown that, at the surface, the electrons "spill out" into the vacuum, creating a dipole layer that increases the energy barrier for electron removal from the material. The energy required to overcome this barrier and remove an electron from the surface of the material is the so-called work function [29].

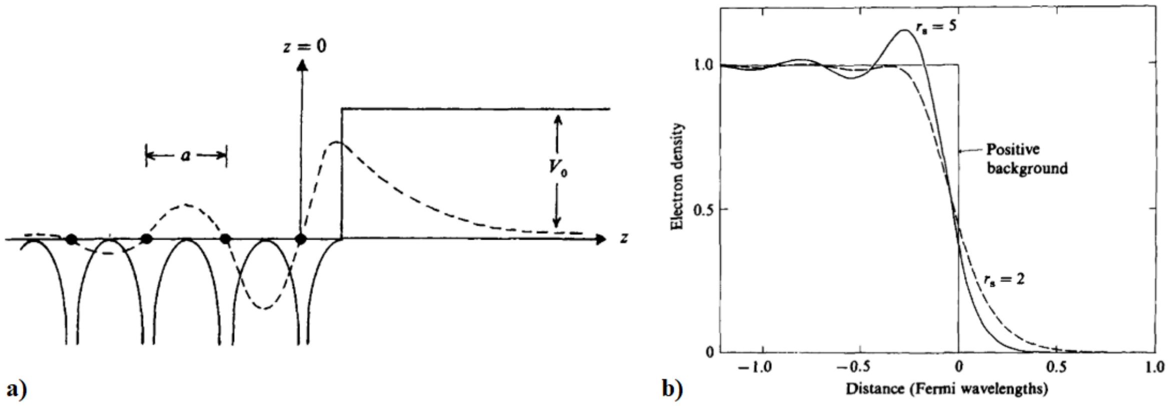

Figure 2.2 - a) One-dimensional semi-infinite lattice model potential (solid curve) and an associated surface state (dashed curve). b) Electron density profile at a jellium surface for two values of the background density, r_s [29].

These models describe the types of surface states that can occur on metal or narrow band gap semiconductor surfaces, as the nearly free electron model is used to solve the Schrödinger equation (so called Shockley states). In other materials where the atoms are more tightly bound and the free electron model isn't accurate, such as wide-gap semiconductors or transitional metals, Tamm states occur. These distinct surface electronic states are associated with the orbitals that would be responsible for bonding in the bulk. In losing their closest neighbours, former bonding orbitals of surface atoms will "stick out" from the surface, in what is called a dangling bond. The energy levels of these states may differ significantly from those of the bulk. Additionally, other electronic states are expected at surface defect sites (vacancies, kinks, ledges, adatoms, etc.), adsorbate sites, or interfaces between two materials, as is often the case with semiconductor devices. The variety of physical and chemical properties of surfaces is explained by the changes in their atomic and electronic structure, and processes such as adsorption, chemisorption or chemical reactions at surfaces may be considerably affected by these changes [27,29].

2.1.1 Surface Science Studies

Possibly the greatest focus of modern surface science studies is on understanding the mechanisms of heterogeneous catalysis. As already stated, in this process, the rate of a certain chemical reaction is increased by the presence of a specific solid surface (the catalyst), without its significant modification or consumption in the reaction. The main role of a catalyst is to reduce the activation energy of a chemical reaction. In principle, the adsorption of the reaction species (one or both) on the catalytic surface leads to an change of some of its properties, which in turn increases the reaction probability, i.e. the catalytic surface acts as a playground for the components of the reaction to interact with each other in a certain, desired way. One of the most important mechanisms in this process is the capability of a catalytic surface to enable efficient dissociative adsorption of one of the reaction molecules. The example in Figure 2.3 shows how the dissociation of the H_2 molecule on a catalytic surface leads to the facilitated hydrogenation of ethylene into ethane. The highest barrier in this reaction corresponds to the energy necessary to break the bond between the H atoms in the H_2 molecule. Since this step is performed by the catalytic surface on adsorption, the reaction rate between H_2 and C_2H_4 is thus increased [30].

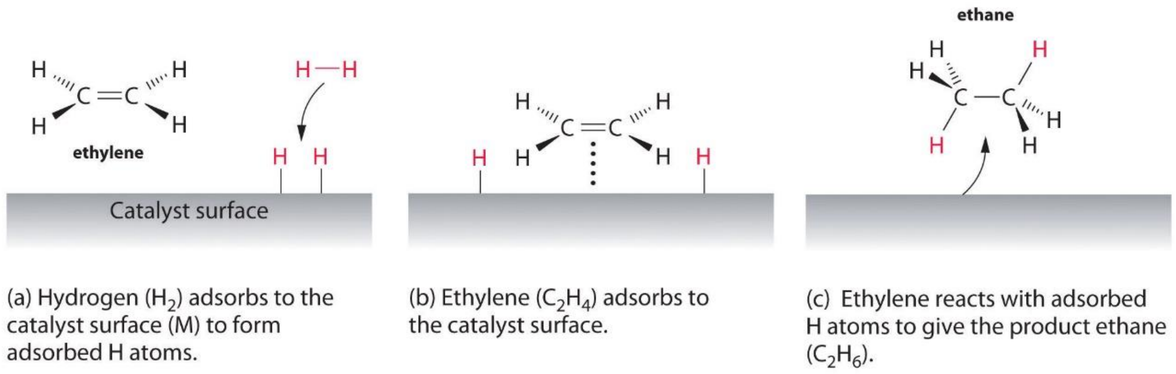

Figure 2.3 – Hydrogenation of ethylene on a heterogeneous catalytic surface. The adsorption of the H_2 molecule replaces the H-H bonds with new M-H, leading to the more reactive, individual H atoms to react with the ethylene molecule [30].

The role of surface science in heterogeneous catalysis studies is to describe the adsorption mechanisms, find a link between the adsorption efficiency and the surface characteristics of the catalytic material, and finally comprehend how this affects the rate of certain reactions. Understanding and controlling these processes will ultimately lead to the creation of more efficient catalysts. In the last decades this field has grown considerably, driven by the growing concern related to the environmental impact of greenhouse gas emissions, and the need of producing catalysts capable of reducing these emissions.

Modern material research in the field is focused on the growth of catalytic nanostructures, which can either be supported on highly porous surface substrates (maximizing surface to volume ratio), or grown on micro powder supports. In this way, the surface-to-volume ratio of the substrate is maximized, while the properties of the catalytic active nanostructures can be tuned for enhancing specific reactions. Analysis techniques have also been advanced to study these materials in increasingly realistic scenarios, such as the study of the interaction between the catalyst and reaction gases at ambient pressures, instead of the classic studies performed at UHV vacuum levels [30].

A different focus of surface science is the study of material corrosion [28]. The corrosion process generally occurs when the surface of a material, typically a metal, is exposed to an oxidant, typically oxygen or water, which continually reacts to create a more stable compound (metallic oxide). Since this process transforms the base material and changes its properties, it is important to understand it. Different surface analysis techniques are used to study this oxidation process. This includes the study of the chemical nature of the oxides formed at the surface, the depth profile of the oxide layer, or how the surface segregation of specific species affects the oxidation process. Performing this type of research requires analysis techniques which are extremely surface sensitive, having an information depth of few atomic monolayers, as well as the ability to remove these layers of material in a controlled manner, typically achieved through ion bombardment (sputtering). Surface studies are also focused on the different methods to protect a surface from corrosion. This protection can be made by applying protective coatings such as paints or galvanization, or by manipulating the properties of the oxide layer itself to prevent further oxidation, with processes such as anodization, or the addition of specific impurities to the material, which segregate to the surface and create a more stable oxide layer. This method is often used to create metallic alloys with lower corrosion rates, such as the addition of chromium (as well as other elements in smaller quantities) to stainless steel.

Surface science is also a very important part of the semiconductor industry [28]. The properties of semiconductor junctions are highly dependent on the surface characteristics of the materials, and the chemical reactions that are expected between the two. Because semiconductor devices are generally built on well-oriented single crystal materials (mainly Si and different III-V and II-VI semiconductors), the typical knowledge acquired in fundamental surface science analyses is of direct interest for this application. The growth and analysis of different structures/thin-films on semiconductor substrates using techniques such as molecular beam epitaxy or photolithography is also a focus of surface science studies. In order for these multi-layer devices to be correctly manufactured, the thin-film growth process on these materials must be well understood.

Aside from the aforementioned industry-related applications, surface science studies which are focused on particle-surface interactions are of great importance for some scientific research fields. These play a crucial role on fusion reactors due to the interaction between the plasma and the inner walls of the reactor, and will also be present in any plasma reactor, such as those used on magnetron-based coatings [31]. They are also a major reason for the reduction of particle beam quality in particle accelerators, due to the electron cloud effect, where stray electrons are hit by the particle beam, are accelerated and collide with the walls, which in turn generates more electrons (secondary electrons), resulting in a potentially exponential process [32]. This is also the process by which charged particle detectors based on electron multiplication work, as shown in Figure 2.4. A single charged particle (electron or ion) creates a chain reaction of secondary electron emission inside the detector, which results in a measurable current pulse.

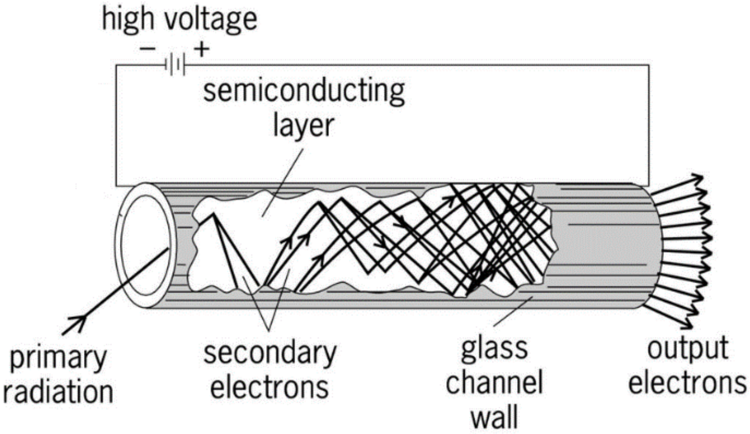

Figure 2.4 – Cutaway view of an electron multiplier [33].

2.1.2 UHV in Surface Analysis

Ultra-high vacuum is defined as an environment with a pressure lower than 1×10^{-9} mbar. UHV conditions are essential to prevent contamination of a surface during the analysis process, while also allowing its exposure to other species in a controlled way [27,28,34,35]. The number flux of gas particles J_N for an ideal gas (i.e., the number of atoms/molecules passing through a surface of unit area in unit time) is given by:

$$J_N = \frac{P}{\sqrt{2\pi k_B T m}} \tag{2.1}$$

where P is the pressure, k_B is the Boltzmann constant, T is the gas temperature, and m is the mass of the particles. From this value it is possible to estimate the contamination level of a surface. At room temperature, and a pressure of 10^{-8} mbar of pure N_2, 5 minutes is enough for the adsorption of a new monolayer (assuming all impinging particles stick to the surface). For this reason, pressures in the 10^{-10} mbar range are essential, as the duration of surface analysis experiments can be in the hours range, and the surface must remain unaltered during this period.

There are additional reasons for the requirement of very low pressures in surface analysis, related to the analysis techniques themselves. These techniques usually require the surface to be bombarded with some type of particle (ions, electrons, photons), and the subsequent detection of emitted particles from the surface following this bombardment. It is therefore required that the mean free path of these particles while travelling through the vacuum system is sufficiently long to reach the sample/detector without interacting with the particles from the environment, i.e., without colliding with gas particles in the system. The mean free path of an ideal gas particle in a pressurized environment is given by:

$$l = \frac{k_B T}{\sqrt{2}\pi d^2 P} \tag{2.2}$$

where πd^2 can be considered as the effective cross-sectional area for a spherical particle of equivalent diameter d. In the UHV pressure range, this distance is in the tens of km range, which becomes relevant only in the largest particle accelerators. An additional reason for using low pressure values for surface analysis is the common necessity of applying high voltages across a few millimetres inside the vacuum system, which is a typical requirement when focusing and accelerating charged particles, as well as for the generation of X-ray radiation. High-vacuum levels are thus required to prevent an electrical breakdown through the gas due to these strong electrical fields. Even though UHV pressure levels are already a requirement for a stable surface during analysis, in some cases, such as with ambient pressure XPS, the sample is exposed to gases at relatively high pressures, while the detection system must remain in high to ultra-high vacuum levels. Through the addition of several differential pumping stages between the sample and the detector, it is possible to maintain the region surrounding the sample at a high pressure, while sufficiently reducing the pressure in the detector so that emitted particles are still able to reach it.

2.1.3 Surface Analysis Techniques

The variety of surface analysis techniques that have been developed provide researchers with insights into the structure, composition, electronic states and vibrational properties of the analysed surfaces [27,28]. In general, all surface analysis techniques work in a similar way: a) the surface is irradiated by a particle beam (electrons, ions, neutrals or photons), b) as a result of particle-surface interactions, other or the same particles are emitted c) the properties of outgoing particles (energy, mass, wavelength etc.) are measured. The different combinations of ingoing and outgoing particles in different energy ranges encompass almost all surface analysis techniques. Additionally, these techniques may also provide an ability to perform surface microscopy, either by scanning the probing particles through the surface, or by being able to detect the outgoing particles with spatial resolution, creating an image of the surface. Some techniques do not follow this analysis method, such as STM or atomic force microscopy (AFM). These employ a physical probe (tip) that is scanned over the surface with atomic resolution, while performing some type of measurement based on the surface-tip interaction (position, electric current, capacitance, among others).

Surface analysis techniques can be generally divided in four groups [28]. Diffraction methods are typically used to characterize the structure of surfaces, by analysing the patterns of particles/waves which are scattered from the surface. This can be performed by either bombarding the surface with electrons, in techniques such as the Low Energy Electron Diffraction (LEED) or Reflection High-Energy Electron Diffraction (RHEED), atoms in Grazing Incidence Fast Atom Diffraction (GIFAD) [36] or by X-Ray irradiation and analysis of the diffraction patterns in Grazing Incidence X-Ray Diffraction (GIXRD).

Electron spectroscopy methods, which include all techniques involving the measurement of the energy spectrum of electrons emitted/scattered from the surface. In the energy range which is typically measured (5-2000 eV), the inelastic mean free path of electrons travelling through the material, shown in Figure 2.5, is such that the analysis becomes highly surface sensitive, as electrons from deeper layers have a high probability of losing energy on their way towards the surface through interactions with the material.

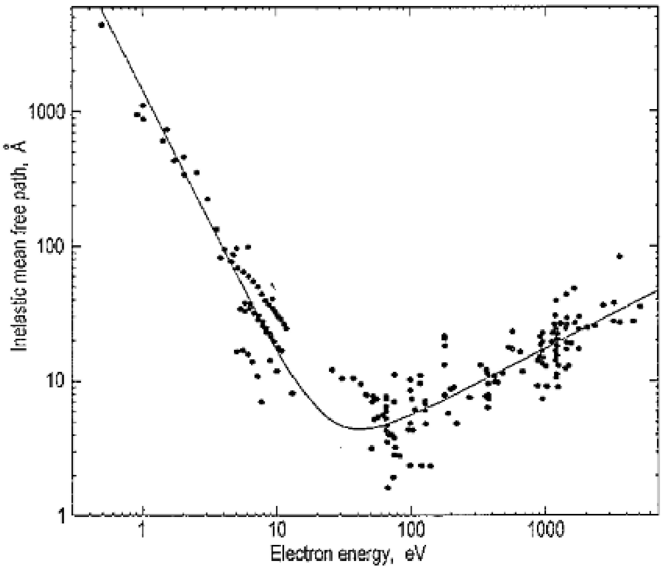

Figure 2.5 – Collection of experimental data of the inelastic mean free path of electrons as a function of their energy above the Fermi level for different materials. The full curve is the empirical least squares fit over the complete energy range [27].

Typically, electrons which have not suffered any energy loss will be identifiable in the spectrum (peaks), and will thus provide information exclusively from surface layers. With these techniques, the energy levels of electrons in the material can be probed, providing insights into the electronic structure of the surface, such as the types of chemical bonds between surface atoms or the presence of surface energy states related to defects or other surface-induced changes. The most common electron spectroscopy analysis methods are AES, Electron Energy Loss Spectroscopy (EELS), or photoelectric effect based techniques, such as XPS or UPS.

Ion probing methods are those involving surface bombardment by ions. While some of these methods cannot be used in all cases due to their destructive nature, in other cases it is essential, such as when performing a depth profile analysis which requires gradual removal of surface atoms. The main analysis techniques based on ion bombardment are the Ion Scattering Spectroscopies (ISS) at low, medium, and high energies, and Secondary Ion Mass Spectroscopy (SIMS). In the former, information on the surface is obtained by measuring the energy loss of scattered ions, while the energy of impinging ions determines the information depth (low energy being more surface sensitive). In the latter, ion bombardment is used to directly sputter ions from the surface, which are then mass analysed.

Microscopy methods are those in which an image of a surface is produced by the analysis. Scanned focused electron beams can be used to produce surface microscopies, in techniques such as Scanning Electron Microscopy (SEM), or Scanning Auger Microscopy (SAM). Other techniques employ the scanning of a mechanical tip over the surface, such as the previously mentioned STM or AFM. With their atomic resolution and ability to probe the surface in various ways, these techniques have been of particular importance in the study of surfaces, being capable of obtaining information on surface structure/reconstruction, concentration and types of surface defects and contamination, adsorption sites for different gases, nucleation sites for growth of nanostructures, diffusion/mobility of adsorbates at the surface, local electronic structure, among other capabilities.

Additionally, there are other surface analysis techniques which do not fall into these main categories, such as those involving the stimulated desorption of material from the surface. One example is Temperature Programmed Desorption (TPD), in which the sample is heated at a certain rate and mass analysis of the desorbed atoms/molecules is performed. A similar concept is used in ESD, where the electron bombardment of a surface at certain energies promotes electron excitations that ultimately result in desorption of surface species. As in the case of TPD, the desorbed species can also be identified by mass analysis. Optical methods can also be used for the study of surfaces. Although most optical spectroscopies have a large information depth, and are thus not considered as surface analysis techniques, this is not the case with non-linear optics methods such as Second Harmonic Generation (SHG) or Sum-Frequency Generation (SFG) [37].

In this work, the main methods of surface analysis which have been used for the study of the TiO_2(110)-(1×1) surface are XPS, and a work function measurement method based on the cut-off energy of secondary electrons (onset method), which can be performed with the same instrumentation as that of XPS. The XPS analysis technique and its instrumentation will be described in detail in the following section, and the work function measurement based on the onset position will be addressed in chapter 4.

2.2 X-Ray Photoelectron Spectroscopy

2.2.1 Introduction

X-ray Photoelectron Spectroscopy, also known as Electron Spectroscopy for Chemical Analysis (ESCA), is a surface analysis technique used to measure the concentration of different elements present at the surface, down to relative concentrations of 0.1%, and which is also able to provide information on their chemical and electronic state. This analysis method is thus used to characterize the composition of surfaces, by quantitatively and qualitatively determining the types of bonds between elements in the material, as well as the presence of surface defects or contaminants [27,28,38].

This technique is based on the measurement of the energy spectrum of core electrons emitted by photoelectric effect, with X-rays as a radiation/excitation source. When a material is irradiated with an X-ray beam, electrons are excited by the X-ray photons, and are consequentially emitted with a certain kinetic energy E_k, as shown in Figure 2.6.

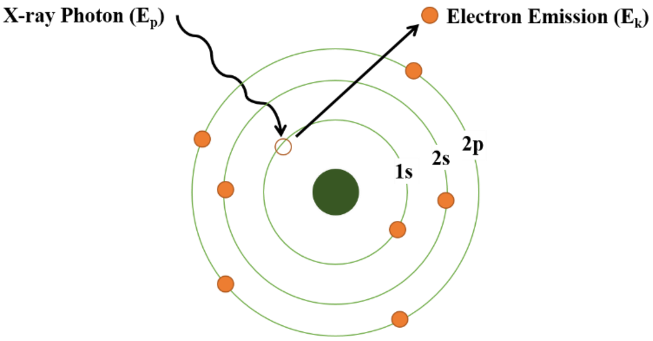

Figure 2.6 – X-ray photon absorption by a core level electron and subsequent photoelectron emission.

For a photoelectron situated just above the sample surface, E_k is equal to the photon energy E_p minus the energy needed to remove the electron from the material, which is the sum of the binding energy E_b and the work function of the sample $\Phi_s = E_{vacuum} - E_{Fermi}$.

$$E_k = E_p - \left(E_B + \Phi_s\right) \tag{2.3}$$

Each core electron in an atom has a binding energy which is a function of its principal quantum number $n = 1, 2, 3...$, orbital quantum number $l = 0, 1, 2...n-1$, and total angular momentum $j = |l + s|$, where s is the magnetic spin number. In XPS analysis, each core level is thus identified with the nomenclature nl_j. Orbital levels with $l > 0$ give rise to a doublet with two states having slightly different binding energies, known as the spin-orbit splitting. The intensity ratio between these doublets is determined by the ratio of the degeneracy of each j state $(2j+1)$.

Table 2.1 – Spin-orbit splitting *j* values for each subshell and intensity ratio of the corresponding doublet

Orbital number (subshell)	***j* values**	**Doublet Intensity Ratio**
s	1/2	-
p	1/2, 3/2	1:2
d	3/2, 5/2	2:3
f	5/2, 7/2	3:4

Table 2.1 sums up the possible values of *j* for each *l* value (subshells *s, p, d* and *f*), and the approximate intensity ratio of the corresponding doublet. It should be stressed that, in practice, this ratio is only correct when the energy splitting is sufficiently small, as the doublet will have different attenuation lengths, photoionization cross sections, and spectrometer transmissions if the energy difference is too large.

Since the binding energies of core-levels differ between elements, the intensity distribution of the photoelectron kinetic energies upon X-ray irradiation (i.e., the amount of electrons emitted for each energy value), called an energy spectrum, is a fingerprint of the element, and can be thus used to identify it, as well as quantifying its relative amount in the analysed material.

The binding energy for each core level as a function of atomic number is shown in Figure 2.7. Each of these levels will appear in the energy spectrum as an intensity peak, at the corresponding binding energy of excited core electrons that leave the sample's surface without losing energy beforehand. With this information, any peak corresponding to a photoelectron originating from direct X-ray excitation can be associated with the corresponding element. Except for hydrogen and helium, all elements of the periodic table can be identified in this way by XPS analysis.

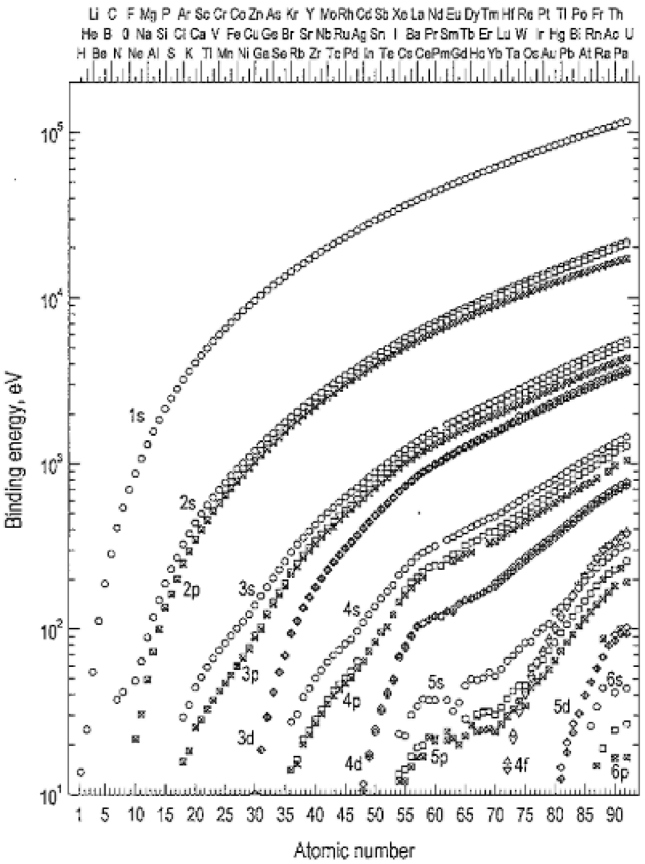

Figure 2.7 – Binding energies of core levels for elements with atomic number up to 90 [27].

The complete energy spectrum (also called survey spectrum) obtained from the irradiation of a clean, pure titanium sample with photons from the Mg Kα transition (1253.6 eV) is shown in Figure 2.8. The peaks from different core electron levels appear at distinct binding energies, and their exact position can be used for the identification of an element. In this case, apart from the highest intensity peaks originating from titanium, traces of argon can also be identified by the presence of two small peaks in the 200-400 eV region, which correspond to the typical binding energy of argon 2s and 2p electrons (argon ions can be implanted on surfaces during the sputter-cleaning process). As will be explained in detail in section 2.2.3, the areas of each peak can be used to calculate the concentration of each element in the analysed surface. Other characteristics and features of typical XPS spectra which can be seen in this spectrum (Auger peaks, inelastic collision tails, satellite peaks, etc.), will also be explained in section 2.2.2.

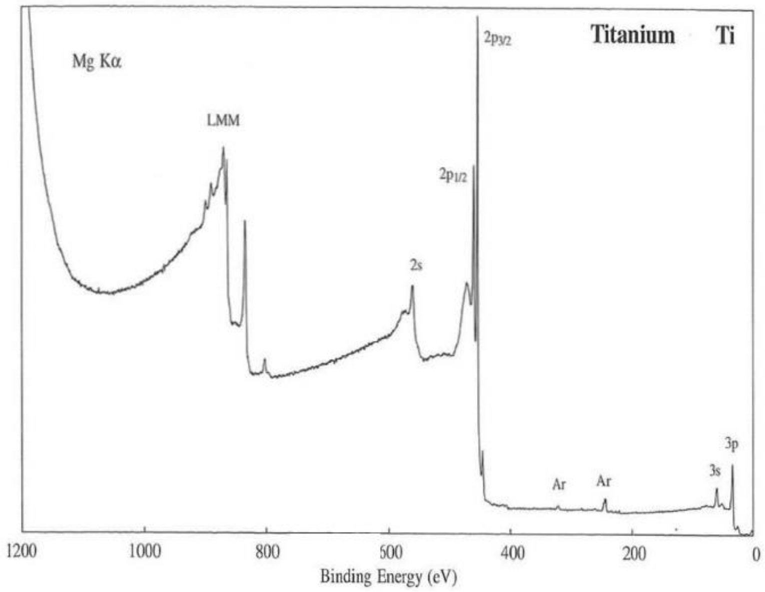

Figure 2.8 – XPS survey spectrum obtained from the irradiation of a titanium sample with photons from the Mg Kα transition [38].

The binding energy of core electrons is also affected by the chemical environment of the atom, creating the so-called chemical shifts. When bound to a more electronegative atom, electron screening (i.e. the weakening of the Coulomb interaction between the positive nucleus and electrons due to the screening provided by the electron cloud) is decreased and, consequentially, binding energies are slightly increased. The opposite effect occurs when an atom withdraws electrons from its neighbours. This shift of core electron's binding energy grants the XPS technique the additional capability to identify the chemical state of surface atoms. Figure 2.9 shows the Ti $2p_{1/2}$ and Ti $2p_{3/2}$ peaks taken from a heat-treated Ti-apatite composite sample [39], with a clear distinction in binding energy for contributions origination from titanium in the metallic form (Ti), and with oxidation states Ti(II) (TiO), Ti(III) (Ti_2O_3) and Ti(IV) (TiO_2). As stated, the loss of electrons (taken by the more electronegative oxygen atoms) leads to an increase in the binding energy of the core 2p electrons, with higher oxidation levels leading to larger energy shifts. Additionally, chemical shifts may also depend on other features such as the crystal structure of the material and different end state effects [40]. For example, in the case of TiO_2, although they have the same stoichiometry, the crystal forms of rutile and anatase will have slightly different energy positions for both the titanium and oxygen peaks [39].

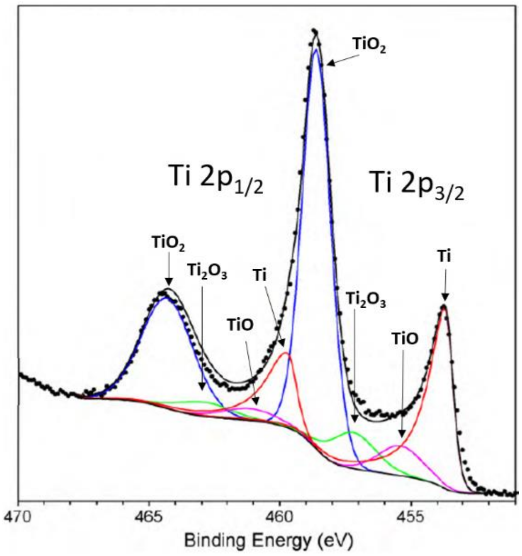

Figure 2.9 - Ti 2p spectrum of a heat-treated Ti-apatite composite, showing the chemical shifts for different oxidation levels of the Ti atom. Figure adapted from [39].

The main peaks analysed in an XPS spectrum correspond to electrons that do not lose energy in the emission process (no inelastic collisions). As explained in section 2.1.3, the surface sensitivity of the XPS and other photoelectron based techniques originates in the relatively small inelastic mean free path of electrons travelling through the material (see Figure 2.5). Assuming that electrons travel in a straight path (no elastic collisions), the intensity of electrons that is able to reach the surface without losing energy in its path, perpendicular to the surface, is equal to $I = I_0 e^{-d/\lambda}$ where d is the depth of emission, I_0 is the intensity at zero depth, and λ is the inelastic mean free path. Consequently, the photoelectron intensity at an emission from a depth of 3λ is reduced to 5% of its initial value. The vast majority of the photoelectrons that compose the peaks analysed in XPS experiments are thus originating at a maximum depth of about 3λ, with roughly 50% of the total intensity actually originating in depths lower than 0.7λ. The photon energies used in most XPS experiments are those of the Mg Kα and Al Kα transitions, with energy values of 1253.6 eV and 1486.6 eV, respectively [38]. For photoelectron kinetic energies in this range (10-1500 eV), the inelastic mean free path has an average value of roughly 20 Å, with the exact value depending on both the electron energy and the electronic structure of the matrix, going from 2 Å up to 60 Å (see Figure 2.5).

2.2.2 Additional Spectrum Features

As can be seen in Figure 2.8, there is a number of features in the photoelectron energy spectrum obtained from X-ray irradiation, in addition to the clearly visible main peaks, with some being used to obtain additional sample information.

One of these features is a clear increase of the background signal following each peak, towards higher binding energies, which corresponds to photoelectrons that suffered inelastic collisions, losing some of their kinetic energy in the emission process. The intensity and energy distribution of this "tail" can be used as an indicator of the depth distribution of the element, as the probability for inelastic collisions is higher for photoelectrons originating from deeper layers. Figure 2.10 shows the calculated spectra of the Cu 2p peak corresponding to different distributions of copper in a gold matrix [41]. Although all of these produce XPS peaks with identical shapes and intensities, the background signal following these peaks differs significantly, and can thus be used to provide a more accurate description of the surface.

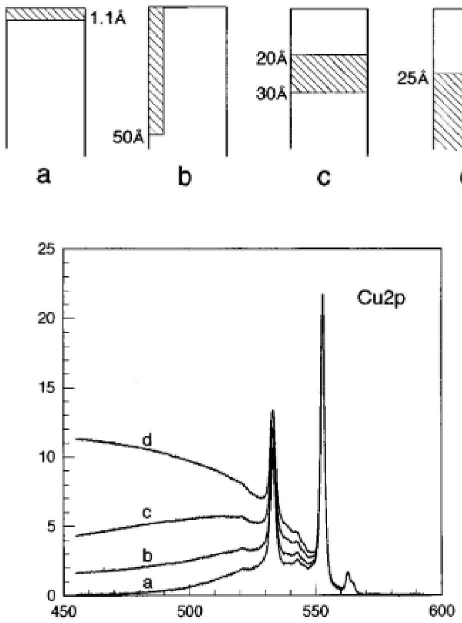

Figure 2.10 – Four widely different surface structures of copper in gold that give identical peak intensities [41].

Besides the main XPS-peaks that correspond to emitted core-level electrons which have been directly excited by the X-ray photons, there is also the presence of Auger peaks, seen for example in the 800-1000 eV binding energy range in Ti survey spectrum presented in Figure 2.8. The emission of an Auger electron is a process involving three electrons. As shown in Figure 2.11, after a vacancy is created in the core levels of an atom (ionization), there is a certain probability that this hole is filled by an electron from a higher layer (relaxation). The energy equal to the difference between the two energy levels is transferred to a third electron which is then emitted from the atom (emission), called the Auger electron. The notation used for Auger electrons consists on the three letters corresponding to the orbitals occupied by each electron in the three-part process. The case exemplified in Figure 2.11 corresponds therefore to a KL_2L_3 Auger transition (L_2 and L_3 correspond to core levels $2p_{1/2}$ and $2p_{3/2}$, respectively).

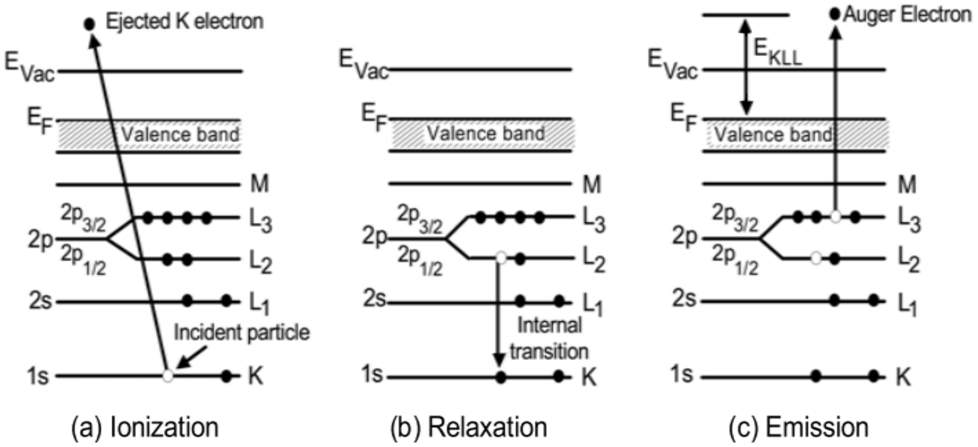

Figure 2.11 – Schematic showing three steps involved in the Auger process. The KL_2L_3 Auger transition is illustrated. The open circles symbolize holes (absence of electrons). Taken from [42].

The energy of the emitted electron in each possible Auger transition has the particularity of being independent of the X-ray energy (or electron energy in case of electron bombardment being the primary radiation source). Auger peaks can be used in a similar way to XPS-peaks to identify and quantify the elements in a sample's surface, by determining their intensity and position. However, since these are wider and with somewhat more complex shapes, they are not as suitable as XPS-peaks for that purpose. A typical use for Auger peaks is via the modified Auger parameter, defined as the sum of the kinetic energy of an Auger peak, and the binding energy of a core level peak [38]. The modified Auger parameter is usually used for chemical state analysis, in cases where sample charging (accumulation of positive charge in the sample's surface due to electron emission and low electric conductivity) hinders accurate determining of the energy position of XPS-peaks, as its value should not depend on sample charging. Other methods to resolve sample charging issues include using the position of adventitious carbon 1s peak as reference (which can be inaccurate as charging is not necessarily uniform (both laterally and in depth), or due to the small electric conductivity between the adventitious carbon and the sample [43]), or using an electron flood gun to bombard the surface with low energy electrons and thus compensate the charge loss.

Additional peaks which may appear in the photoelectron energy spectrum correspond to plasmon losses, shake-up and shake-off peaks. Plasmon losses are related to the fact that, in some materials, when an electron from a core level is emitted from the atom, there is higher probability for the loss of a specific amount of energy due to the interaction with other electrons, creating an oscillation of the free electron gas (plasmon) which will thus be seen as a series of smaller peaks at equally distant higher binding energies. Shake up peaks correspond to photoelectrons that have been emitted with a lower kinetic energy, due to part of the photon energy being used to excite other electrons, and the kinetic energy of the emitted photoelectron is thus lower (perceived as a higher binding energy in the spectrum), while shake-off peaks occur when this electron excitation is to the continuum instead of a bound state. These features will be dependent on the electronic structure of the material and, although they may hinder the analysis of the spectrum, their presence can be used for a reliable assignment of chemical states [39].

Lastly, there is the case of satellite and ghost peaks, which are related to the X-ray source used in the XPS analysis [38]. In non-monochromated sources, the main photon energy line, corresponding to a certain electron transition, typically $K\alpha_{1,2}$ transition from an Mg or Al target, will be accompanied by a $K\alpha_3$ satellite peak of much smaller intensity. Consequently, each XPS line will be followed by its own satellite shifted towards higher binding energies for 8.4 and 9.58 eV for Mg and Al target, respectively. Additionally, due to the Mg and Al targets in these X-ray sources being subject to oxidation and erosion in their usage (revealing the copper substrate), X-rays originating from oxygen or copper atoms may also irradiate the sample, resulting in the so-called ghost peaks. These problems can be overcome by filtering the photon energies that are able to reach the sample, which is done by performing monochromatization of the X-rays (see section 2.2.4.1).

2.2.3 XPS Quantification

The intensity of photoelectrons with kinetic energy *E*, originating from orbital *j* and element *i*, emitted from the surface upon X-ray irradiation is given by:

$$I_{ij} = J \cdot \sigma_{ij} \cdot L_{ij}(\gamma) \cdot D(E) \cdot T(E) \cdot \int n_i(z) \cdot \phi_i(z)\,dz \tag{2.4}$$

where *J* is the flux intensity of the X-ray characteristic line, σ_{ij} is the cross-section for emission of a photoelectron from element *i* and orbital *j*. $L_{ij}(\gamma, \beta_{ij})$ is the angular asymmetry of photoemission, where γ is the angle between incident X-rays and measured photoelectrons. $D(E_i)$ is the detector efficiency and $T(E_i)$ is the transmission of the spectrometer. Further details on the last two magnitudes are given in chapter 3, where their values are experimentally determined for the Kratos XSAM 800 system. $n_i(z)$ is the atom density at depth *z*, and $\phi_i(z)$ is the probability that the photoelectrons emitted at depth *z* normal to the surface reaches the surface without energy losses, also known as depth distribution function (DDF) [44]. Its precise value can be determined from Monte Carlo simulations, or from the solution of the kinetic Boltzmann equation within the transport approximation [45]. The traditional approach to calculating the DDF value is to neglect elastic collisions and use the exponential dependence $e^{-z/\lambda}$, as described in section 2.2.1. As is now known, the cross-section for elastic collisions with atoms cannot be neglected [45], which means that the exponential decay function is not accurate. To compensate this effect, the effective attenuation length λ_{eff} should be used in the exponential decay equation (instead of the mean free path λ), as it takes into account the probability for emission following elastic collisions, providing a good approximation of the true DDF in a limited range of *z*. It should be stressed that this term will depend both on the energy of the photoelectrons and the material through which they travel. The angular asymmetry factor can be calculated from the following expression:

$$L_{ij}\left(\gamma,\beta_{ij}\right)=1+\frac{\beta_{ij}}{2}\left(\frac{3}{2}\sin^{2}\gamma-1\right) \tag{2.5}$$

where β_{ij} is an asymmetry parameter for orbital *j* and element *i*. Typically, XPS systems are designed so that the second term of the equation is equal to zero and the asymmetry factor is neutralized i.e., when $\gamma \approx 54.7^{o}$.

In general, XPS quantification is performed by assuming the case of homogenous samples, where element *i* is uniformly distributed, i.e. $n_i\left(z\right)=N_i$. In this case, equation (2.4) can be written as:

$$I_{ij}=J\cdot\sigma_{ij}\cdot L_{ij}\left(\gamma\right)\cdot D\left(E\right)\cdot T\left(E\right)\cdot N_i\cdot\lambda_{eff\,i}\left(E\right) \tag{2.6}$$

For sample quantification purposes, what is typically required is the atomic fraction of a certain element, and not its concentration N_i. The latter is easier to calculate, as the absolute value of some of these terms, such as the value of the X-ray flux *J*, is typically unknown or hard to determine. The atomic fraction of an element *x* can be calculated with the following equation:

$$C_x=\frac{N_x}{\sum_i N_i}=\frac{I_x/S_x}{\sum_i I_i/S_i} \tag{2.7}$$

where the term S_i is the so-called atomic sensitivity factor, representing the remaining terms in equation (2.6), relative to a certain reference XPS peak:

$$S_{ij}=\frac{\sigma_{ij}\cdot L_{ij}\left(\gamma\right)\cdot D\left(E_{ij}\right)\cdot T\left(E_{ij}\right)\cdot\lambda_{eff\,i}\left(E_{ij}\right)}{\sigma_{ref}\cdot L_{ref}\left(\gamma\right)\cdot D\left(E_{ref}\right)\cdot T\left(E_{ref}\right)\cdot\lambda_{eff\,i}\left(E_{ref}\right)} \tag{2.8}$$

The values of sensitivity factors typically used are those experimentally determined by Wagner and co-authors [46], based on a large set of measurements performed on reference samples (mainly compounds of fluorine and potassium). In their work, a generalization is made and it is assumed that D is constant, $\lambda_{eff} \propto E^{0.7}$, $L=1$, and $T \propto E^{-1}$ (typically $T \propto E^{-n}$, where n is a value dependent on the spectrometer, with $0.5 < n < 1$), and uses the fluorine 1s peak as a reference, i.e., $S_{F,1s} = 1$. It should be stressed that the assumption for the mean free path dependence is a generalization, as the sample is presumed to be homogeneous. By simply considering $\lambda_{eff} \propto E^{0.7}$, the same multiplicative constant K is assumed ($\lambda_{eff} = K \cdot E^{0.7}$), which is only valid for photoelectrons passing through the same matrix in the course of their emission.

The process of performing a simple elemental quantification analysis for a certain sample is thus as follows:

- Obtain the XPS survey spectrum (as shown in Figure 2.8) to determine which elements are present in the sample
- Choose a peak from each element to perform a detailed scan (as shown in Figure 2.9) and determine its total area. Typically the most intense peak of each element is chosen, but in the case of superposition with other peaks (Auger peaks, satellite peaks, etc), other photoelectron emission lines may be better suited.
- Use the areas calculated from each peak and their respective sensitivity factors and apply equation (2.7) directly to obtain the relative atomic concentration of each element.

In order to determine the chemical composition of a sample, each contribution from a single peak must be resolved, as shown in Figure 2.9, and the relative concentration for each chemical state is calculated using the areas belonging to the respective contribution. At the end, the relative concentration from each element should match the stoichiometry of the chemical compounds that were identified.

In the case of non-homogeneous samples, the quantification process can become significantly more complex, as the classic atomic sensitivity factors are no longer applicable since photoelectrons originating from different phases will be differently attenuated. This scenario is actually very common, as it is usual for analysed samples to have oxidized and hydrocarbon contamination layers at the surface [38]. Additionally, it is also common to perform the XPS analysis on surfaces with deposited materials, which can form homogeneous thin films or island aggregates at the surface, resulting in both depth and lateral non-uniformity.

One possible initial approach to resolve the quantification problem for non-homogeneous samples is to use Angle Resolved XPS (ARXPS), which consists on performing the regular XPS analysis on a sample rotated by an angle θ. With this change, the depth of analysis is reduced by a factor of $\cos\theta$, as shown in Figure 2.12.

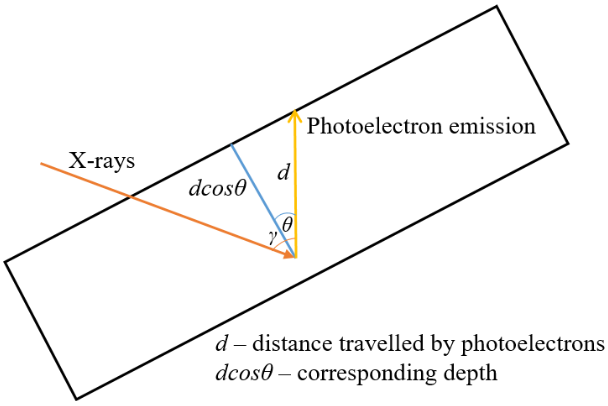

Figure 2.12 – Depth of analysis in ARXPS.

By monitoring the change of the relative concentrations from each contribution as a function of θ, an initial picture of the depth distribution can be attained. The next step is to calculate the total attenuation of each photoelectron by integrating the attenuation probability through the electrons' path, taking into account the fact that the effective attenuation length constant depends on the energy of photoelectrons, the material, and the emission angle. In this process, a guess/approximation is used for sample structure, and the relative concentrations for each element are calculated. The assumed structure is then adjusted and the calculation process is repeated, until a self-consistent solution is reached.

2.2.4 XPS Instrumentation

In order to perform XPS analysis, a number of instruments are required. First, an X-ray source is needed to produce photons that excite core electrons on the sample's surface. Next, an electron-optics column is used to collect and transfer emitted photoelectrons from the sample to the entrance of the energy analyser, an instrument used to filter the energy of these photoelectrons. Finally, a charged particle detector is placed on the output of the energy analyser to measure the photoelectron intensity after filtering. The sample is typically placed in a sample holder device, in line with the X-ray beam and the entrance to the energy analyser. It should be possible to put the sample holder on a defined electrical potential U, and, in order to perform ARXPS, it should also offer the possibility of rotation around an axis perpendicular to the direction along which the detected electrons are emitted, as well as translation along all axes for correct positioning of the sample. As previously explained in section 2.1.2, this is typically performed inside a UHV system, since a minimum pressure of 1×10^{-8} mbar is required for proper analysis.

2.2.4.1 X-ray Sources

The conventional X-ray sources present in a lab produce soft X-rays in the 1200-1500 eV energy range. These operate by bombarding a solid target with high-energy electrons (typically 10-15 keV). Upon bombardment, core electrons from the target material, also known as anode, are emitted, and electrons from outer levels will fill in the core hole, emitting a characteristic photon line in the de-excitation process. Typically, these X-ray sources will have both a magnesium and an aluminium anode, with characteristic photon lines of energies 1253.6 eV and 1486.6 eV, and line widths of 0.7 eV and 0.85 eV, respectively (other target materials can be used to produce X-rays with different energies). These characteristic lines correspond to the K_α transitions of both elements. As stated in section 2.2.2, other characteristic lines and braking radiation with different energies will also be emitted, although with lower intensities. To avoid the bombardment of the sample with these “extra” photons, X-ray sources may be equipped with a monochromator, which consists of a precisely positioned quartz crystal. It serves as a diffraction grating, allowing reflection of the incident X-rays at a specific energy-dependent angle, therefore providing energy filtering. Its parabolic shape focuses most of the reflected monochromatic radiation into a small area of the sample surface, thus providing much larger X-ray fluxes than in the case of non-monochromatic sources.

In the last decades, the development of synchrotron facilities has opened a possibility to perform XPS analysis with synchrotron radiation as an excitation source. The X-ray beam produced in this way has many advantages, such as much higher photon flux, better collimation, and the ability to continuously tune the X-ray energy in a wide energy range. In combination with advanced spectrometers and detection systems, such devices provide many possibilities including XPS imaging, fast measurements (thus providing in situ monitoring of different processes), XPS diffraction, angle-resolved photoelectron spectroscopy, etc. [47].

2.2.4.2 Energy Analyser

There are essentially three ways to determine the energy of charged particles. By measuring the time of flight of a known mass over a known distance, by applying a retarding electric potential that will reduce the particle’s energy to zero, or by deflection of the particles through an electric/magnetic field. Deflection based energy analysers will separate the particles by energy, by exposing them to the deflecting field, with the change of trajectory depending on their energy and charge. By placing a charged particle detector in a specific location in the energy analyser, which is only accessible to particles with a particular energy, it is possible to determine the particle intensity for a specific energy. Deflection based analysers can have different geometries, such as cylindrical, parallel plate, or spherical. Most modern XPS systems use the latter form of energy analyser, particularly the hemispherical energy analyser shape, shown in Figure 2.13. Compared to other deflection analysers, the main advantage of the latter is a higher transmission for the same energy resolution, due to the focusing on both the energy-dispersive and non-dispersive planes.

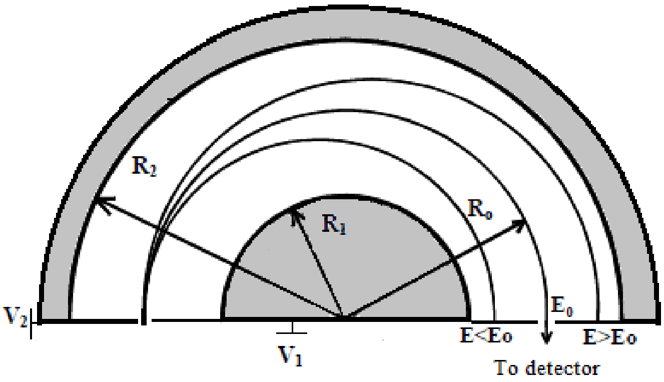

Figure 2.13 – Diagram of a hemispherical energy analyser, with two concentric electrodes with radius R1 and R2, at voltages V1 and V2 respectively, showing the path that allows passage to the detector at energy E0.

This type of energy analyser consists of two concentric hemispheres, with a voltage difference applied between them. The charged particles enter the analyser through a slit, and are subsequently deflected by the electric field between the hemispheres. Particles with different energies will have different curvature radius, and only those with a certain kinetic energy E_0, called the pass energy, will be able to leave through the exit slit towards the detector. It can be shown that this pass energy is equal to [48]:

$$E_0 = \frac{qk}{2R_0} \tag{2.9}$$

where q is the particle's charge, R_0 is the radius of the central path, and k is a constant equal to:

$$k = \frac{\left(V\left(R_2\right) - V\left(R_1\right)\right) R_1 R_2}{R_2 - R_1} \tag{2.10}$$

where R_2 and R_1 are the radii of the outer and the inner electrodes, respectively. The voltages of these electrodes are given by:

$$V_{outer} = \frac{E_0}{e}\left(2\frac{R_0}{R_2} - 1\right) \tag{2.11}$$

$$V_{inner} = \frac{E_0}{e}\left(2\frac{R_0}{R_1} - 1\right) \tag{2.12}$$

The resolution of the energy analyser, i.e., the range of energies that is able to pass through the exit slit for a given pass energy, is equal to:

$$\frac{\Delta E}{E_0} = \frac{W}{2R_0} + \frac{\alpha^2}{2} \tag{2.13}$$

where W is average of the entrance and exit slit widths, α is the acceptance semi-angle in the deflection plane, i.e. the maximum entrance angle that still allows particles to exit through the exit slit, and ΔE is the width of the resulting peak at half-maximum intensity. It should be stressed that the measured XPS-peak represents a convolution of the energy distribution of emitted photoelectrons, the energy profile of the characteristic X-ray line and the instrumental function of the spectrometer. The latter is typically in the form of a Gaussian with a full width at half maximum equal to ΔE. Consequently, the final width of the XPS-peak will depend on the characteristic X-ray line width, the natural photoelectron line width, and the resolution of the energy analyser.

Between the sample and the energy analyser, there is typically an electron-optical column consisting of a series of electrostatic lenses (cylindrical electrodes). Its purpose is to collect the photoelectrons emitted from the sample, and focus these into the entrance slit of the energy analyser, thus significantly increasing the amount of analysed photoelectrons. Further details on how the electron-optical column operates are given in chapter 3. Figure 2.14 illustrates the complete process of XPS analysis, from photon bombardment, followed by photoelectron emission, focusing of the electron beam in the electron-optical column, energy filtering in the hemispherical energy analyser, and finally detection in the charged particle detector.

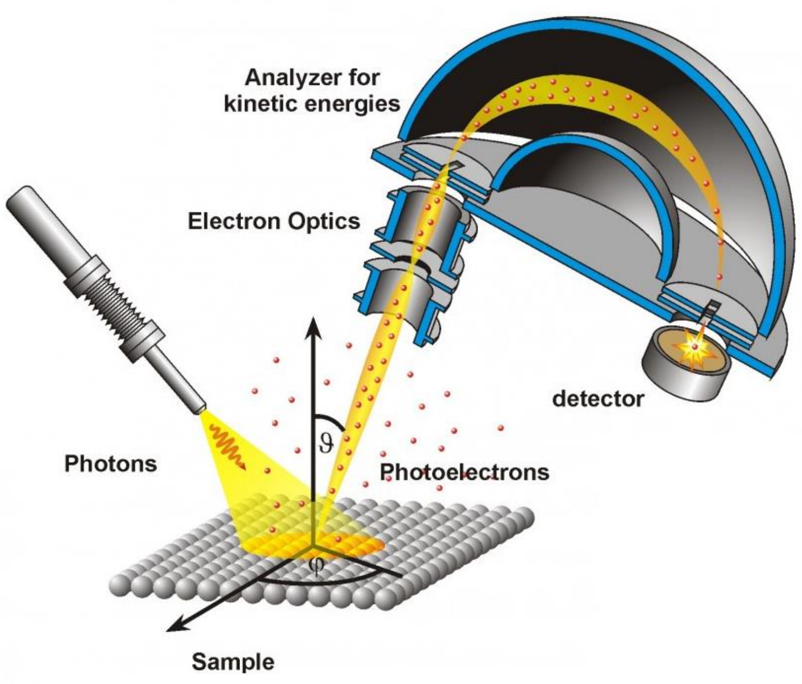

Figure 2.14 – Illustration of the XPS analysis procedure, from photon bombardment, followed by photoelectron emission, focusing of the electron beam in the electron-optics column, energy filtering in the hemispherical energy analyser, and finally detection in the charged particle detector. Picture adapted from [49].

2.2.4.3 Spectrum Production

An energy analyser can be usually operated in two modes – fixed analyser transmission (FAT) and fixed retard ratio (FRR). In FAT mode, the pass energy of the analyser is constant for all measured kinetic energies, resulting in a constant analyser energy resolution and transmission, which makes this mode ideal for producing XPS spectra. In order to produce a spectrum in this mode, the photoelectrons emitted from the sample are accelerated/decelerated in the electron-optics column before reaching the analyser's entrance, by applying a voltage difference between the sample and the entrance slit. In practice, the sample is kept at a constant potential, and all voltages of the electron-optics column and energy analyser are scanned, thus keeping the pass energy constant, while scanning the energy of photoelectrons that are able to pass through the analyser and reach the detector.

For analyses purposes, it should be stressed that the kinetic energy of detected electrons is not given by equation (2.3), as it does not account for spectrometer's work function. Thus, the actual kinetic energy of detected photoelectrons is equal to:

$$E_k = E_p - E_B - \Phi_a \tag{2.14}$$

where Φ_a is the work function of the spectrometer. In order to correctly calculate the binding energy of a certain photoelectron peak, Φ_a must be experimentally determined. This is accomplished by measuring the spectrum of a reference sample, such as silver or gold, and use the position of their XPS peaks to calculate Φ_a. This value should be periodically determined (ideally, once for each time a new sample is analysed), as the work function of the spectrometer might change with time due to adsorption or reaction with residual gas, and the calibration of the electronics system that produces the voltages of each electrode may also change with time.

2.2.4.4 Charged Particle Detectors

Charged particle detectors used in XPS systems are based on electron multiplication, as mentioned in section 2.1. Older XPS spectrometers use these channel electron multipliers to detect the energy-filtered charged particles, placed after the exit slit of the energy analyser. In the case of more than one detector being used, an equal number of exit slits is used, and each detector will be associated to photoelectrons with slightly different pass energies. The typical amplification of such a detector is of the order of 10^8, which allows single particle detection.

More advanced XPS spectrometers use an improved version of the “single” electron multiplier, the microchannel plate detector. It consists of a disk-like component composed of numerous individual electron multipliers, as shown in Figure 2.15, which is placed in the exit plane of the energy analyser.

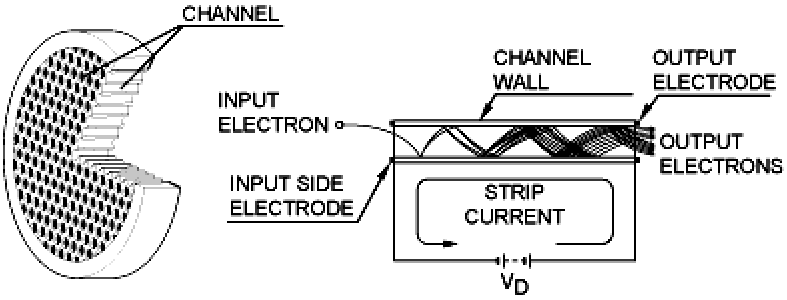

Figure 2.15 – Diagram of a microchannel plate detector, showing the individual electron multiplier tubes. Taken from [50].

When the overall detector system is position sensitive, there is no need for a slit to filter the exit passage of photoelectrons (each position in the detector will correspond to slightly different pass energies, and therefore photoelectron kinetic energies). It should be stressed that the typical amplification of micro channel plate detectors is ~10^3. In order to secure single particle detection a set of 2 or 3 detectors are mounted in series. Position sensitive detection is frequently performed by bombarding a phosphor screen by the multiplied electrons exiting the microchannel plates. Emitted photons are then detected by a charge-coupled device (CCD) detector. The absence of an exit slit significantly increases the total amount of detected photoelectrons, thus producing a more intense signal and increasing the sensitivity of the XPS analysis. The use of microchannel plate detectors also introduces the possibility to perform XPS imaging, as it is possible with intricate electron-optics systems to focus the emitted photoelectrons and project a direct image of the sample in the detector, in a technique called photoemission electron microscopy (PEEM). For the practical application of PEEM, it is essential to have very high X-ray flux. Therefore, this technique is realized in synchrotron facilities.

3

3 Kratos System and its Upgrade

3.1 The Kratos XSAM 800 System

Kratos XSAM 800 is a surface analysis system, produced in the 1980s by Kratos Analytical. A unit of this model, shown in Figure 3.1, was recently acquired by the surface sciences group of CEFITEC. It is a multi-purpose ultra-high vacuum system designed for performing surface science experiments.

Figure 3.1 – Picture of the Kratos XSAM 800 system, taken in the surface science lab of CEFITEC.

The system is divided in three chambers: sample insertion, treatment and analysis chambers. The treatment chamber is designed for gas exposure and film growth. In addition, it is equipped with a Secondary Ion Mass Spectroscopy (SIMS) setup – an ion source and a mass quadrupole. The analysis chamber is prepared for X-ray Photoelectron Spectroscopy (XPS), Auger Electron Spectroscopy (AES) and Low Energy Ion Scattering (LEIS) techniques. For XPS analysis, it is equipped with two radiation sources, a double anode Mg/Al X-ray source, and a monochromated Al X-ray source. An energy spectrometer with a hemispherical energy analyser and 3 channel electron multipliers is used for the energy analysis and detection of charged particles. An electron flood gun for sample charge compensation is also included. Two separate ion sources are used for LEIS analysis and sample cleaning by ion sputtering. Inside the analysis chamber, the samples can be manipulated with a fork, or placed on a motor-operated carrousel sample holder, which is able to carry up to 10 samples, and conveniently place each one in the analysis position. The Scanning Auger Microscopy (SAM) analysis is not present in this equipment, due to the lack of an electron gun suitable for this technique.

The whole system was originally controlled by a PDP-11 computer. When performing XPS experiments, the computer was controlling the high-voltage power supplies to generate the necessary spectrometer voltages for energy analysis, while counting the pulses produced by the pre-amplifiers connected to the detectors. This system for control and data acquisition was obsolete and fully incompatible with modern day technology, and was therefore replaced with a newly developed system. Additionally, a characterization of the spectrometer was performed, by measuring the non-linearity of the detection system, and the transmission function of the electron-optical column, without which it is not possible to perform reliable XPS analyses. Finally, the replacement of the control system allowed for the implementation of an optimization algorithm that will maximize the spectrometer’s transmission function, thus improving the sensitivity of the instrument.

The following sections in this chapter contain a general description of the vacuum equipment, instrumentation used for different analysis techniques, implementation of the new control and acquisition system, and characterization of the spectrometer, which includes the introduction of a new method to measure its transmission function, based on sample-biasing, and finally the use of a differential evolution algorithm to optimize the signal intensity. The work presented in this chapter has been published, focused on the novel transmission function measurement method, and the spectrometer’s optimization procedure [51].

3.2 System Details

3.2.1 Vacuum System

As previously described, the system is divided in two main chambers (treatment and analysis), separated by a gate valve, and a third small chamber designed for the introduction and removal of samples without directly exposing the rest of the system to atmosphere. The system is schematically represented in Figure 3.2.

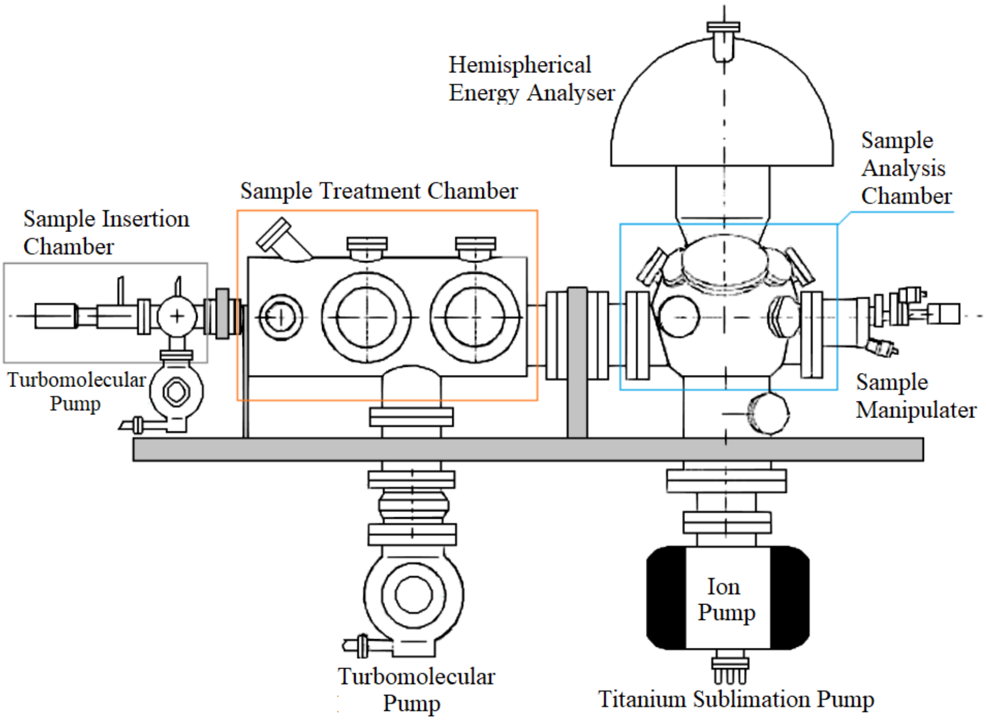

Figure 3.2 – Schematic of the Kratos XSAM 800 vacuum system.

To reach ultra high-vacuum, the system is pumped in stages. Primary vacuum is initially achieved by pumping the whole system from atmospheric pressure to 10^{-2} mbar range using a rotary pump, which is equipped with a foreline trap to avoid the contamination of the system by oil back streaming. High-vacuum is then reached in both chambers using a single 300 l/s water-cooled turbomolecular pump, which has the capacity to pump the whole system down to 10^{-8} mbar range. In the analysis chamber, ultra high-vacuum is reached with a 220 l/s ionization pump coupled with a titanium sublimation pump, which is equipped with a liquid nitrogen trap. To reach the low 10^{-10} mbar range, a full system bake-out at 150ºC is required, followed by proper degassing of all filaments in the system. A second smaller ionization pump (8 l/s) is used to directly pump the X-ray sources. The ion-guns in the analysis chamber are connected to the treatment chamber, and are thus pumped by the turbomolecular pump. The pressure reading is performed by two thermocouple gauges in the primary vacuum stage, and a double piezo/Pirani gauge in the gas line. Two Bayard-Alpert ionization gauges are used in the treatment and analysis chambers to read the pressure in the 10^{-4} to 10^{-11} mbar range. More information on the system can be obtained in the thesis of Lima W., where it is described in more detail [52].

3.2.2 XPS Instrumentation

The instrumentation required for XPS analysis includes an X-ray source, aimed at the sample, to excite and provide the emission of its core electrons, and a spectrometer for the energy analysis and detection of emitted electrons. This XPS system is equipped with two radiation sources. A dual anode X-ray source, with aluminium and magnesium anodes (Kα lines at 1486.6 eV and 1253.6 eV, respectively), and a monochromatic X-ray Source (Al Kα line), both operating at a maximum voltage of 15kV and 25 mA emission current. The measured angle between the incident direction of the X-ray beams and the direction of the emitted photoelectrons reaching the energy analyser is $\gamma = 69^\circ$.

The spectrometer is divided in three sections. An electron-optical system (column) that focuses and decelerates photoelectrons emitted from a sample, a hemispherical energy analyser, which bends the electron beam, separating the electrons by energy, and three electron multipliers that detect the electrons that escape through the energy analyser's exit slits.

The electron-optical column is composed of 6 cylindrical electrodes and an entrance slit (into the energy analyser), with an adjustable width of 1 to 8 mm. It is able to operate in two magnification modes, high and low, which determine the size of the analysed area of the sample, corresponding to small and large acceptance areas, respectively. A different set of voltages in the electron-optical column is attributed to each magnification mode, with the first two electrodes being grounded in the low magnification mode. Figure 3.3 shows a drawing of the column's electrodes (with cylindrical symmetry), which was amongst the documentation that came with the system[1]. The hemispherical analyser has a mean path radius of 127 mm, and operates at pass energies of 5, 10, 20, 40, 80, 160 or 320 eV, determined by the voltage difference between the two hemispheres. The choice of pass energy and slit width determines the analyser transmission and resolution. Higher pass energies and wider slits produce a higher signal intensity, and are typically used for the acquisition of survey spectra. Lower pass energies and a narrow slit will decrease the signal's intensity, but improve its energy resolution, and are thus used for detailed peak scanning.

---

[1] While this scheme, which is copied from a bad quality print, was amongst the system's documentation, the documentation itself provided no information apart from the drawing. The dimensions shown in Figure 3.3 are only approximations, particularly the distance between different electrodes, since it was not possible to reconstruct them accurately from the drawing. Moreover, we cannot be certain that the drawing corresponds to the actual configuration of the Kratos system electron-optics column, due to the lack of information in the document.

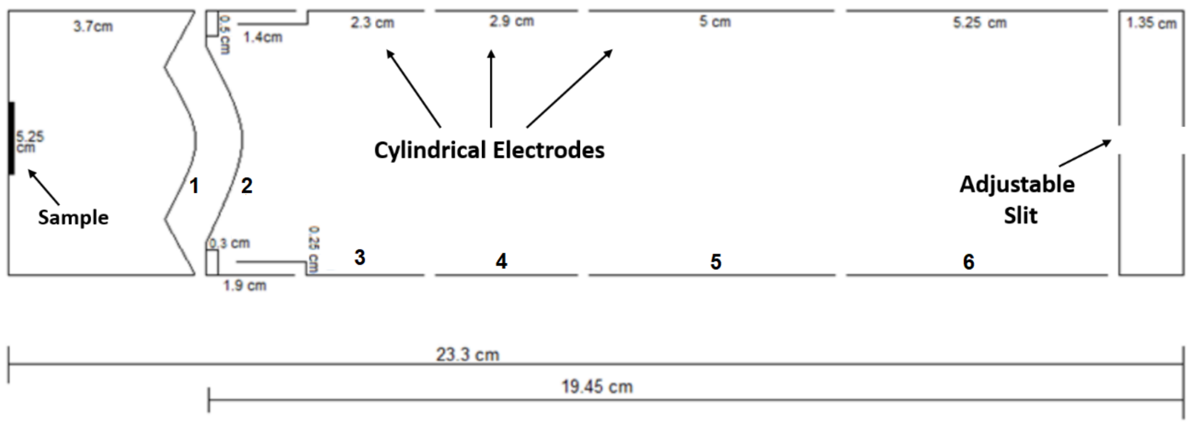

Figure 3.3 – Possible design of the electron-optical column, in a cylindrical symmetry. Measurements shown correspond to a 2:3 scale.

The detector system is composed of three channel electron multipliers (channeltrons). One is positioned along the central path, with the other two being at equal distances from the first. The position of each detector corresponds to an electron trajectory with a slightly different radius, and consequently different energy. This energy difference, proportional to the pass energy, must be taken into consideration when piling-up the spectra acquired from the 3 detectors.

The dimensions of the energy analyser and the detector system are shown in Table 3.1. The radius of the inner and outer hemispheres was calculated based on equations (2.11) and (2.12). Both R_0 and the values of V_{inner} and V_{outter} were obtained from the system's documentation (i.e. the voltages of the inner and outer electrodes, for specific pass energies). The size of the detector slits was measured during an opening of the system for replacement of the channeltrons. A picture of the detector system (slits + channeltrons), taken during this opening, is shown in Figure 3.4.

Table 3.1 – Dimensions of the hemispherical energy analyser and detector slits.

Energy Analyser				**Detector slits (3)**		
R_0	R_{inner}	R_{outer}	Entrance slit	Width	Length	Spacing
127 mm	101.8 mm	152.5 mm	1-8 mm	6 mm	18 mm	8 mm

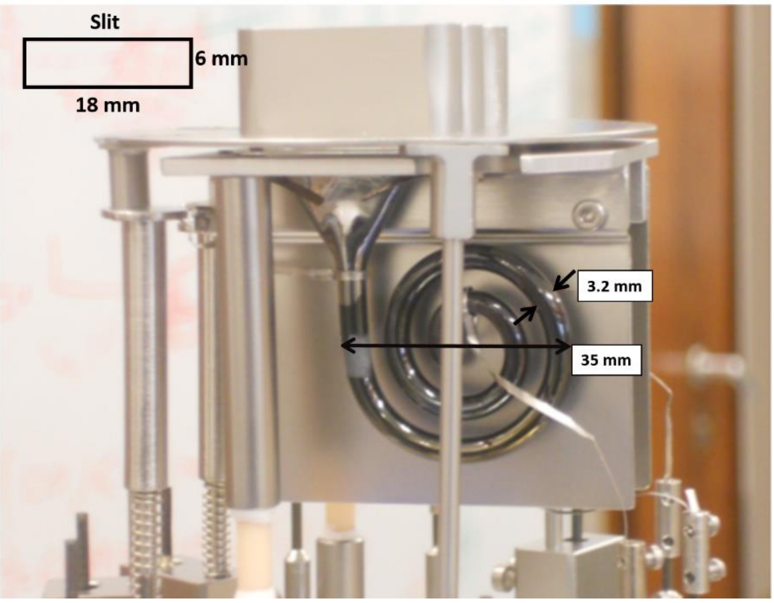

Figure 3.4 – Picture of the channeltron detectors and respective slits.

3.3 Control and Acquisition System

In its original configuration, the spectrometer of the XPS system was completely controlled by a PDP-11 computer, while both X-ray sources were operated manually on the control units. The PDP-11 computer regulated the high-voltages of the electron-optical column, the energy analyser, and the detectors. This computer also performed the acquisition of the signal, i.e., counting the pulses generated by the pre-amplifiers that are connected to the detectors' output.

The electron-optical column consists of 6 electrodes, as shown in Figure 3.3, denoted by numbers in ascending order along the particle trajectories from the sample to the analyser entrance. The voltage for each of these electrodes is generated by independent power supplies, as shown in Figure 3.5, except for electrodes 3 and 4, which are shortcut. The hemispherical energy analyser is controlled by two power supplies. The first one generates a voltage V_{HT}, which defines the kinetic energy of the electrons being detected. The second power supply generates a fixed voltage $V_{pass,}$ on top of V_{HT}, which defines the pass energy. An internal set of voltage dividers then defines the values of each electrode (entrance and exit slits, inner and outer hemispheres and fringing field correctors) as different fractions of V_{pass}. During the acquisition of an energy spectrum, the value of V_{HT} is scanned and the value of V_{pass} is fixed, thus scanning the analysed kinetic energy, while keeping the pass energy constant.

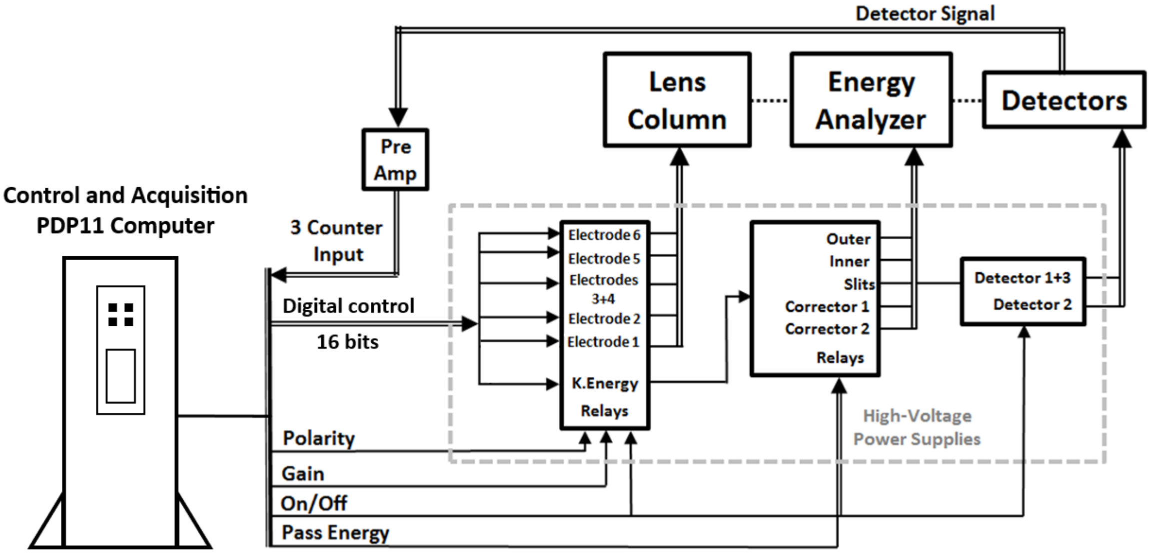

Figure 3.5 – Schematic diagram of the original control and acquisition system, with a PDP-11 computer.

The power supplies were controlled by a set of digital channels, operated by the PDP-11 computer. The high-voltage output was controlled by 16 bit lines, which were connected to Digital-to-Analogue Converters (DACs) inside the power supplies. The other digital lines controlled the relays that define the polarity, gain (ratio between output and control voltage), and pass energy of the analyser.

Although the original control system based on the PDP-11 computer was still operational, it was unfortunately obsolete, and fully incompatible with present information technologies. Therefore, this system had to be replaced by a newly developed one, as described in the following section.

3.3.1 New Control System for the XPS Spectrometer

Replacing the original control and acquisition system of this spectrometer, based on the PDP-11 computer, with a modern Windows PC, requires first that new control lines for the power supplies are setup. A NI PCIe-6323 board was used for this task. It is a multifunction device with a variety of programmable input/output channels.

Controlling the high-voltage power supplies requires replacing the original communication channels of the PDP-11 computer. The new acquisition system is presented in Figure 3.6. The 16 bit digital lines that controlled the value of the high-voltage output of each power supply were replaced by the analogue outputs (AO) of the NI PCIe-6323 board. The original DACs were bypassed, and the AOs were directly connected to the control voltage input of the power supplies. There are four AO channels, which control the voltages of electrodes ‘3+4’, ‘5’, ‘6’, as well as V_{HT}. In the low magnification mode, electrodes ‘1’ and ‘2’ are grounded, and in high magnification mode, their control voltage is defined as a fraction of the AO line that controls V_{HT}, produced by adjustable voltage dividers. A manual switch has to be operated to change between the two settings. The rest of the PDP-11 digital lines were directly replaced by the digital lines of the new board, in order to control the remaining relays inside the power supplies.

The analogue and digital output lines are connected to the power supplies via voltage followers and optocouplers, respectively. In order to produce a stable high-voltage output, it was also essential to isolate the ground of the control voltage inside each power supply from the general/common ground line. This common ground is shared with the other power supplies, and suffers from interferences between them. Small voltage changes of the ground level were directly affecting the value of the control voltages, and consequently altering the high-voltage output. Finally, each of the three outputs of the pre-amplifiers were connected to the counter inputs on the NI PCIe-6323 board, via line receiver integrated circuits. The representation of the new connections is shown in Figure 3.6.

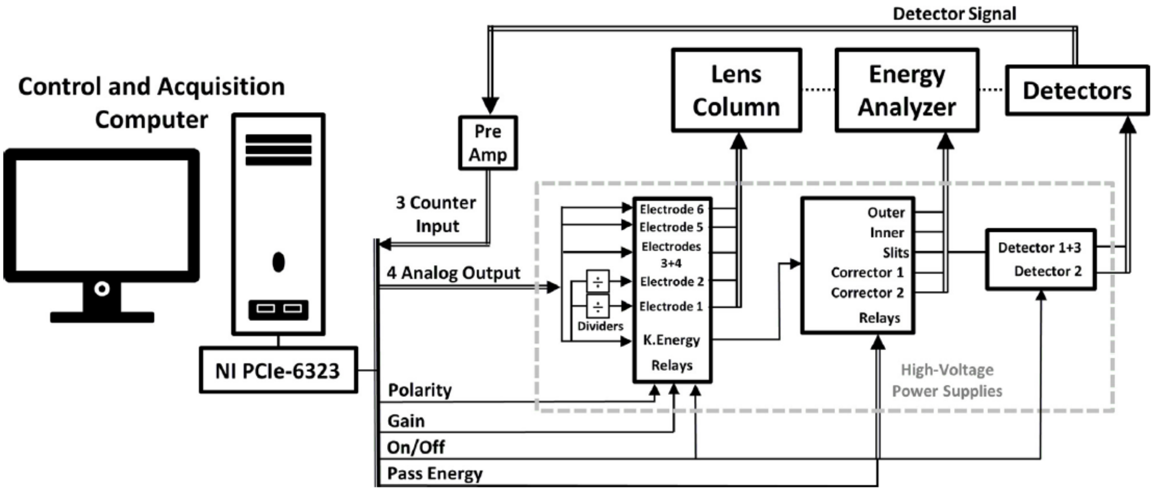

Figure 3.6 – Diagram of the new control and acquisition system.

In order to perform the XPS/LEIS analysis, new software was developed using the LabVIEW 2012 platform. The new software is structurally based on the software used to control the *Multitécnica* system [1], and was adapted to control the NI PCIe-6323 board. The user defines the scanning parameters (first energy, energy span, energy step, dwell time, pass energy and magnification mode), and the software performs the energy scan, providing the adequate voltages to all electrodes, while measuring the signal intensity. Some useful functionalities are also included, such as the creation of independent scan windows, with different scan parameters for each window, the possibility to perform automatic repeated scans with auto-saving and the choice to accumulate the signal on each scan, the ability to choose a fixed kinetic energy and follow the corresponding count rate, among others. The voltage values for electrodes ‘1’-‘6’, as a function of kinetic energy, pass energy, and magnification mode, were taken from plain text files found in the memory of the PDP-11 computer. Synchronization is essential to perform a reliable energy scan, since the software has to define the electrodes’ voltages for each step of the analysed kinetic energy, and count the pulses from the three electron multipliers during the dwell time. This is ensured by using the 4th counter as a clock signal for triggering both the analogue outputs and the counter input channels of the acquisition board (see Figure 3.6). The data is displayed in real time as the scan progresses, and can be saved as an ASCII file according to ISO 14976:1998 (VAMAS format). The signals from each electron multiplier correspond to slightly different kinetic energies. This energy difference has to be calibrated, and the spectra from each detector have to be shifted by this value before performing the pile-up. The developed software has the ability to adjust this energy difference, as well as the option to automatically perform the pile-up, or save the signal from each channel multiplier as an independent file. The main window of the XPS software is shown in Figure 3.7.

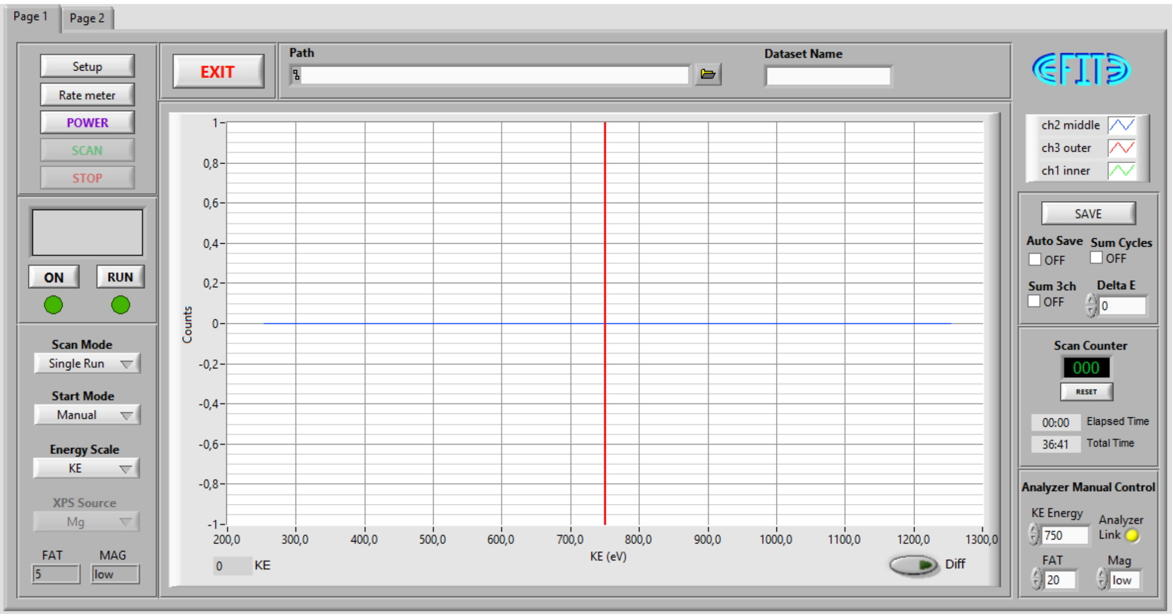

Scan Mode: Single Run
Start Mode: Manual
Energy Scale: KE
XPS Source: Mg
FAT: 5
MAG: low
0 KE
Auto Save ☐ OFF
Sum Cycles ☐ OFF
Sum 3ch ☐ OFF
Delta E: 0
Scan Counter: 000
00:00 Elapsed Time
36:41 Total Time
KE Energy: 750
FAT: 20
Mag: low

Figure 3.7 – Main window of the software developed for performing XPS/LEIS in the Kratos system.

The upgrade of the control and acquisition system to a modern PC significantly improves the versatility of this spectrometer, as most parameters of the system are now programmable, and can be easily defined or adjusted. This gave us the possibility to optimize the transmission function of the spectrometer, by individually changing the control voltages of the electron-optics column, as will be described in section 3.5. Apart from this improvement, the versatility of the software allows other functionalities to be easily added.

3.3.2 Ion Gun Control

The ion guns are controlled by their respective electronic units, and didn’t require interaction with the PDP-11 computer to be operated. Each ion gun is controlled by two units, one that provides the voltages that define the beam current, energy and focusing, and a second unit that generates the deflection voltages, used to scan the beam across the sample.

One useful tool for ion guns is the ability to generate an image based on the position of the beam. The contrast of the picture is usually obtained from the sample current, which is proportional to the ion flux impinging the surface, but other quantities may be useful, such as the signal from the XPS/LEIS spectrometer. The imaging functionally allows users to correctly position the beam on the sample surface, ensuring that the desired areas are being irradiated. This is a very important feature, since the total time required to sputter clean a sample may be greatly reduced by adjusting the sputtering area within the edges of the sample surface. It also allows the beam positioning in a specific area for LEIS or WF analysis, or even to perform imaging with these techniques, if the conditions allow it (this requires a narrow beam and computer control of its position, in order to synchronize it with the spectrometer’s energy scan).

For these reasons, a simple software designed to produce the sample image was developed, using the LabVIEW 2012 platform. Figure 3.8 shows the main front panel of the software. Since the beam scan is automatically performed by the control unit, which cannot be externally controlled, the software simply reads the beam position versus the sample current or the spectrometer’s signal, and draws the corresponding picture. The beam can then be adjusted directly on the control unit, and the effects seen on the computer. The X and Y coordinates of the beam position are read from their respective analogue outputs on the control units, which are connected to two of the several analogue input channels of the NI PCIe-6323 board. A third analogue input is connected to the sample contact via a current-to-voltage converter, thus obtaining a 0 to 10 V signal proportional to the sample current. The equivalent picture with the spectrometer’s signal can be obtained by defining the measured kinetic energy in the XPS software.

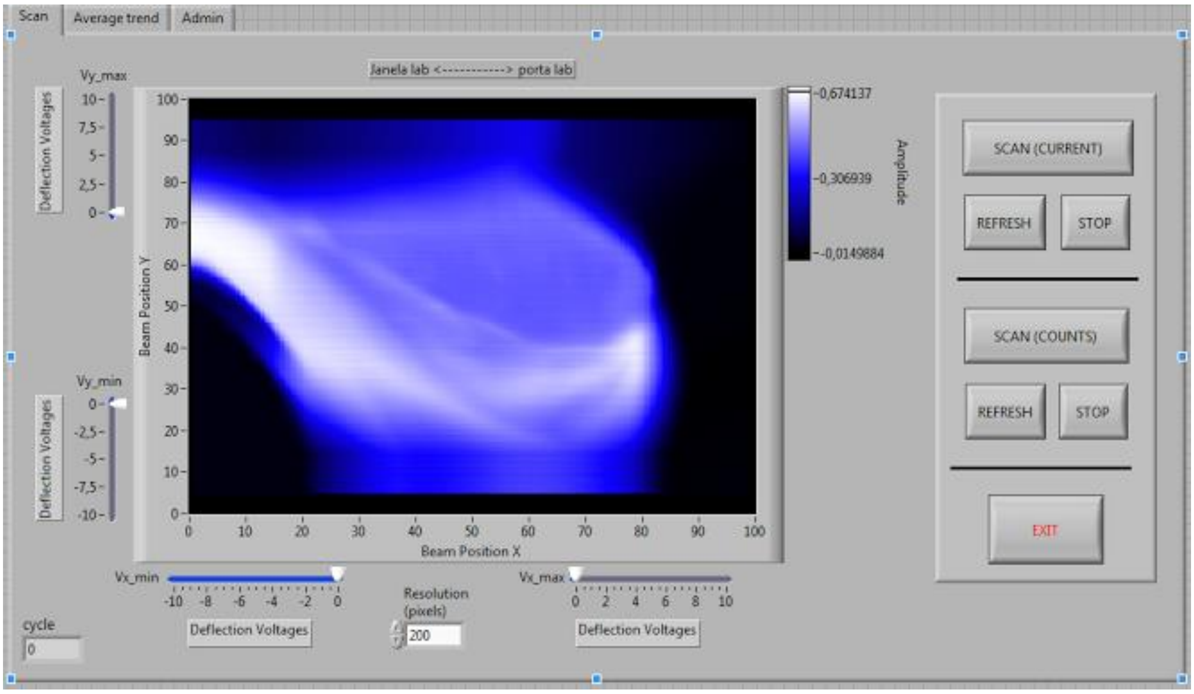

cycle 0

Resolution (pixels) 200

Figure 3.8 – Main window of the software developed for the Ion Gun.

A second tool was also added to the software, which appears to be quite useful in making the sputter cleaning procedure more efficient, related to the time evolution of the average sample current during the sample sputtering. The sample current is the sum of the current of ions impinging the surface and secondary electrons leaving it. The secondary electron yield is affected by the surface conditions, and it is known that the secondary electron yield for ion energies in the keV range generally increases with the amount of surface impurities [53]. Consequently, as the surface is sputtered, the sample current will be decreasing until reaching a steady state, which indicates that an equilibrium in the surface composition has been reached. The software draws a graph of the sample current averaged over the sputtered area as a function of the number of scans. This allows users to follow the secondary electron emission yield as the sample is sputtered, and thus estimate the time evolution of the concentration of surface impurities. When the sample current reaches the aforementioned stability, the sample can be considered as approximately clean, given the assumption that the ion beam intensity was stable during the sputtering process.

Since the electrical feedthroughs for the deflection plates are in a separate flange/plug, it was possible to simply connect them to a separate, software controllable power supply, thus generating the deflection voltages in a programmable way. The software developed for the ion gun of the *Multitécnica* system can be used together with this power supply [1], thus allowing a complete control of the beam position, and with it, the option to perform a microscopy of the work function or LEIS techniques. With a proper electron gun, the software can also be used to perform SAM analysis.

3.4 Spectrometer Characterization

3.4.1 Introduction

As described in section 2.2.3, XPS quantification analysis is performed by comparing the intensities (peak areas) of different elements in the same sample, and extracting the relative atomic concentrations from equation (2.8) (repeated below), using the appropriate sensitivity factors.

$$S_{ij} = \frac{\sigma_{ij} \cdot L_{ij}(\gamma) \cdot D(E_{ij}) \cdot T(E_{ij}) \cdot \lambda_{eff\,i}(E_{ij})}{\sigma_{ref} \cdot L_{ref}(\gamma) \cdot D(E_{ref}) \cdot T(E_{ref}) \cdot \lambda_{eff\,ref}(E_{ref})}$$

While the values of $L_{ij}(\gamma)$, σ_{ij} and $\lambda_{eff\,i}(E_{ij})$ are characteristics of the specific elements and compounds, and can be obtained from the literature, $T(E_{ij})$ and $D(E_{ij})$ are dependent on the instrument, and their value must be known to perform the quantification analysis.

$T(E)$ is the transmission function of the complete spectrometer at kinetic energy E, which encompasses all instrumental parameters, such as the acceptance area and the acceptance solid angle. $D(E)$ is the detector efficiency. Since XPS analysis with this instrument is performed in FAT mode, E in $D(E)$ is constant and equal to the sum of the pass energy and the energy gained by electrons after being accelerated between the exit slit and the detector. Both of these values are constant, which means that $D(E)$ only changes when detector non-linearity occurs (i.e. when the signal of the detector is not proportional to the number of impinging particles).

A systematic study of the transmission function of a variety of XPS systems has showed that its value is not only model dependent, but even differs among instruments of the same model (differences higher than 30% have been reported for the Kratos XSAM 800). Additionally, the transmission function is also gradually changing with time and usage [54]. This may occur for several reasons, such as the change of the work function of the electrodes inside the vacuum system due to surface deposits/contamination, the aging of the electric components of the high-voltage power supplies, changes to the control voltages made by the users/manufacturers, or even small displacements of the complex internal structure of the spectrometer while transporting and mounting/dismounting the system.

For these reasons, the transmission function of spectrometers must be measured periodically, in order to maintain the reliability of the XPS quantification analysis. Moreover, with the change of the control system of this spectrometer, it is fair to expect changes of the transmission function, due to possible different calibrations of the high-voltage output of the power supplies.

It is also advisable to measure the detector's nonlinearity [55], which may appear at high count rates, due to the detector system's dead-time, i.e. the minimum time interval required to detect two events in a row. Although the nonlinearity of these types of detectors should be negligible in the typical count rates of XPS peaks, it may not be so in the low-energy/secondary electron part of the spectrum, where work-function measurements are performed. Moreover, it is possible that the new acquisition system has a higher than expected dead-time, and measuring the system's non-linearity is one way to ensure that the acquisition was correctly setup.

3.4.2 Detector Nonlinearity

When two particles reach the detector in a time interval shorter than the detector's dead time, the second particle will not be detected. The probability of this event increases with signal intensity, resulting in a non-linear dependence of detected particles vs particles impinging the detector. The non-linearity of the detection system is determined by the characteristics of both the detector and the data acquisition system.

Prior to measuring the detector system's non-linearity, some qualitative tests were performed in order to determine if it is described by a paralyzable model [56]. In a paralyzable behaviour, an event during the detector dead time will restart the dead time, and thus an increase of the signal's intensity eventually decreases the detected count rate to zero, while in non-paralyzable behaviour this does not occur, and the detected count rate is saturated to the inverted value of the dead time. A wave generator was connected to the pre-amplifier's entrance, and the final count rate was measured by the computer as a function of the input signal's frequency. In the case of square pulses with a 50% duty cycle, the ratio of these quantities appeared to be 1 up to a certain frequency in the 10-30 MHz range, when it was abruptly falling to zero. This immediate loss of the count rate clearly suggests that the acquisition system is described by a paralyzable model, which is characterized by a dead time τ. Upon further analysis by adjusting the shape of the input signal, it was clear that the dead time is caused by both the width of the TTL pulse τ_w and the minimum recovery time of the detector τ_r, i.e., the minimum time between the end of one pulse and the beginning of the next one required to resolve the two pulses. Consequently, $\tau = \tau_w + \tau_r$. This qualitative analysis showed the existence of a dead time for the detector system, which inevitably introduces nonlinearity.

The value of τ_w was later determined by connecting an oscilloscope to the exit of the preamp and measuring the width of the pulses, which revealed that $\tau_w \approx 25\,\text{ns}$. To determine τ_r, the wave generator was connected to the counter input of the NI PCIe-6323 board. The duty cycle of the square wave was increased until the signal was lost. At this point, the time interval between the pulses, being about 40 ns, represents the recovery time τ_r. The total dead time of the preamp is thus estimated to be about 65 ns. Figure 3.9 shows a schematic of the square wave as observed in the oscilloscope, with the respective pulse width, recovery, and dead times.

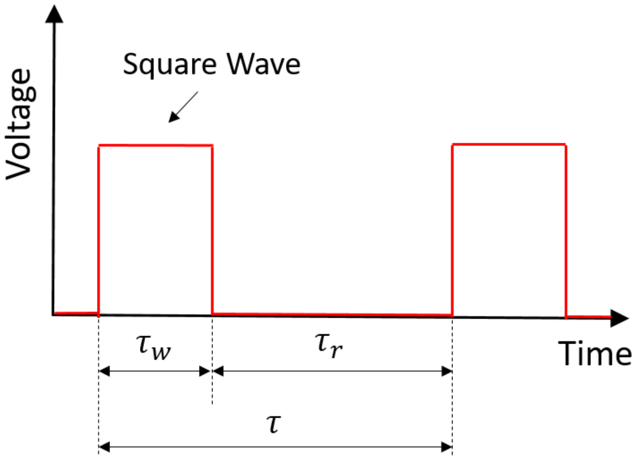

Figure 3.9 – Schematic representation of the pulse width τ_w, the recovery time τ_r, and the dead time τ.

To measure the detection system's dead time in a more realistic and reliable way, the procedure proposed in [57] was followed. In this approach, the time fraction in which the detector is active is first considered to be $1 - R\tau$, where R is the measured count rate. The true count rate R_0 can then be written as $R_0 = R/(1 - R\tau)$, which is valid as long as $R \ll \tau^{-1}$, while the probability of more than two particles reaching the detector in the time interval [0, τ] is still small. Using this equation, τ can be determined. However, the true count rate R_0 cannot be experimentally measured, as it is not possible to shoot an electron beam of known current directly into the detector. To work around this limitation, R_0 can be controlled with the X-ray power P_x, since $R_0 \propto P_x$, which is valid when the X-ray high voltage is kept constant, and P_x is changed solely by adjusting the emission current of the X-ray gun I_x [55]. It may thus be written $R_0 \propto a \cdot I_x$, where a is a proportionality constant to be determined. The photoelectron current I_{ph}, measured at the sample's electrical contact to ground, is also linearly dependent on I_x [58], and consequently measuring the linearity of I_{ph} vs I_x will confirm the $P_x \propto I_x$ relation. Indeed, this dependence was measured and fitted to a linear function with the square of the correlation coefficient $R^2 = 0.99998.$ Hence, it may be written that $R/I_x = a - a \cdot \tau \cdot R.$ The detector's nonlinearity can then be determined by measuring the count rate R as a function of I_x, in a region of the energy spectrum in which the intensity is roughly flat so that charging issues are avoided [55,57,58]. The values of the constant a and detector dead time τ can finally be obtained by fitting R/I_x vs R to a linear dependence.

Following this procedure, the count rate of a single detector was measured in the flat part of the secondary electron spectrum of a rutile $TiO_2(110)$ sample, as a function of I_x, at a constant high voltage of the X-ray gun of 10 kV. The results are shown in Figure 3.10, fitted to a linear dependence, from which the detector's dead time was determined as 61±3 ns. This result is in an excellent agreement with the preliminary tests performed with the oscilloscope and wave generator. The value obtained for the dead time means that in regular XPS measurements the detector's non-linearity should be negligible. Nevertheless, the correction factor was added to the software to convert the measured count rate to estimated one.

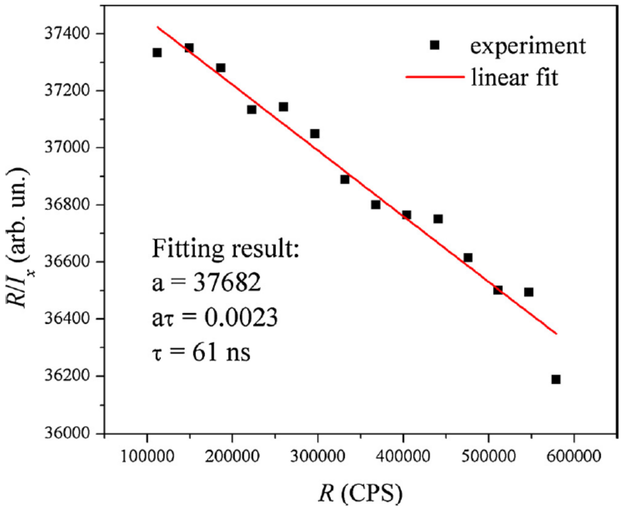

Figure 3.10 – The measured R / I_x vs R dependence, fitted to a linear function.

3.4.3 Transmission Function Measurement

The transmission function may be separated in two contributions, that of the electron-optical column, and of the energy analyser itself. The transmission of the electron-optical column is related to the efficacy of the beam focusing, and so depends on the voltages applied to each of its electrodes. It is therefore a function of the kinetic energy being measured, but will also depend on the pass energy and the magnification mode. The transmission of the energy analyser depends only on its pass energy, which means that in the fixed analyser transmission (FAT) mode, it is constant for all kinetic energies during the scan. The transmission must therefore be measured as a function of the kinetic energy, for the different available pass energies and magnification modes. Most methods used to determine the transmission function of XPS systems are only able to measure the relative transmission, i.e., the transmission for a certain kinetic energy relative to some other kinetic energy, and not the absolute transmission. The relative transmission may still be used in equation (2.8) for quantification purposes, but both intensities must come from measurements performed for the same pass energy and the same magnification mode.

3.4.3.1 The First Principles Method

There are several reported methods to measure the transmission function of an XPS spectrometer [58–60]. Perhaps the most commonly used approach is known as the first principles method [59], which is based on the comparison of the intensities of different photoelectron lines of the same element, taken from the same clean and in-depth uniform sample. Because the atomic concentration N_i is the same for both lines, the ratio of the measured intensities of photoelectron lines *j* and *l*, located at kinetic energies E_j and E_l, may be expressed as

$$\frac{I_j}{I_l} = \frac{\sigma_j \cdot L_j(\gamma) \cdot \lambda_{eff\,j}(E_j)}{\sigma_l \cdot L_l(\gamma) \cdot \lambda_{eff\,l}(E_l)} \cdot \frac{T(E_j)}{T(E_l)} \tag{3.1}$$

The ratio of detector efficiencies was omitted since they should be equal, and therefore cancelled in eq. (3.1). Since all other parameters are known or may be calculated, the ratio of transmission functions can be obtained in this way from the ratio of the measured line intensities. For quantification purposes, it is sufficient to know the relative transmission, i.e., the value of the transmission normalized to some specific kinetic energy (typically 986 eV, which corresponds to the kinetic energy of photoelectrons originating from the C 1s line, excited by the Mg Kα line). By measuring the XPS line intensities of several samples, and using different photon energies, it is possible to obtain enough values of ratios of transmission functions to reconstruct the overall $T(E)$ dependence, for a certain pass energy and magnification mode.

Although this method has some advantages, such as the simplicity of the procedure, and the fact that it is based solely on theoretical calculations (first principles) and does not depend on experimental results or empirical laws, there is one major drawback to this approach: in order to obtain a satisfactory density of points in the whole energy range relevant for XPS analysis, it is necessary to thoroughly prepare a considerable set of samples. This is a time-consuming approach, mainly due to the long sputter cleaning procedures, which are necessary to fully remove the surface contamination of each sample prior to measurement. Depending on the number of samples that can be simultaneously kept in the analysis chamber, an additional exchange of samples might be required, which implies an additional waiting time for the system to return to its base pressure. There is also the possibility of introducing significant errors, if some of the photoelectron lines required produce a rather weak signal.

Other approaches to the transmission function measurement face different drawbacks. One method requires direct comparison of spectra from the same sample taken from two instruments, one with known and other with unknown transmission function [61]. This method is completely dependent on the reference sample being prepared in the same way. Even if the reference sample is from the same material source, the exposure of the sample to air before its introduction in the vacuum system may produce different contaminations on its surface, and the ion sputtering cleaning procedure that follows may introduce different types and quantity of defects that will affect the XPS spectrum, such as surface roughness or ion implantation. A second method consists of measuring the intensity of a photoelectron line vs. pass energy, and fitting it to the dependence $I \propto T \propto E_{pass} \cdot \left(E_{pass} / E \right)^n$ in order to determine n [59]. The $T\left(E_{pass}, E \right)$ presumed dependence is not necessarily correct (as will be shown by some of the results presented in this work). Another method consists of using small voltages to bias the sample, but it requires the use of the background signal to acquire enough density of points [60]. The background at a specific kinetic energy is not only related to the signal coming from photoelectrons reaching the detector with that energy, but also from the noise generated inside the analyser from possible electron reflections on its walls or other noise sources, and may therefore be a poor indicator of the transmission function. There is a larger issue with this method, related to the fact that it neglects the effect of the sample biasing on the measured transmission function, which will be explained further in section 3.4.3.3.

3.4.3.2 First Principles Method: Experimental Procedure and Results

As a first approach in measuring the transmission function, the well-established first principles method was employed. $T(E)$ was determined for the scan modes typically used to perform XPS analysis, with pass energies of 20, 40 and 80 eV, in the low magnification mode and with a fully opened entrance slit. In order to produce a satisfactory density of points, samples of nickel, gold and copper were used, irradiated by both non-monochromatic Mg and Al Kα X-ray lines. The samples were square shaped, with an area of ~10×10 mm^2, which should be larger than the acceptance area of the spectrometer, but smaller than the X-ray irradiated area. The contaminated layers (typically hydrocarbons and oxides) of all samples were thoroughly cleaned via ion sputtering. It is essential that these layers are completely removed, as they add an extra attenuation factor that is not taken into account by equation (3.1), and is energy dependent, affecting particularly the peaks at lower kinetic energies. The photoionization cross sections and the asymmetry parameters were taken from [62] and [63], respectively. The value for quantitative attenuation length was used for λ_{eff}, in order to properly take into account the elastic scattering of photoelectrons inside the sample material, and was obtained from the NIST database [64]. The inelastic mean free path, used to calculate λ_{eff}, was determined from the optical data available in the same database. All these parameters are summarized in Table 3.2, for each of the photoelectron lines measured.

Table 3.2 - Photoionization cross sections [62], asymmetry parameters [63] and quantitative attenuation lengths [64] of photoelectron lines of interest excited by Mg Kα photons. The data corresponding to Al Kα irradiation is also given for gold lines measured using both photon energies (Mg Kα/Al Kα).

Line	***E*(eV)**	**σ (arb.un.)**	**β**	**λ_{eff} (nm)**
Au 4f	1168/1401	17.47/17.12	1.006/1.032	1.378/1.585
Au4d	909/1142	15.92/19.8	1.165/1.241	1.164/1.343
Au 4p$_{3/2}$	707/940	4.55/5.89	1.565/1.625	0.933/1.144
Au 4p$_{1/2}$	611	1.53	1.565	0.844
Au 4s	492/725	1.45/1.92	2/2	0.608/0.937
Ni 3p	1184	0.0451	1.535	1.498
Ni 3s	1140	0.0168	2	1.437
Ni 2p$_{3/2}$	398	0.3128	1.396	0.662
Ni 2p$_{1/2}$	381	0.1564	1.396	0.643
Cu 3p	1179	0.0501	1.548	1.678

Cu $2p_{3/2}$	322	0.3565	1.344	0.648

The area/intensity of each photoelectron line was determined by its fitting to a Gaussian-Lorentzian distribution, after defining and subtracting a Shirley background, and the relative transmission functions were then obtained by applying equation (3.1). In order to merge and normalize all the data so that $T(968\,eV)=1,$ the following procedure was adopted:

1. For each sample '*i*', a set of points for the relative transmission was obtained, and fitted to the typical exponential dependence of the transmission function $T_i\left(E\right)=A_i E^{-n}$ [59].
2. For each sample, a normalization factor $NF_i = T_i(968\,eV)$ was calculated from the fit in step 1, and each transmission point was then divided by its respective factor, so that $T(968\,eV)=1.$
3. All normalized measured values from all samples are finally merged in the same data set, and fitted to a single analytical expression $T\left(E\right)=AE^{-n}.$

It should be stressed that the two sets of values obtained from the measurements of the gold sample, irradiated by the Mg and Al Kα X-ray lines, must be treated as independent data sets (different samples) in step 1, as equation (3.1) is only applicable for identical X-ray beam characteristics. Figure 3.11 shows the normalized values of the transmission function for pass energies of 20, 40 and 80 eV, in the low magnification mode.

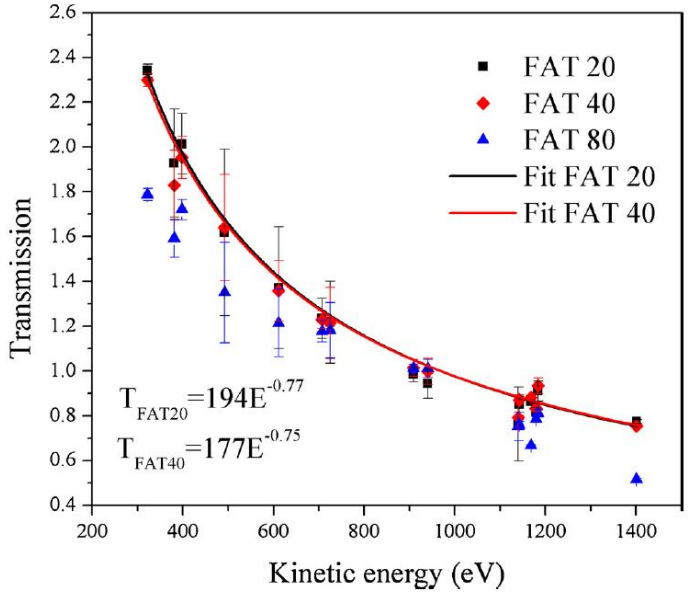

Figure 3.11 – Normalized transmission function determined by the first principles method, for pass energies of 20, 40 and 80 eV, fitted to the power law.

The points corresponding to the pass energies of 20 and 40 eV were successfully fitted to the power law, with both fits passing through the point (968 eV,1), and yielding very similar values for the exponential coefficient n. The values obtained for the pass energy of 80 eV show a different behaviour, as the points are more scattered, and it was not possible to properly fit them to a power dependence. For comparison purposes with the other pass energies, the data was still normalized at 968 eV, although in an arbitrary way, simply by using the linear interpolation of the neighbouring points to obtain the value of the normalization factor $T_{FAT80}(968\,eV)=1$. However, since each “FAT 80” data set from each sample was still individually fitted and normalized to the power law (step 1 of the merging procedure), which is now known to be completely inadequate for this pass energy, these results must be completely discarded, and a different procedure should be used to merge and fit them. The increased scattering of these points (lack of trend) should be explained by the poor fits of the individual data sets, as they are not represented by the power law.

The unusual behaviour of the transmission function for the pass energy of 80 eV should not be due to measurement error, since this pass energy produces a signal with the highest signal-to-noise ratio of the three, and the measurements were performed under the same conditions as those of the 20 and 40 eV pass energies. This behaviour might be explained by an un-optimized set of voltage values for the electron-optical column, which provide a defective collection of the emitted electrons, such as an acceptance area with an abnormal size (too large/small) or shape, or considerable changes to the acceptance area radius or acceptance solid angle as a function of the kinetic energy.

Another issue with the measurement is the rather high relative error of some of the experimental points. The experimental error is determined by the peak-fitting software (casaXPS), which calculates the statistical noise assuming the count rate obeys the Poisson distribution. The software determines the final error by automatically changing the background level according to the calculated noise, and calculating how this change affects the value of the peak’s area [65]. The points with a high error are either those corresponding to peaks that simply have a small intensity, or those with low ratios between its maximum and background level. While the former can be overcome by increasing the acquisition time or the X-ray flux, the latter is harder to avoid since the signal to noise ratio is proportional to the square root of the acquisition time. It should be stressed that the measured areas of these peaks have a very strong dependence on the chosen background level, as well as the energy range in which the integration is performed. As most XPS operators will know, the choice of these parameters is somewhat arbitrary, and it strongly depends on the operator's knowledge and experience, as the background level may be subtly affected by a variety of spectrum features, such as X-ray satellites, shake-up peaks, ghosts, etc.

The high experimental error of some points, the sensitivity of the peak intensities to the sample cleanliness and the necessity of working with several samples, are all factors against employing the first principles method to measure the transmission function. This, together with the poor results for the 80 eV pass energy, drove us to search for an alternative method.

3.4.3.3 The Sample-Biasing Method

When performing XPS analysis, the sample is generally grounded during the measurement. If the sample is biased to a positive voltage *U*, the measured kinetic energy of electrons leaving the sample with energy E_j will be equal to $E_j - eU$, effectively shifting the whole energy spectrum for the value of eU.

In equation (2.6), which describes the signal's intensity from a homogeneous sample, only the transmission function factor is affected by sample biasing. The effective attenuation length $\lambda_{eff\,i}\left(E\right)$ depends on the energy of electrons still inside the sample, and so is unaffected by the sample biasing. If it is assumed that the transmission function term is simply shifted in energy to $T\left(E_j - eU\right)$, determining the transmission function is simply a matter of following the line intensity as a function of the biasing voltage, as performed in [60] and [66]. This approach ignores the fact that biasing the sample produces an additional electrical field between the sample and the entrance of the electron-optical column, which will affect the photoelectron's trajectories as they are emitted from the sample's surface. This means that the signal's intensity is not only affected by the change of the transmission function due to the energy shift, but also by the additional electrical fields. Ebel and co-authors [60] assumed that for small biasing voltages this effect was negligible. The biasing voltage was kept small, and $T\left(E\right)$ was constructed by measuring a series of $dI\left(E\right)/dU$ points, for different values of E across the energy scale (some points using the background signal), which were then fitted to a polynomial function, and integrated. However, this is a questionable approach, as there is no experimental or theoretical evidence that the change of the signal's intensity due to the transmission function change is not of the same order of magnitude as its change due to the additional electrical fields.

The goal of this work is to apply higher biasing voltages, so that using the background signal is not necessary, and the whole measurement can be performed with a single sample. This means that the additional electrical fields will not be negligible, and so an attempt was made in this work to create a theoretical model that estimates this effect. Moreover, the effect can be determined experimentally, as will be shown.

The electron-optical column of the XPS spectrometer is schematically presented in Figure 3.12. The trajectories shown are those of the photoelectrons that are able to reach the detector.

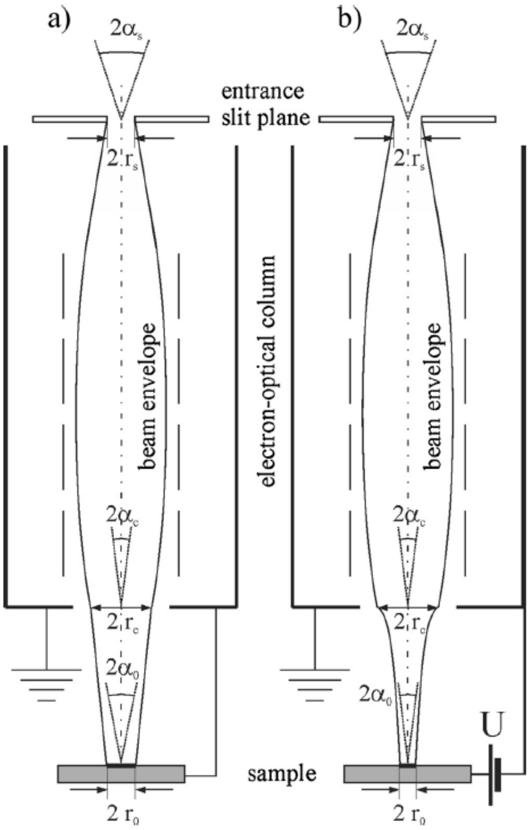

Figure 3.12 – Schematic of the electron beam inside the electron-optical column when the sample is a) grounded and b) biased to a positive voltage *U*.

In order to be detected, an electron has to reach the entrance slit plane with a distance to the axis shorter than the entrance slit radius r_s, and an angle between its trajectory and the optical axis (represented with a dashed line) smaller than the analyser acceptance angle α_s. To simplify the problem, it is assumed that this angle is the same in the dispersive (α_s) and non-dispersive (β_s) planes, i.e., $\alpha_s = \beta_s$, which is generally not true. The electrons that reach the slit plane and fulfil these conditions correspond to those that are emitted from the sample's surface with a maximum distance from its centre of r_0 (from an area *A*), and a maximum emission angle of α_0 (corresponding to a solid angle Ω). At the plane of the electron-optics entrance, located a few centimetres above the sample, the beam is described by the magnitudes (r_c, α_c).

Apart from reducing the energy of emitted electrons to that of the analyser's pass energy, the main role of the electron optical column is to effectively transfer the electrons emitted from the sample surface into the energy analyser, i.e., to focus the beam into the entrance slit. The signal's intensity is obviously proportional to the total amount of electrons detected, and is therefore proportional to the acceptance area *A* and solid angle **Ω** [67]. Assuming a cylindrical symmetry, the acceptance area is a circle with area $A = \pi r_0^{\,2}$, while the solid angle is equal to $\Omega = 2\pi\left(1-\cos\alpha_0\right)$. For values of $\alpha_0 \ll 1$, $\Omega \propto \alpha_0^{\,2}$, and thus the signal's intensity $I\left(E\right) \propto \left(r_0\alpha_0\right)^2$.

The electron-optical column transforms the electron beam cross-section $\left(r_c,\alpha_c\right)$ into $\left(r_s,\alpha_s\right)$. Since r_s and α_s are defined by constant parameters of the analyser, such as the entrance slit width, the analyser's geometry (radius, fringing field correctors, detector placement and slit size, etc), and the specific pass energy at which the analysis is being performed (in FAT regime), they may be considered constant during the energy scan, and so the energy dependence of the transmission function is related exclusively to the electron-optical column. Since r_s and α_s are constant, the kinetic energy being analysed actually affects the beam at the entrance of the electron-optical column, i.e., the values of r_c and α_c. If ε is the energy of detected electrons at any point along the column, so that $\varepsilon = E_a$ at the sample plane, and $\varepsilon = E_{pass}$ at the entrance slit plane, then, according to the Liouville's theorem applied to the propagation of charged particles [68], the quantity $r \cdot \alpha \cdot \varepsilon^{1/2}$ is constant along the beam's trajectory.

Figure 3.12 a) shows the standard case of XPS measurements, where the sample is grounded, and there is no electrical field between the sample and the entrance to the electron-optical column. In this case, it may be written that $T\left(E_a\right) \propto \left(r_c\alpha_c\right)^2$, where E_a is the energy of electrons at the moment of emission. Since ε is constant between the sample and the entrance of the electron-optical column, it may also be written $T\left(E_a\right) \propto \left(r_0\alpha_0\right)^2$.

Furthermore, by applying Liouville's theorem, $r_0 \cdot \alpha_0 \cdot E_a^{\,1/2} = r_c \cdot \alpha_c \cdot E_a^{\,1/2} = r_s \cdot \alpha_s \cdot E_{pass}^{\,1/2}$, and $T\left(E_a\right) \propto \left(r_c\alpha_c\right)^2 = \left(r_s\alpha_s\right)^2 E_{pass}/E_a$. The relation obtained following this approach $T\left(E_a\right) \propto 1/E_a$ is the theoretically expected dependence of the transmission function, i.e., the $T\left(E\right) \propto E^{-n}$ dependence with a value of $n = 1$ [54]. The discrepancy from this dependence with values of *n* smaller than 1 is common [58–61,67], due to beam restrictions in the electron-optical system other than the analyser's entrance slit. From Liouville's theorem, as E_a decreases, α_a increases. If the value of α_0 is higher than the maximum acceptance angle θ between the sample and the entrance to the electron-optical column, the beam will be restricted at this point, and the $T\left(E_a\right) \propto 1/E_a$ dependence will not apply. When considering these aberration effects of the spectrometer, the transmission function can be well described by the $T(E) \propto E^{-n}$ dependence with *n* being in the range [0.5, 1] [69].

Figure 3.12 b) illustrates the case when the sample is biased to a positive voltage *U*. In this case, the electrons are decelerated between the sample and the entrance to the electron-optics column. Their energy is now reduced from E_a to $E_a - E_b$ (with $E_b = eU$), and then from $E_a - E_b$ to E_{pass} at the entrance slit plane. Since the energy of electrons at the entrance of the electron-optics column is $E_a - E_b$, the corresponding transmission function is now $T(E_a - E_b)$, and electrons emitted with energy E_a are detected as having energy $E_a - E_b$.

From Liouville's theorem, it may be written for this case: $r_0 \cdot \alpha_0 \cdot E_a^{1/2} = r_c \cdot \alpha_c \cdot (E_a - E_b)^{1/2} = r_s \cdot \alpha_s \cdot (E_{pass})^{1/2}$. Since $I(E_a - E_b) \propto (r_0\alpha_0)^2$, then $I(E_a - E_b) \propto (r_c\alpha_c)^2 \cdot (E_a - E_b)/E_a$. Because $T(E_a - E_b) \propto (r_c\alpha_c)^2$, the ratio of intensities for the same photoelectron line, measured from the biased and unbiased sample, may be written as:

$$\frac{I(E_a)}{I(E_a - E_b)} = \frac{T(E_a)}{T(E_a - E_b)} \cdot \frac{E_a}{E_a - E_b} \tag{3.2}$$

The second factor on the right side of equation (3.2) is denoted as a correction function ξ:

$$\xi(E_a, E_b) = \frac{E_a}{E_a - E_b} = 1 + \frac{E_b}{E_a - E_b} \tag{3.3}$$

Further analysis shows that the contributions to the change of $I(E_a - E_b)$ with the value of E_b from $T(E_a - E_b)$ and $\xi(E_a, E_b)$ are of the same order of magnitude. Since $I(E_a - E_b) \propto T(E_a - E_b)/\xi(E_a, E_b)$, the relative change of intensity is $dI/I = dT/T - d\xi/\xi$. Assuming the general dependence $T(E) = AE^{-n}$, then, $dT/T = n \cdot dE_b/(E_a - E_b)$, and $d\xi/\xi = dE_b/(E_a - E_b)$. With the parameter *n* typically ranging from 0.5 to 1, these two contributions are therefore of the same order of magnitude, regardless of the biasing voltage. Consequently the original biasing method proposed by Ebel and co-authors has to be incorrect.

Since the effect of the sample-biasing on the signal's intensity can now be calculated, the relative transmission can be determined experimentally by measuring both intensities and applying equations (3.2) and (3.3), so that:

$$\frac{T(E_a - E_b)}{T(E_a)} = \frac{I(E_a - E_b)}{I(E_a)} \cdot \xi(E_a, E_b) \tag{3.4}$$

By following the intensity of the same photoelectron line as it shifts in energy as the value of E_b is scanned, the transmission function can be easily determined. However, it should be stressed that the expression for the correction function was derived for some assumptions and simplifications that may not apply. First, the entrance to the electron-optical column must be on ground potential. Second, the acceptance solid angle Ω is the same for all points inside the acceptance area *A*, which is only an approximation. Consequently, the value derived for the correction function in equation (3.3) may not be accurate, for the same reasons that the $T\left(E_a\right) \propto 1/E_a$ dependence is also not, and its value should therefore be determined experimentally.

The correction function $\xi\left(E_a, E_b\right)$ can be measured in a relatively simple manner, in a similar way to the first principles method. Consider two different photoelectron lines from the same element, of energies E_a and E_k, taken from the same sample, which should again be monoatomic and thoroughly cleaned. The ratio of intensities for these two lines will be described by equation (3.1). When measuring the intensity of line '*a*', if the sample is biased to a voltage *U*, so that $E_b = E_a - E_k$, and this line is shifted to the position of line '*k*' (when it is not biased), combine equations (3.1) and (3.4) can be combined to obtain:

$$\frac{I_a\left(E_k\right)}{I_k\left(E_k\right)} = \frac{\sigma_a \cdot L_a\left(\gamma\right) \cdot \lambda_{eff\,a}\left(E_a\right)}{\sigma_k \cdot L_k\left(\gamma\right) \cdot \lambda_{eff\,k}\left(E_k\right)} \cdot \xi\left(E_a, E_b\right) \tag{3.5}$$

The kinetic energy of electrons at the entrance of the electron-optics column is the same for both lines, and so the two transmission function terms $T\left(E_k\right)$ are cancelled. This allows us to determine the correction function for one value of E_b. Other values of E_b can be used, corresponding to the energy difference between E_a and the other photoelectron lines of the element. Once enough points to accurately plot $\xi\left(E_a, E_b\right)$ have been determined in this way, for an energy span large enough to cover the typical XPS energy scale, the method described to calculate the transmission function using equation (3.4) can be applied.

The biasing method here proposed should cover most of the problems found with the first principles method. First of all, the time and work needed to measure the transmission function is drastically reduced, as the measurement can be theoretically performed with a single sample, which doesn't require cleaning, as only one photoelectron line is measured (the surface contamination layer produces a different attenuation on electrons with different kinetic energies). Since only one high-intensity line is measured (at different biasing voltages), the experimental error is small, and there is no need for long acquisition times required in the first principles method. Also, the problems with the correct choice of integration range and background type are minimized, since these are kept constant. Finally, the density of points can be arbitrarily high.

Some of the problems already stated in the case of the first principles method will appear when experimentally determining the correction function. However, the measurement can still be performed with a single sample, preferentially one with several peaks spread across the whole energy scale. Moreover, it is not expected that small fluctuations of $T\left(E\right)$ have a significant impact on the correction function, which means that ξ should be determined only once during the system's lifetime, assuming that the transmission measurements are performed under the same conditions, particularly with the same distance between the sample surface and the entrance into the electron-optical column. Changing the position of other objects or introducing new ones to the chamber might also affect the electrical fields when the sample is biased, which will influence the value of the correction function.

3.4.3.4 Sample-Biasing Method - Experimental Results

The transmission function measurements with the sample-biasing method were performed on a clean gold sample. As in the case of the first principles method, thorough sputter cleaning of the sample is essential to provide a reliable measurement of the correction function ξ. In order to minimize the uncertainty of the measurement, its most intense line, Au $4f_{7/2}$, was used, having a kinetic energy of about 1170 eV when excited by the X-ray Mg Kα line. Using equation (3.5), the correction function was determined by biasing the sample with voltages that shifted the Au $4f_{7/2}$ line to the positions of the Au 4d, Au $4p_{3/2}$, Au $4p_{1/2}$ and Au 4s lines, which provided data for biasing voltages up to 680 V. To increase this range further, the Cu 3p and Cu $2p_{3/2}$ lines of a clean copper sample were also used, corresponding to a biasing voltage of about 850 V. Since the Au $4f_{7/2}$ and Cu 3p lines are at a distance of only 5 eV from each other, it is considered that the data from the copper sample fits very well to the correction function $\xi\left(1170\,eV,-eU\right)$ obtained from gold. The peak positions, as well as the magnitudes of the photoionization cross sections, asymmetry parameters and quantitative attenuation lengths are shown above in Table 3.2.

The correction function was measured in the low magnification mode, for 20, 40 and 80 eV pass energies. The obtained values of $\xi\left(E_a,E_b\right)$ are shown in Figure 3.13, as a function of the ratio between the bias voltage and the measured kinetic energy $E_k = E_a - E_b$.

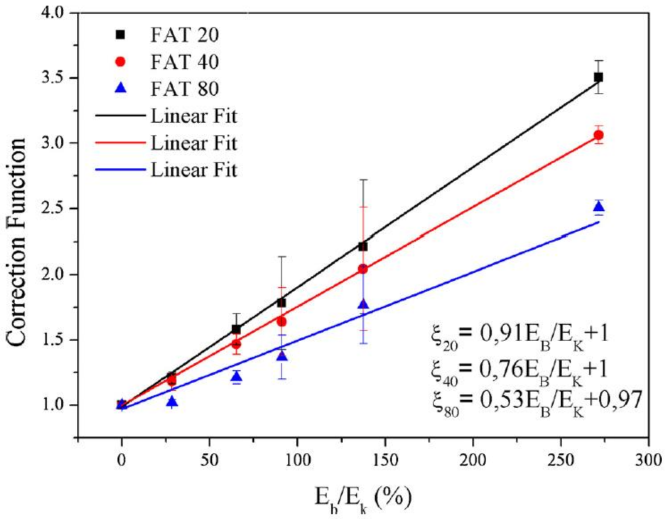

Figure 3.13 – Correction function for 1170 eV (Au 4f$_{7/2}$ line), and E$_{pass}$ of 20, 40 and 80 eV, fitted to linear dependences.

The results were successfully fitted to a linear dependence for all pass energies, as suggested by equation (3.3), with the pass energy of 80 eV showing a worse but still acceptable linear fit. The slope of $\xi\left(E_a, E_b\right)$ is smaller than 1, and is changing with the pass energy. This suggests that the theoretical conditions under which equation (3.3) was derived are not fulfilled, which was actually expected, as none of the measured transmission functions display the theoretical proportionality to $1/E$. This implies that the beam is probably restricted by the aperture of the electron-optics column, as discussed in the previous section. Moreover, this restriction should be more pronounced when the angular magnification of the optical system is smaller, i.e., for larger E_{pass}/E ratios. This is confirmed by the decreasing slope values of $\xi\left(E_a, E_b\right)$ as the pass energy is increased, as can be seen in Figure 3.13.

Once the correction function $\xi\left(E_a, E_b\right)$ was determined, the sample-biasing method based on equation (3.4) was employed to measure the transmission function, in the kinetic energy range from 313 to 1163 eV (starting at the Au 4f$_{7/2}$ energy, with biasing voltages up to 850 V). The obtained results are shown in Figure 3.14, normalized so that $T\left(968\,eV\right)=1$. As for the case with the first principles method, the transmission functions for 20 and 40 eV pass energies can be readily fitted to the power law, while the 80 eV pass energy shows an abnormal shape. The discrepancy of the transmission function from the theoretical $1/E$ dependence $\left(n<1\right)$ increases with the pass energy, confirming the results obtained for the correction function.

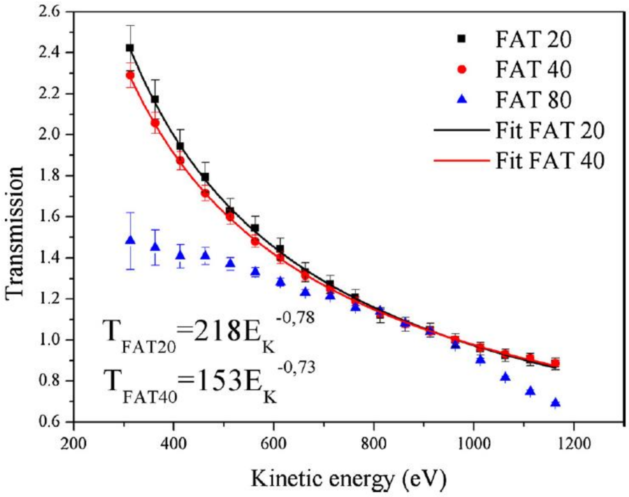

Figure 3.14 – Normalized transmission function determined by the sample-biasing method, for pass energies of 20, 40 and 80 eV.

The biasing method here presented is validated by the fact that the values of *n* determined with the sample-biasing are very close to those obtained with the first principles method. Moreover, as was anticipated, the measurement uncertainty is now much less pronounced, and the higher density of points produces more reliable results. It can be concluded that the biasing method not only produces a reliable measurement of the transmission function, but does so in a superior way compared to the commonly used first principles method.

Having determined its transmission function and non-linearity, this spectrometer is now ready to perform XPS analysis in a reliable way. However, the upgrade of the system is not complete, as there is an opportunity to actually improve the transmission function of the spectrometer by adjusting the voltages applied to the electrodes of the electron-optics column, as will be described in detail in the following section. If a new set of voltages is to be used, the transmission function will have to be determined again for this new configuration.

3.5 System Optimization

3.5.1 Introduction

As previously stated, total transmission function of the spectrometer is the product of the energy analyser and the electron-optical column independent transmissions. The energy analyser’s transmission is defined by the pass energy and slit width. Since the energy resolution is affected by these magnitudes, it is not possible to increase the analyser transmission without increasing its resolution as well. The only way to improve the compromise between the transmission and the resolution of the analyser is by making changes to its geometry, particularly to the design of the fringing field correctors [70]. The transmission of the electron-optical column can, however, be improved without changing the system's geometry by adjusting the voltages applied to its electrodes (electrostatic lenses), provided that the exit slit voltage is not changed, as it defines the detected particle's kinetic energy.

There are several reasons to perform an optimization of the transmission function. As was previously established in section 3.4.1, the transmission of these instruments is changing with time, and, considering the age and wear of this particular model, it is reasonable to expect that considerable changes have already occurred. Furthermore, the voltages used in the transmission function measurements were taken from the PDP-11 computer, but it is not clear if these were the original voltages or if they have since been modified. These measurements revealed some clear problems with the beam focusing, as is evident by the abnormal shape for the 80 eV pass energy. Although the 20 and 40 eV pass energies were still described by the power law, the fact that $n < 1$ shows that the beam is probably restricted in the column, which means that there may still be room for improvements. Finally, in spite of the system's history, optimizing the spectrometer transmission function will improve its sensitivity. This may prove itself particularly useful when performing analysis on the detection limit of the instrument, as is the case with the XPS measurements related to the adsorption of various gases/particles and surface defects studies performed on the TiO_2(110)-(1×1) surface in the context of this work.

One way to maximize the signal of the spectrometer is to search for an ideal set of the electrode voltages of the column, by following the output signal as each voltage is individually adjusted. This procedure can be implemented in this spectrometer, as the new control system allows for the individual and programmable control of each voltage, as opposed to the *Multitécnica* system where all voltages are automatically generated by a single control voltage and a fixed set of voltage dividers [1,26].

Another approach in searching for an ideal set of voltages is to use an electron optics software (such as SIMION) to quickly scan the voltages and analyse the resulting beam, as performed by Sise and co-authors [71]. In their work, they use SIMION to perform a complete scan of two electrodes' voltages, and choose the set that minimizes the system's resolution (energy width of the XPS peaks). Unfortunately, it is not possible to use this approach with the Kratos system, as the detailed geometry of the optical column is not available from the manufacturer, and so the system cannot be correctly simulated in the software. A different method is therefore required to perform the system's optimization, based on a more experimental approach.

Without the detailed knowledge of the system’s internal geometry, the search for a set of voltages that maximizes the signal has to be performed by individually varying the voltages of each electrode, while measuring the magnitude of the output signal. However, since there are 5 independent voltages to control inside the electron-optics column, each one with voltages spanning in the range of at least 1000 V, the number of possible combinations is so vast that it is impossible to use a brute-force approach and test all of them. This means that a search algorithm has to be employed in order to find an optimal voltage set in a timely manner.

Although the algorithm will search for the set that maximizes the output signal, some restrictions have to be added to the possible solutions. First of all, it is very important that the system’s energy resolution is not increased, which may occur if the new focusing strategy increases the entrance angle into the energy analyser. The signal should not be increased solely by the increase of the background signal, as it will simply introduce more noise without increasing the peaks’ intensity. The acceptance area should not be too large, as there is a limit to the size of the samples that fit the sample holder, as well as the limited radius of the area irradiated by the X-ray beam. Finally, it is also important that the new voltages are continuous as a function of energy, so that when performing the energy scan there are no abrupt voltage changes. These would result in larger waiting times between energy steps, as the time required for the power supplies to shift from one voltage value to another increases with the difference between them.

The search for the optimized voltage set can be solved by meta-heuristics i.e. procedures designed to optimize any type of problem by finding its global maximum (not guaranteed), and can thus be used as “black boxes”. This is quite useful for cases where there is an incomplete or incorrect information on the problem to be optimized (the detailed geometry of the column is unknown), or a limited computational capacity (the signal’s acquisition is not instantaneous).

Evolutionary algorithms are a type of meta-heuristics, inspired by biological evolution processes, which are ideal for this type of task. In fact, they were initially introduced by Rochenberg specifically to optimize experimental parameters of scientific instruments [72]. Evolutionary algorithms employ a natural selection based approach to optimization. Starting with a population group whose members represent a possible solution to the optimization problem, each member is subjected to mutations and crossovers, and is then selected based on its performance. As the population is repeatedly subjected to these changes, its members will become increasingly optimized, as represented in Figure 3.15 with the mutation, crossover and selection phases.

For the task of optimizing this spectrometer's transmission function, the use of Differential Evolution is proposed, developed by Storn and Price [73], which is a type of evolutionary algorithm widely used and adapted for a variety of scientific and engineering applications. It can be easily implemented, due to the small number of control parameters, and a very simple algorithm, which exhibits a fast conversion, as is capable of handling most types of problems (non-differential and non-linear), regardless of the initial conditions [74,75].

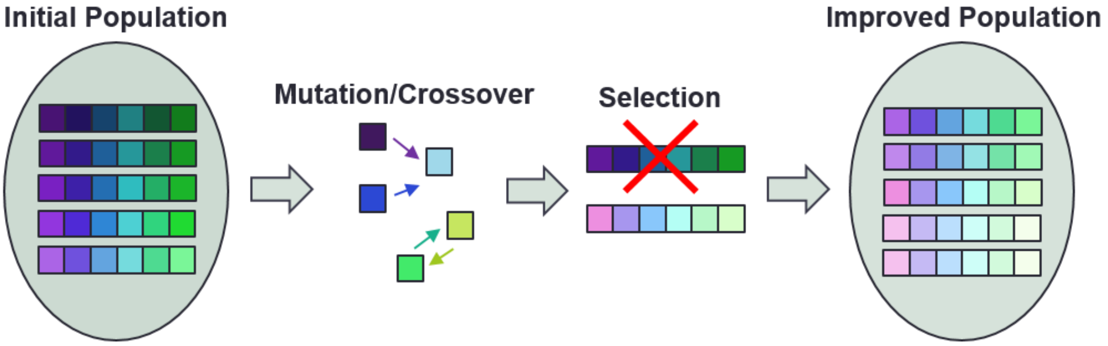

Figure 3.15 – Schematic representation of evolutionary algorithms with mutation, crossover and selection phases.

3.5.2 Differential Evolution Algorithm

Consider an arbitrary real function of *m* variables $f : \mathbb{R}^m \to \mathbb{R}$, called the fitness function, which is to be maximized by the algorithm (or minimized, depending on intent or how the function is defined). In this case, *f* should be the measured count rate, which is a function of *m* voltages. A set of *m* voltages can be represented as an *m*-dimensional vector. A set of *NP m*-dimensional vectors can be created, where *NP* is the number of vectors that form a population (population size), and each element of the population is a vector that is a possible candidate for the global maximum of function *f*. Apart from the population size *NP*, only two additional parameters have to be defined in this algorithm: the differential weight $F \in [0,2]$, and the crossover probability $CR \in [0,1]$. The optimization procedure is performed by following these steps:

For each population member $z = (z_1, z_2, \dots z_m)$, do:

1. *Mutation phase*. Three distinct members of the population, *a*, *b* and *c*, different from *z*, are randomly chosen and used to form another vector $x = a + F \times (b - c)$.
2. *Crossover phase*. A random integer $N \in [1, m]$ and a set of *m* random real numbers $r_i \in [0,1]$ are generated. Then, a vector $z' = (z'_1, z'_2, \dots z'_m)$ is formed from *z* and *x* in the following manner: if $r_i > CR$ and $i \neq N$, $z'_i = x_i$; otherwise, $z'_i = z_i$, for. $i = (1, 2 \dots m)$.

3. *Selection phase.* Function *f* is evaluated for vectors *z* and *z'*. If $f(z') > f(z)$, vector *z* is replaced by *z'* in the population; otherwise, *z* is kept.

By applying these steps through all members of the population, a new and improved generation is created from the previous one (a new set of *NP* *m*-dimensional vectors), with the population from the first iteration being created randomly. The cycle is repeated, creating a new generation at each iteration, until a fitness criterion is reached. Different criteria may be used, such as the convergence of the obtained maximum value of *f*, i.e., when new generations do not improve the fitness function, the convergence of the population itself, or when a pre-determined number of iterations or total time spent is reached. When the fitness criterion is reached, the best member of the population is chosen as the solution to the problem.

The choice of values for the control parameters (*NP*, *F* and *CR)* can have a large impact on the method's performance. In this case, these parameters were chosen based on the meta-optimization of the differential evolution algorithm, performed by Pedersen [76]. In his work, the optimal values for the control parameters are determined, as a function of *m* and the maximum number of cycles imposed. It should be stressed here that there is no need for any prior knowledge concerning the shape of the fitness function $f(z)$ to implement the algorithm. This fact, together with its simplicity, makes the method highly versatile and particularly suitable for these types of automatized optimizations.

3.5.3 Applying the Differential Evolution Algorithm to the Kratos Spectrometer

The optimization of the transmission function of the electron-optical column consists basically in maximizing the count rate, in the whole range of kinetic energies relevant for XPS analysis. The optimization procedure has to start by correctly defining the fitness function. This is the function that returns the value that should be maximized, and so the procedure will fail if it is not correctly defined. In this case, it should be defined in such a way that the conditions previously mentioned in section 3.5.1 are kept. These include: a) an increase of the count rate should not be uniquely due to the increase of the background signal; b) the energy resolution of the spectrometer has to be preserved. Both of these conditions can be fulfilled by defining the fitness function as the difference between the count rate of a photoelectron peak's maximum, and its base (the base is defined on a fixed energy, at a position corresponding to less than 5% of the peak's intensity). In this way, an increase of the background will not increase the value of the fitness function, and a widening of the peak will only increase the "base" signal, and thus decrease the function's value. Ideally, a complete scan of the peak could be performed, and its area and width could be calculated for each evaluation of the fitness function. However, this would considerably increase the time required to perform the optimization, with only a limited advantage. The remaining conditions, keeping the acceptance area's size and the voltage continuity, will be fulfilled by using samples with a limited size for the optimization procedure, and by studying the trend of the optimized voltages as they are determined as a function of the kinetic energy, possibly choosing the vector from the final generation that follows the established trend, or including vectors in the initial population that are expected to follow that same trend. Having in mind that the optimization is solely performed on kinetic energies centred on XPS peaks, the signal of only one of the three detectors was used, as each one corresponds to slightly different kinetic energies.

After defining the fitness function, the next step is to define which voltages are going to be changed. A schematic of the electron-optical column is presented in Figure 3.16. The optimization was performed in the low magnification mode, in which electrodes 1 and 2 are grounded, according to the original voltages, and will be kept as such. The entrance slit must also be at a defined voltage, which means that the transmission function is defined by the voltages of electrodes 3-6 (electrodes 3 and 4 are on the same potential), V_{3+4}, V_5 and V_6.

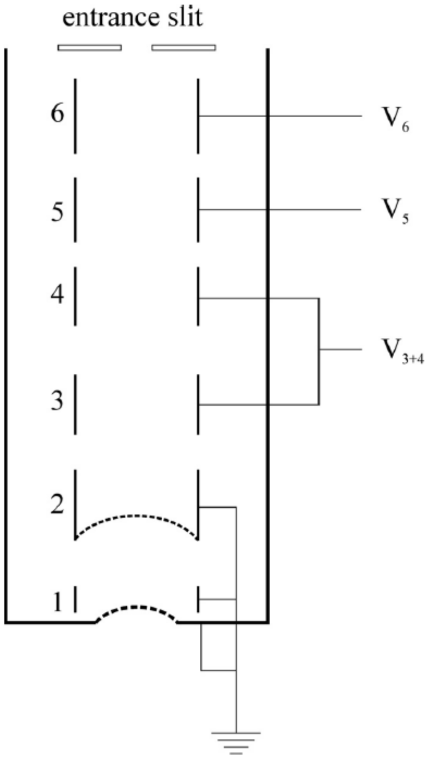

Figure 3.16 – Schematic representation of the electron-optical column operation in the low magnification mode.

Some additional features were added in order to minimize the time required to run the optimization procedure. Adequate limits for the randomly generated voltages have to be set, for each kinetic energy being optimized. The initial population is not entirely random. A vector with the original voltages is added, as well as one with the voltages established from the optimization trend. These two vectors should produce a reasonable signal, and so it is expected that they push the optimization in the correct direction. Finally, a compromise on the signal acquisition time has to be reached. Since the signal has inherent noise, short acquisition times will produce unreliable results, while acquisition times that are too long will greatly increase the time required to finish the procedure. The acquisition time will have to be a function of the intensity of the specific peak being measured, which will depend on the element/line, and the pass energy.

The values of the parameters NP, F and CR were chosen according to the recommendations from [76], as 13, 0.9096, and 0.747, respectively. The convergence criterion was eventually decided as the algorithm run, and was established to be the point in which the fluctuation of the fitness function between subsequent iterations is in the frame of the noise level (assuming Poisson distribution) and there is no increasing trend. Alternatively, the convergence criterion may also be established as the point when the population itself converges, i.e., when there is no change to the population between iterations, or all members are very similar.

The algorithm developed to maximize the transmission function was implemented in LabVIEW, which runs the differential evolution procedure, controls the voltages and evaluates the fitness function. Excluding the computation time, which should be negligible, the time required to perform the optimization for a single photoelectron line and pass energy is governed by the chosen acquisition time, and the waiting time necessary for changing the electrode's voltages. The latter is significantly larger than during the normal spectra acquisition, when these voltages are increased/decreased in continuous steps, corresponding to small changes of the measured energy, as opposed to jumping between the (random) values of each population member.

The optimization was performed on a set of photoelectron lines spread along the whole energy range of interest, for the pass energies of 20, 40 and 80 eV. A sufficiently high density of points in different energies is achieved by using several samples. A typical size of 10×10 mm^2 was used, and the analysed samples are listed in Table 3.3, along with the corresponding photoelectron lines. These were measured using the Mg Kα X-ray line, with the exception of the Au $4f_{7/2}$ line, which was also measured using the Al Kα X-ray line, in order to extend the optimized energy range. This choice of lines allowed us to perform the optimization in the kinetic energy range 200-1400 eV.

Table 3.3 –Samples, photoelectron lines and respective kinetic energies used for the optimization of the transmission function. All lines were excited by Mg Kα photons, apart from Au 4f$_{7/2}$, which was also excited by the Al Kα X-ray line.

Sample	**Line**	***E* (eV)**
Gold	Au 4f$_{7/2}$	1170 (Mg Kα)
		1403 (Al Kα)
Tantalum	Ta 4f	1227
Molybdenum	Mo 3d$_{5/2}$	1026
Graphite	C 1s	969
Silver	Ag 3d$_{5/2}$	886
	Ag 3p$_{3/2}$	681
	Ag 3p$_{1/2}$	650
Indium	In 3d$_{5/2}$	810
Indium	In 3p$_{3/2}$	589
TiO_2	Ti 2p$_{3/2}$	795
TiO_2	O 1s	724
Cobalt	Co 2p$_{3/2}$	476
Nickel	Ni 2p$_{3/2}$	402
Copper	Cu 2p$_{3/2}$	322
	Cu 2p$_{1/2}$	303
Zinc	Zn 2p$_{3/2}$	232
	Zn 2p$_{1/2}$	209

The time required to optimize a single energy depends mainly on the intensity of the signal, i.e., on the line being measured, and the pass energy. This time ranged from 30 to 60 minutes. With 18 different energies being optimized, the full optimization takes a total time 9-18 hours, for each pass energy. The optimization was successfully performed for the three pass energies. The original and optimized voltages are presented in Figure 3.17 as a function of the kinetic energy, with similar results being obtained for all pass energies. The value of the slit potential, V_{slit}, is shown as well. The ‘focusing strategy’ is apparently the same for the two sets of voltages, with electrons beings first decelerated by V_{3+4}, accelerated by V_5, and decelerated again by V_6 to an energy value close to the pass energy. The first deceleration stage is now stronger, due to the increase of the slope of V_{3+4}. The acceleration stage is dramatically changed, with V_5 showing now a high positive voltage, which is energy independent. For the pass energies of 20 and 40 eV, the slope of V_6 was originally very similar to V_{slit}, and remained so after the optimization. The original slope of V_6 for the pass energy of 80 eV was comparatively much lower, which may justify the abnormal shape of its transmission function. Its optimized value now follows the same behaviour as that of the lower pass energies. At this final stage the detected electrons have a very low kinetic energy, which means that small changes to V_6 may still be very influential to its trajectories.

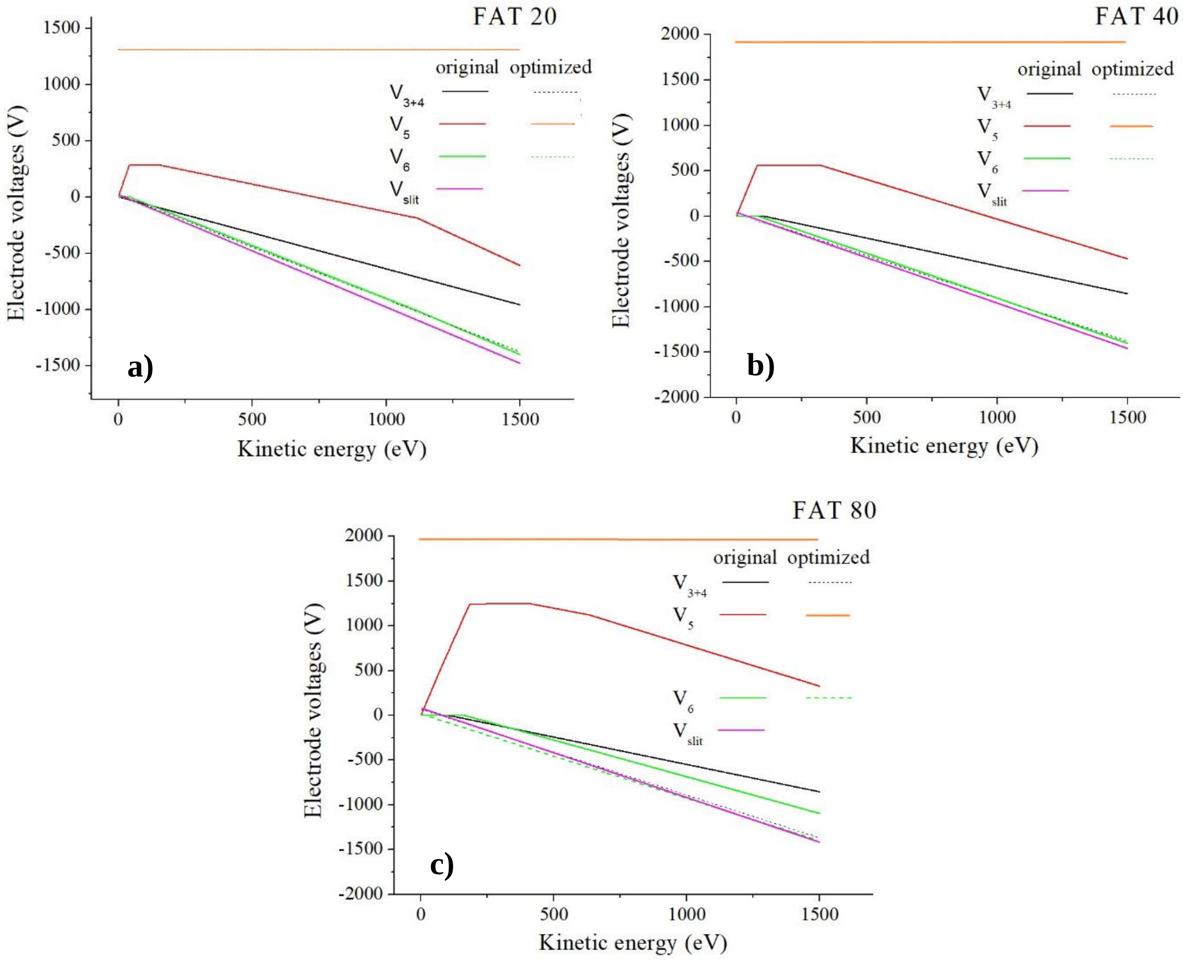

Figure 3.17 – Original and optimized electron-optical column voltages vs kinetic energy, for a) E_{pass} = 20 eV, b) E_{pass} = 40 eV and c) E_{pass} = 80 eV.

To better understand the focusing effect of the optimized voltage set, the electron-optical column was simulated on SIMION, using the drawing shown in Figure 3.3 as a basis for its design. A 400 eV electron beam originating from the sample surface was directed into the entrance of the column, and the focusing was tested with the original and optimized voltages, for the pass energy of 80 eV, as shown in Figure 3.18. The simulations showed a clear increase of the acceptance area, evident by the fact that the source of the electron beam with the original voltages has a smaller radius, but is not able to go through the exit slit. In the optimized voltage set, V_6 is actually lower than V_{slit}, and this produces a second acceleration stage that effectively focuses the beam into the exit slit. However, this is not true for all kinetic energies, as the slope of V_{slit} is slightly higher than V_6, and the two eventually cross each other as the kinetic energy increases, as is shown in Figure 3.17 c)

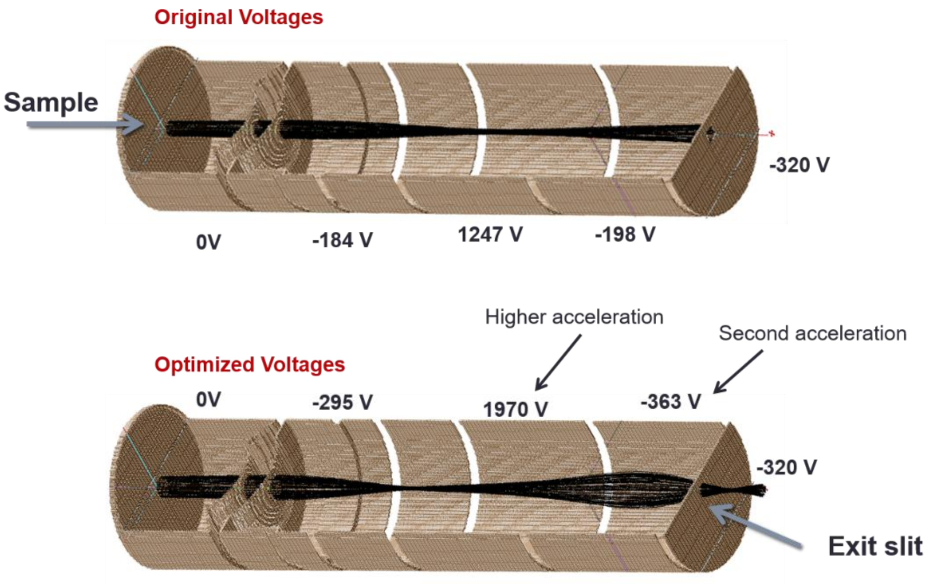

Figure 3.18 – SIMION comparison of the electron beam inside the electron-optical column, for the original and optimized voltages, with E_{pass} = 80 eV, and an electron energy of 400 eV.

The optimization factor, here defined as the ratio between the new and the old transmission function (T_{new} and T_{old}, respectively), before normalization, is shown in Figure 3.19, and represents the signal's increase.

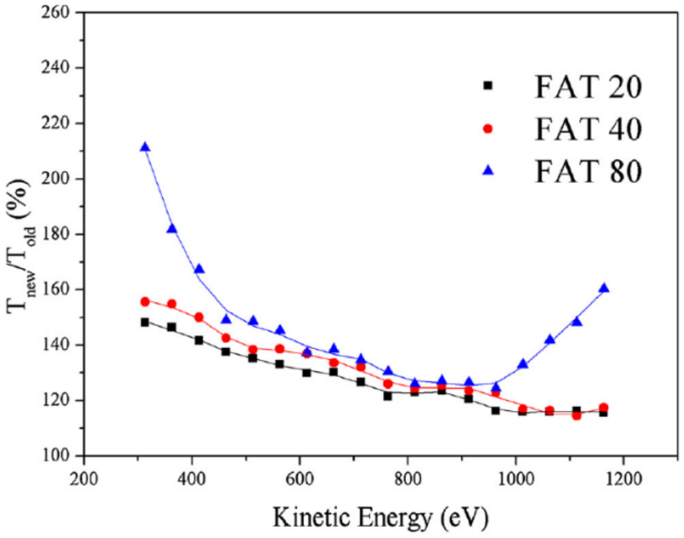

Figure 3.19 – Optimization factor, defined as the ratio T_{new}/T_{old} vs Kinetic energy.

Overall, the signal was successfully increased in the whole range of kinetic energies, for the three pass energies. For pass energies of 20 and 40 eV, the signal was increased by 10-50%, with both pass energies showing the same shape of the optimization factor, i.e., a monotonous decrease of T_{new}/T_{old} with the increase of the kinetic energy. The optimization for the 80 eV pass energy provided a much higher optimization compared to the lower pass energies, with a signal increase in the range of 25-110%. This improvement is particularly high in both ends of the kinetic energy scale, with the middle range following the same behaviour as the lower pass energies. With this shape of the optimization factor for $E_{pass} = 80$ eV, it is expected that the shape of $T\left(E\right)$ for this pass energy will be significantly changed, while it should be generally preserved for the lower pass energies.

The new transmission function, measured for all pass energies with the sample-biasing method, is shown in Figure 3.20 a), and the corresponding correction functions are shown in Figure 3.20 b). The abnormal shape of the original $T_{FAT80}\left(E\right)$ curve, observed in the measurements performed with the original voltage set (see Figure 3.14), was successfully corrected by the optimization procedure, and all pass energies now follow the power law. For the lower pass energies, the transmission functions are overlapping, with $n \approx 0.985$. This is very close to the theoretical $1/E$ dependence, predicted by Liouville's theorem, and it shows that there was a reduction or even elimination of the beam restriction inside the electron-optical system. This is also supported by their respective correction functions, which are now equal to the derived expression shown in equation (3.3), in the frame of the experimental error. Furthermore, both $T_{FAT80}\left(E\right)$ and $\xi_{80}\left(E\right)$ are closer to their predicted dependencies after the optimization, although not completely corrected.

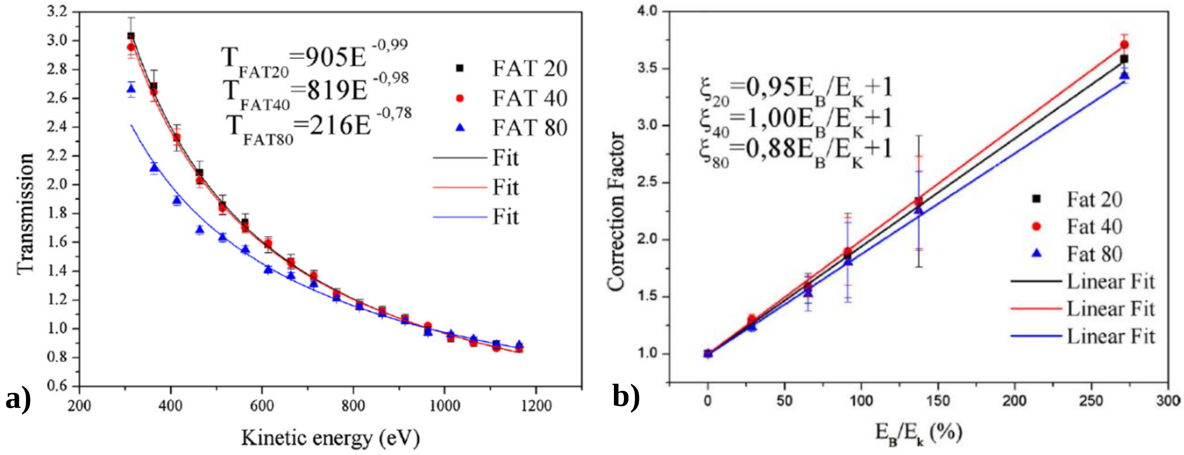

Figure 3.20 – a) Normalized transmission function measured with the sample-biasing method. b) Corresponding correction factors.

From this comparison of the new and old transmission functions, the optimization procedure appears to have been successful. However, an assessment of the XPS spectra must also be performed, to ensure that the imposed conditions were fulfilled, i.e., the spectrometer's resolution was not worsened, and there was no significant increase of the noise. To perform this comparison, the Au 4f and Cu $2p_{3/2}$ photoelectron lines were measured, from pure gold and copper samples, respectively, for the two sets of voltages (original and optimized), and the pass energies of 20, 40 and 80 eV. The results are shown in Figure 3.21, and the respective line widths *w* (FWHM) and areas are summarized in Table 3.4. It should be stressed that all parameters were kept constant for the analysis (X-ray intensity, scan parameters, sample position, etc.), and only the voltages of the electron-optical column were changed (V_{3+4}, V_5 and V_6). Apart from the clear increase of intensity for all pass energies, which follows the values calculated for the optimization factor shown in Figure 3.19, both lines look very similar, with the same shape, width, and position, confirming that the optimization didn't introduce errors or unwanted artefacts in the XPS measurements.

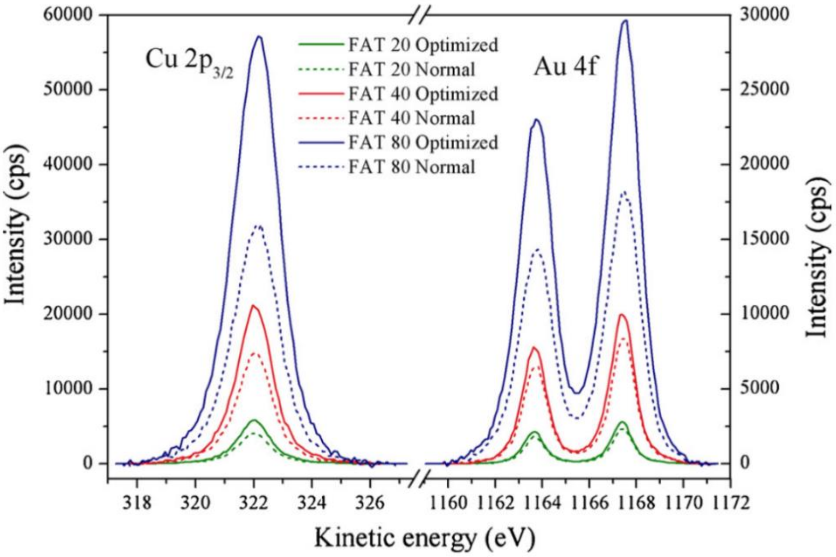

Figure 3.21 - XPS spectra of Cu 2p3/2 and Au4f lines, taken from pure copper and gold samples, respectively, after removal of the Shirley background. The spectra were taken in FAT 20, 40 and 80 modes, for the original and optimized sets of voltages.

Table 3.4 – Intensities and FWHMs of the lines taken in different FAT modes using original and optimized voltage sets.

Line	**Voltage Set**	**E_{pass} = 20 eV**		**E_{pass} = 40 eV**		**E_{pass} = 80 eV**	
		w (eV)	area	*w* (eV)	area	*w* (eV)	area
Au $4f_{7/2}$	Original	0.99	3097	1.06	12553	1.44	35638
	Optimized	0.98	3558	1.06	14713	1.43	57536
Cu $2p_{3/2}$	Original	1.27	6518	1.27	25566	1.56	67385
	Optimized	1.26	9381	1.27	37490	1.54	122450

All reported results show that the optimization procedure was successful, and the transmission function of the spectrometer was improved for all pass energies. Furthermore, the abnormal shape of the transmission function for the pass energy of 80 eV was corrected, and all now follow the power law, which is frequently encountered in the literature [58–61,67]. From the simulations performed on SIMION, the higher transmission appears to be due to an increase of the acceptance area, but further experimental measurements should be performed to confirm this result, due to the questionable origin of the design used to simulate the electron-optical column. The optimized voltages will therefore be particularly useful for the XPS characterization of samples with large areas, around 1 cm^2, which was the main goal.

The procedure used to optimize the system should be applicable to any XPS system that allows individual control of electrode voltages, as nothing else is needed to implement the differential evolution algorithm, apart from the required computation. Furthermore, the approach can be used to optimize the system in the high magnification mode. This can be accomplished by using a set of small samples instead, having an area comparable to that of the desired acceptance area. Further improvement of the transmission function can be reached by adding two programmable analogue outputs to the computer (only four are available at the moment), and connecting them to the high-voltage power supplies of electrodes 1 and 2, which were grounded during the optimization. There is, however, a likely possibility that the addition of these two additional variables will greatly increase the required population size, as well as the number of iterations needed to reach the convergence criterion of the algorithm, significantly prolonging the time required to optimize the system.

4

4 Work Function Measurement Based on the Onset Method

4.1 Introduction

The work function of a material is defined as the energy difference between the Fermi level E_F and the vacuum level. Figure 4.1 shows a representation of this magnitude on metals and semiconductors. The work function is extremely sensitive to surface properties, such as its structure and composition, or adsorption, including surface contamination. Although not frequently monitored in surface analysis, it is one of the fundamental characteristics of surfaces, which can be used to understand and predict physical processes behind interactions of a material with its surroundings, such as adsorption, heterogeneous catalysis or electron emission processes.

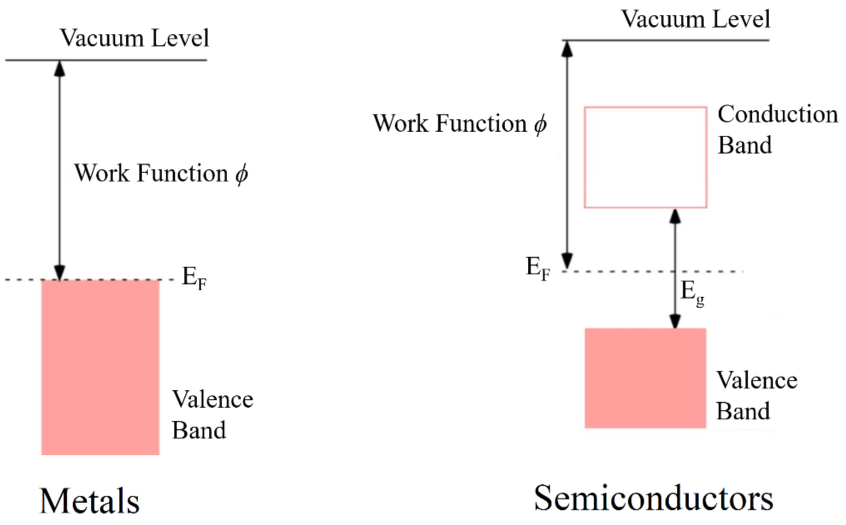

Figure 4.1 - Diagram showing the work function in the band diagram of metals and semiconductors.

Work function measurement is therefore a useful tool when studying the interaction of surfaces with the environment. It can be also used to study surface structure and composition, as the work function is sensitive to the amount and type of surface defects, as well as to different crystal planes. Following the time evolution of the work function during certain processes can be particularly interesting, since it reflects their dynamics. Different techniques available to measure the work function are used to monitor surfaces while they are subjected to modifications, such as corrosion, adsorption/desorption processes, oxidation, thin film deposition, among others. Finally, work function imaging methods can be used to study the orientation of different crystal facets in a surface, the number and type of surface defects, follow thin film growth, among other possibilities [28,77,78].

There is a wide variety of experimental methods used to measure the work function. They can be generally separated in two groups, the methods that provide an absolute measurement of the work function, and those that provide only its relative measurement. The latter are typically based on the measurement of the contact potential between the sample and the measurement device (e.g. reference electrode), and are particularly useful to follow changes of the work function due to modifications of the sample's surface. The Kelvin Probe and the onset method (measurement of the secondary electron emission energy threshold) are two of the main methods that provide a relative work function measurement. If the instruments are calibrated with a sample of known work function, the relative measurement can then be converted to the absolute one. The methods that directly provide an absolute measurement are based on the electron emission triggered by different stimuli. Such methods include heating of a material to cause electron thermionic emission, electron excitation by irradiation with ultraviolet light [79], and the emission of electrons induced by an electric field, called field emission, which works by applying a local electric field strong enough to bend the potential energy curve, reducing the barrier height and width, creating the conditions for electron tunnelling from the Fermi level into the vacuum [78]. The main processes behind these techniques can be used with other instruments to provide work function imaging, such as using the narrow electron beam of a Scanning Auger Microscope instrument to map the secondary electron emission energy threshold, using an Atomic Force Microscope as a Kelvin probe to provide relative work function mapping with atomic resolution, or using a photoelectron emission microscope with a UV source to map the absolute work function [77].

4.1.1 Work Function Definition of uniform and non-uniform surfaces

Considering a metallic surface, the work function Φ is defined as the energy required to remove an electron from that surface to the vacuum. As shown in Figure 4.2, valence electrons are situated in a potential well formed by the metallic ions. $\bar{\mu}$ represents the highest occupied energy by valence electrons (in metallic surfaces, this is equal to Fermi level at 0 K), so the height of this barrier is $\Phi_b - \bar{\mu}$. Breaking of the translational symmetry of the crystal at the surface causes the electron cloud to spill above the surface, creating a surface dipole that originates an energy barrier for electron removal, equal to $\Delta\Phi$.

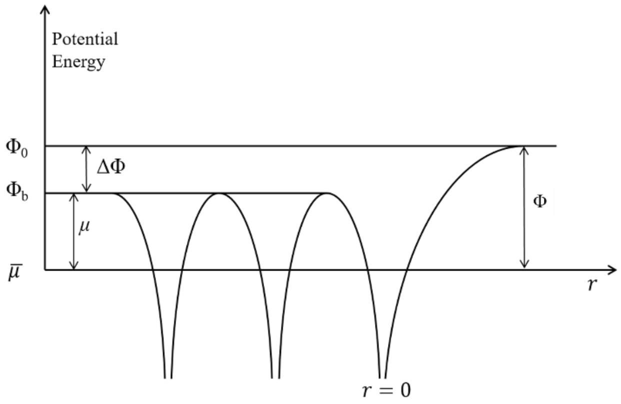

Figure 4.2 – Representation of the potential energies of electrons in a material perpendicular to the surface, where r is the distance to the surface.

The work function can be defined as the difference between the potential energy $\bar{\mu}$ of electrons inside the material and the potential energy Φ_0 of electrons above the surface [28,78]:

$$\Phi = -\Phi_0 - \bar{\mu} \tag{4.1}$$

The electric potential of an electron above the surface is a function of the distance 'r' from the surface. In the absence of external electric fields, for a homogenous surface, this magnitude, well known as image potential in classical electrodynamics, is equal to:

$$V(r) = -e/16\pi\varepsilon_0 r \tag{4.2}$$

where ε_0 is the vacuum permittivity. Φ_0 corresponds to the potential energy in vacuum, i.e., when $V(r)$ is approximately constant, which happens for values of r above 100 nm.

For non-homogenous surfaces, the definition of work function is more complex. Consider a surface with different patches, caused by the adsorption/deposition of different species, or simply from the different orientation of the crystal structure in the patches. Each patch i will be characterized with its local work function Φ_i. The electrical contact between the patches with different work function causes the formation of a contact potential between them. In equilibrium, the electrochemical potential $\bar{\mu}$ is constant in the material due to the flow of electrons from higher to lower potential energies, causing the non-uniform electric charge distribution along the surface. This results in electrostatic potential difference at the interface between the patches i.e. in local contact potential. At a certain distance r_0 from the surface of a patch i , much smaller than the characteristic patch dimensions, this potential energy depends only on the patch characteristics and equals Φ_{0i}. The work function of each patch, defined as the local work function, is then equal to:

$$\Phi_i = -\Phi_{0i} - \bar{\mu} \tag{4.3}$$

At larger distances from the patch surface the potential energy distribution becomes affected by the surrounding patches. Finally, at distances much larger than the patch dimensions, the potential energy becomes equal to some constant value Φ_0. It can be shown that its value is equal to:

$$\Phi_0 = \sum_i f_i \Phi_{0i} \tag{4.4}$$

where f_i is the fraction of the total surface area occupied by patch 'i'. The average work function is then defined as:

$$\begin{aligned} \bar{\Phi} &= -\sum_i f_i \Phi_{0i} - \bar{\mu} \\ &= -\sum_i f_i \left(\Phi_{0i} + \bar{\mu} \right) \end{aligned} \tag{4.5}$$

Replacing equation (4.3) in equation (4.5), the average work function of a surface can be understood as the weighted average of the local work function of all patches

$$\bar{\Phi} = -\sum_i f_i \Phi_i \tag{4.6}$$

4.1.2 Work Function Measurement Based on the Secondary Electron Emission

One of the common ways to perform work function measurements is to measure the position of the low energy cut-off (onset) of the secondary electron energy distribution. This approach, also known as the onset method, has been used to measure and follow the work function of conductive surfaces for more than 40 years [80,81]. The low energy cut-off of secondary electrons for gold and molybdenum samples, shown in Figure 4.3, corresponds to electrons that leave the sample with the minimum amount of energy required to reach the detector.

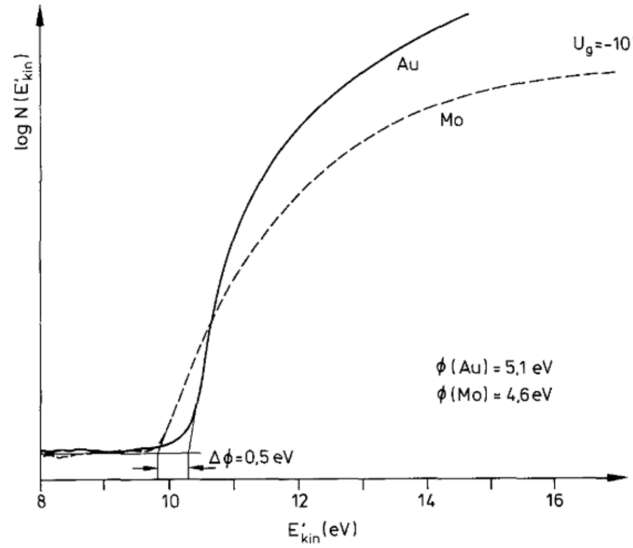

Figure 4.3 – Low energy cut-off (onset) of the secondary electron energy distribution, for gold and molybdenum samples. [82].

The onset position corresponds to a relative measurement of the work function, which can be converted to the absolute value by calibrating the measurement with a sample of known work function. The secondary electron energy distribution is measured with a charged particle analyser, and the electrons are usually produced by photon irradiation [22,24,90–93,79,83–89], but other radiation sources can be used, such as electron/ion beams [82,94–100]. Any surface science equipment prepared for XPS/AES is therefore providing a possibility to perform this measurement. In systems equipped with a UV-light, it is possible to get a direct measurement of the absolute work function, without system calibration, as proposed by Park and co-authors [79]. If the system is equipped with an electron gun that provides positioning of a narrow beam, it is also possible to perform the surface mapping of the work function, with a resolution comparable to that of SAM, in a technique known as Work Function Microscopy (WFM).

[94,96,97]. Depending on the dipole moment of the adsorbed molecules, the detection limit can be significantly below that of regular XPS systems, as in the case of water adsorption on TiO_2 [22,24,83], mainly due to the ultimate surface sensitivity of the work function. The principle of the onset method is based on the contact potential difference between the sample and the energy analyser, i.e., the work function difference, as shown in Figure 4.4.

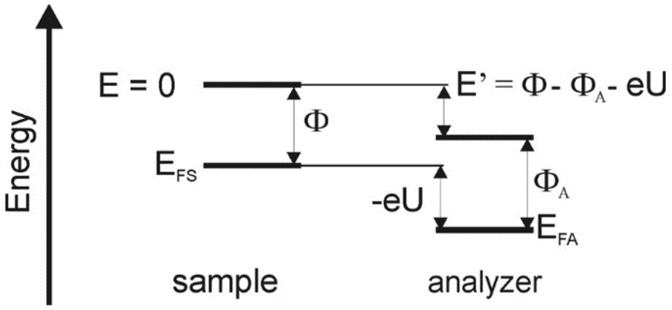

Figure 4.4- Energy diagram of the sample and energy analyser during work function measurements. EFS and EFA correspond to the Fermi levels of the sample and analyser, respectively.

Electrons leaving the sample with kinetic energy *E*, will have kinetic energy *E'* in front of the energy spectrometer, equal to.

$$E' = E + \Phi_s - \Phi_A - eU = E + \Phi_s + E_0 \tag{4.7}$$

Where Φ_s and Φ_A are the work functions of the sample and the energy analyser, respectively. *e* is the electron charge, *U* is the voltage applied to the sample, and $E_0 = -\Phi_A - eU$ [96]. Since the onset position corresponds to electrons leaving the sample with kinetic energy $E = 0$, the sample is typically biased to a negative voltage $U < (\Phi - \Phi_A)/e$, which assures that these electrons overcome the contact potential barrier (when $\Phi_A > \Phi$), and reach the detector. The onset position is the value of E' when $E = 0$, which is equal to $\Phi + E_0$. Since E_0 is constant, a shift of the onset position corresponds directly to a change of the sample's work function. The technique is therefore suitable for following the work function change during modifications of the material's surface, such as adsorption/desorption or deposition processes. If the work function of the analyser is known, by calibrating the system with a sample of known work function, this relative value can be easily converted to the absolute one.

4.1.2.1 Analysis of the Onset Position

The secondary electron region of the energy spectrum is characterized by a very intense signal, typically several orders of magnitude higher than that of XPS peaks. This part of the spectrum can therefore be reliably obtained with very short acquisition times. With a suitable "scanning" tool/software, the work function can be followed in real time by continuously acquiring new spectra. The total time required for the spectrum acquisition is of a few seconds, which is sufficiently short to allow this technique to be used as a tool to measure adsorption dynamics of relatively fast processes, such as work function drop due to adsorption of water on the surface of $TiO_2(110)$-(1×1) [23–25].

Typically, this type of analysis requires calculating the onset position for hundreds of spectra. The data analysis has to be performed by a script, which is written to automatically calculate the onset position of the low energy cut-off region. The quality of the results depends on the chosen algorithm for the onset position calculation.

As shown in Figure 4.3, the onset position is roughly determined by extrapolating the initial increase of the signal, corresponding to the region with the highest slope. The "tail" of the energy cut-off is caused by the finite instrumental function width of the analyser, and should be ignored when performing this procedure. One simple way to calculate the onset position in a reproducible manner is to find the maximum of the first derivative in the region where the signal intensity is increasing, perform a linear extrapolation at that point, and look for the interception of the extrapolated line with the background intensity level. Additionally, the data can be smoothed using some type of polynomial interpolation, which should increase the precision of the procedure. Depending on the specific data set and instrument, different variations of the onset fitting algorithm may produce results of better quality, and it could therefore be useful to test different variations on the same data. An example of this influence is shown in Figure 4.5, which compares the onset position calculated with different methods.

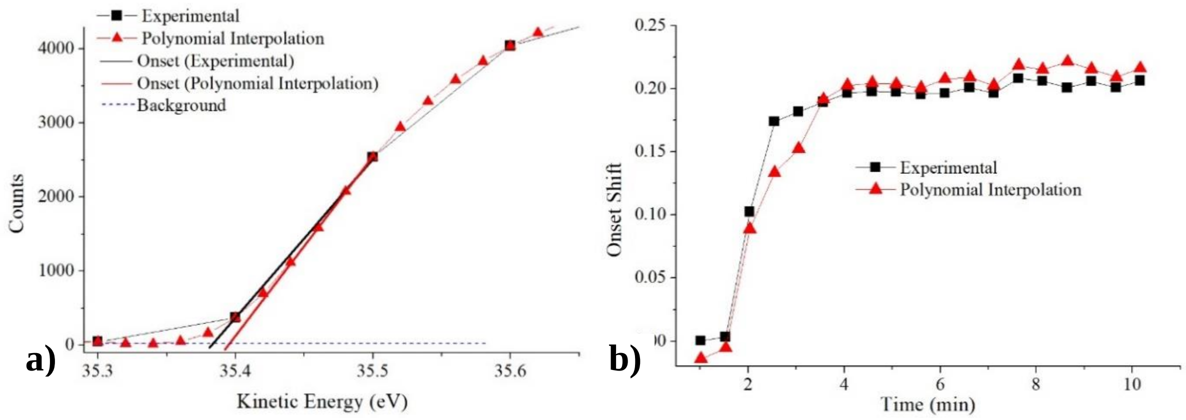

Figure 4.5 – Comparison of the onset calculation for the experimental and smoothed data. a) Secondary electron distribution and onset calculation b) Work function change using different calculations.

Figure 4.5 a) shows the difference of the onset calculation using the experimental data (resolution of 0.1 eV) and the data smoothed with spline interpolation. Figure 4.5 b) shows the onset shift vs. time, during the exposure of the $TiO_2(110)$-(1×1) surface to O_2, which increases its work function. The data that was treated with the spline interpolation offers a smoother transition when determining the onset position.

The precision of the onset position can be further improved by modifying the control system of the energy analyser, with the aim of increasing the resolution of the energy steps. Since secondary electrons are in the range of 0-50 eV, and most energy analysers are capable of measuring kinetic energies up to 5000 eV, the minimum energy step of the system in the secondary electron range can be improved by dividing the output voltages by a certain factor. This will reduce the maximum kinetic energy that can be scanned, while decreasing the minimum energy step. Some XPS models already provide this option in their respective control units [1,26]. Alternatively, if this feature is not provided, the same outcome can be reached by adding voltage dividers to the control voltages generated by the computer controlling the system, or, alternatively, by increasing the resolution of the Digital-to-Analogue converters in case of computer control.

4.1.3 Work Function changes on Semiconductor Surfaces

The experimental work presented in chapter 6 concerns the measurement of the work function change of the $TiO_2(110)$ surface when exposed to different adsorbates or when defects are created at the surface. It is therefore important to also understand the meaning of the work function change measurement on a semiconductor surface. The band-diagram of a semiconductor, and how it is affected by the presence of adsorbates, is shown in Figure 4.6.

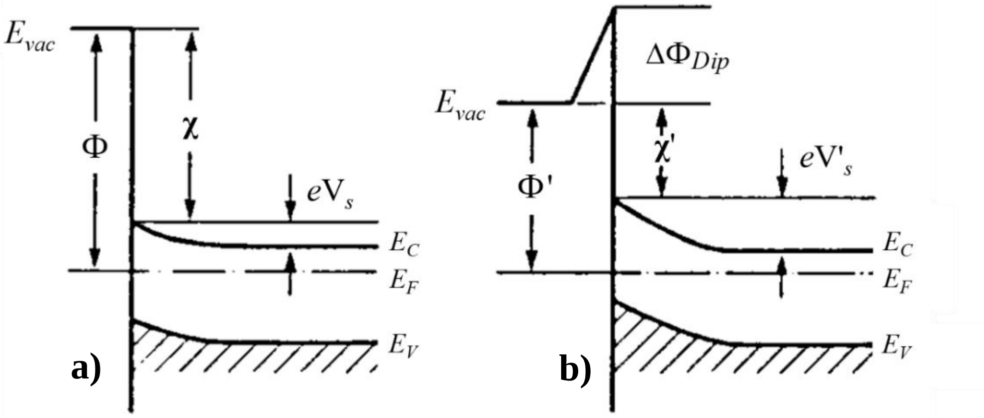

Figure 4.6 - Qualitative electronic-band diagrams of semiconductor surfaces for: a) clean surface b) adsorbate-covered surface. χ is the electron affinity, eV_s represents the band-bending at the surface, and E_C, E_F, and E_V are the bulk conduction, Fermi, and valence levels, respectively. $\Delta\Phi_{Dip}$ is the contribution to the work function change associated with the dipole moment of the adsorbate, and the adsorption changes the band bending into eV'_s. Figure adapted from [101]

It is convenient to define the work function of a semiconductor surface as [101]:

$$\Phi = \chi + eV_s + (E_C - E_F)_{bulk} \tag{4.8}$$

where χ is the electron affinity, eV_s is the band bending at the surface, E_C and E_F are the bulk conduction and Fermi levels, respectively. The adsorption of atoms or molecules on the semiconductor surface results in the presence of new surface dipoles, as well as an additional band bending. The change of the work function due to these effects is given by:

$$\Delta\Phi = \Delta\Phi_{Dip} + e\Delta V_s \tag{4.9}$$

where $\Delta\Phi_{Dip}$ is the change attributed to the surface dipole, also equal to the change of the electron affinity, and ΔV_s is the additional band bending.

The dipole contribution to the work function change may be due to the dipole moment of the adsorbed molecule itself, in the case of strong chemisorption the charge shift between the substrate and the adsorbate also creates additional surface dipoles, and even in the case of weak physisorption, image charges below the surface are created, thus introducing an additional contribution to the dipole layer. These effects associated with shifting charges will also be present with surface defects such as steps or vacancies [101].

The work function change attributed to surface dipoles can be quantitatively described by different models, among which that of Topping [102] being used [90,91,93]. In this model, the work function change is calculated from the concentration of surface dipoles, originated from the adsorbed species, and is given by:

$$\Delta\Phi_{Dip} = -\frac{e}{\varepsilon_0} \cdot \frac{n \cdot \mu}{1 + \frac{\alpha}{r^3}} \tag{4.10}$$

where n is the concentration of dipoles at the surface created by the adsorbed species, μ is the dipole moment at small surface coverages. The depolarization term $1 + \alpha/r^3$ is included to account for the decrease of the dipole moment due to the proximity between dipoles (leading to their depolarization), where α is the dipole polarizability, and r is the average distance between dipoles.

In the case of semiconductor surfaces, the Fermi level is located in the band gap, where there are no available states for electrons. Consequentially, when measuring the onset position from a semiconductor surface, the electrons emitted from the highest occupied level are thus origination from the top of the valence band, and not from the Fermi level. While the absolute value of the work function measured in this way will thus be incorrect, the work function change will be accurate, provided that only the electron affinity is changed, i.e., the position of the Fermi level relative to the valance band maximum is not affected, the band-bending is negligible. This can be evaluated by isolating the two contributions, as the band-bending will affect the binding energy of core-levels, resulting in a shift of the XPS peaks [103].

Through the course of the work here performed with the TiO_2(110)-(1×1) surface, presented in chapter 6, and involving both the adsorption of different species and the creation of surface defects, no noteworthy shift of the O 1s and Ti 2p peaks was observed, and hence it is always assumed that, during these experiments, the work function changes are strictly attributed to a change of the dipole layer.

4.2 Secondary Electron Emission from Non-Uniform Surfaces

The Topping model, presented in section 4.1.3, assumes that the surface is uniform during the adsorption process, which is generally not the case, as the presence of surface defects is common [101], and thin films typically grow in locally uniform patches [104]. Nevertheless, the Topping model is generally used without checking the uniformity of the analysed surface during the adsorption/deposition process, and is regularly applied to surface coverages up to 1 monolayer [88–93].

For non-uniform samples, the energy spectrum of secondary electrons emitted from the whole surface is composed of the sum of different contributions, each corresponding to areas/patches with different local work functions. It is usually considered that in this case the onset position is related to the local value of the area/patch with the minimum work function [79,87], and the Topping model relates the change of the onset position with the local coverage of that area/patch. Similarly, if a scanning focused beam is used as irradiation source (usually an electron beam), the onset position at each point will be determined by the minimum local work function of the area irradiated by the beam. Such an experiment, known as Work Function Microscopy (WFM), is expected to provide surface distribution of the work function with a lateral resolution comparable to the beam diameter [82,94–98].

4.2.1 Patch Field

As will be shown, the onset position is actually not directly related to the local work function, which makes the previous assumptions incorrect. A non-uniform distribution of the work function implies a contact potential difference between the different regions, as already mentioned in section 4.1.1.

This difference creates an electric field (patch field), as shown in Figure 4.7, which will alter the potential energy distribution above the surface. As explained in the same section, the electrostatic potential at a sufficiently long distance from the surface is equal to the weighted average of the potential directly above each patch (see equation (4.4)). Electrons leaving the surface will face this additional electric field, and be accelerated/decelerated by the potential energy difference, depending on the local work function of the area they are emitted from.

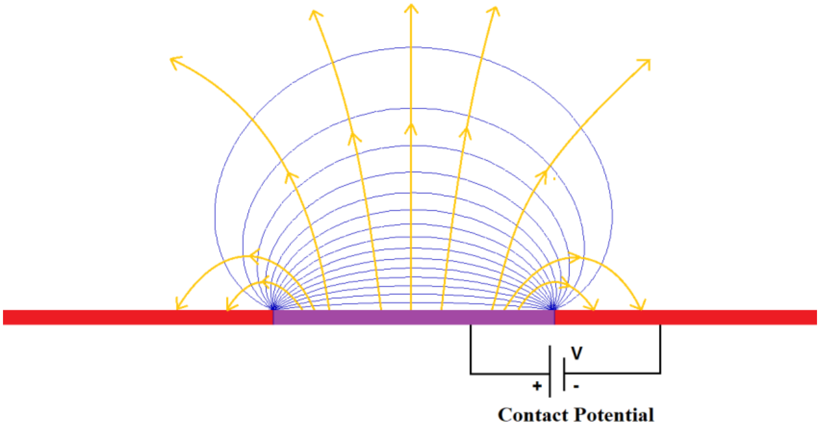

Figure 4.7 – Diagram of the electric field (yellow lines) and equipotentials (blue lines) due to the contact potential difference between surface patches with different work functions

Consider a surface with two types of uniform patches, with high (H) and low (L) local work functions Φ_H and Φ_L, respectively. From equation (4.6), the average work function is equal to $\langle\Phi\rangle = \eta \cdot \Phi_L + (1-\eta) \cdot \Phi_H$, where η is the coverage of low work function patches. The potential energy above a patch, calculated using the software SIMION, as a function of distance to the surface, is shown in Figure 4.8, for the case where $\Phi_L = 4$ eV, $\Phi_H = 5$ eV, $\eta = 0.5$, for a single, circular patch of diameter 10 µm, located at the centre of the sample. Both cases are shown when the patch's work function is equal to Φ_L or Φ_H. Since the fraction of the surface occupied by the patch is 50%, the average work function $\langle\Phi\rangle = 4.5$ eV. Additional details on the SIMION simulations are provided below in section 4.2.3. At distances at least one order of magnitude shorter than the patch diameter, the electron potential energy above the patch is approximately equal to its local work function. As the distance *z* increases, the potential energy changes due to the patch field, towards the value of $\langle\Phi\rangle$. At distances greater than the patch diameter, the electron potential energy is stable and equal to $\langle\Phi\rangle$.

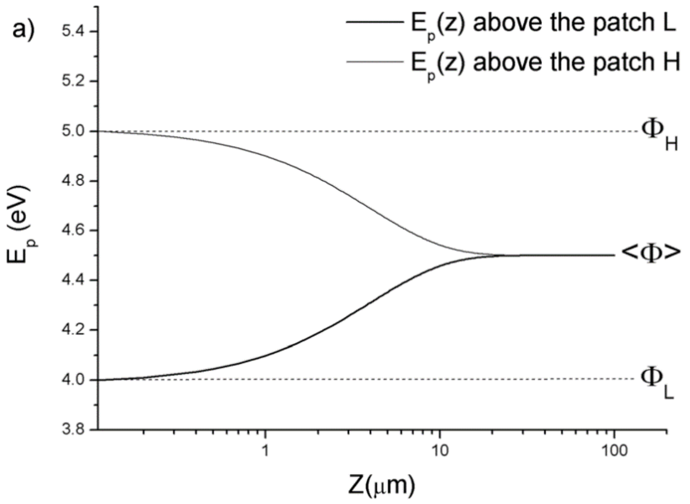

Figure 4.8 – Potential energy distribution above circular patches of 10 μm diameter, with Φ_L = 4 eV, Φ_H = 5 eV, and average work function $\langle\Phi\rangle$ = 4.5 eV.

Consider electrons emitted from regions with local work function $\Phi_{loc} < \langle\Phi\rangle$, which will face an additional energy barrier, equal to $\langle\Phi\rangle - \Phi_{loc}$. The height of the overall energy barrier for the emission of these electrons is thus equal to $\langle\Phi\rangle$. In the case where electrons are emitted from regions with local work function $\Phi_{loc} > \langle\Phi\rangle$, they will be accelerated when leaving the surface, with an energy increase equal to $\langle\Phi\rangle - \Phi_{loc}$. The height of the energy barrier for electron emission in this case is not affected. From this analysis, and knowing that secondary electrons are detected far from the surface, it can be concluded that the onset position does not correspond to the minimum work function Φ_L, but to the average work function $\langle\Phi\rangle$. As previously stated, the onset corresponds to electrons leaving the surface with kinetic energy equal to zero. If there is an additional potential energy barrier above the surface, these electrons do not reach the energy analyser, and the onset corresponds to electrons that are able to overcome this additional barrier of final height $\langle\Phi\rangle$. The patch field will also affect WFM measurements in the same way. This means that the technique does not provide true mapping of the local work function, since the minimum work function that can be measured is equal to $\langle\Phi\rangle$ (it may however provide proper mapping of patches with $\Phi_{loc} > \langle\Phi\rangle$). While this effect has long been known for work function measurements based on the diode method [105] and more recently studied in field emission measurements [106], it has not been considered for those based on the onset method until our recent work [107,108].

The potential energy dependence shown in Figure 4.8 is valid only in the absence of external fields. If the sample is biased relatively to the energy analyser, which is generally the case in WF measurements based on the secondary electron emission, the additional electric field will modify the energy barrier created by the patch field. The influence of the external field on this barrier must also be calculated, in order to properly understand how the onset position is related to the work function of the surface.

4.2.2 Influence of an External Electrical Field

Consider a surface with a uniform distribution of the work function, i.e. without patches. In the presence of an external electric field, which accelerates electrons emitted from the surface, the local work function is reduced. Figure 4.9 shows the potential energy distribution above the surface, and how its barrier height, which corresponds to the work function Φ, is reduced to Φ_E when an external field is applied.

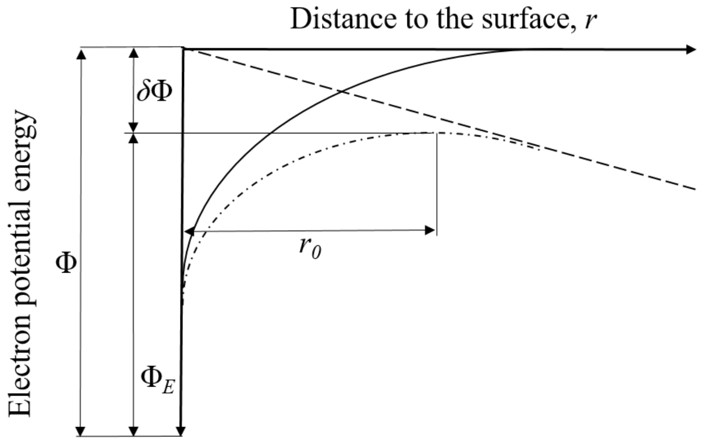

Figure 4.9 – Effect of an external field on the electrostatic potential above the surface of a homogeneous sample.

This reduction of the potential barrier for electron emission is relevant for thermionic emission, and the increase of emission current due to this reduction (i.e. in the presence of the strong electric field) is known as the Schottky effect [78]. The decrease in work function as a function of the external field's intensity can be calculated from equation (4.2). In the presence of a uniform electric field *E*, the electrostatic potential above the surface is now equal to:

$$V(r) = -\frac{e}{16\pi\varepsilon_0 r} - Er \tag{4.11}$$

The electric field causes the maximum of the potential energy to be reduced by $\delta\Phi$. This decrease can be calculated after determining the position of the potential energy maximum from the condition

$$\left(dV/dr\right)_{r=r_0}=0$$

From the potential barrier dependence, given by equation (4.11), the value of r_0 is obtained:

$$r_0=\sqrt{\frac{e}{16\pi\varepsilon_0 E}} \tag{4.12}$$

Having in mind that the maximum value of the potential in the absence of external field equals zero, the drop of the potential barrier $\delta\Phi$ can be obtained from the magnitude of the new potential barrier maximum:

$$\delta\Phi=-V\left(r_0\right)=\sqrt{\frac{eE}{4\pi\varepsilon_0}} \tag{4.13}$$

When a surface has a non-uniform distribution of the work function, the influence of the external field is more complex, due to the patch field created by the contact potential between the regions with different work function. Before reducing the value of the local work function as explained above, which requires extremely high values of electric field (in the order of 10^8 – 10^9 V/m), the external field will firstly reduce the additional potential energy barrier created by the patch field, effectively changing the value of the average work function (i.e. the barrier height for the electron emission). The latter phenomenon is known as anomalous Schottky effect [109]. In order to quantify this influence, the value of the new potential energy barrier in the presence of the external field must be determined. This requires knowledge of the potential energy distribution above a non-uniform surface. The latter can be obtained by solving the Laplace equation in the space above the surface, which has already been done for some specific geometries of high symmetry that simplifies the calculation [110]. Alternatively, this distribution can be calculated numerically for an arbitrary geometry. Convenient tools for such calculations are charged particle optics simulators, such as SIMION. The software can be used to calculate the potential energy distribution for any shape of the patches on the surface, and hopefully reach an empirical model that supports a broad range of geometries.

4.2.3 Calculation of the Potential Energy Distribution Above a Non-Uniform Surface

The patch field was described by simulating different surfaces in the well-known software SIMION ver. 8.0 [111], typically used for simulations involving charged particles. A non-uniform sample was modelled as a set of flat adjacent electrodes, all lying in the same plane, each corresponding to a uniform area with local coverage equal to 1. The voltage difference between the electrodes corresponds to the contact potential difference, i.e. to the difference between the local work functions. The boundaries of the volume inside which the electric potential is calculated were kept at 0 V, which simulates the walls of the vacuum chamber where work function measurements experiments are performed, and this volume was chosen to be sufficiently large to reduce the electric field originating from the potential difference between the sample and the boundaries. The number of grid units in the equivalent 3D volume in which the potential distribution has been calculated is 10^9. The convergence objective relative to the electrode voltage was 5×10^{-7} in all simulations. An increase of the number of grid points and decrease of the convergence objective did not contribute to any significant change in accuracy.

First, the accuracy of the numerical model had to be tested on a system with available analytical solution. The potential energy distribution above the centre of a circular conductive patch of diameter d on a potential V_0, located on an infinite grounded substrate can be expressed as [110]:

$$V\left(\frac{z}{d}\right)=V_0\cdot\left[1-\frac{\frac{z}{d}}{\sqrt{\frac{1}{4}+\left(\frac{z}{d}\right)^2}}\right] \tag{4.14}$$

Since infinite objects cannot be treated numerically in a straight forward manner, the numerical calculation in SIMION was performed for a circular patch ($d=1$ mm, $V_0=1$ V) laying on another grounded circular electrode of comparatively greater diameter, equal to 5.7d, as shown in Figure 4.10 a). The potential distribution normal to the surface above the centre of the patch, $V(0,0,z)$, is shown in Figure 4.10 b). The distribution above the substrate $V(1.5d,1.5d,z)$ is also shown. In both cases, the potential distribution from the surface till the distance at which $V(z)$ reaches the value of the surface averaged potential $\langle V\rangle$ is presented, with the distance from the surface, as was previously shown in Figure 4.8. The analytical dependence based on equation (4.14) is also shown in Figure 4.10 b). The two models show a very good match for $z/d < 0.75$, and diverge no more than 0.05 V after this value. This discrepancy is mainly due to the finite size of the substrate in the numerical simulation, since the size of the larger electrode was considered to be infinite in the analytical model. Indeed, when the sample diameter was increased to 50 *d*, this discrepancy was reduced to values lower than 1 mV. From this comparison, it can be concluded that the SIMION simulations are very accurate, and can be used as a basis for the calculation of the potential distribution above non-uniform surfaces.

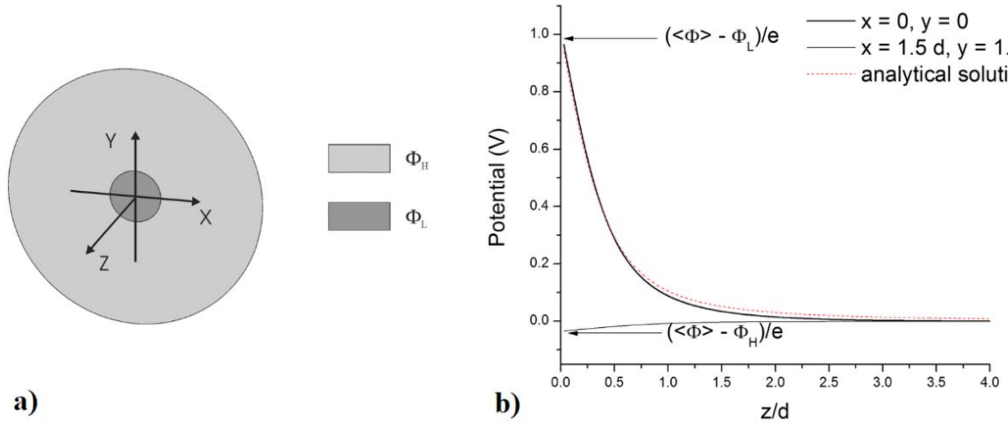

Figure 4.10 – Potential distribution atop a non-uniform surface consisting of a circular low work function patch of diameter d deposited on a circular substrate with a higher work function and a diameter equal to 5.7*d*; a) work function distribution; b) potential distributions $V(0, 0, z)$ and $V(1.5d, 1.5d, z)$. The contact potential equals 1 V. The analytical solution for $V(0, 0, z)$ is based on equation (4.14)

After several simulations with different surface geometries, it was concluded that the potential energy distribution above the centre of a patch can be generally well described by an exponential decay dependence. Taking the Fermi level as a reference, this dependence is equal to:

$$E_p(z) = \langle \Phi \rangle - \left(\langle \Phi \rangle - \Phi_{loc} \right) \cdot e^{-\frac{z}{z_0}} \tag{4.15}$$

where $\langle \Phi \rangle$ is the surface averaged work function, Φ_{loc} is the local work function, i.e., the value of $E_p(x, y, 0)$, and z_0 is a parameter that depends on the specific surface geometry. It was found that this exponential dependence is generally applicable to surfaces with any number of patches evenly distributed across the surface, meaning that the distance between the patches should be roughly constant. By changing parameters such as the size, coverage and shape of the patches in the SIMION simulations, it appears that z_0 can be well described as:

$$z_0 = k(1-\eta)\sqrt{A} \tag{4.16}$$

where η is the fraction of the surface area filled with patches, A is the patch area, and k is a constant parameter that depends on the shape of the patches. For patch shapes that are not too elongated, such as squares or circles, $k = 0.48 \pm 0.03$. While the exact dependence of k with the patch shape has not been determined, it is known that its value decreases with the aspect ratio of the shape (a rectangular patch will have a smaller z_0 value than a squared patch of the same area).

In order to reveal the effect of external fields on the potential distribution above the surface, an extraction field was introduced to the geometry of the SIMION simulation presented in Figure 4.10 a), by biasing a circular plate with a diameter of 14.4 d to a positive extraction voltage U_{ex}. This extraction plate was placed parallel to the sample, as shown in Figure 4.11, at a distance of 5d.

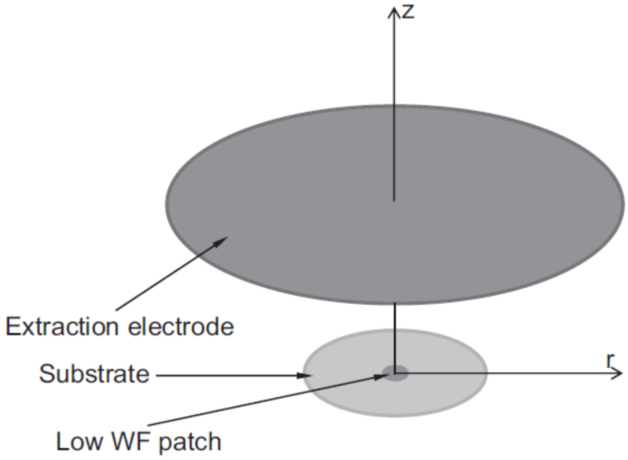

Figure 4.11 – Drawing of the SIMION modell used, with a sample consisting of substrate and low WF patch, with the addition of a biased circular plate that creates an extraction (electrical) field, placed parallel to the sample.

The central patch and the substrate were modelled as uniform areas with local work functions of $\Phi_L = 4$ eV and $\Phi_H = 5$ eV, respectively. The potential distribution $E_p(r,z)$ obtained from the numerical simulation is shown in Figure 4.12 for two different intensities of the external field, corresponding to different values of U_{ex}. The geometry of the simulated system has a cylindrical geometry, and so the potential distribution can be shown as a function of the distance z to the surface, and distance r from the centre of the sample. These initial results show that the extraction field has a clear influence on the additional barrier created by the patch field. In Figure 4.12 a), the external field is of a moderate value. In this case, electrons emitted from the patch still have to overcome an additional barrier, which is slightly reduced by the field. In Figure 4.12 b), the external field is high enough to completely suppress the additional patch field barrier, and electrons emitted from the patch surface are immediately accelerated. It is clear that if the work function measurements based on the secondary electron emission are performed under these conditions (high external field), they will actually reflect the local value of the work function and not the average one.

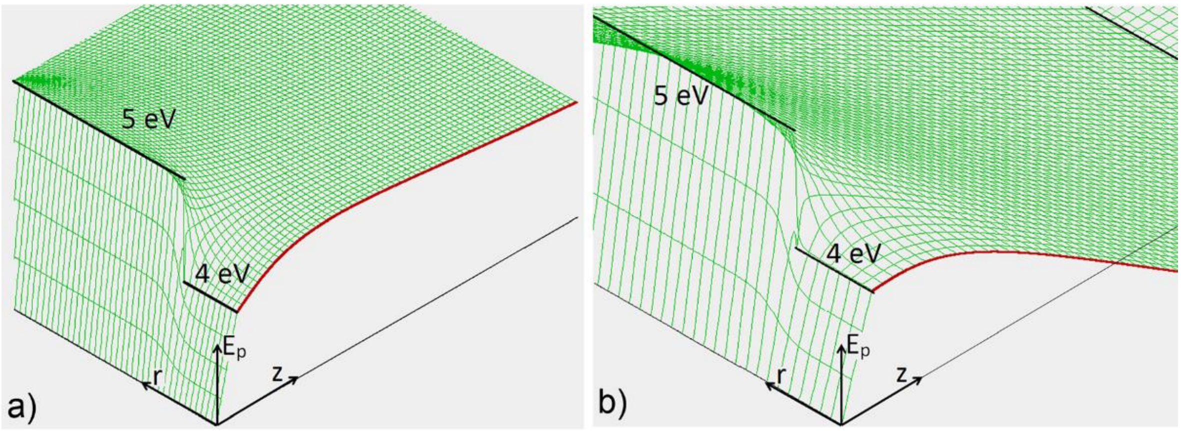

Figure 4.12 – Potential energy distribution $E_p(r,z)$ above the sample with work function distribution presented in Figure 4.10 a) in the presence of an extraction field. a) $U_{ex} = 10$ V; b) $U_{ex} = 65$ V. Patch and substrate work functions are 4 eV and 5 eV, respectively. The distance between the sample and the extraction plate of diameter 14.4*d* is 5*d*

A set of simulations was performed for different values of U_{ex}, and the results for the $E_p(z)$ dependence at $r = 0$ are shown in Figure 4.13. The height of the potential barrier for different values of U_{ex} is marked by the dotted horizontal lines. As the extraction field increases, the total potential barrier is reduced from $\langle\Phi\rangle = 4.98$ eV, to the local value of the patch $\Phi_L = 4$ eV, at $U_{ex} \approx 65$ V. Further increase of U_{ex} will not create an additional reduction of the barrier height, unless its value is high enough to reduce the local value of the work function itself, as explained in section 4.2.2.

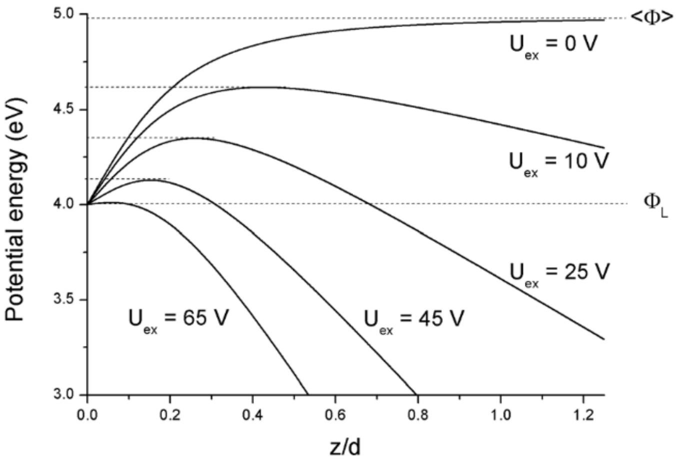

Figure 4.13 – Potential energy distribution along the z-axis in the presence of an extraction field as shown in Figure 4.12. The energy barrier height for each extraction voltage is marked by dashed lines.

Depending on the intensity of the extraction field, the work function measurements based on the secondary electron emission (WFS) may therefore correspond to the average work function, the minimum local work function, or some value in-between. Since WFS and WFM measurements are always performed in the presence of an extraction field, it is essential to calculate the influence of this field on the height of the patch field barrier above low work function patches, in order to properly interpret the results.

Returning to Figure 4.12 b), it is also evident that, while the extra barrier was completely suppressed at $r = 0$ (red curve), this is not true for higher values of *r*. As electrons are emitted from points closer to the higher work function substrate, the height of the extra barrier they need to overcome increases (in the presence of external field). While this does not change the onset position in WFS measurements, since detected electrons are emitted from the whole surface, and the onset corresponds to the lowest potential barrier (the centre of the patch), WFM measurements will be affected. To further illustrate this effect, Figure 4.14 presents the potential energy distribution $E(r,z)$, for several fixed values of *r*.

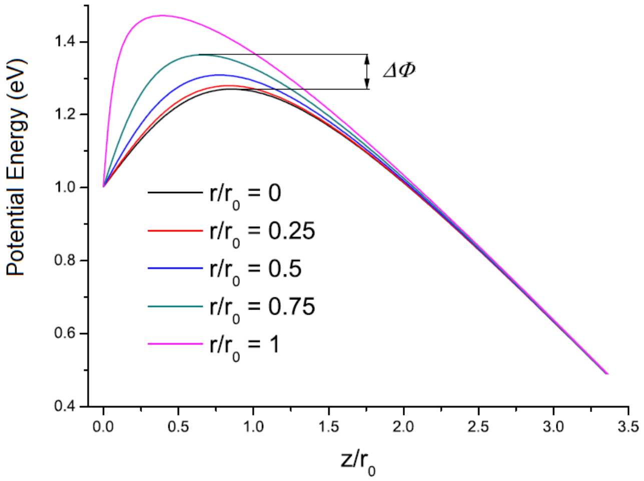

Figure 4.14 – Potential energy distribution above the sample for several fixed values of *r; r_0* is the patch radius. The minimum potential energy along *z* is decreasing with *r*, meaning the patch field creates an additional barrier which increases with *r*. *ΔΦ* is the height of the additional barrier for $r = 0.75 r_0$.

The geometry of the system is based on Figure 4.11, with a substrate radius of 10 r_0, and the electrode, with radius 25.5 r_0, is placed at a distance of 35.6 r_0 from the sample, with r_0 being the radius of the patch. The work function difference between the patch and the substrate is 1 eV, and the extraction voltage is equal to $U = 0.45 \cdot U_0$, where U_0 is the extraction voltage required to completely suppress the barrier at $r = 0$. It is clear that the potential barrier grows with r/r_0 and increases considerably faster when $r/r_0 > 0.5$. The actual significance of this effect on the onset position is however not clear, as the horizontal component of the patch field bends the electron trajectories towards the centre of the patch, effectively allowing them to bypass the extra potential barrier above the edges of the patch. Additionally, the "step-like" voltage transition between the patch and the substrate, implying an infinite parallel component of the patch field at the interface, is not physical. Therefore, for a proper evaluation of this effect, the true potential distribution at this transition should be precisely calculated.

Assuming the potential distribution above low work function patches $\left(\Phi_L < \langle\Phi\rangle\right)$ is well described by equation (4.15), and that the extraction field is constant in the near-surface region, the potential distribution above the centre of the patches equals:

$$E_p\left(z\right) = \langle\Phi\rangle - \left(\langle\Phi\rangle - \Phi_L\right) \cdot e^{-\frac{z}{z_0}} - e \cdot F \cdot z \tag{4.17}$$

where F is the value of the uniform extraction field. By following the procedure in equations (4.11)-(4.13), the position of the barrier maximum z_m can be calculated as:

$$z_m = z_0 \cdot \ln \frac{\langle\Phi\rangle - \Phi_L}{eFz_0} \tag{4.18}$$

The maximum of the potential barrier, which corresponds to the onset position, is given by:

$$E_{p\max} = \langle\Phi\rangle - eFz_0 \left(1 + \ln \frac{\langle\Phi\rangle - \Phi_L}{eFz_0}\right) \tag{4.19}$$

Since z_m has to be positive, this is valid only when $F \leq \left(\langle\Phi\rangle - \Phi_L\right) / \left(ez_0\right)$. This limit corresponds to the value of the extraction field when the patch field barrier is completely suppressed, i.e. when $E_{p\max} = \Phi_L$. Denoting this value as $F_0 = \left(\langle\Phi\rangle - \Phi_L\right) / \left(ez_0\right)$, and since the extraction field scales linearly with the extraction voltage, i.e. $F/F_0 = U_{ex}/U_{ex}^0$, equation (4.19) can be rewritten as:

$$E_{p\max} = \langle\Phi\rangle - \left(\langle\Phi\rangle - \Phi_L\right) \cdot \frac{U_{ex}}{U_{ex}^0}\left(1 + \ln \frac{U_{ex}}{U_{ex}^0}\right) \tag{4.20}$$

With $0 < U_{ex} \leq U_{ex}^0$. In this form, this solution can now be compared with the corresponding numerical results shown in Figure 4.13. This comparison is shown in Figure 4.15, presenting a very good agreement between the two results. There is a small discrepancy between the two curves, which is possibly due to the non-uniformity of the extraction field in the near-surface region, and a potential failure of equation (4.15) in accurately representing the potential distribution above the patch. Nevertheless, the results are very similar, and both show that:

- For $F \le 0.01F_0$, $E_{p\max} \approx \langle \Phi \rangle$,
- For $F_0 > F > 0.01F$ the energy barrier decreases with F
- Finally for $F \ge F_0$, $E_{p\max} = \Phi_L$.

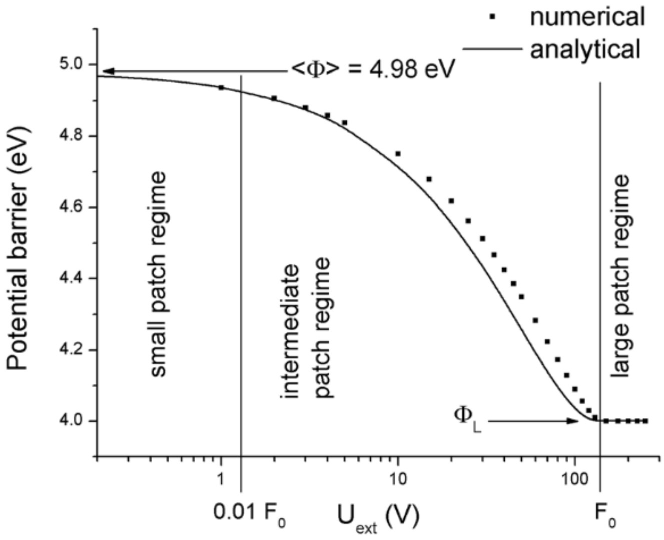

Figure 4.15 – Numerical and analytical calculation of the potential barrier for electrons emitted from a low work function patch vs. the extraction field. The numerical results are taken from the calculations shown in Figure 4.13. The analytical results are based on equation (4.20), assuming that F_0 corresponds to $U_{ex}^{0} = 65$ V.

Alternatively, since $E_{p\max}$ depends on the product $F \cdot z_0$, and z_0 is proportional to the patch diameter *d* (see equation (4.16)), the dependence shown in Figure 4.15 can be drawn between the potential barrier and the patch size *d*, if *F* and η are kept constant. This dependence was also confirmed in the numerical simulations. It indicates that, for a fixed extraction field, the onset position will correspond to different physical quantities, depending on the size of the patches. Three regimes are identified in Figure 4.15. The onset position corresponds to

- $\langle \Phi \rangle$ in the small patch regime,
- Φ_L in the large patch regime,
- A value in-between for intermediate sized patches.

Consequently, as the size of the patches increases, there may be a change in the measurement regime when performing WFS or WFM. It should be stressed that F_0 depends on both the difference $\langle \Phi \rangle - \Phi_L$ and η, which means that the measurement regime might also be altered due to the change of these values during the deposition/adsorption experiment. The same phenomenon can be considered from the point of view of static surface measured in different external fields: for the lowest fields the measurements are performed in the small patch regime so that the onset position corresponds to the surface averaged work function; at very high external fields the results are performed in the large patch regime in which the onset position corresponds to the minimum work function patches; for the intermediate fields, the results cannot be clearly interpreted. Clearly, WFM measurements should be performed exclusively in the large patch regime. The same stands for the LEEM/PEEM measurements in which the observed image contrast is attributed to work function surface distribution [112,113], without actual considering whether the external field is sufficiently strong.

4.2.4 Experimental Confirmation

With a regular WFS setup, the transition between the identified measurement regimes with the intensity of the external field can be tested by gradually increasing the value of the sample biasing (which corresponds to U_{ex}), while measuring the onset position. The extraction field is established between the biased sample and the grounded entrance into the electron-optical column of the electron spectrometer. This will confirm both the presence of the patch field, and the influence of the external field on the measurement regime. With this purpose, a special sample was prepared, based on the geometry presented in Figure 4.10 a). A hole with a diameter of 1.6 mm was drilled in a mechanically polished, 10×10 mm^2 polycrystalline nickel sheet (Goodfellow, 0.1 mm thickness, 99% purity). The nickel sample was then pressed onto a 1 mm thick indium plate (Goodfellow, 99.999% purity), creating an indium patch in the middle of the nickel substrate. The work functions of these metals are $\Phi_{Ni} \approx 5.2$ eV and $\Phi_{In} \approx 4.1$ eV, and due to the small coverage of the indium patch, the averaged work function of the sample is approximately Φ_{Ni}. It is expected that, for very small values of U_{ex}, the onset measurement of electrons emitted exclusively from the indium patch is performed in the small patch regime, which means that its position should follow the biasing voltage according to equation (4.7), and correspond to $\langle \Phi \rangle \approx \Phi_{Ni}$. As U_{ex}, is sufficiently increased, an additional onset shift will appear that should depend on U_{ex}, as described by equation (4.20). For $U_{ex} > U_{ex}^{0}$, the onset will correspond to indium's local work function, and should again follow equation (4.7).

It is assumed for the purpose of this experiment that both the indium and nickel surfaces are uniform in terms of work function. This is in fact not true, as both surfaces are polycrystalline, and the nickel sheet is of a modest purity. However, since the typical dimension of these non-uniformities is in the micrometre range, the patch field between regions of this size is too strong to be affected by the external fields applied in the experiment. Precise calculations reveal that the value of the extraction field required to enter the intermediate regime would actually be 6 times larger than the one required to completely suppress the barrier created by the patch field between the indium patch and the nickel substrate (i.e. to observe the In patch in the large patch regime). Consequently, both nickel and indium surfaces may be considered uniform since their non-uniformities cannot be resolved, i.e. they will be observed in the small patch regime. The local value of the nickel and indium work functions will therefore correspond to the average work function of their micrometre sized grains/patches, and should not change during the measurement.

The experiment was performed in a surface analysis system with a base pressure in the 10^{-10} mbar range, equipped with the necessary instrumentation to perform XPS and Low Energy Ion Scattering (LEIS) experiments [26]. The secondary electron energy distribution measurements were performed in the FAT 10 mode, with electrons being collected perpendicularly to the surface. The sample was sputter cleaned with 3 keV Ar^+ before the measurement, and the electron emission was obtained by bombardment of the sample with the same Ar^+ beam at 4 keV, at an incidence of 45º. The diameter of the ion beam under these conditions was considerably smaller than the indium patch size, so that the electrons were being emitted exclusively from either the indium patch or the nickel substrate. This was experimentally confirmed by performing LEIS analysis of the scattering area: when exclusively bombarding the indium patch, the scattering peak corresponding to nickel was absent, and vice-versa.

Some preliminary measurements were performed in a clean single crystal Ag(100) surface. In order to reassure that, in a homogenous surface (no patch field), the onset position follows equation (4.7), i.e. the extraction voltage, the secondary electron emission from the Ag(100) surface was measured for biasing voltages ranging from -10 V to -500 V. Indeed, the onset followed U_{ex} with a standard deviation of 0.08 eV, which is considered to be within the expected experimental error. This result confirms that there is no influence of the charged particles optics on the onset shift due to the sample biasing.

The onset position of the indium patch and nickel substrate was measured as a function of U_{ex} in the range of -5 V to -300 V. The results are shown in Figure 4.16, with the zero of the onset scale corresponding to the mean position of measured nickel onset.

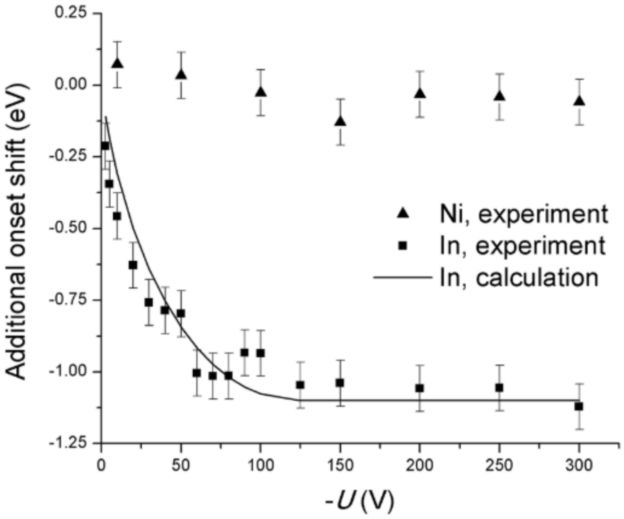

Figure 4.16 – Additional onset shift vs. the biasing voltage obtained from the energy spectrum of secondary electrons emitted from a 1.6mm In patch and a Ni substrate. The zero of the onset scale corresponds to the mean onset position of the spectra recorded from Ni. The experimental error is estimated as ± 0.08 eV (see text). The calculation is based on equation (4.20) for $U_0 = 125$ V, $\Phi = \Phi_{In}$ and $\langle \Phi \rangle = \Phi_{Ni}$.

As expected, the position of the nickel onset follows the biasing voltage, within the experimental error of the instrument. This confirms both the fact the onset position originating from regions with a local work function higher than the average is not affected by the patch field or by external fields, and that the intensity of the external field applied is too weak to resolve the non-uniformity of the nickel surface itself. On the other hand, the onset position of electrons emitted from the indium patch does not follow the biasing voltage, and shows an additional shift that is increasing with U_{ex} up to about 1 eV towards lower work functions, which saturates at an external voltage of approximately $U_{ex}^0 = -125$. This overall shift fits very well with the expected difference between the Ni and In work functions of about 1.1 eV. Knowing that the distance between the sample and the entrance to the energy analyser is about 7 cm, the field at which In patch is observed in large patch regime is $F_0 \approx 1.79$ V/mm. Although the field estimation is rough (it is obtained by modelling the whole system as a parallel plate capacitor i.e. $F_0 = 125/70$ V/mm), its value is close to our prediction, namely, $F_0 = \left(\langle \Phi \rangle - \Phi_L\right) / \left(ez_0\right) = 1.65$ V/mm. Using the experimentally obtained value of U_{ex}^0, equation (4.20) can be used to calculate the onset shift as a function of the extraction voltage, as is also shown in Figure 4.16. There are relatively small discrepancies between the experimental results and the analytical calculation, which can be related to surface cleanliness/roughness (both affect the local work function), to the possible non-uniformity of the extraction field in the near-surface region, and due to the fact that the field is likely not perfectly normal to the surface due to the presence of other grounded objects relatively close to the sample. Nevertheless, the results show a clear proof that the interaction between the extraction field and the patch field is influencing the onset position, and can alter the measurement regime. Equally important, it appears that the simple model introduced here (represented by equation (4.20)), describes the dependence of the additional onset shift with the extraction voltage very well. A clear transition is seen from the intermediate patch regime, where the onset position depends on the value of the extraction voltage, to the large patch regime, in which the onset saturates to the local work function of indium. The small patch regime is not observed in Figure 4.16 because the transition to the intermediate patch regime would theoretically begin at $\approx 0.01U_0 = -1.25\,\text{V}$, which is lower than the minimum extraction voltage needed to accurately perform the measurement (~-5V).

With these experimental results, it was established that the interpretation of work function measurements based on the onset position is more complex than originally thought. In the case of non-uniform surfaces, it is possible to properly interpret the onset position only for the known external field and the surface structure (size and shape of patches). The later can be achieved by implementing the proposed model. In the case of the experiments performed with the TiO_2(110)-(1×1) surface, presented in chapter 6, the work function measurements are always performed in the small patch regime, due to the small extraction voltage applied to the sample, and the fact that the adsorbed species (mainly O_2 and H_2O adsorption) do not coalesce into islands on the surface. Hence, the average work function, and not the minimum local one, is measured, which explains the previous results obtained for the adsorption of different species on the TiO_2 surface, as mentioned in chapter 1. The gradual decrease of the work function, when a lower work function species (such as water) is deposited, and the increase of work function when a higher work function species (e.g. gold) is deposited, are now understood. Since the surface concentration of these species is changing during the adsorption process, so is the value of the surface averaged work function.

The effect on the image potential can be also included in the present version of the model in a straight forward manner. While this should be mandatory in LEEM/PEEM measurements, when the external field is in the range of 10^9 V/m, the present version of the model is sufficient for our current research due to the low external fields employed.

It is worth noting that the presence of the patch field will affect the work function measurement using other techniques as well. In methods based on determining the threshold of electron emission by measuring the sample current, such as the thermionic emission and photoelectric methods, this threshold is still influenced by the patch field. Electrons that leave the surface with kinetic energy lower than the height of the extra barrier will be pushed back to the sample, resulting in zero-sum current. The work function measurement based on UPS, although providing absolute measurement of the work function, is essentially an onset method, and will be influenced by the patch field in the same way. In WFM measurements performed in the small patch regime, all patches with local work functions below the average value will be identical, while patches with higher values will be correctly resolved. Other methods involving the contact potential measurement, such as the Kelvin Probe and the Diode methods, will also be related to the surface averaged work function.

In some of the more advanced mapping techniques, such as the Kelvin Probe Force Microscopy (KPFM) or the Energy Filtered Photoemission Electron Microscopy (XPEEM), it is essential to know the details of some experimental parameters and surface geometry. In KPFM measurements, the cantilever is placed at a very small distance from the surface (0.2 – 10 nm) [114]. It is possible that this distance is actually lower than z_m, effectively bypassing the height of the patch field barrier. In these conditions, the contact potential measured with the probe will only correspond to the local work function if the patch size is at least one order of magnitude larger than the distance of the tip to the surface, as shown in Figure 4.8. XPEEM measurements are performed with a high-voltage extraction electrode placed close to the sample. In this case, the intensity of this extraction field has to be compared to the value of F_0 for the measured surface, in order to determine the measurement regime.

5

5 Surface Defects, Water and Oxygen adsorption on the TiO_2(110)-(1×1) surface

5.1 The Rutile TiO_2(110)-(1×1) Surface

The rutile TiO_2(110)-(1×1) surface is amongst the most thoroughly studied metal oxide surfaces. Besides its study on applications for catalysis, solar cells, or gas sensors, it plays a very important role in fundamental studies, and is used as a model for metallic oxide surfaces [2,10,20,115]. This surface serves as a reactive playground for the study of a wide variety of processes, which include the adsorption and dissociation of atmospheric gases such as O_2 and H_2O, both playing a critical role in surface catalytic reactions. The rutile TiO_2(110)-(1×1) surface has been ideal for fundamental surface science studies so far due to a number of factors:

- Good availability of single crystals produced with high quality (good stoichiometry and high purity)
- Relatively straight forward procedures required for the preparation of the (1×1) surface
- Good electrical conductivity, which allows the use of different analytical techniques without inducing charging effects, such as STM, XPS, UPS, or other electron spectroscopies.

The reactivity of the rutile TiO_2(110)-(1×1) surface is governed by the surface reduction state, which is associated with the concentration of bridging oxygen vacancies (BOVs) in the first layer. These are favourable adsorption sites for different molecules, with the excess charge associated with each BOV playing an important role in the dissociation of O_2 and H_2O. The coverage of BOVs is generally determined by the procedure and parameters used for the surface preparation, as well as sample history. The fresh (1×1) reconstructed surface is typically prepared by applying cycles of ion sputtering followed by annealing, with adjustable parameters being the ion energy and fluence, annealing duration and temperature, and partial gas pressure during annealing. A perfect stoichiometric surface can be obtained by annealing in oxygen atmosphere. Sputtering followed by annealing in UHV conditions in the 700-1000 K range increases the reduction state of the crystal, and creates a surface populated with a relatively small percentage of BOVs.

5.1.1 Rutile TiO_2(110)-(1×1) Bulk and Surface Structure

In a simplified picture, TiO_2 can be considered as an ionic crystal in which O and Ti atoms are in -2 and +4 oxidation states, respectively (O^{2-} and Ti^{4+}). Consequently, oxygen atoms have fully occupied 2p orbitals, whilst the 4s and 3d orbitals of titanium are empty. From this bond results a strong hybridization between the O 2p and Ti 3d states, which compose the valence and conduction bands, with a ~3 eV band gap, as shown in Figure 5.1.

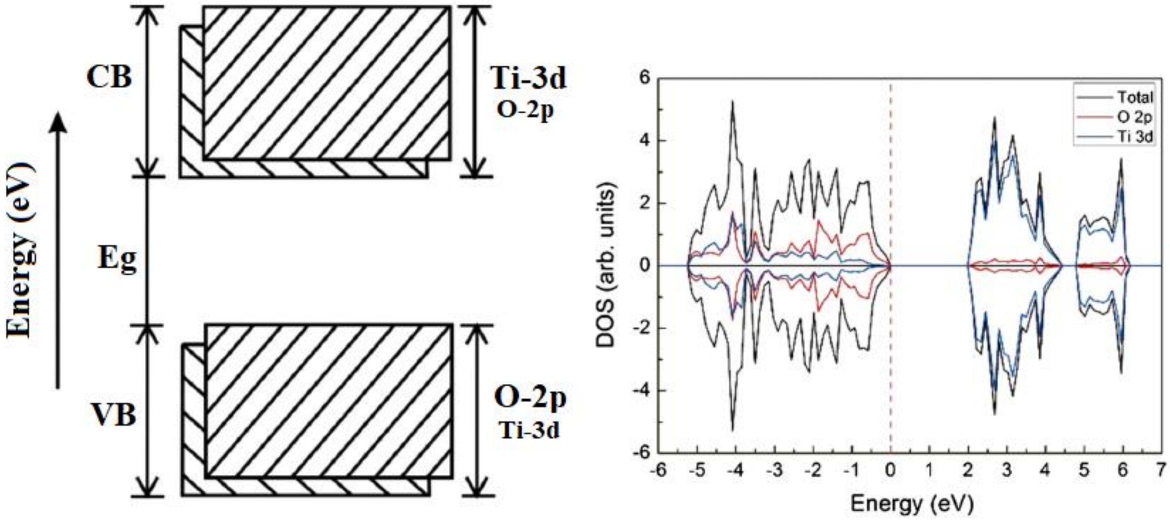

Figure 5.1 – Rutile band diagram and corresponding calculated density of states. Adapted from [116]

Every Ti atom in the bulk is bonded to six oxygen atoms (6-fold coordinated), while oxygen is 3-fold coordinated, forming an octahedral shape with a Ti atom in the centre. The unit cell of rutile TiO_2 is shown in Figure 5.2 a), showing these bonds. The structure of the rutile TiO_2(110)-(1×1) surface follows the bulk structure of the crystal, with alternating oxygen rows in the [001] direction being removed for the surface formation, as shown in Figure 5.2 b), with the dotted line representing the cut made to form the (110)-(1×1) surface.

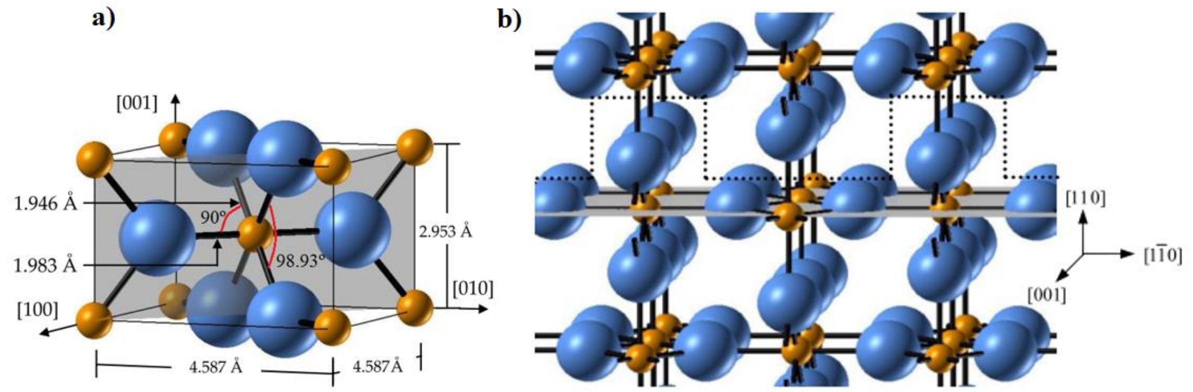

Figure 5.2 – Ball and stick model of a) The rutile TiO_2 unit cell, with dimensions. Blue and yellow spheres represent oxygen and titanium atoms, respectively. The 110 plane is shown in grey shade. b) The bulk structure of the TiO_2 crystal. The dashed line represents the cut made to form the (110)-(1×1) surface. Adapted from [117].

The formation of this surface results in a structure with alternating types of Ti and O atoms, forming rows along the [001] direction. These include rows of 5-fold and 6-fold Ti atoms, and 3-fold and 2-fold oxygen atoms (atop the 6-fold Ti row). The latter are typically designated as bridging oxygen species, as shown in Figure 5.3.

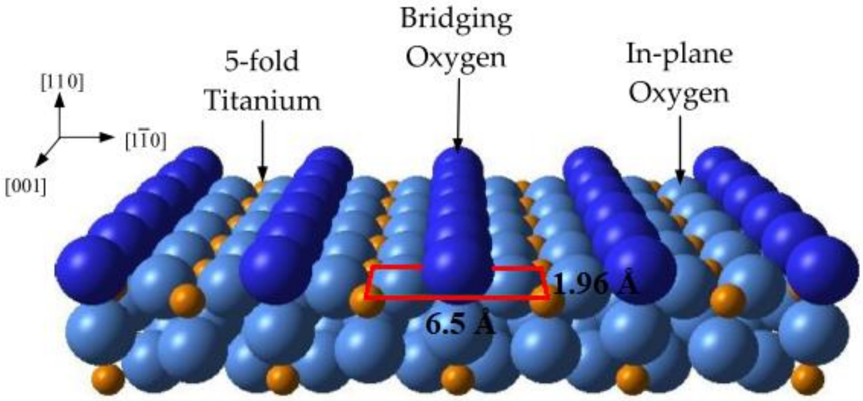

Figure 5.3 –Model of the stoichiometric TiO_2(110)-(1×1) surface. The (1×1) surface unit cell is illustrated by the red rectangle, with corresponding dimensions. Adapted from [117].

The most common defect present in this surface is the bridging oxygen vacancy, shown in Figure 5.4 a). It represents the absence of one oxygen atom in the bridging oxygen rows, which can be caused by sputtering and annealing in UHV, or by electron bombardment. This results in the presence of extra charge from the broken bonds between the two (former) 6-fold Ti atoms and the removed bridging oxygen, reducing the two Ti^{4+} ions that are directly below the BOV to Ti^{3+}. A second type of defect is also present in the near-surface region, which consists of Ti^{3+} ions in-between the surface lattice, referred to as Ti^{3+} interstitials, as shown in Figure 5.4 b). The origin of Ti interstitials is thought to come from the preferential removal of oxygen during sputtering and annealing. During the annealing process, the stoichiometry of the surface is partially restored by diffusion of the excessive Ti ions towards the bulk, creating Ti interstitials, present in the crystal as Ti^{3+}. When annealing is performed on O_2 atmosphere, the near-surface Ti interstitials diffuse towards the surface to react with oxygen adatoms, and create fresh (1×2)/(1×1) layers in this process [16].

At high reduction levels, typically achieved by annealing at higher temperatures, or with a long history of sputter-anneal cycles, the (1×1) reconstruction is no longer energetically favourable and the (1×2) reconstructed surface is obtained [2]. As the crystal is increasingly reduced, it will change colour from transparent to dark blue, due to the presence of Ti 3d electrons in a band-gap state associated with Ti^{3+} interstitials, which affect the optical properties of the crystal.

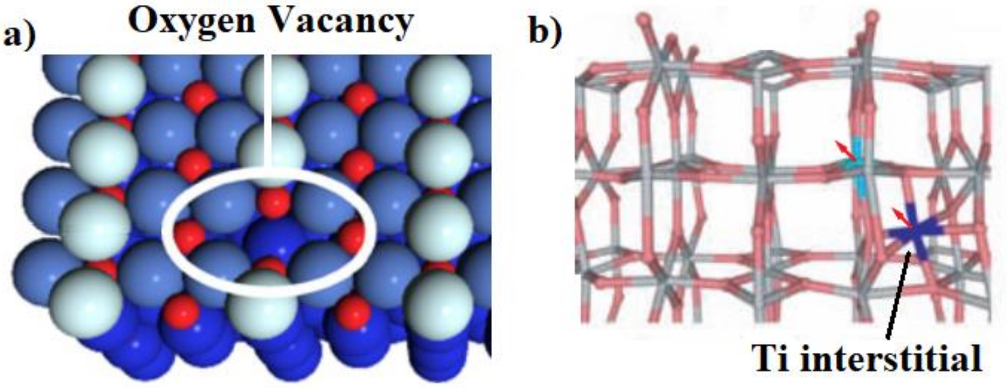

Figure 5.4 – a) Bridging oxygen vacancy on the TiO_2 surface. Figure adapted from [118]. b) Model for Ti interstitials in the crystal lattice. Figure adapted from [11].

5.1.2 Detection of Surface Defects

The presence of both BOVs and Ti interstitials is associated with an increased density of titanium atoms in the Ti^{3+} oxidation state. These ions can be detected using certain surface sensitive techniques, such as XPS, UPS, or EELS. The contribution of Ti^{3+} ions on the Ti 2p XPS peak is shifted for ~1.5 eV towards lower binding energies, as shown in Figure 5.5 a). As an alternate method of detection, the extra electron in Ti^{3+} ions occupies the Ti 3d band gap state, approximately 0.9 eV below the Fermi level, and can thus be detected by scanning the valence band region of the electron energy spectrum with UPS, as shown in Figure 5.5 b). The band-gap state is also detectable with EELS. The inelastic collision associated with this state appears as a loss peak shifted for 0.85 eV relative to the elastic scattered beam peak, as shown in Figure 5.5 c).

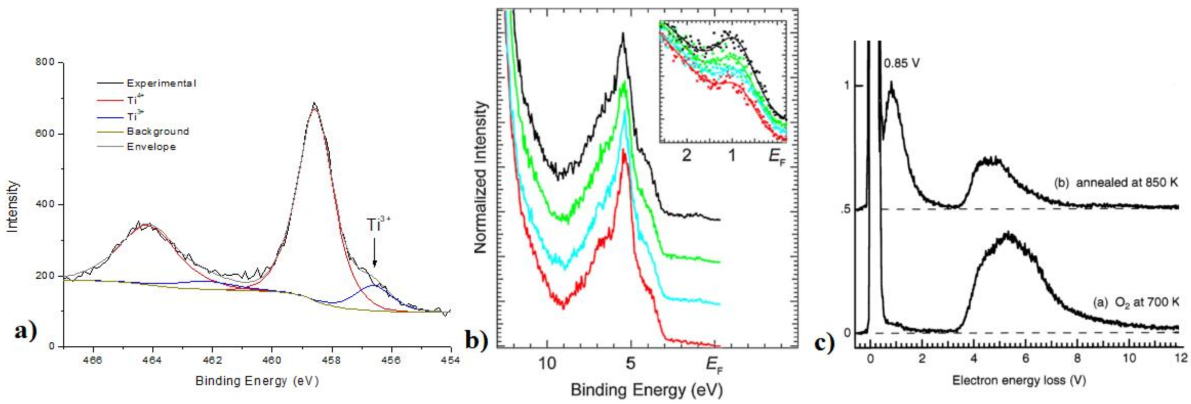

Figure 5.5 – a) XPS spectrum of the Ti 3p peak. The Ti3+ contribution is labelled with an arrow. b) UPS spectrum in the valence band region for surfaces produced with increasing number of BOVs. The inset shows the band-gap state associated with Ti 3d electrons. The surface concentration of BOVs is correlated with the area of the band-gap state. Adapted from [119]. c) Electron energy loss spectrum of the TiO_2(110) surface annealed in (a) O2 atmosphere and (b) UHV. The UHV annealed surface shows a loss of energy at 0.85 V related to the same Ti 3d band-gap state. Adapted from [120].

While the presence of Ti^{3+} ions is detectable with the aforementioned surface analysis techniques, they do not provide direct quantification on the partial concentration of either BOVs or Ti interstitials. However, it is still possible to obtain separate information on these defects by changing the concentration of one in a controllable way, while keeping the other constant, and monitoring the change of the Ti^{3+} contribution. Since Ti interstitials are located below the surface, this is typically accomplished by introducing first layer changes, i.e., changing the concentration of BOVs. For example, in the work of Yakshinskiy and co-authors [121], the concentration of BOVs was increased by electron bombardment, and the Ti^{3+} contribution was monitored by XPS. Wendt and co-authors [11] decreased the concentration of BOVs by exposure to oxygen, while monitoring the band-gap state with Photoelectron Spectroscopy (PES). Furthermore, BOVs can be identified by STM analysis, where they show up as relatively bright spots along the darker oxygen rows.

Both BOVs and Ti interstitials have been shown to contribute to the presence of the band-gap states and the surface reactivity. It is clear from STM analysis that BOVs play a crucial role in the dissociation of both O_2 and H_2O molecules [18,122], and the intensity of the Ti 3d line (band-gap state) has been shown to increase linearly with the number of surface BOVs [119]. However, Wendt and co-authors have shown that the band-gap states are also related to Ti^{3+} interstitials [11]. The chemical reactivity of BOVs is strongly related to the localized charge in Ti 3d states, originating from neighbouring Ti^{3+} ions, which is available to electronegative species such as oxygen in O_2 or H_2O, promoting their dissociative adsorption. As explained in more detail in section 5.2.2, dissociative adsorption of an oxygen molecule in a BOV site leads to the presence of oxygen adatoms (O_a), located on top of 5-fold Ti rows. The charge provided from Ti interstitials has also been given as one of the reasons for the apparently excessive density of these oxygen adatoms, compared to the number of available BOVs [12]. At the same time, Du and co-authors argue that the charge necessary for O_a stabilization is provided by delocalized charges associated with BOVs, and that this is the proposed explanation why in some cases oxygen adsorption is saturated before all BOVs are filled [123].

5.2 Adsorption of Oxygen and Water on Rutile TiO_2(110)-(1×1)

The interaction between the O_2 and H_2O molecules and the rutile TiO_2(110)-(1×1) surface is of particular importance due to its influence on the reactivity of the surface, namely on its catalytic activity. It has been thoroughly studied with a variety of surface analysis techniques, with STM analysis being particularly useful in providing a comprehensive understanding of the various reaction processes [16,17,20,122,124,125].

The adsorption of these species has been studied by work function analysis in a relatively small number of works [22,24,90,126–128]. The work function is a physical property highly sensitive to first-layer changes, and is therefore a suitable tool for adsorption studies, with particular sensitivity for the adsorption of molecules/atoms that introduce strong surface dipoles, such as the adsorption of molecular water or the dissociative adsorption of oxygen. However, a review of these works reveals some conflicting results, as will be shown in more detail in the sections below. Furthermore, these work function measurements were performed by analysis of the secondary electron distribution, and have not been interpreted taking into consideration the influence of the patch field on the work function measurement, as demonstrated in chapter 4.

5.2.1 Water Adsorption

It is generally accepted that water is adsorbed non-dissociatively on the Ti rows at room temperature. A closer inspection of the process also reveals a relatively low barrier for the H_2O dissociation on Ti rows, in which one proton ‘jumps’ back and forth between the water molecule and one of the neighbouring bridging oxygen atoms [13,122]. The water molecule diffuses extremely fast along the row, and is dissociated when it reaches a BOV site, creating one OH pair in the process. One OH group replaces the BOV (OH_V), and the remaining hydrogen of the original H_2O molecule bonds to one of the adjacent bridging oxygen atoms, forming the second OH group (OH_B), as shown in Figure 5.6 [18,129,130].

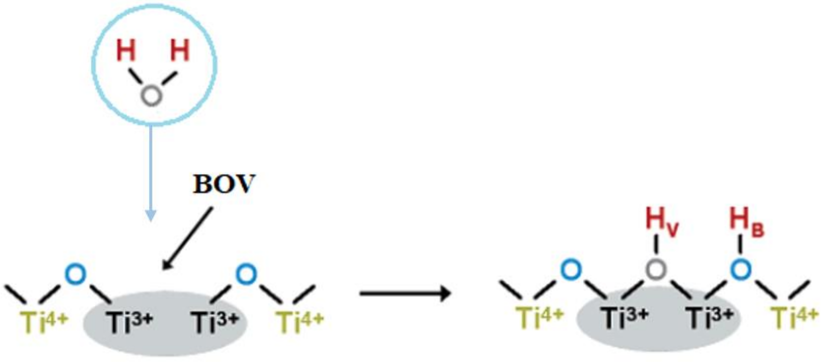

Figure 5.6 – Representation of the water adsorption on the TiO2(110)-(1×1) surface on a BOV site.

In Figure 5.7 a), it can be seen how the presence of OH groups is observed by STM. They are imaged as bright spots along the bridging oxygen rows (II), brighter than BOVs (I), with paired OH groups being even brighter (III). The existence of OH groups on the surface is nearly unavoidable, due to the presence of water in UHV systems. OH groups are able to diffuse along the surface in two ways. At room temperature, the hydrogen atom can spontaneously jump between BOs. Separation of the hydroxyl pair is significantly enhanced by water molecules adsorbed on Ti rows, due to their short-term dissociations [129]. Through this mechanism, the water molecule can be in a dissociative state (one of the protons jumped onto a neighbouring bridging oxygen) while in the vicinity of the hydroxyl pair. In this scenario, the water molecule can be re-established by the jump of the proton from the hydroxyl pair, resulting in the apparent jump of the proton from one bridging oxygen row to another.

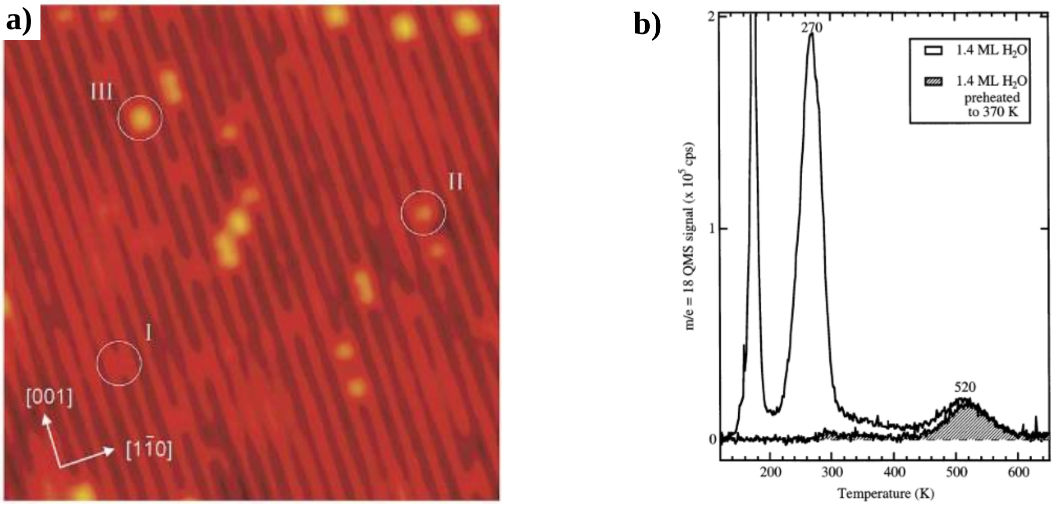

Figure 5.7 – a) STM picture of the rutile TiO_2(110)-(1×1) surface showing three types of encircled defects. I corresponds to BOVs, II to a single OH group, and III to an OH pair. Adapted from [18]. b) TPD of the rutile TiO_2(110)-(1×1) surface exposed to 1.4ML of water at 120 K. Figure adapted from [131].

The two OH groups that are formed when an H_2O molecule is dissociated on a BOV site are not equal. The OH_B group has been found to diffuse with a probability ten times higher than OH_V, which indicates a strong inequality on the binding configuration of these groups [129,132,133]. This is further supported by the experimental observation that upon water dissociation on a BOV site, which is replaced with an OH_V group, the electronic structure associated with the BOV (band-gap states) is hardly affected, and is therefore distinct from neighbouring BOs [131].

As shown in Figure 5.7 b), it was revealed by Temperature Programmed Desorption (TPD) that, at lower temperatures, a second layer of water is formed by hydrogen-bonding with surface OH groups, with a TPD peak centred at 180 K. Water adsorbed on Ti rows has a TPD feature at 270 K. Surface OH groups will recombine to desorb as water at higher temperatures, associated with the TPD peak centred at 520 K [131]. Furthermore, when exposed to ambient conditions of water pressure, OH groups also act as nucleation centres for the adsorption of a second water layer [134].

The study of the kinetics of water adsorption by work function monitoring has been performed by different groups [22,24,90,126–128]. This analysis is typically performed by measuring the change of the work function, since its absolute value will depend on many factors that are hard to reproduce [134] A review of the available works performed by the author shows conflicting results, which are likely related to unreliable surface preparation and/or poor vacuum conditions (presence of contaminating species).

Figure 5.8 a) and b) show the results obtained for water adsorption at room temperature, presented in the work of Onda and co-authors [90], and the first published results on water adsorption by our group in the work of Marques and co-authors [22], respectively.

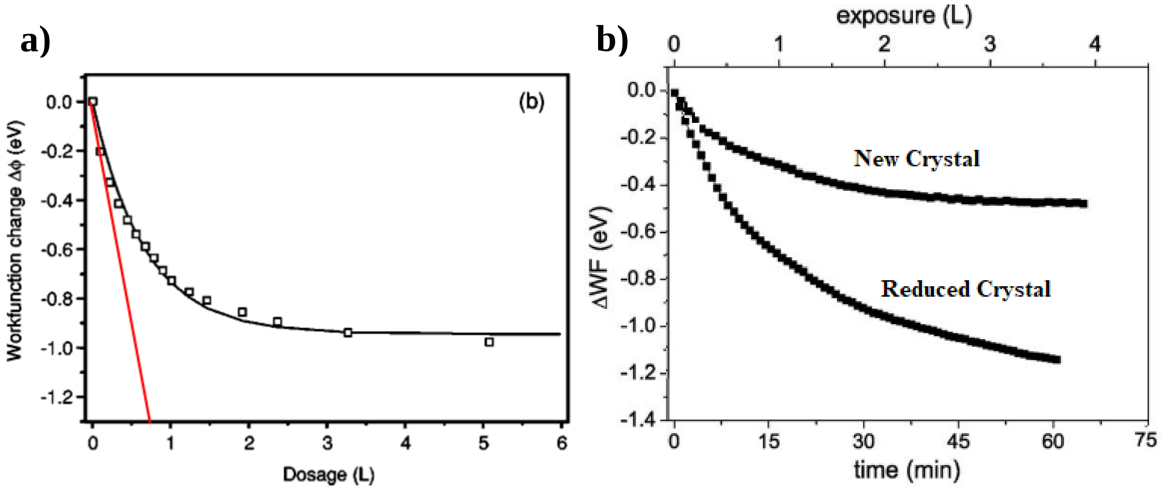

Figure 5.8 – Work function change as a function of water dosage, adapted from the works of a) Onda and b) Marques [22,90]

Both results show a somewhat slow adsorption rate, with the saturation level being highly dependent on the reduction level of the crystal. As expected, the addition of H_2O/OH species to the surface introduces dipoles oriented towards the vacuum, which decreases the work function. However, these results are not in agreement with the dynamics of water adsorption observed by STM. On a (1×1) reconstructed $TiO_2(110)$ surface, the rate of adsorbed/desorbed H_2O on Ti rows should quickly reach an equilibrium, and due to their fast diffusion rate across Ti rows, BOVs are rapidly filled with dissociated water. Since there is no formation of a second water layer, which, at room temperature, is only observed for ambient water pressures [131,134], the work function should stop decreasing rather quickly, which is clearly not the case. A possible explanation for these results is that the surfaces used in the studies were not properly prepared. They could have been very defective and consequently (1×2) reconstructed. Alternatively, the surfaces could have been contaminated due to the insufficient sputter cleaning, and/or bad vacuum conditions.

In the subsequent studies performed by our group [24,127,128], the fast nature of water adsorption has been clearly observed, confirming the unreliability of the previous results. Three different types of adsorption sites have been observed, corresponding to a fast adsorption on Ti rows and BOVs in the (1×1) unreconstructed surface, and a slow adsorption on the (1×2) reconstructed surface areas. Furthermore, desorption of water from Ti rows was also observed when the water pressure is turned off. This is expected since, at room temperature, most water on Ti rows should be desorbed (see Figure 5.7 b).

Figure 5.9 shows the work function change due to water exposure on a fresh surface and a long-term annealed surface. The latter should be more defective, and therefore with a higher coverage of (1×2) reconstructed patches. This is associated with a smaller amplitude of the initial fast work function drop, followed by a steeper, slow decrease. When the water flow is turned off, there is a clear increase of the work function on the fresh surface, which is associated with desorption from Ti rows. There are still some important questions remaining, regarding the work function change during the water adsorption, mainly related to the slow drop of the work function, even in fresh, well prepared surfaces, together with the correct modelling of water desorption.

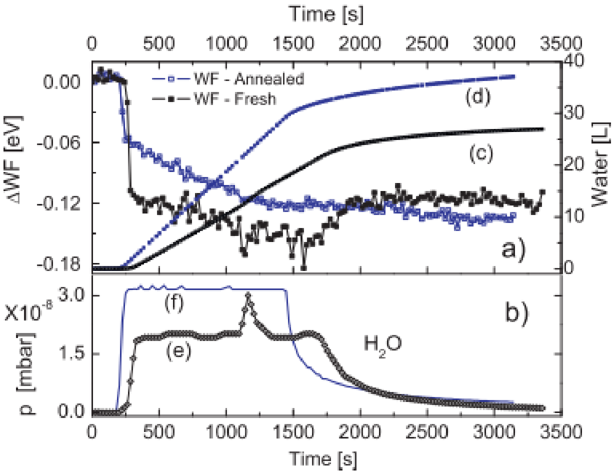

Figure 5.9 – a) Change of the work function over time during water exposure for the fresh and long-term annealed surfaces b) Water partial pressures for each experiment. (c) and (d) represents the water exposure in Langmuir units [24]

In the latest work of our group before the beginning of this project [128], water adsorption was performed in cycles (see Figure 1.6), and an attempt was made to model the slow drop of the work function as the separation/diffusion of OH groups according to the Topping model. When in close proximity, there is a depolarization effect which decreases their dipole moment. This dipole should be stronger as the OH groups separate over time, thus further decreasing the work function. However, the model was not conclusive, as it required a very high value of the water molecule polarizability in order to explain the total amplitude of the slow work function drop, and so a convincing interpretation is yet to be reached. There are distinct additional possibilities for the observed slow drop of the work function, such as adsorption of different unwanted contaminants present in the system (possibly molecular/atomic hydrogen, water, and different carbon based species), or the possible creation of BOVs caused by the X-ray irradiation. Also, it is still an open issue if different parameters such as the sticking coefficient, dipole moment of H_2O or OH group, desorption rate etc. could be measured. Additionally, these kinds of experiments also open the possibility to understand the temperature dependence of the H_2O adsorption dynamics on $TiO_2(110)$ rutile surface.

5.2.2 Oxygen Adsorption

The adsorption of O_2 on a perfect $TiO_2(110)$ surface is not thermodynamically favourable. For the molecule to be chemically adsorbed, it requires available electronic charge in the surface and near-surface regions, associated with reactive sites such as BOVs, OH groups and possibly near-surface Ti interstitials [11]. As shown in Figure 5.10, when the oxygen molecule is adsorbed on a BOV site, it is dissociated, healing the defect, and introducing an oxygen adatom to the adjacent Ti row. This adatom has a high energy barrier for surface diffusion (~1.14 eV), and is thus stable at room temperature [11].

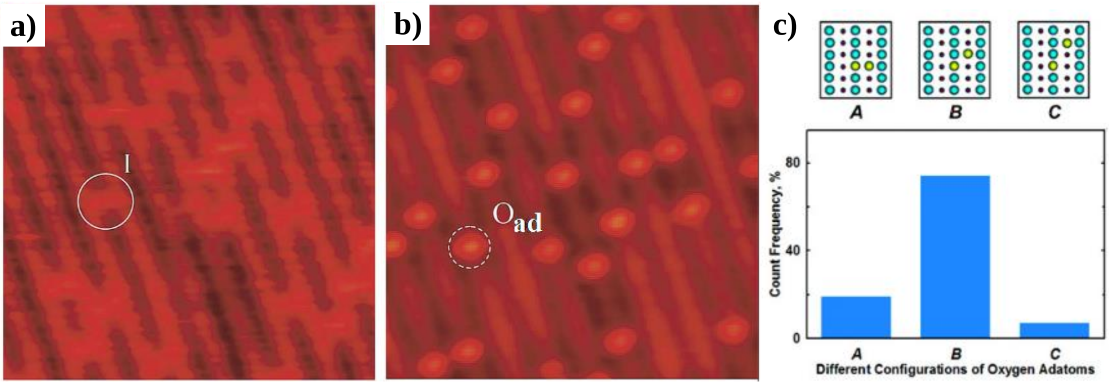

Figure 5.10 – STM picture of the rutile $TiO_2(110)$ (1×1) surface before (a) and after (b) oxygen exposure. Circles sites correspond to BOVs (I) and Oxygen adatoms (O_a). Figure adapted from [18]. c) Possible configurations of the oxygen adatom with respect to the initial BOV site, and respective frequency. Adapted from [135].

Adsorption on Ti rows and dissociation into two O_a is also observed (paired O_a), with comparatively lower probability. It is not possible to completely remove all BOV sites by oxygen exposure, as the adsorption of O_2 molecules saturates before all vacancies are filled. The proposed mechanism to explain this behaviour is that the delocalized charge associated with BOV sites is used to stabilize O_a atoms on Ti rows, thus decreasing the reactivity of these sites. The charge from Ti interstitials has been found to play a similar role in the stabilization of O_a [12,123]. STM experiments showed that around half of BOVs may remain on the surface after oxygen exposure, according to the results obtained by Du and co-authors, shown in Figure 5.11 [123]. This ratio may however depend on the overall reduction level of the crystal, due to the role of Ti interstitials in oxygen adsorption and dissociation.

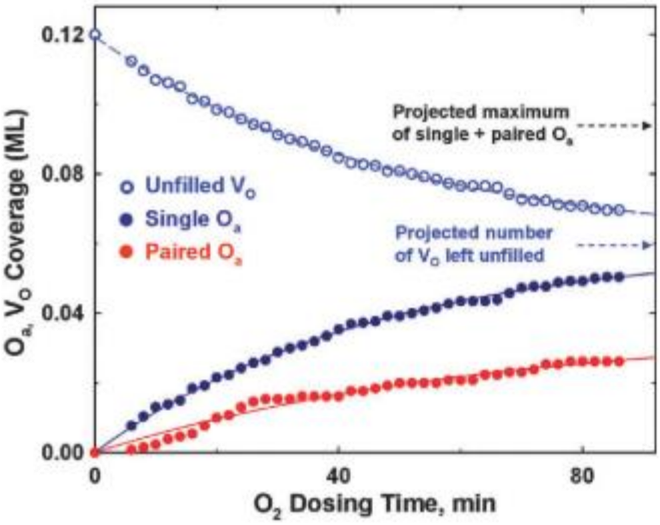

Figure 5.11 – Coverage of BOVs (V_O), single, and paired O_a atoms, as a function of O_2 dosing time. Adapted from [123].

Work function change during oxygen exposure at 100 K, causing a work function increase, was measured by Onda and co-authors [90]. The experiment was performed for slightly and strongly reduced surfaces, as well as for the Ar^+ sputtered surface. A saturated total work function increase of 0.2, 0.4 and 0.7 eV was measured for each surface treatment, respectively. It should be pointed out that the density of the measured points (as a function of oxygen exposure) is insufficient to perform a detailed analysis of the adsorption kinetics. Moreover, it would also be important to perform this experiment under room temperature conditions.

5.2.3 Interaction between Adsorbed Water and Oxygen

The interaction between different species related to O_2 and H_2O adsorption is complex, with the possibility for the formation of various intermediate structures during the reaction [17,20,124,136]. O_a species can react with bridging OH groups or H_2O adsorbed on Ti rows, to create OH groups adsorbed on Ti rows (OH_t). O_2 which is nondissociatively adsorbed on Ti rows can also react with bridging OH groups to create HO_2 species, as shown below in Figure 5.12. These processes can be described by the following reactions:

- $OH_b + O_a \rightarrow OH_t + O_b$
- $H_2O+O_a \rightarrow 2OH_t$
- $OH_b + O_2(g) \leftrightarrow O_b + HO_2$

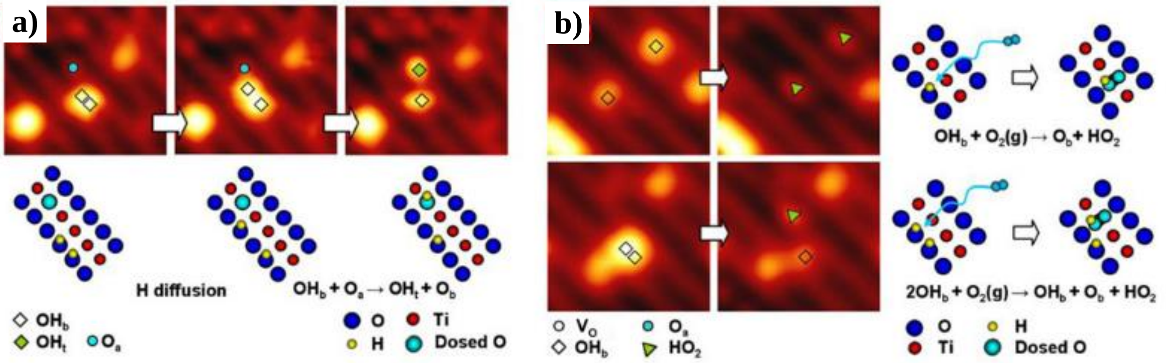

Figure 5.12 – Time-lapse of the formation of OH_t and HO_2 species observed by STM. a) Diffusion of OH_b towards O_a and reaction to form OH_b. b) Adsorption of O_2 on Ti rows and reaction with single and paired OH_b groups, forming HO_2. Adapted from [137].

The OH_t and HO_2 species that are formed in this way can then recombine between themselves or with OH_b groups to form H_2O, which can diffuse along the Ti row to dissociate in a BOV, or simply be desorbed from the surface. These processes are described by the following reactions:

- $OH_b + HO_2 \rightarrow O_b + O_a + H_2O_t$

- $OH_b + OH_t \rightarrow O_b + H_2O_t$

It should be stressed that the presence of H_2O increases the mobility of different surface species, allowing the diffusion of O_a and OH_t groups across Ti rows. Water thus works as a catalyst for further reactions that create more water, which is eventually desorbed, or dissociated on BOVs [136]. In this way, a nearly stoichiometric surface can be formed by exposing a defective surface to water and oxygen, as shown in Figure 5.13. The bright spots that can be observed on Figure 5.13 c) following a much longer exposure of 40 L are interpreted as OH_t species. The reactivity of the nearly perfect surface shown in Figure 5.13 b) is associated with sub-surface Ti interstitials [11].

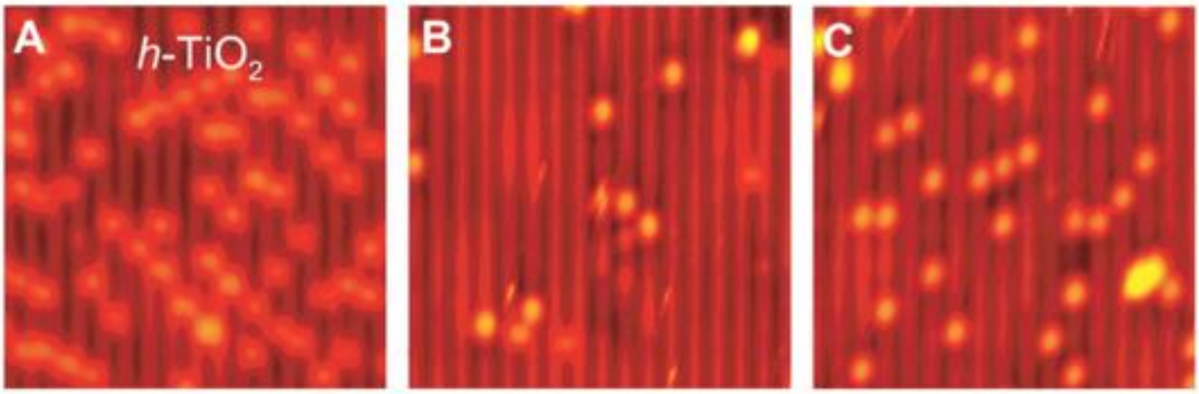

Figure 5.13 – Time-lapse of STM pictures taken of a fully hydroxilated TiO_2(110)-(1×1) surface (a), and after oxygen exposure of (b) 4L and (c) 40L. Adapted from [11].

The work function change of the hydroxilated surface following oxygen exposure was measured by Marques and co-authors [22], and the results are shown in Figure 5.14. In addition to the issues related to the kinetics of water adsorption mentioned in section 5.2.1 (explained by a possible (1×2) surface reconstruction), the work function increase following oxygen exposure is also much lower than expected for a (1×1) surface reconstruction, according to the observations by Wendt and co-authors [11].

Let us assume for a moment that the surface OH groups formed after water exposure are entirely removed from the surface by a few Langmuir oxygen exposure, as shown in Figure 5.13 b), so that a nearly perfect surface is created. A rise of the work function to values higher than its initial value, before water exposure, is then expected, since the nearly perfect surface should have a higher work function than the defective, initial one. This was clearly not the case, as the work function is shown to decrease 0.5 eV following water exposure, and increase only 0.1 eV due to oxygen exposure.

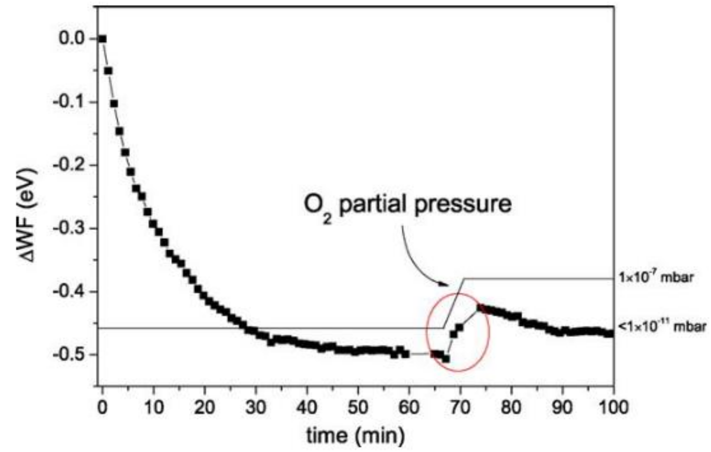

Figure 5.14 – Work function change of the $TiO_2(110)$ –(1×1) surface following water exposure, and subsequent oxygen exposure. Adapted from [22].

5.2.4 Experimental plan to study the H_2O and O_2 adsorption process on the $TiO_2(110)$-(1×1) surface with XPS and WFS

The uncertainty of the results involving water and oxygen adsorption on the $TiO_2(110)$-(1×1) surface studied by work function change, presented in the sections above, is a clear motivation to carefully perform a new set of experiments on a properly prepared $TiO_2(110)$-(1×1) surface. First, a good surface preparation must be assured. One criterion for this would be a fast decrease of the work function when exposed to water vapour, as shown in Figure 5.9. Since the presence of surface defects changes the work function, ideally, a correlation between the initial work function values and the surface reduction state can also be achieved. The $TiO_2(110)$-(1×1) surface reduction level will be altered by adjusting the sputter-anneal process (duration, temperature, oxygen pressure).

Concerning the analysis of water adsorption, a detailed study of the slow drop of the work function, which was previously observed, will be performed. The different features of the work function change associated with water adsorption will be monitored in different conditions, specifically relating to the surface preparation, in the presence of different gases, X-ray irradiation power, or at higher temperatures, hopefully providing some definitive answers on the subject. The kinetics of the water adsorption/desorption process will be studied, in particular, the apparent relationship between the slow drop of the work function, and its increase when water flow is turned off. This increase will be measured for different water exposure times, and a new adsorption model which correctly describes the results will be sought. Additionally, the work function measurement will be used to study the effect of surface temperature on the water adsorption process. The results of this experiment can be compared with those of TPD, and be used to confirm parts of the water adsorption model, while also reinforcing the versatility of onset technique as tool for surface analysis.

The oxygen adsorption process will be studied at room temperature by monitoring the work function change in real time, for surfaces prepared with different reduction levels. Since oxygen exposure is associated with the oxidation of Ti^{3+} species into Ti^{4+}, it should also be possible to quantify oxygen adsorption by XPS analysis of the Ti 3p peak, and relate it to total work function change. The analysis of the oxygen adsorption kinetics for surfaces with different reduction levels may provide insights into the oxygen adsorption process, and its relation to the BOV and Ti interstitial concentrations. Furthermore, the interaction between adsorbed water and oxygen species will be studied by monitoring the work function change while alternately exposing the surface to these gases. This change will be correlated with the expected reactions occurring at the surface, which should modify the adsorbed surface dipoles, and create/reintroduce adsorption sites for these gases.

A detailed description of these experiments and a discussion of the results will be presented in chapter 6.

5.3 Electron Stimulated Desorption on the TiO_2(110) Rutile Surface

5.3.1 Introduction

Numerous experiments performed in the last fifty years reveal the possibility to promote desorption of different surface species by electron bombardment. In contrast to ion bombardment, which typically causes desorption of surface species by the momentum transfer (ion sputtering), the kinetic energy directly transferred upon electron-atom collision is too low to break chemical bonds, due to the large mass difference between the collision partners. The energy transferred in this way will only cause desorption of weakly bound physisorbed species, which have a small residence time and are thus present in extremely small surface concentrations in UHV conditions. However, collision processes that involve electronic excitations of surface atoms may result in desorption of ions, neutrals, or other species in excited states. This process of Desorption Induced by Electronic Transitions (DIET) can be also achieved with photon bombardment in addition to electrons.

The initial theoretical description of DIET observations is based on the Franck-Condon principle, which assumes that electron impact causes an electronic transition without affecting the position of the nuclei. This assumption is justified by the extremely low efficiency of momentum transfer in the electron-atom collision. In this case, the Franck-Condon principle implies a vertical transition (constant z) between the potential energy curves associated with the surface/adsorbate ground state, and with an excited state (e.g. ionic, anti-bonding, or non-bonding states). The potential energy curves for an adsorbed/surface species in its ground and excited states are illustrated in Figure 5.15. The first model describing the ESD process, introduced by Menzel, Gomer, and Redhead (MGR model), is also presented. This model explains in general terms the desorption of ions and neutrals, due to the excitation of a bonding electron to an ionic, anti-bonding or non-bonding state [27].

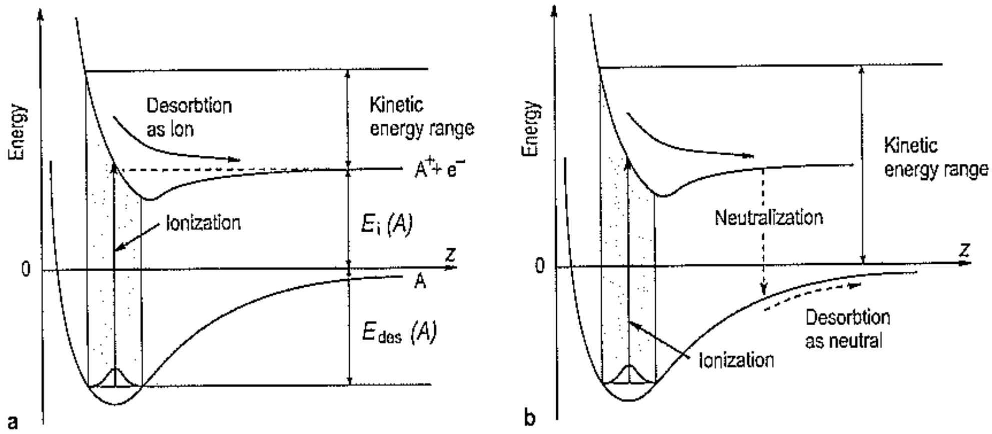

Figure 5.15 – Potential energy diagrams illustrating the MGR desorption model. The adsorbate A is ionized leading to its desorption a) as an ion, or b as a neutral species, if neutralization occurs during the desorption process. Taken from [27].

Figure 5.15 a) illustrates the case when electron impact causes ionization of the adsorbed species. Since the chemical bond is broken, the ion species is only bound to the surface by the image force, and the equilibrium position (minimum potential energy) moves slightly away from the surface plane. Because of this, the vertical transition takes part into the repulsive part of the ion-surface potential energy curve, and the adsorbed species can be repelled (i.e. accelerated away from the surface) and desorbed as an ion. However, due to the high Auger neutralization rate of ions close to the surface [138], the emission as an ion is uncommon, as it was experimentally confirmed by Redhead [139]. As illustrated in Figure 5.15 b), while being accelerated away from the surface, the ion can be neutralized, causing a vertical transition to the ground state energy curve. If, at this point, the kinetic energy gained by the adsorbed particle while being in the ionised state, is high enough to overcome the remaining potential barrier, the species will be desorbed as a non-excited neutral. This mechanism for desorption is also valid when electron impact causes electronic excitation into anti-bonding state, and does not necessarily require ionization of the adsorbed species.

The MGR model has been successfully used as a framework to provide understanding of different ESD processes [140]. However, it fails to explain the high ESD cross section of certain species that have a negative formal charge in the lattice, but are desorbed as positive ions. This was first observed by Knotek and Feibelman [141], who measured the ESD of positive ions from different metal-oxide surfaces in which the metals are in their highest oxidation state (TiO_2, V_2O_5, WO_3), and found the O^+ ions to be the dominant desorption species. Moreover, the energy threshold for its desorption was higher than the available valence transitions, and coincided with core level excitation energies of the corresponding metals, as shown in Figure 5.16. These facts were an indication that interatomic electron transitions are involved in the process.

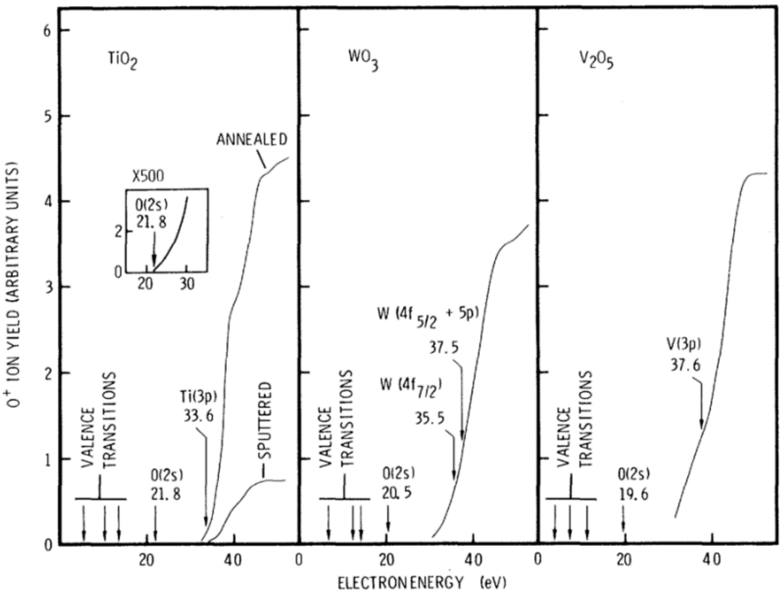

Figure 5.16 – O^+ ion yields as a function of electron energy for ESD experiments performed on TiO_2, WO_3 and V_2O_5 [141].

According to the mechanism introduced by Knotek and Feibelman (KF model), a hole is initially created in the metal core level by electron impact. Afterwards, the relaxation of the excited metal has to occur through an interatomic Auger process, due to the deficiency of available valence electrons on the metal atom itself (the metals are in the maximal valency state, with higher-lying occupied electronic states belonging to the oxygen atom). One electron from a nearby oxygen ion fills the hole in the metal core, leading to the emission of one or more Auger electrons. In the process of losing its charge to the metal ion, and the resulting emissions of Auger electrons, the negative oxygen ion becomes an O^+ ion, which is readily desorbed from the surface due to Coulomb repulsion with the surrounding positive metallic ions. According to this process, ESD thresholds will correspond to metal core-hole creations. With this in mind, it is possible to use ESD as a tool to scope the bonds between different surface species/adsorbates.

The KF mechanism was later revised by Tanaka and co-authors [19,142] to properly explain the DIET measurements of several other metal oxides. By using electron-ion coincidence spectroscopy (EICO) on the TiO_2 surface, they were able to properly assign each O^+ ion desorption to specific electronic excitations/transitions. It appeared that the KF mechanism failed to explain the O^+ desorption from certain metal oxides that do not satisfy the “maximal valency” condition of the KF mechanism. Furthermore, theoretical studies have since showed that the “maximal valency” configuration assumed for TiO_2 in the KF mechanism, with all valence electrons being in the O 2p orbital, is not correct, as there is a hybridization between the O 2p and Ti 3d orbitals (see Figure 5.1).

According to the revised mechanism, instead of charge transfer via an inter-atomic Auger decay, which should be a very slow process compared to the intra-atomic one, the hole created in the Ti 3p pulls down the energy of the 3d levels (due to the reduced screening of the Ti nucleus by the electron cloud, similarly to the chemical peak shift in XPS), increasing the hybridization with the O 2p level and enabling the charge transfer, as shown in Figure 5.17. By considering this process, known as the “Kotani-Toyozawa” mechanism [143], Tanaka and co-authors were able to successfully explain most DIET experimental results obtained so far.

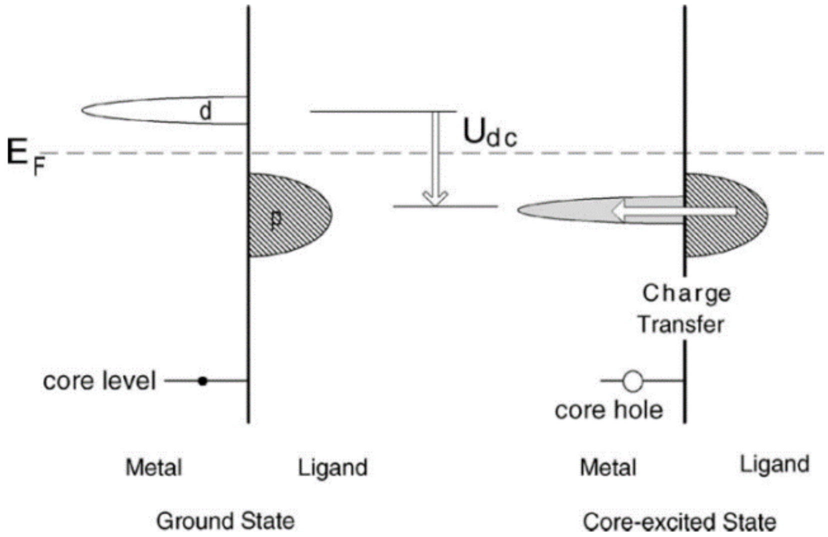

Figure 5.17 . Kotani-Toyozawa mechanism. The creation of a core-hole in the Ti (Metal) pulls the energy of its 3d level closer to the oxygen 2p level (Ligand), increasing the probability of charge transfer between the two [19].

5.3.2 ESD of TiO_2 and Adsorbates

The TiO_2 surface has been the subject of ESD experiments in a number of studies. In the previously mentioned ESD experiments performed on a clean TiO_2(110)-(1×1) rutile surface, desorption of lattice oxygen in its O^+ ionic state was observed, creating a BOV. The creation of BOVs following ESD introduces electrons to the Ti 3d valence band [119,144], which in turn decreases the charge transfer between the oxygen and titanium valence bands, effectively decreasing the ESD cross section for BOV creation [141]. When annealed in UHV, the maximum coverage of BOVs observed by STM is ~10% of a ML (1 ML corresponding to the concentration of the unit cell) [18]. In the case of BOVs created by ESD, at a relatively low electron flux, a slightly higher threshold is observed, around 10-12% ML (after an electron fluence of $\sim 1.26 \times 10^{16}$ cm^{-2}, at an energy of 75 eV). Higher fluences will also start to create shallow pit features, with a relatively low coverage (~0.15 ML% at two times higher fluence) [118,119]. Following the formation of an oxygen vacancy on the TiO_2(011)-(2×1) surface, the desorption cross section of nearest and next-nearest oxygen neighbours is reported to decrease by a factor of 100 and 10, respectively [145]. It is supposed that a similar effect is taking place on the TiO_2(110)-(1×1) surface, where the reported saturation of BOVs induced by ESD is attributed to the local presence of 3d states in the vicinity of each BOV. Additionally, if the bombardment is performed with higher electron fluxes and energies, it may induce surface reconstruction. STM pictures of the electron bombarded TiO_2(110)-(1×1) surface, with 300 eV electrons and an electron flux of 0.3 mA/cm^{-2}, have shown that the surface underwent reconstruction to different $1 \times n$ structures, which suggests that it has been heated by the bombardment (rate of energy transferred to the surface was ~0.1W) [118]. A similar effect was also observed by STM on the TiO_2(011)-(2×1) surface bombarded with 300 eV electrons, which underwent reconstruction to one-dimensional strands of oxygen atoms [145].

ESD of different adsorbed species on the TiO_2 surface has also been studied. These mainly involve ESD of hydrogen, water, and oxygen covered surfaces [119,146–151], but also include other species such as NH_3, SO_2, CO, or Li [152–155]. In some of these studies, STM imaging has been used together with ESD to directly observe the effect of electron bombardment on the surface, as well as changes introduced to its structure [118,119,145,148,149,154,155].

Following water adsorption, ESD of H^+ and OH^+ species has been observed with a threshold energy of ~20 eV, corresponding to the binding energy of the O 2s level. An experiment performed with adsorbed D_2O has shown that the desorbed H^+ is originating not only from the dissociated water species, but possibly also from hydrogen atoms trapped in the near-surface region [150]. STM analysis have revealed that the hydrogen adatoms on bridging oxygen atoms, which are the result of water dissociation on BOV sites, are removed from the surface following electron bombardment, with an ESD cross-section in the 10^{-19} cm^2 range for 20 eV electrons, as shown in Figure 5.18 [149]. The STM analysis also showed that the surface was not significantly damaged during the electron bombardment. Part of the energy transferred to the surface via electron bombardment will contribute to heating up the surface. However, if the electron flux and energy are kept low, the thermal energy transferred to the surface in this way should only cause a negligible temperature increase, insufficient to trigger desorption of H^+ species.

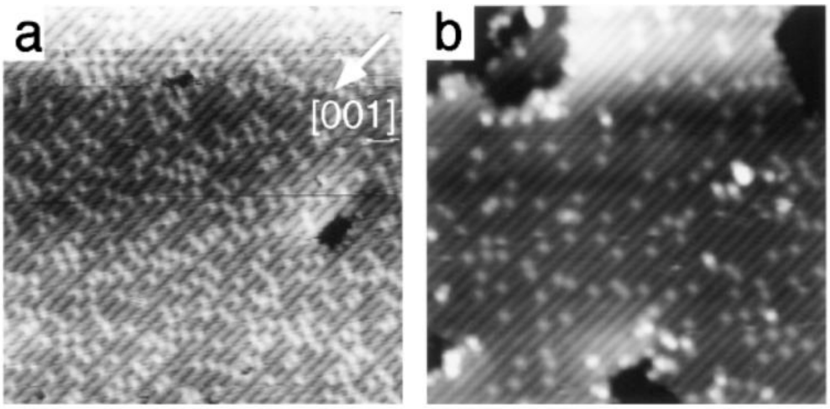

Figure 5.18 – STM pictures of the hydrogen filled surface a), and the electron bombarded surface b). Electron energy is 20 eV, with the beam current of 5.4 µA measured on the sample [149].

As described in section 5.2.2, the adsorption of O_2 on a BOV is dissociative, with one atom filling an oxygen vacancy, and the second one being adsorbed on the adjacent Ti atom as an oxygen adatom. Lee and co-authors [148] have measured the O^+ yield following ESD of the TiO_2 surface exposed to O_2. The threshold energy for desorption of oxygen adatoms was measured to be ~34 eV, which is the same as for lattice oxygen, and corresponds to the excitation of Ti 3p electrons. However, the cross section for the oxygen adatoms is approximately 600 times higher than that of lattice oxygen, which could be due to a number of potential reasons, such as an efficient resonant charge transfer between O_{ad} and Ti^{5+}, a weaker neutralization of the positive oxygen ion as it leaves the surface, or a more positive formal charge compared to lattice oxygen, which would reduce the amount of transferred electrons needed to produce the O_{ad}^+ ion.

5.3.3 Experimental plan to study the ESD of oxygen and hydrogen from the TiO_2(110)-(1×1) surface with WFS

The original ESD studies by Menzel and Gomer [156,157] were performed by following the work function change of different surfaces, obtained from field electron emission measurements. Although desorption products were not directly detected in this way (by mass analysis or other techniques), information on the surface change can still be obtained, by careful analysis of the time-dependence of the work function change.

It should be possible to study the electron stimulated desorption of different species from the TiO_2(110)-(1×1) rutile surface in the same way, by following its work function change obtained from the secondary electron energy cut-off. As shown in section 5.2, the creation/healing of BOVs and the adsorption of water and oxygen molecules is accompanied by a change of the work function, due to the surface dipole moment of these species. Consequently, desorption of the same species induced by electron bombardment should produce an opposite work function change. By establishing a correlation between this change and surface coverage, it should be possible to obtain a relative measurement of the ESD cross section for distinct species and different electron energies.

It should be emphasized that, since the work function change depends directly on modifications of the surface composition and/or structure, desorption yields measured in this way should be sensitive to the desorption of species in both ionic and neutral states. According to the MGR model, initially ionized surface species have a high neutralization probability that depend on various factors, including the local work function. Consequently, the intensity of desorbed ions will not always be representative for the overall desorption phenomenon, which may provide inaccurate information on surface modifications [158].

Starting from a clean TiO_2(110)-(1×1) rutile surface, with a nearly perfect stoichiometry, or a small amount of surface defects, the surface bombardment with 35 eV electrons (or higher) will introduce BOVs, and should thus decrease the average work function. As the number of BOVs increases with total electron fluence, the rate of the work function change should decrease, and finally saturate, due to the expected reduction of the oxygen ESD cross section with the number of BOVs, with a value in the 10-12% range [118,141]. It is not clear what effect the observed “pits” will have on the work function, as not much information can be found on their structure. The model proposed by Pang and co-authors [118], based on STM observations, considers the simple removal of a portion of the top layer, which exposes a second layer having the regular TiO_2(110) rutile structure, as shown in Figure 5.19.

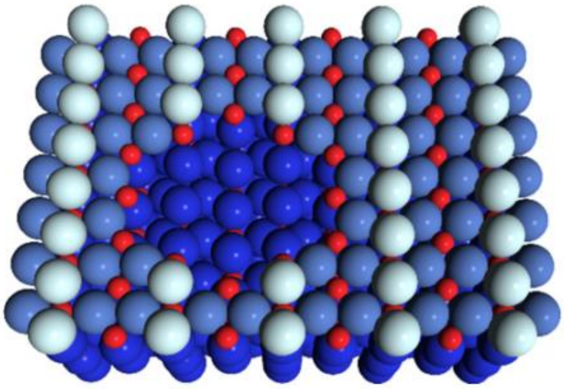

Figure 5.19 – Proposed model for the “pits” observed on the TiO_2(110)-(1×1) surface [118].

With this in mind, it is reasonable to assume that the pit formation does not cause a significant work function change, although the influence of the step at the pit edge should also be considered. Furthermore, as pit formation is mainly observed if the surface keeps being bombarded after reaching the saturated BOV coverage, reaching a relatively low coverage of ~0.15 ML for twice the electron fluence required for BOV saturation [15], it is relatively safe to assume that the initial rate of WF change during bombardment is mainly due to BOV creation. The flux and energy of electron bombardment should be limited in order to prevent surface reconstruction by heating. It should however be stressed that the creation of BOVs by ESD has been observed to increase the adsorption rate of hydrocarbons [121]. For this reason, it is also important that the bombardment is not too prolonged, i.e., the electron flux shouldn’t be too low. Based on the reported cross-sections for oxygen desorption, an electron flux of a few $\mu A/cm^2$ (at 75 eV) should be high enough to reach BOV saturation in a few minutes of bombardment, while preventing surface heating.

The same experiment can be performed on a defective TiO_2(110)-(1×1) rutile surface initially exposed to molecular oxygen, therefore replacing some BOV sites with BO and O_{ad} pairs. In this case, the work function change should show a faster decrease relative to the clean surface, due to the higher ESD cross-section for the O_{ad} species, as measured by Lee and co-authors [148]. A larger total work function change for the O_{ad} covered surface is also expected, due to the removal of both BO and O_{ad} species, which contribute to a higher work function value with surface dipoles oriented away from the vacuum.

The bombardment of the water exposed surface with +20 eV electrons causes desorption of H^+ species [141]. If electron energy is kept below 35 eV there should be no creation of additional BOV sites, as STM results have also shown [149]. Since no BOVs are created, the electron bombardment of the water exposed surface should increase the surface averaged work function, due to the removal of surface dipoles oriented towards the vacuum (OH groups).

A set of experiments will be performed on the TiO_2(110)-(1×1) rutile surface, aimed at confirming the assumptions here presented. The work function change caused by ESD of oxygen species, both from lattice oxygen (BOs) and O_{ad} species obtained after oxygen exposure, will be measured. The experiments will be performed for electron bombardment at different energies, a desorption model which explains the results will be sought, and the cross-section for ESD of oxygen species will be calculated (for each energy). Similarly, the work function change caused by ESD of H species present on the surface after water exposure will be measured, and its cross-section will be determined. A detailed description of these experiments and a discussion of the results will be presented in chapter 6.

6

6 Work Function and XPS Combined Study of Surface Defects, Water and Oxygen Adsorption on the TiO_2(110)-(1×1) Surface

Work function measurements based on the onset position have been combined with XPS analysis to study the TiO_2(110)-(1×1) surface. A series of experiments have been performed to study surface defects and their influence on the adsorption of water and oxygen species. The TiO_2(110)-(1×1) surface has been prepared with different reduction levels, either by adjusting the parameters for surface preparation (sputtering energy, annealing temperature and duration, oxygen partial pressure, etc.) or by electron bombardment (ESD), followed by a detailed study of the adsorption kinetics of water and oxygen species. Moreover, modelling of the ESD process for oxygen and hydrogen species has also been performed.

Some of the results shown in this chapter have been published [159], in particular those concerning the adsorption and electron-stimulated desorption of oxygen species, although with a much less comprehensive analysis of the results when compared to the discussion here presented.

6.1 Experimental Setup

The (1×1) unreconstructed surface of the TiO_2(110) rutile single crystal was prepared by sputtering/annealing cycles. The sputtering procedure was performed with 1000 eV Ar^+ beam, at an incident angle of approximately 30º. The total sputtering time and pressure were adjusted depending on the surface contamination level, and were prolonged/increased until the C 1s peak was no longer detected by XPS. The sample is annealed by direct electron bombardment of the sample holder, generated by a heated tungsten filament. The heating power due to the electron bombardment can be calculated from the product of the voltage difference between the sample and the filament, and the total current measured on the sample. The experimental setup here described is schematically shown in Figure 6.1, and was mounted on the Kratos XSAM 800 system.

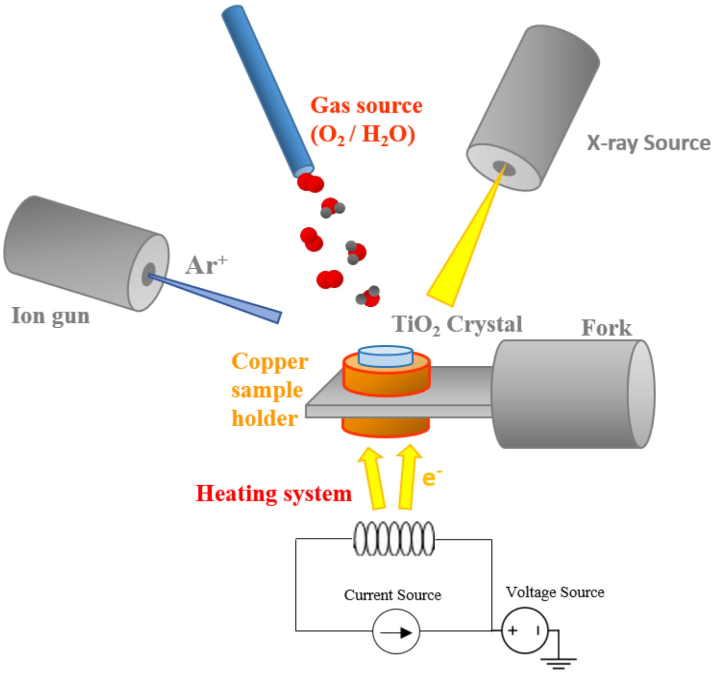

Figure 6.1 – Illustration of the experimental setup used for the preparation of the TiO_2(110)-(1×1) surface, exposure of the crystal to different gases, and irradiation source (X-ray) used for the work function measurements.

The annealing time of each cycle was ~10 minutes, at temperatures in the 770-870 K range, under UHV conditions or with an O_2 partial pressure in the 1-3×10^{-7} mbar range. Both annealing temperature and partial O_2 pressure were adjusted depending on the desired surface reduction state (concentration of BOVs). The base pressure of the system was around 3×10^{-10} mbar, rising approximately for one order of magnitude at the maximum annealing temperature. All experiments were performed at room temperature unless stated otherwise. In the experiments performed at higher temperatures, the sample was heated by photon irradiation of the sample holder from the hot filament. Using electrons to heat the sample prohibits the use of the energy analyser to detect secondary electron emission, as they create too much background noise. Consequentially, the heating of the sample with this method was limited to ~400 K.

The secondary electrons required for work function measurement are generated by irradiating the surface with X-rays, using the XPS X-ray source, operated at a lower power. Onset measurement is typically performed with an electron-gun as radiation source [82,95,96]. However, as explained in section 5.3, direct electron bombardment will create surface modifications by ESD effect, which should be avoided while performing the onset measurement. While the secondary electrons generated by the X-ray irradiation may indeed interact with surface atoms when leaving the surface, and induce electronic excitations that may result in ESD [160], the vast majority of these electrons are emitted with a kinetic energy lower than 10 eV, which is not enough to induce significant surface modifications by ESD.

Water and oxygen (or other gases) are introduced into the analysis chamber via a capillary, and the gas flow is controlled by a variable leak valve which enables a precise control of partial pressures in the 10^{-9} mbar range, with the pressure being monitored by an ionization gauge, recorded for subsequent data analysis, and adjusted for the specific gas. The water gas is obtained from the evaporation of Milli-Q water, which was additionally purified by freeze-pump-thaw cycling. Moreover, the gas line piping is kept at a high temperature (~100 ºC) to prevent adsorption, which may lead to undesired contamination.

Electron bombardment of the $TiO_2(110)$ rutile surface was performed by placing the annealing filament close to the sample's surface. With this setup, the electron bombardment current can be adjusted by changing the filament current, and the electron energy can be tuned by the voltage difference between the filament and the sample. The proximity of the heated filament to the sample may be problematic if too much gas contaminants are released (mainly CO, CH_n, WO_n,, and H/H_2), or if the thermal radiation causes a significant temperature increase of the surface. The filament has been strongly outgassed during the annealing procedure, where it operates for a long time at a much higher current (4 A), when compared to its use in ESD experiments (~2.5A). In the latter case, no pressure increase is observed, the brightness of the filament is of very low intensity, and placing the thermocouple sensor in close proximity shows no significant temperature increase. Preliminary tests with XPS and work function measurements were also performed, to confirm that placing the heated filament in relative proximity to the sample (without electron emission/bombardment) was not inducing substantial surface modifications. Furthermore, it should be stressed that this method has been successfully used for the same purpose in other works [118,119]. The measurement of the secondary electron energy spectra was performed alternately with the electron bombardment, due to the need to reposition the sample in the analysis position, and the requirement of turning off the electron emission from the filament to perform the measurement.

6.2 Surface Preparation

An initial, qualitative analysis of the surface reduction state can be obtained either by quantification of the Ti^{3+} contribution from the Ti 2p XPS peak, or by comparison of the initial onset position between different surfaces.

A comparison between the XPS Ti 2p peak of the sputtered, UHV and O_2 annealed surfaces is shown in Figure 6.2.

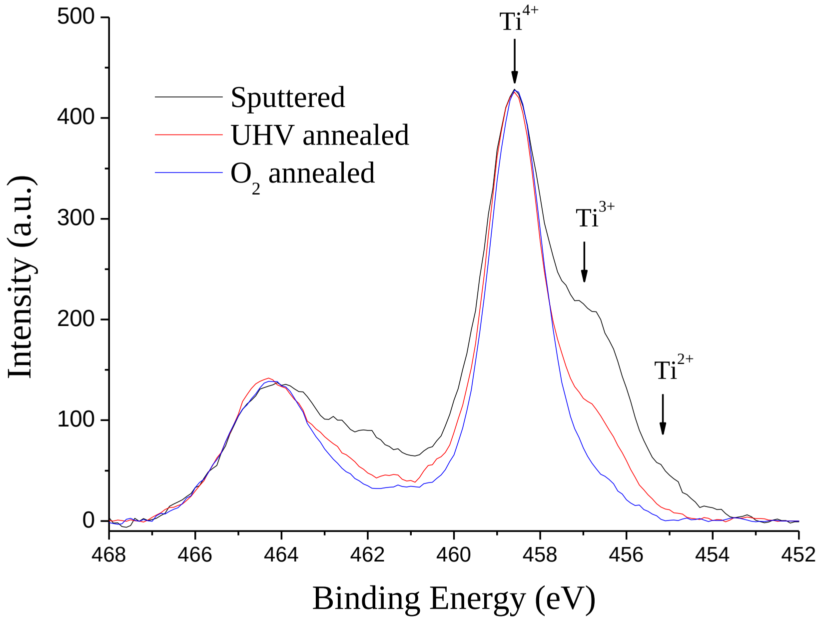

Figure 6.2 - Comparison of Ti 2p peak between the sputtered, UHV annealed, and O_2 annealed $TiO_2(110)$-(1×1) surface

The surface annealed in O_2 atmosphere shows a near-stoichiometric surface, with the lowest Ti^{3+} contribution, and a slight narrowing of the peaks. The exact difference between these surfaces ($Ti^{2+/3+/4+}$ relative percentages and the peak width) will depend on several parameters, such as sputter time and energy, annealing temperature and duration, O_2 partial pressure during annealing, and, more generally, the annealing history of the sample. Since the Ti^{3+} contribution is attributed to the presence of both Ti interstitials and Ti^{3+} originating from BOVs, it is not possible to directly quantify the concentration of each from the XPS peak. However, when inducing changes exclusively to the first layer, any change of the Ti^{3+} contribution should mostly be due to the increase/decrease of BOVs.

Figure 6.3 shows the work function shifts associated with the $TiO_2(110)$-(1×1) surface prepared in different ways, and following exposure to water and oxygen. The horizontal red line shows the range of relative work function values between the UHV and O_2 annealed surfaces, resulting in highly reduced and stoichiometric surfaces, respectively. The maximum difference observed between the perfect and the highly reduced surface (but still with (1×1) structure) was around 0.4 eV, which is in agreement with the literature [126].

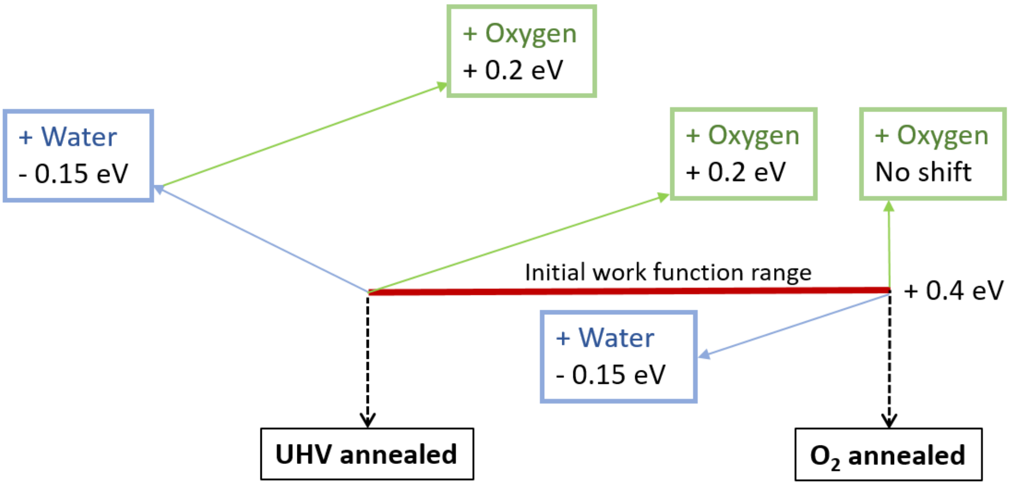

Figure 6.3 - Schematic representation of the work function shift as function of surface preparation, and subsequent exposure to water/oxygen.

The work function change observed upon adsorption of either water or oxygen on these surfaces is also shown. Water adsorption results in $\approx -0.15\mathrm{eV}$ shift of the work function, whether adsorbed on the highly reduced surface or the stoichiometric one. The work function shift due to oxygen adsorption depends on the initial reduction level of the surface, ranging from 0 eV on the perfect surface to 0.2 eV on the highly reduced one. It should be stressed that following the exposure of the sample to these gases, there is no measurable shift of the XPS peaks, which is a confirmation that these work function shifts are exclusively due to modifications to the sample's surface, and not due to a change of the analyser's work function. A detailed study of these shifts is presented in the sections below.

6.3 Adsorption of Water on the TiO_2(110)-(1×1) Surface

6.3.1 Nature of the Slow Work Function Decrease

As was previously mentioned in sections 1.1 and 5.2.1, the fast onset shift upon water exposure is followed by a slow decrease of the work function, for which a definitive explanation has not yet been provided. The TiO_2(110)-(1×1) surface was exposed to different gases that may cause a work function decrease, which are present in UHV systems in small partial pressures, in order to reach a possible explanation for the slow drop. Other processes such as radiation-induced damage, gas released from filaments or from the ion pump, were also tested.

The initial test was performed with water itself. If the slow drop is due to the adsorption of water, it should depend on its partial pressure in the system. Figure 6.4 a) shows the work function change over time, with water being introduced to the system either at start or the end of the experiment, at a pressure of 1×10^{-8} mbar. Both experiments start when the crystal reaches room temperature. It is clear that the overall slope of the slow drop is similar, as the final value of the onset shift is the same for both cases, while the total water exposure is obviously much higher when water is introduced right away. From this experiment it can be concluded that the nature of the slow drop is not related to the water adsorption, at least not in an obvious, direct manner.

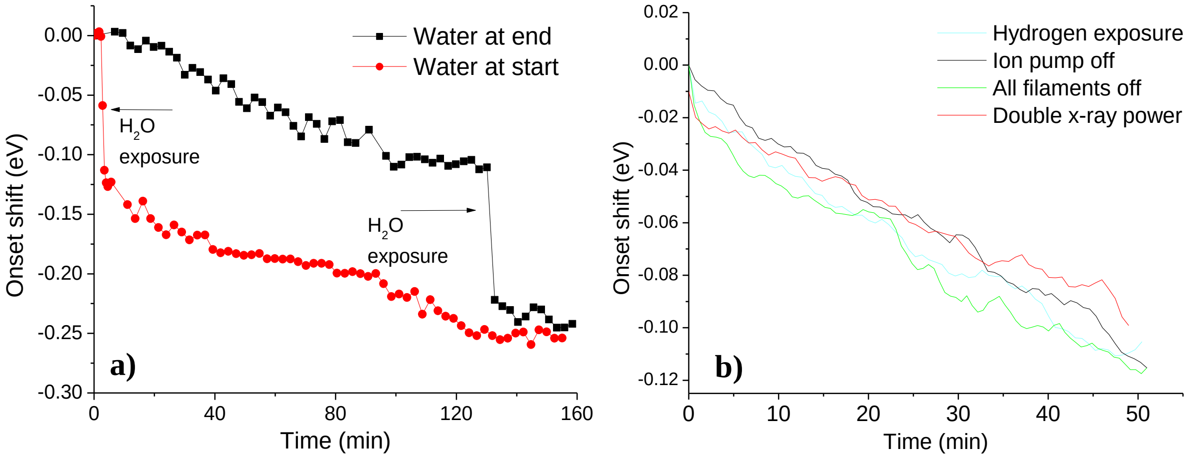

Figure 6.4 – Time-lapse of the work function change a) when water is introduced at different times in the system, b) for other possible effects that could affect the surface.

Figure 6.4 b) shows the onset shift for other processes that may induce slow surface modifications. The first test was the exposure to hydrogen, which is always present in UHV systems. The surface was exposed to molecular hydrogen at a pressure of ~1×10^{-8} mbar, which should be partially dissociated in the presence of nearby hot filaments, such as the one from the ionization gauge used for pressure measurement. Consequently, the surface was exposed to both H_2 and H. The sample was also irradiated with two X-ray intensities, to test eventual radiation-induced defect creation. In addition, the measurements were performed with all filaments and ion pumps turned off, in order to exclude possible outgassing of contaminants. The data is smoothed and presented in lines for clear visualization. In all cases, there was no observable change of the slope of the slow work function drop, which led us to conclude that it is not caused by any of these processes. It should be stressed that the experiments presented in Figure 6.4 a) and b) were performed at somewhat different times with different sample and vacuum system recent history, and so the slope of the slow drop is not necessarily comparable between the two.

The XPS analysis performed before and after some of the experiments with the TiO_2 surface typically reveals the adsorption of small quantities of carbon-based species, which is expected in UHV systems (hydrocarbons can be added to a baked UHV system in a number of ways – introduction of new samples, external or virtual leaks, filament outgassing, etc.). However, since the XPS sensitivity factor for the C 1s peak is quite small, it is nearly impossible with the current XPS system to correlate its intensity with the change of the work function. To test the possibility of hydrocarbon adsorption being related to the slow work function drop, the system with a base pressure in the mid 10^{-10} mbar range, which had not been baked for some time, was baked for the second time in order to remove hydrocarbon species that may have accumulated during the experimental work. The onset shift was measured on the freshly baked system and compared with the previous results and is shown in Figure 6.5.

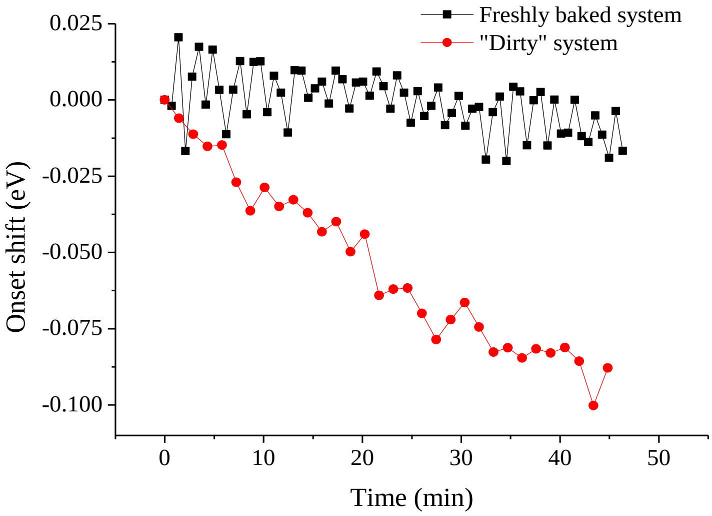

Figure 6.5 – Time-lapse of the onset shift for the freshly baked and the “dirty”/worked system.

It is entirely clear that the slow drop is considerably less pronounced on the freshly baked system (the slope is 5-10 times lower). XPS analysis of the C 1s peak over a long period of time confirms that the adsorption of hydrocarbons is also much less pronounced after the baking procedure. This indicates that the slow drop that has been observed in different works [22–25] is most likely due to the adsorption of hydrocarbon contaminants, instead of the hypothesized OH group separation [25], defect creation or adsorption of other species. It should be stressed that the base pressure in both cases was in the mid 10^{-10} mbar range, with the freshly baked one being only marginally lower. This indicates that a very small amount of hydrocarbon species present in the system will still have considerable effects on the TiO_2 surface.

6.3.2 Water Adsorption Kinetics and Influence by Hydrocarbon Contamination

As it was previously established for the TiO_2(110)-(1×1) surface, there is a work function increase when the valve used to introduce water vapour is closed (see Figure 5.9). This work function recovery can be associated with desorption of water molecules from Ti rows, as they are oriented with hydrogen atoms facing the vacuum. Consequently, the orientation of their dipoles is such that water adsorption on Ti rows reduces the work function according to the Topping model [102,107]. TPD experiments on H_2O/TiO_2(110) rutile system reveal that the surface concentration of molecular water is considerably reduced at ~350 K (see Figure 5.7 b). To test if the work function increase is indeed caused by the water desorption from Ti rows, the water vapour exposure experiments were performed at room temperature and at 353 K. In both measurements the surface was exposed to water at a pressure of ~1×10^{-8} mbar for one minute. The results of both experiments are shown in Figure 6.6.

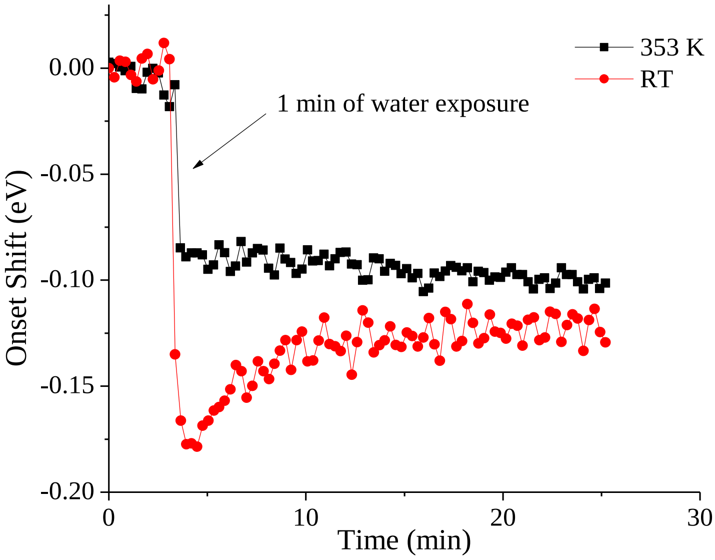

Figure 6.6 – Time-lapse of the onset shift during water exposure for 1 minute (~1×10^{-8} mbar), comparison between sample at room temperature and 353 K.

A partial work function recovery was observed in the experiment performed at room temperature, which was not the case in the experiment conducted at 353 K. This appears to confirm the previous assumption that the observed work function recovery is related to water desorption from Ti rows. Furthermore, the fact that the fast drop of the work function is still present in the experiment performed at 353 K indicates that, even though the time spent on the surface by the H_2O molecule is considerably shorter, their mobility across Ti rows is still high enough to almost immediately fill all BOV sites.

A closer analysis reveals that both the surface diffusion time constant τ_{dif} and the residence time at the surface τ_{res} decrease with the temperature according to the Arrhenius law. However, their ratio $\tau_{res} / \tau_{dif} \propto e^{\frac{E_{des}-E_{dif}}{kT}}$, which is proportional to the number of adsorption sites probed by a molecule, is decreasing with temperature since the activation energy for surface diffusion E_{dif} is smaller than that for desorption E_{des} [101,161]. In other words, the number of bridging oxygen sites probed by a water molecule before being desorbed increases with the surface temperature.

Over the course of many experiments that were performed, it has been observed that the magnitude and time dependence of this recovery/desorption is not constant, and appears to be correlated with the time interval between water being introduced and removed from the system. The recovery/increase of the work function is inversely proportional to this interval, as if a time-dependent process occurring on the surface is affecting the bonding of the H_2O molecules, preventing their desorption. If the slow drop of the work function (due to hydrocarbon adsorption as is now known) is related to this phenomenon, a difference between the water desorption from the freshly-baked and “dirty” vacuum systems should be seen.

A series of experiments were performed to test this hypothesis, where the onset shift was measured for different durations of water exposure. The results are separately shown in Figure 6.7 a) and b), for the unbaked (“dirty”) and freshly baked (“clean”) vacuum systems, respectively. The data was smoothed and presented in lines for a clear distinction between the different curves. It can be confirmed from these results that indeed the work function recovery, which occurs after closing the valve used to control water vapour flow, is consistently lower with increasing exposure times. Additionally, on the cleaner vacuum system, the amplitude of this recovery decreases very slowly with the water exposure time, when compared to the “dirty” vacuum system. In the latter, the recovery has a value of ~0.06 eV for 1-2 min exposure times, and quickly decreases to ~0.02 eV for 10-13 min exposures. In the former however, while the recovery on the “1 min” experiment is equivalent to the one on the “dirty” vacuum system (no time for a considerable amount of hydrocarbons to be adsorbed), a waiting period of 40 min still yields a ~0.04 eV recovery. This appears to indicate that the presence of hydrocarbons on the surface inhibits desorption of H_2O molecules. It is possible that when travelling along the Ti rows, water molecules find carbon-based adsorbed species, to which they are then bonded, preventing their desorption (at room temperature). In other words, adsorbed hydrocarbons appear to become new chemisorption sites for water molecules.

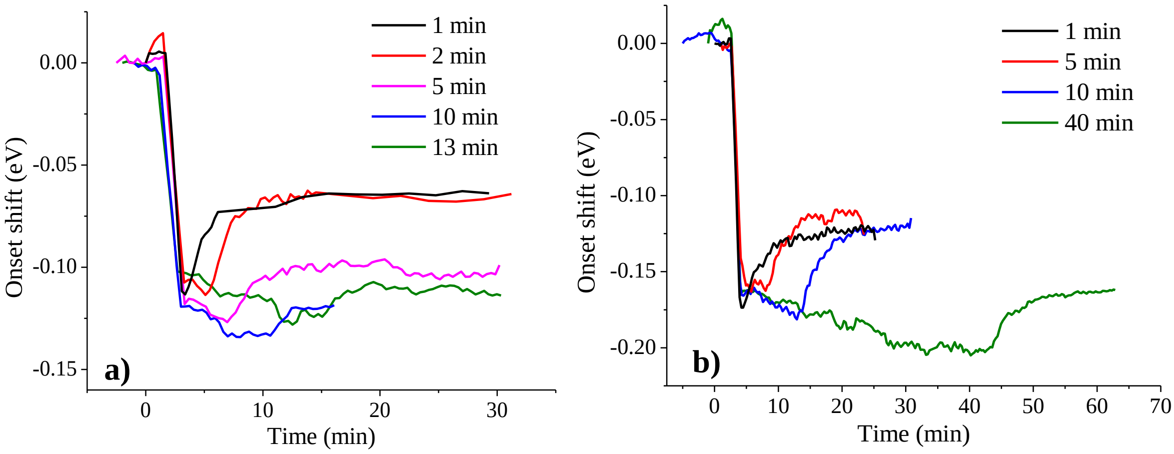

Figure 6.7 – Time-lapse of the onset shift during the introduction of water vapour to the system (water pressure of ~1×10^{-8} mbar), and subsequent interruption of the water flow on a) “dirty” vacuum system and b) “clean” (freshly baked) vacuum system. Data is smoothed for clear visualization.

The kinetics of the water adsorption process here observed can be quantitatively described with a Langmuir adsorption model [27]. It is not possible to perform a reliable analysis of the adsorption kinetics when water vapour is introduced into the system, due to the relatively fast nature of the process, and its relative complexity which makes it difficult to model accurately. At the moment of its introduction, water adsorption is associated with two distinct adsorption sites and mechanisms. Adsorption on Ti rows, which occurs with a certain probability when water from the gas phase “lands” on an adsorption site, and adsorption on BOVs, which has a higher probability of occurring through an additional process. The water mobility on Ti rows is known to be very high (as supported by density functional theory (DFT) calculations and STM observations [13]), with adsorbed water molecules travelling along Ti row sites until finding a BOV site, where they can be dissociated forming two OH groups. A kinetics analysis can however be performed on the desorption part of the experiment, which is noticeably slower and, at room temperature, should only occur from water desorbed from Ti rows. It is thus assumed in the model that at the moment when water vapour inflow is interrupted and the work function starts increasing, all BOV sites have been replaced with OH pairs, which will not be desorbed during the relatively short duration of the experiment.

The average work function change over time observed in these experiments is due to the adsorption/desorption of both hydrocarbon and water species, and can be expressed as $\Delta\Phi_{total}\left(t\right)=\Delta\Phi_{H_2O}\left(t\right)+\Delta\Phi_{hc}\left(t\right)$, where $\Delta\Phi_{total}$ is the average work function change of the whole surface, $\Delta\Phi_{H_2O}$ and $\Delta\Phi_{hc}$ are the water and hydrocarbon related contributions, respectively. As has been previously shown, the adsorption of hydrocarbons is a rather slow process, especially when compared to water adsorption, and, in the time-scale of these experiments, appears not to be affected by the presence of water molecules at the surface. On the other hand, water desorption is clearly inhibited by the presence of hydrocarbon species, and appears to be correlated with their concentration.

In order to model the work function change associated with hydrocarbon adsorption, it is assumed that the rate of hydrocarbons impinging the surface is constant for each system during the course of the experiment, and its adsorption rate does not depend on water coverage or exposure. As such, the concentration of hydrocarbon species can be obtained from the approximation of a simple adsorption model. The rate of hydrocarbon concentration change is equal to:

$$\frac{dn_{hc}}{dt} = \phi_C \cdot P_{ads} \tag{6.1}$$

where n_{hc} is the surface concentration of hydrocarbons, ϕ_C is the flux of hydrocarbon species hitting the surface, and P_{ads} is the probability of adsorption when one of these species hits the surface. This probability is equal to the probability of hitting an adsorption site, multiplied by the sticking coefficient at zero coverage for hydrocarbon species s_{0hc}. Thus, it can be written:

$$\frac{dn_{hc}}{dt} = \phi_C \cdot s_{0hc} \frac{n_a}{n_t} = b\left(n_0 - n_{hc}\right) \tag{6.2}$$

where n_a is the concentration of free adsorption sites, given by $n_a = n_0 - n_{hc}$, with $n_0 = n_a\left(0\right)$, and n_t is the concentration of all surface atoms. The solution to the above differential equation is given by $n_{hc} = n_0\left(1 - e^{-bt}\right)$, with $b = \phi_C \cdot s_{0hc}/n_t$.

In order to correlate the concentration of adsorbed species with the work function measurement, the Topping Model is applied [102,107]. In light of the effect of the patch field in this measurement and assuming that hydrocarbon species are evenly distributed, i.e., they do not coalesce into islands on the surface, the measurements are performed in small patch regime. The change of the onset position therefore corresponds to a change of the surface averaged work function. According to the Topping model, the latter should be proportional to the concentration of adsorbed hydrocarbon species: $\Delta\Phi_{hc}\left(t\right) = A\left(1 - e^{-bt}\right) \propto n_{hc}$, with A encompassing all proportionality constants (n_0, dipole moment of adsorbed species, elemental charge, vacuum permittivity etc.).

In order to model the concentration of water species on the surface, the following sites are considered:

1. Free adsorption sites (Ti row sites), with concentration n_{free}.
2. H_2O occupied sites (H_2O molecule atop a Ti row site), with concentration n_{H_2O}.

3. H_2O chemisorption sites, i.e., adsorption sites from where water does not desorb due to hydrocarbon presence (presumably), with concentration n_{chem}.

In addition, the total concentration of adsorbed water is also defined, as $n_{total} = n_{H_2O} + n_{chem}$.

H_2O molecules will be adsorbed on free sites, where they remain until being desorbed, but can be also immobilized on the chemisorption sites. Note that the total concentration of adsorption sites (free, occupied and chemisorbed) is equal to the concentration of the unit cells $n_c = n_{free} + n_{chem} + n_{H_2O} \approx 5.2\times10^{14} cm^{-2}$. The rate of the change of n_{H_2O} is then equal to:

$$\frac{dn_{H_2O}}{dt} = \phi_{H_2O}\cdot s_{0H_2O}\frac{n_{free}}{n_t} - n_{H_2O}\cdot\alpha_{H_2O} =$$
$$\phi_{H_2O}\cdot s_{0H_2O}\frac{n_c - n_{chem} - n_{H_2O}}{n_t} - n_{H_2O}\cdot\alpha_{H_2O} \tag{6.3}$$

The left and right terms of the expression describe adsorption and desorption of water molecules from Ti rows, respectively. α_{H_2O} is the desorption rate of water molecules adsorbed on Ti rows, which can be expressed as $\alpha_{H_2O} = \nu\cdot e^{-\frac{E_{des}}{KT}}$, where E_{des} is the energy barrier for desorption, and ν is the oscillation frequency of adsorbed water molecules, expressed in Hz, i.e., the number of attempts of the molecule to leave the surface per second. ϕ_{H_2O} is the flux of water molecules hitting the surface from the gas phase, and can be calculated from the water partial pressure P_{H_2O} as $\phi_{H_2O} = P_{H_2O}\big/\sqrt{2\pi m_{H_2O}k_B T}$. s_{0H_2O} is the sticking coefficient at zero coverage for the adsorption of water on Ti row sites. With the goal of modeling the work function increase due to water desorption when the valve is closed, n_{chem} is calculated for each data set, using the first experiment of each set (1 min of water exposure) . It is presumed in this specific case that a very small amount of hydrocarbons have been adsorbed, which means that $n_{chem} \approx 0$, and thus $n_{total}(t_0) \approx n_{H_2O}(t_0)$, where t_0 is the time instant when the water valve is closed. Then, presuming that $n_{total}(t_0)$ is the same for all experiments in each system, which should be true assuming the surface is identical at the beginning of each experiment (they were prepared in the same way), $n_{chem} = n_{total}(t_0) - n_{H_2O}(t_0)$.

According to the Topping model, and considering that measurements are performed in the low patch regime, the change of the surface's average work function, corresponding to the change of the onset position, is proportional to the concentration of water molecules (dipoles) adsorbed on the Ti rows, and is given by:

$$\Delta\Phi_{H_2O} = -\frac{e}{\varepsilon_0}\mu_{H_2O}\cdot n_{H_2O} \tag{6.4}$$

where μ_{H_2O} is the dipole moment of the adsorbed water molecule, here taken to be 1.85 D [162]. It is also assumed that the concentration of water species is sufficiently low to disregard the depolarization term. This assumption can be confirmed later if the results obtained from the data fitting correspond to a relatively low coverage.

The first step into performing the quantitative analysis of the water desorption kinetics with the model presented above is to remove the contribution of the hydrocarbon adsorption to the work function change. By fitting the exponential equation describing $\Delta\Phi_{hc}(t)$ to the portion of the experiment with the slow work function drop, i.e. between the fast drop and the slow rise, constants A and b were calculated for the "dirty" and "clean" vacuum systems. The longer experiments were used for this calculation,"13 min" and "40 min", respectively. Afterwards, the hydrocarbon contribution was removed from the data by subtracting from it the values calculated with the fit. It should be noted that since the data used in the fitting process is still in the linear part of the exponential decay $(b \times t \ll 1)$, it is likely that the individual values of A and b determined in the fit are not correct. Nevertheless, the slope, equal to $A \cdot b$ (obtained from the approximation of the exponential function to the first two terms of the Taylor series expansion $f(t) = A(1-e^{-bt}) \approx f(0) + f'(0) \cdot t = Ab \cdot t$), should be accurate. Figure 6.8 shows the onset shift corresponding to the experimental performed on the freshly baked system, for a 40 min waiting time, before and after removal of the hydrocarbon contribution.

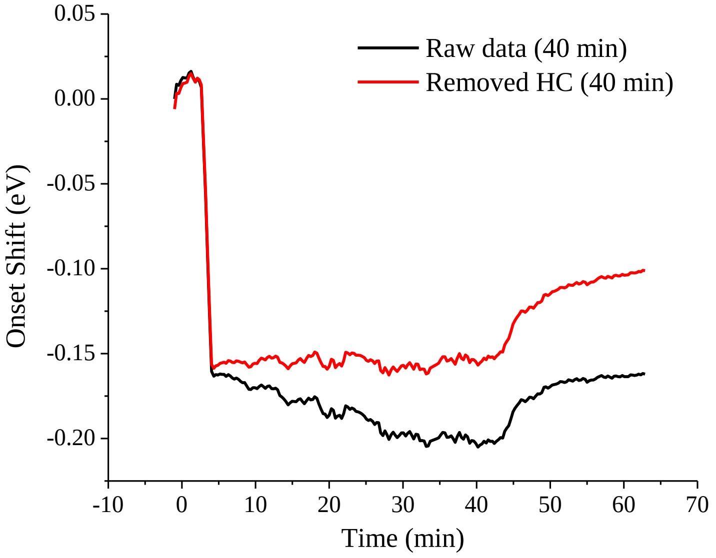

Figure 6.8 – Onset shift before and after removal of the hydrocarbon contribution, for the longer experiment performed in the freshly baked system

After the removal of the hydrocarbon adsorption contribution from the experimental results, it is now possible to quantify the kinetics of water adsorption on Ti rows. When the valve that controls the water flow is closed, its partial pressure begins to decrease, although rather slowly, due to the accumulation of water on the walls of the system (slower for longer exposures, due to more water being accumulated). Because of this, the value of ϕ_{H_2O} is time-dependent, and the differential equation (6.3) has to be solved numerically. $n_{H_2O}(t)$ is calculated with equation (6.4), and the values of s_{0H_2O}, α_{H_2O} and $n_{H_2O}(t_0)$ are then adjusted until the experimental and numerical results are in agreement. The process of matching the numerical model with the experimental results was performed manually, according to the procedure described ahead. Before the water valve is closed, the work function value is stable, and the concentration of water molecules n_{H_2O} is in an equilibrium state, determined by the value of the water partial pressure. To facilitate, the time scales are shifted so that $t_0 = 0$ for the 1 min experiment (see Figure 6.10). Then, combining equations (6.3) and (6.4), and considering $dn_{H_2O}(0)/dt = 0$, the value of the work function shift in its stable region is equal to

$$\Delta\Phi_{H_2O} = -\frac{e}{\varepsilon_0}\mu_{H_2O} \cdot \frac{\phi_{H_2O} \cdot k\left(n_c + n_{H_2O}(0) - n_{total}\right)}{n_t + \phi_{H_2O} \cdot k}$$

where $k = s_{0H_2O}/\alpha_{H_2O}$. An initial estimate of k and $n_{H_2O}(0)$ is then obtained by adjusting their values until the work function shift on the stable region, as well as its final value (i.e. when all of the non-chemisorbed water has been desorbed, which depends mainly on $n_{H_2O}(0)$) both match. Once k and $n_{H_2O}(0)$ have been determined in this way, the value of s_{0H_2O} is adjusted until the time-dependence of the rising slopes match (after the water valve is closed). If needed, the values of k and $n_{H_2O}(0)$ are then readjusted and the process is repeated. In the end, the desorption rate is calculated as $\alpha_{H_2O} = s_{0H_2O}/k$. Figure 6.9 illustrates the fitting process for the "5 min" experiment performed on the "clean" system.

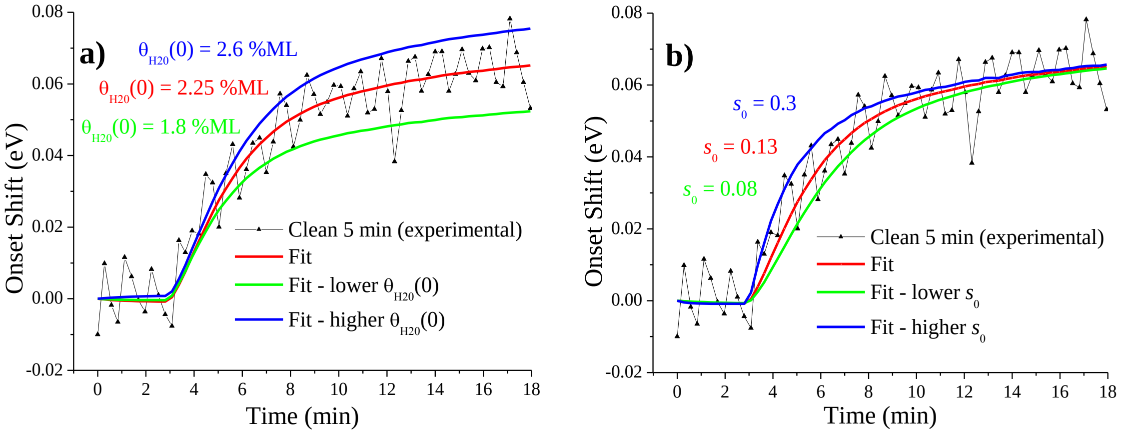

Figure 6.9 – Fitting process of the water adsorption model. In a), the fit using different water coverages at $t = 0$ (before the water vapour valve is closed) is shown, and *k* is adjusted for each fitting curve so that $dn_{H_2O}(0)/dt \approx 0$. In b), the fit using different sticking coefficients is shown.

In Figure 6.9 a), the fitting for different initial water coverages is shown, while *k* is adjusted so that $dn_{H_2O}(0)/dt = 0$. In Figure 6.9 b), having determined the values of $n_{H_2O}(0)$ and *k*, only the sticking coefficient is adjusted. It can be seen how this change has little influence on the final onset shift, which remains mainly dependent on the parameters previously determined. In each step of the process, the parameters are chosen to maximize the coefficient of determination, R^2.

The experimental results of the water desorption taken from those shown in Figure 6.7, with removed hydrocarbon contribution, and the corresponding final numerical fits obtained according to the process described above, are shown in Figure 6.10.

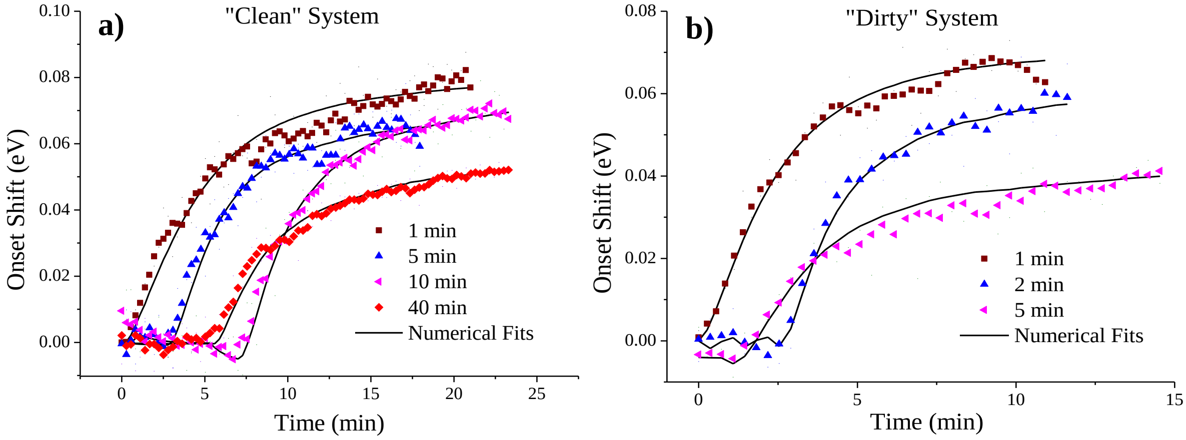

Figure 6.10 – Time-lapse of the onset shift associated with water desorption from experiments shown in Figure 6.7 a) and b), with the corresponding numerical results.

The best fitting parameters obtained for each data set are shown in Table 6.1. The initial coverage of water $\theta_{H_2O}(0)$ and the coverage of chemisorbed sites θ_{chem} are shown, instead of their concentration. These are calculated with respect to the unit cell concentration, $\theta_i = n_i/n_c$.

The ratio s_{0H_2O}/n_t used in the fit is shown, which can be interpreted as the equivalent to an adsorption cross section. The values of the sticking coefficient s_{0H_2O} can be calculated using the value of n_t for the TiO_2(110)-(1×1) surface, being $n_t = 2.08\times10^{15} cm^{-2}$ [2]. Additionally, the value of the energy barrier calculated from the desorption rate is presented, assuming an oscillation frequency of 1×10^{13} Hz.

Table 6.1 – Summary of fitting parameters for the numerical modeling of the water desorption experimental results

System	**Exposure**	s_{0H_2O}/n_t (cm^2)	α_{H_2O} (s^{-1})	$\theta_{H_2O}(0)$	θ_{chem}	E_{des} (eV)
Clean	1 min	2.7×10^{-17}	5.6×10^{-3}	2.4 %	0 %	0.90
	5 min	6×10^{-17}	1.3×10^{-2}	2.25 %	0.05%	0.88
	10 min	7×10^{-17}	1.4×10^{-2}	2.4 %	0 %	0.87
	40 min	7×10^{-17}	1.6×10^{-2}	1.9 %	0.5%	0.87
Dirty	1 min	4.5×10^{-17}	1.1×10^{-2}	2.1 %	0 %	0.88
	2 min	1×10^{-16}	2.3×10^{-2}	1.9 %	0.2 %	0.86
	5 min	5×10^{-17}	1.5×10^{-2}	1.4 %	0.7 %	0.87

A first analysis of these results shows that the calculated energy barrier for desorption E_{des} is in excellent agreement with DFT calculations, which indicate a value of 0.86 eV [13]. It should however be noted that this method of calculation relies in part on the value of the oscillation frequency assumed, which can't be accurately known for this specific case, and is also quite sensitive to the value of the temperature used in the calculation (the temperature is measured with a thermocouple wire on the sample holder, not on the sample's surface). Hence the energy barrier here determined, despite its match with theoretical calculations, is considered as an approximation. Considering the uncertainty related to the fitting adjustment of the desorption rate to be approximately 10%, a temperature uncertainty at the surface of ±5 K, and an oscillation frequency in the range 5×10^{12} to 2×10^{13} Hz (half and twice the value initially considered), the desorption energy is estimated to have a final uncertainty of approximately ± 0.03eV.

There is a correlation between θ_{chem} and the expected amount of hydrocarbon contamination. On the "clean" vacuum system, the value of θ_{chem} is close to 0% up to 10 min exposures, rising to 0.5 % after a 40 min exposure. On the "dirty" vacuum system, this value increases more rapidly, rising to 0.7 % after only 5 min, confirming that a significant portion of the adsorbed water molecules is affected by hydrocarbon presence. There appears to be an increasing trend on both s_{0H_2O} and α_{H_2O} with the value of θ_{chem}, although the results are somewhat scattered for this to be clear, and a more extensive experimental campaign would be required to confirm it.

There is a second time-dependent effect that should affect the bonding of water molecules adsorbed on Ti rows, which is related to the separation of OH groups on oxygen rows. It was shown that the main contribution affecting desorption of water from Ti rows on these experiments is related to hydrocarbon adsorption. However, it is still possible that the preferential bonding of water molecules to OH groups formed from water dissociated on BOVs [131,134] also plays a role in desorption kinetics. This contribution, which was not taken into account in this analysis, could perhaps lead to changes of s_{0H_2O} or α_{H_2O}. Other limitations of the model include the fact that, according to DFT calculations, the binding energy of the water molecules on Ti rows depends on their proximity to each other. When two water molecules travelling along the same row meet, it is possible for one water molecule to jump over the other, as shown in Figure 6.11 [13].

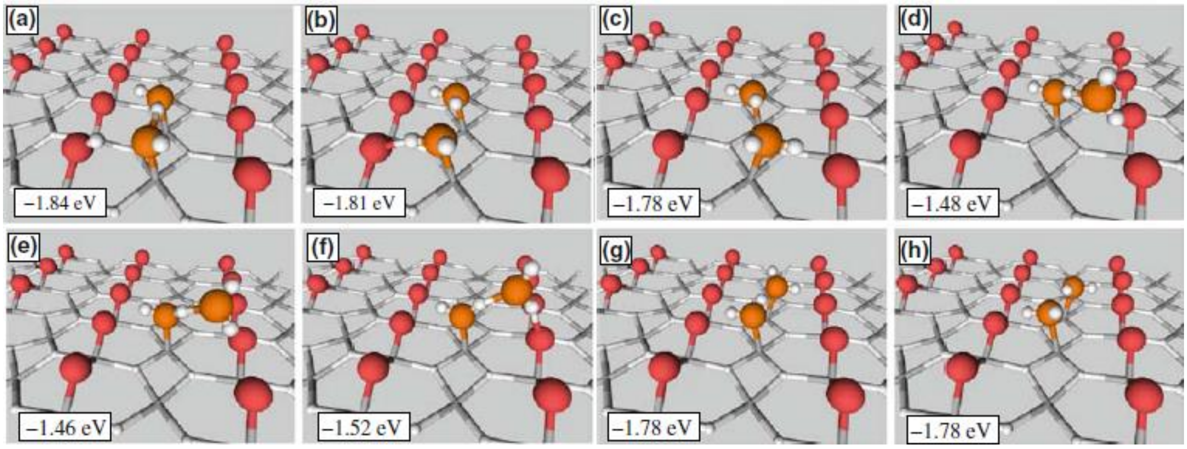

Figure 6.11 - Configurations and adsorption potential energies of the adsorbed water dimer on $TiO_2(110)$. a–c Various forms of initial state before a diffusion event. d–f Various transition states for one water molecule jumping over the other. g-h Configuration after the jump. Adapted from [13].

During the hopping stage (d-f), the binding energy of each molecule decreases from 0.86 eV (binding energy when isolated) to 0.73 eV (1.46 eV total of the dimer), representing a significant decrease of the residence time from 30 to 0.2 seconds. When in this configuration, it is thus expected that the water molecules will have higher desorption rate. The probability for the formation of a water molecule dimer increases with the concentration of adsorbed molecules. This process of desorption was not considered in the kinetics model presented above. Another part of the model which might not be accurate is the assumption that the water dipole is vertically oriented. DFT calculations show a variety of different orientations of the water molecule, and hence the dipole moment assumed in the calculation of the water concentration may not be accurate. Assuming lower values of the dipole moment (i.e. an orientation which is not entirely vertical) would lead to higher water concentrations in the fitting results.

Finally, it is possible to estimate the concentration of water molecules adsorbed on BOV sites by performing further analysis of the experimental results. The work function drop due to water adsorption on both BOV and Ti row sites is about 0.16 eV (see Figure 6.7 b)), and the work function recovery (desorption of water from Ti rows) totals about 0.08 eV (in the "cleanest" situation). The 0.16 eV drop can thus be separated into two contributions, 0.08 eV from water on Ti rows, and the remaining 0.08 eV from water on BOV sites. From the water dissociation on BOV sites, two OH groups are formed, next to each other. The work function change associated with this adsorption process is described by the Topping model as:

$$\Delta\Phi = -\frac{e}{\varepsilon_0} \cdot n_{H_2OonBOV} \cdot \left(\frac{2\mu_{OH}}{1+\frac{\alpha}{r^3}} - \mu_{BOV} \right) \tag{6.5}$$

where μ_{OH} is the dipole moment of the OH group, equal to 1.66 D [163], α is the polarizability of the OH dipole, equal to 4.5 Å^3 [164], r is the distance between the two OH dipoles, equal to 1.96 Å (obtained from the unit cell size, as shown in Figure 5.3), and μ_{BOV} is the dipole moment associated with a BOV site. One way to estimate this value is to take the work function difference between the "perfect" surface (one with ~0% BOVs) and the highly reduced surface (~10% ML coverage of BOVs), and applying the Topping model in the same way. From the experimental results obtained in the course of this work, the estimated work function difference between these two surfaces is about 0.3 eV, i.e., between a nearly stoichiometric surface (one without BOVs, but also without excess of oxygen species such as oxygen adatoms), and the highly reduced surface. Here it is assumed that the highly reduced surfaces, obtained through annealing in UHV at higher temperatures (~600 ºC) or by electron bombardment, have a BOV coverage of ~10%. A value of 1.44 D is thus obtained for the dipole moment of the BOV site, which in turn leads to a calculated coverage of water on BOV sites, using equation (6.5), of ~6.6% ML. This value perfectly fits with the expected concentration of BOV sites in a reduced TiO_2(110)-(1x1) rutile surface (<10% ML) [2], as should be the case for the surfaces used in these water adsorption experiments, which were prepared by annealing in UHV. Therefore, the model findings (e.g. concentration of BOVs, desorption energy of water on Ti rows) are consistent with the current understanding of the TiO2(110)-(1x1) rutile surface.

Despite the many limitations of the model here presented, with some described above, it was possible to quantify the kinetics of water desorption, leading to an acceptable fit between the experimental results and the numerical model. It was shown that the hydrocarbon contamination plays an important role in the adsorption/desorption of water on the TiO2 surface. The parameters obtained from the fit are apparently in very good agreement with the expected values, as the desorption energy obtained for the water molecule on Ti rows, and to our knowledge experimentally obtained for the first time, corresponds very well to that of the DFT calculations. In addition, the equilibrium concentration of H_2O molecules adsorbed on Ti rows at room temperature is estimated from the experiments. It should be emphasized that such a quantity cannot be obtained by means of the most frequently used experimental techniques applied on this system, namely, STM under UHV conditions and UPS.

6.3.3 Using Work Function Change to Follow Temperature-Induced Water Desorption

In order to further strengthen the versatility of the onset measurement technique as a means to perform surface analysis, this technique was used to monitor the temperature-induced desorption of water from the rutile TiO_2(110)-(1×1) surface. The sample was exposed to water at room temperature, followed by heating up to 390 K while monitoring the onset position, and the results were compared with the same experiment performed on the clean surface. Both results are shown in Figure 6.12.

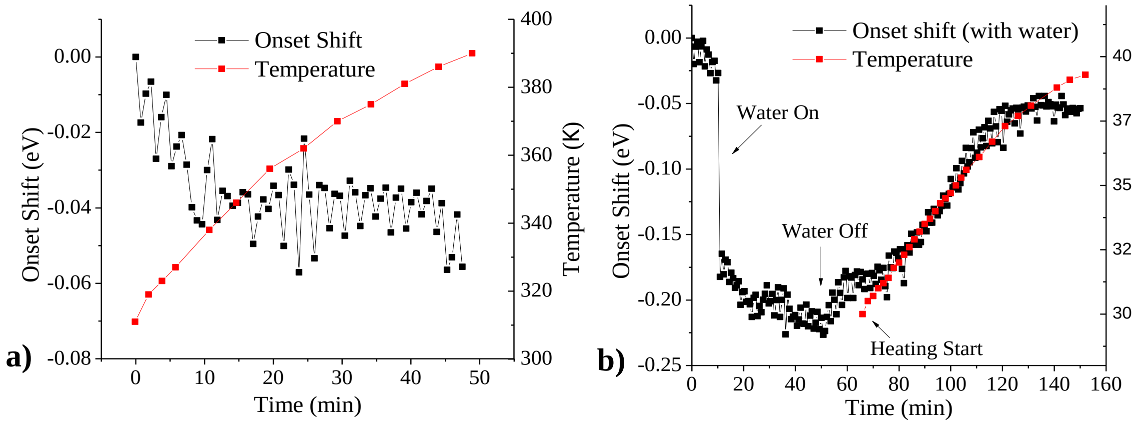

Figure 6.12 – Onset shift during sample heating up to 120 ºC, for the a) clean surface, and b) water exposed surface.

Heating the clean surface (Figure 6.12 a)) shows no significant change of the work function, apart from the initial slow decrease that is likely due to hydrocarbon adsorption, which appears to be slowed down at higher temperatures (>340 K). Heating the water exposed surface resulted in a large increase of the work function, associated with water desorption. It was also observed that the work function stops increasing at the ~370 K mark, a point at which all molecularly adsorbed water has apparently been desorbed. This value is perhaps associated with the minimum position of the H_2O signal measured on TPD experiments (see Figure 5.7 b). The same TPD experiment shows that, at higher temperatures, OH groups recombine to desorb as H_2O (TPD peak centred at 520 K). While it would also be interesting to measure the work function change associated with this desorption, it was not possible to bring the sample to this temperature with the current heating method, due to the reasons already presented in section 6.1. Furthermore, while these results appear to agree with TPD experiments, further analysis needs to be performed to reach definite conclusions, as TPD results depend on the temperature slope, and it is not guaranteed that the work function change is single-handedly attributed to water desorption, as other temperature-induced effects, possibly affected by water presence, could be taking place at the surface.

6.4 Adsorption of Oxygen on the TiO_2(110)-(1×1) Surface

Work function increase is expected when adsorbing oxygen on the rutile TiO_2(110)-(1×1) surface, due to the healing of BOVs and adsorption of O_a on Ti rows, which results in the neutralization of surface dipoles oriented towards the vacuum (the electronegative oxygen species are positioned atop the positive titanium ions). Since O_a species have a high activation energy for surface diffusion/desorption, the adsorption processes of the O_2 molecule at room temperature can be described by a simpler model, compared to H_2O adsorption. The adsorption/dissociation of an O_2 molecule will be considered to take place only when directly impacting a BOV site. This is a simplification, as the dissociative adsorption of O_2 on Ti rows has also been observed, although with a reduced probability, which is also possibly associated with the concentration of sub-surface Ti interstitials [11]. This results in a considerably slower adsorption rate when compared to water, and it should then be possible to quantify the adsorption dynamics of oxygen exposure by following the work function change in real time (with water adsorption experiments, only the time dependence of water desorption was analysed). Additionally, if the TiO_2 surface is prepared with different initial concentrations of BOVs, it should be possible to observe a correlation between the saturated increase of the work function after O_2 exposure, and the initial BOV concentration of the surface (i.e., the surface reduction level). This concentration could be estimated by performing XPS analysis of the Ti 2p peak. The healing of BOVs by oxygen exposure should result in a decrease of the Ti^{3+} contribution. If the XPS system proves to have sufficient sensitivity, it should be possible to establish a correlation between the total increase of the work function, and the Ti^{3+} contribution from the Ti 2p peak. With this in mind, the TiO_2 surface was initially prepared by annealing in O_2 atmosphere, thus creating a near-stoichiometric surface where O_2 adsorption is not thermodynamically favourable. Subsequently, the surface was annealed in UHV at increasingly high temperatures, producing surfaces with increasing surface reduction levels, which correlates with BOV concentration (also Ti interstitials, presumably). For each annealing cycle, the surface was exposed to O_2, while monitoring both the onset shift in real time and the XPS Ti 2p peak before and after exposure.

6.4.1 Kinetics of Oxygen Adsorption

At room temperature, the O_2 molecule is dissociatively adsorbed on BOVs located on the rutile TiO_2(110)-(1×1) surface. Describing this adsorption process with a Langmuir adsorption model [27], as performed for the water adsorption experiments presented in section 6.3.2, with zero desorption rate, the rate of adsorbed oxygen species is:

$$\frac{dn_{O_{BOV}}}{dt} = -\frac{dn_{BOV}}{dt} = \phi_{O_2} \cdot n_{BOV} \cdot \sigma_{O_2} \tag{6.6}$$

where $n_{O_{BOV}}$ and n_{BOV} are the surface concentrations of healed BOV and BOV sites, respectively (note that each adsorbed O_2 is dissociatively adsorbed, and will in turn correspond to one healed BOV and one oxygen adatom O_a, so that $dn_{O_{BOV}} = -dn_{BOV} = dn_{O_a}$). ϕ_{O_2} is the flux of oxygen molecules hitting the surface from the gas phase, and can be calculated from the O_2 partial pressure P_{O_2} , which was kept constant during the experiment, as $\phi_{O_2} = P_{O_2} \big/ \sqrt{2\pi m_{O_2} k_B T}$. σ_{O_2} is what can be called the adsorption cross section for the O_2 molecule, in cm^2. The product $n_{BOV} \cdot \sigma_{O_2 ads}$ corresponds to the probability of adsorption P_{ad} , which can also be expressed as $P_{ad} = s_{0O_2} \cdot f_{BOV}$, where f_{BOV} is the fraction of the area occupied by BOV sites, equivalent to the probability for O_2 molecules to encounter an adsorption site when hitting the surface, and s_{0O_2} is the sticking coefficient at zero coverage. By solving the above differential equation, the following time dependence for the coverage of BOVs and adsorbed oxygen species during exposure is obtained:

$$n_{BOV}\left(t\right)=n_{BOV}(0)e^{-\phi_{O_2}\cdot\sigma_{O_2}\cdot t} \tag{6.7}$$

$$n_{O_{BOV}}\left(t\right)=n_{O_a}\left(t\right)=n_{BOV}(0)\left(1-e^{-\phi_{O_2}\cdot\sigma_{O_2}\cdot t}\right) \tag{6.8}$$

where $n_{BOV}(0)$ is the coverage of BOV sites (adsorption sites) at the beginning of the experiment. According to STM analysis [123], nearly half of BOVs can remain on the surface after O_2 adsorption saturation. In this case, the adsorption of one O_2 molecule can be associated with the neutralization of two adsorption sites (one BOV is healed, and the other is "neutralized" and no longer considered as an adsorption site). In this case, equation (6.6) is re-written as:

$$\frac{dn_{O_{BOV}}}{dt}=-\frac{dn_{BOV}}{dt}=-\frac{1}{2}\frac{dn_{ad}}{dt}=\phi_{O_2}\cdot n_{ad}\cdot\sigma_{O_2} \tag{6.9}$$

where n_{ad} is the concentration of adsorption sites, with $n_{BOV}\left(0\right)=n_{ad}\left(0\right)$. By solving the differential equation above, $n_{ad}\left(t\right)=n_{BOV}\left(0\right)e^{-2\phi_{O_2}\sigma_{O_2}t}$ is obtained. Then, by considering $2\cdot dn_{O_{BOV}}/dt=-dn_{ad}/dt$ and $2\cdot dn_{BOV}/dt=dn_{ad}/dt$, equations (6.7) and (6.8) are recalculated as:

$$n_{BOV}\left(t\right)=\frac{n_{BOV}\left(0\right)}{2}\left(e^{-2\cdot\phi_{O_2}\cdot\sigma_{O_2}\cdot t}+1\right) \tag{6.10}$$

$$n_{O_{BOV}}\left(t\right)=\frac{n_{BOV}\left(0\right)}{2}\left(1-e^{-2\cdot\phi_{O_2}\cdot\sigma_{O_2}\cdot t}\right) \tag{6.11}$$

It should be also stated that the above expressions are valid only in the case of constant oxygen flux (partial pressure). Otherwise, the set of differential equations should be solved numerically.

6.4.2 Adsorption of O_2 as a Function of the Surface Reduction State

The onset shift due to oxygen adsorption was measured for surfaces prepared with different reduction levels. The results obtained for three different surfaces are shown in Figure 6.13, as a function of total oxygen exposure.

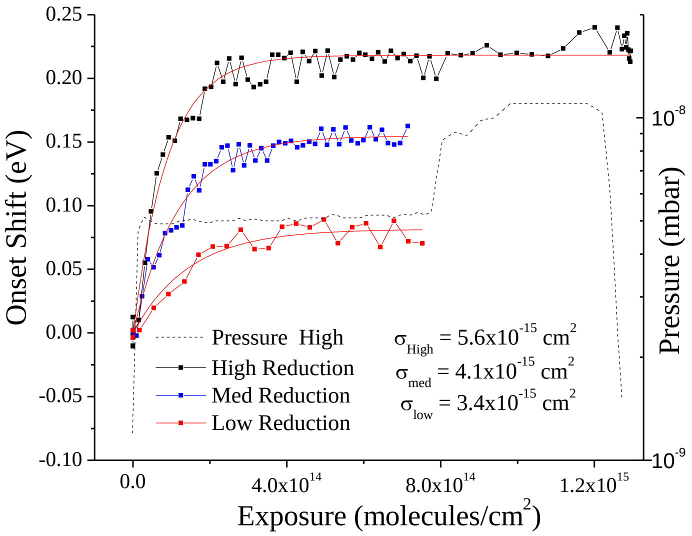

Figure 6.13 - Onset shift as a function of oxygen exposure for different surface reduction levels. The pressure values correspond to the pressure evolution for the high reduction case

The $TiO_2(110)$-(1×1) sample was exposed to a constant oxygen partial pressure of 5×10^{-9} mbar, with each curve corresponding to samples prepared with different surface reduction levels. As expected, the work function increases with exposure, reaching different saturation levels depending on the surface reduction level. In the case of the highest reduction, the oxygen pressure was additionally increased after reaching the saturation level (shown as a dotted line), and later on reduced to zero. No change of the work function during this pressure change is observed, suggesting that the concentration of adsorbed species after saturation does not depend on the oxygen pressure (all adsorption sites are filled, and there is no measurable desorption at room temperature, which would affect the equilibrium concentration of adsorbed oxygen species). Contrary to the case of the water exposure, there is no desorption, as assumed in the kinetics model presented in the previous section. Since the work function measurement is performed in the small patch regime (the average work function change is proportional to $n_{O_{BOV}}(t)$), and the oxygen flow is constant, the results were fitted to equation (6.11). The cross-sections for oxygen adsorption obtained for the different reduction levels are also shown in Figure 6.13. The fact that this value increases with the reduction level of the surface, and that it is two to three times higher than the area occupied by a unit cell (2×10^{-15} cm^2) suggests that the process does not depend solely on the concentration of BOVs, as a cross-section value of this magnitude implies a sticking coefficient larger than 1. The large value of the cross section could be due to oxygen molecules being able to probe more than a single BO site (for example through weak adsorption and subsequent surface diffusion). The fact that this value is also changing with the reduction level could be an indication that there are additional adsorption sites that become available at higher reduction levels. These could originate from the presence of Ti interstitials in the sub-surface region (which should increase with the reduction level, together with BOVs), which play a role in the adsorption/dissociation of the O_2 molecule, providing the necessary charge for bonding of O_a pairs on Ti rows, and for the dissociative adsorption of the O_2 molecule on Ti rows [11,12].

The XPS spectrum of the Ti 2p line taken before and after exposure on the highly reduced surface is shown in Figure 6.14. As expected, the intensity of the Ti^{3+} contribution decreases when exposed to O_2, suggesting the healing of surface BOVs by O_2 dissociation (each BOV is associated with two Ti^{3+} ions).

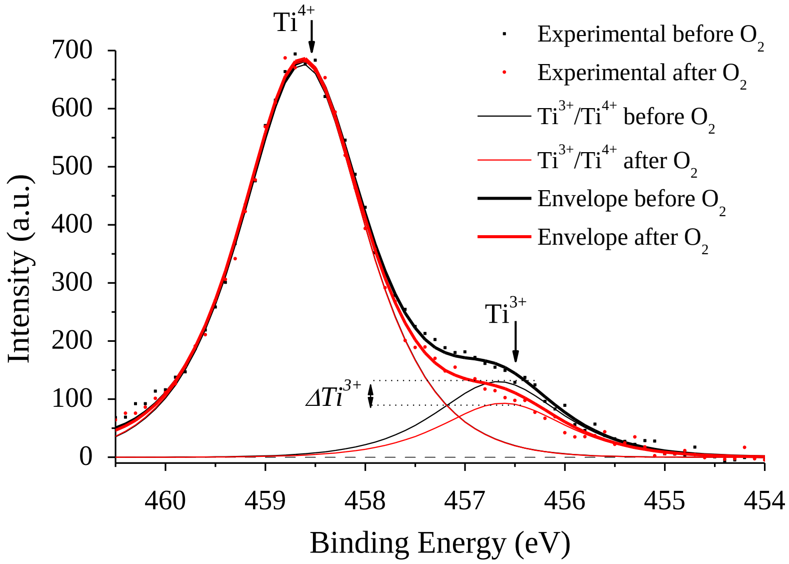

Figure 6.14 –XPS spectra of the Ti $3p_{3/2}$ peak before and after oxygen exposure, taken from the highly reduced surface, illustrating the decrease of the Ti^{3+} contribution.

It is not possible to accurately estimate the concentration of surface defects based on the initial relative contribution of the Ti^{3+} peak, since it is related to both BOVs and Ti interstitials. In addition, the depth distribution of Ti interstitials in the sub-surface layers is unknown. However, the change of the Ti^{3+} contribution (equal to ΔTi^{3+}, which corresponds to the difference between the areas of each Ti^{3+} contribution) after O_2 exposure should be well correlated with the concentration of BOVs. The total increase of the work function for differently reduced surfaces should thus be proportional to ΔTi^{3+}. This dependence was explored in a set of experiments, in which the onset shift was monitored for a wide variety of surfaces prepared with different initial reduction levels during O_2 exposure. The saturated work function change vs. ΔTi^{3+} is shown in Figure 6.15, for the surfaces produced with different reduction levels.

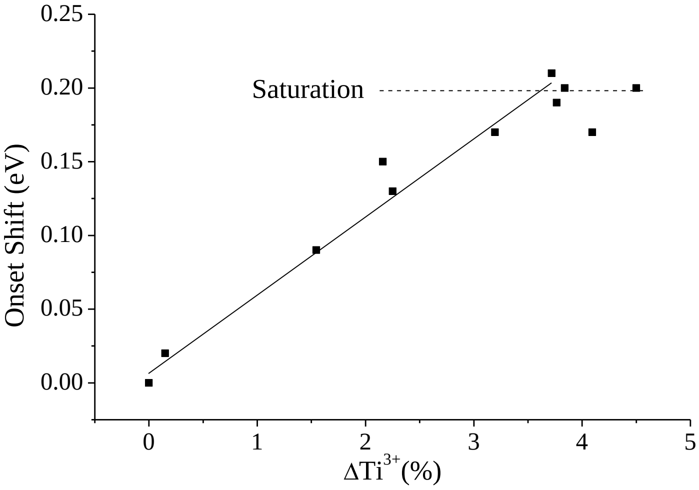

Figure 6.15 – Total onset shift vs. change of the relative Ti^{3+} contribution obtained from XPS analysis of the Ti 3p peak.

The dependence between the two quantities is roughly linear up to an onset shift of ≈ 0.2 eV for $\Delta Ti^{3+} \approx 3.5\%$ at which point the work function increase appears to be saturated, while larger ΔTi^{3+} values are still observed. As it was previously established, both the healing of BOVs and the adsorption of O_a are associated with an increase of the work function (healing BOVs neutralizes a dipole oriented towards the vacuum, while O_a atop Ti rows can be seen as a dipole in the opposite direction from that of BOVs). With this in mind, an explanation for the observed behaviour could be in the possible interaction of O_a species with sub-surface Ti interstitials. It is reasonable to expect that the surfaces with higher reduction levels also have a higher concentration of these species in the near-surface region (second layer). Indeed, the value of the Ti^{3+} concentration left after oxygen has been adsorbed, obtained from the XPS measurements, is higher for the larger onset shifts, indicating higher Ti interstitial concentrations for the surfaces with higher BOV concentrations, although with unknown depth distribution. The adsorption of O_2 could be inducing their segregation and subsequent reaction with O_a species, neutralizing their associated dipole (with the creation of new (1×1) stoichiometric regions), while also increasing ΔTi^{3+}.

As was previously mentioned in section 5.1, this process is known to be in the origin of fresh (1×1)/(1×2) layers of the $TiO_2(110)$ surface, only at elevated temperatures, typically when annealing in O_2 atmosphere. Indeed, the dissociative adsorption of O_2 without the healing of BOVs (dissociation into an O_a pair on Ti rows) has been found to be more likely on highly reduced surfaces, and the diffusion of Ti interstitials towards on these surfaces also occurs at comparatively lower temperatures (down to 360 K) [12]. It appears that this experiment supports this observation, and that Ti interstitials play a comparatively more important role on O_2 adsorption on highly reduced surface, as was also concluded from the previous analysis, which had revealed a relatively large cross-section value for oxygen adsorption on BOV sites, with its value increasing with the surface reduction level.

6.5 Interaction between Adsorbed Oxygen and Water

The analysis of the interaction between adsorbed oxygen and water species was tested by exposing the rutile TiO_2(110)-(1×1) surface to these gases in alternating cycles. The time-lapse of the onset shift during this alternated exposure is shown in Figure 6.16. The exposure was performed on a highly reduced surface (annealed in UHV), in order to maximize the number of adsorption sites.

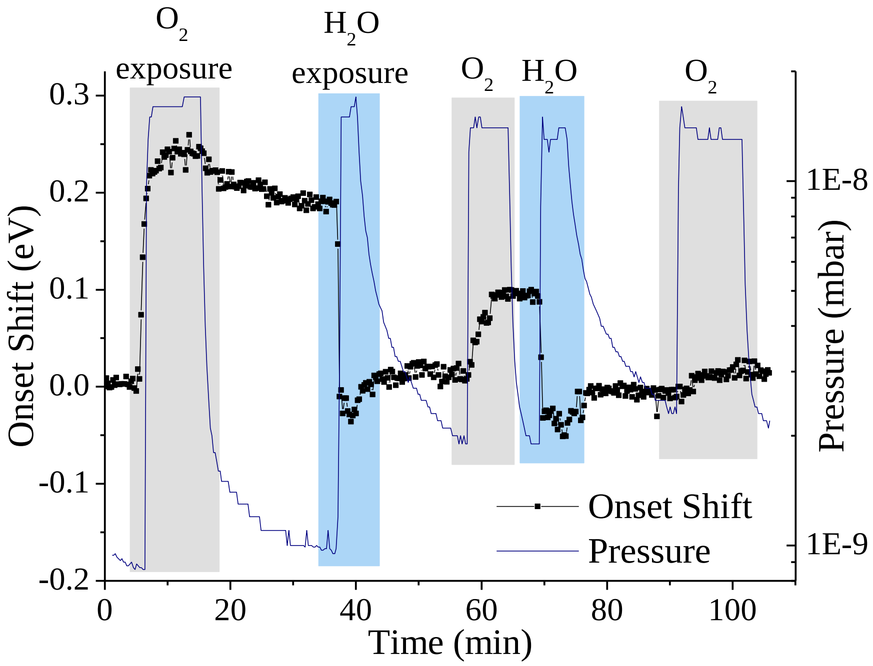

Figure 6.16 – Time evolution of the onset shift during alternate exposure of the reduced surface to oxygen and water.

The initial O_2 exposure results in an onset increase of ~ 0.24 eV, which is slightly above the previously obtained saturation for O_2 adsorption. This could be due to the increased age of the crystal used in this experiment (higher total number of annealing cycles and consequentially higher reduction level), which started to show a light blue hue. Subsequently, and despite the fact that adsorption on BOVs should be saturated after O_2 exposure, a large and fast decrease of the work function when exposing the surface to water is still observed. This is in line with the STM observations that H_2O molecules adsorbed on Ti rows and OH_b groups will interact with O_a species to form OH_t or HO_2 [122], resulting in a decrease of the work function. This is further supported by the fact that a second exposure to oxygen will still yield a considerable work function increase, suggesting that more reaction paths are created for the O_2 interaction following water exposure (all adsorption sites for O_2 were saturated before water exposure), specifically the reaction with OH_t and OH_b groups, as described in section 5.2.3. It appears that for each O_2/H_2O cycle, the surface alternates between higher concentrations of O_a and OH species, possibly reaching an eventual equilibrium level where most BOVs have been healed, and very few adsorption/reaction sites remain (see last exposure to oxygen).

Although the fast work function decrease after water exposure was related to its dissociation on BOV sites, it is seen here that this is likely not always the case. Other (fast) adsorption paths may also be present on the surface instead. For example, the fast decrease of the work function was also observed on the stoichiometric surface (prepared in O_2 atmosphere), with a total shift that is comparable to that of the reduced surface. If very few BOVs exist on this surface, this adsorption has to be linked with other adsorption sites (surface defects). STM observations have revealed that the surface prepared in O_2 atmosphere will have a considerable density of steps, due to the formation of fresh (1×1) islands by reaction of O_a with Ti interstitials segregated to the surface during the thermal annealing. STM and DFT studies have showed that step edges are associated with a second channel for dissociative adsorption of water [165,166], which might explain the observed behaviour.

In general, STM analysis tends to look at what happens on the surface on large terrace sites. In turn, the work function analysis here performed provides averaged information of the whole surface, possibly revealing processes that have been overlooked by STM.

6.6 ESD of Oxygen Species

An initial, qualitative experiment was performed to show the possibility to detect the electron stimulated desorption of both BO and O_{ad} species from the $TiO_2(110)$-(1×1) rutile surface by measuring the onset shift. The TiO_2 sample was initially annealed in O_2 atmosphere (1×10^{-7} mbar) to create a nearly perfect surface. As it was discussed in Section 6.2, exposure of this surface to O_2 does not affect the sample’s work function. The surface was bombarded with 45 eV electrons for 1 minute, at 1.5 µA, followed by O_2 exposure at a pressure of 1×10^{-8} mbar. The measurement of the onset position has been interrupted during electron bombardment. The onset shift measured during this experiment is shown in Figure 6.17. As expected, the creation of BOVs caused by ESD had the effect of decreasing the work function, with the onset shifting towards lower kinetic energies for ~0.15 eV following electron bombardment. The Ti 2p XPS peak was measured before and after the bombardment, and revealed a small increase of the Ti^{3+} contribution (similar to the one shown below in Figure 6.20 b)) which is also an indication that surface defects (mainly BOV sites) have been created. These BOV sites will then act as adsorption/dissociation sites for the O_2 molecule, as verified by the relatively large increase of the work function following the first O_2 exposure. As stated, exposing this surface in its initial condition to O_2 does not result in an observable change of the work function. The oxygen adsorption that is observed, i.e. the onset increase during exposure to O_2 is therefore attributed to the previous creation of BOV sites by electron bombardment.

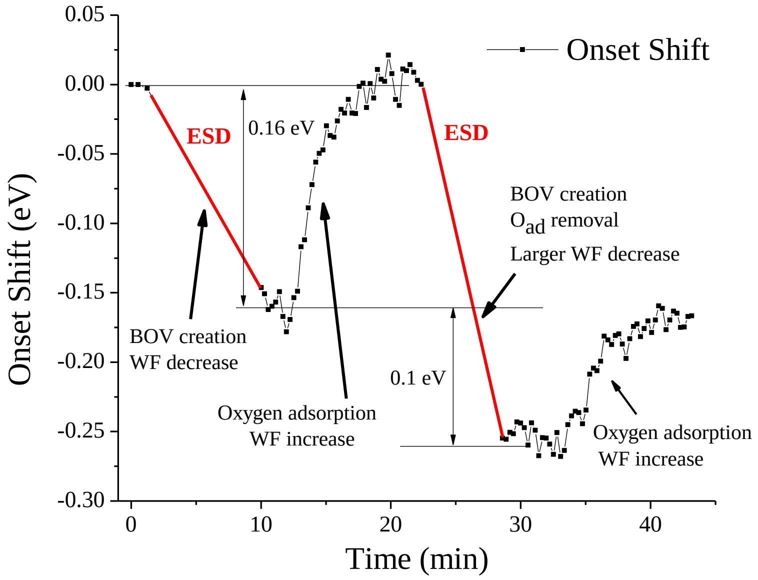

Figure 6.17 – Onset shift during electron bombardment of the $TiO_2(110)$ surface prepared in O_2 atmosphere, followed by exposure to O_2 at 1×10^{-8} mbar, twice. Surface bombarded by 45 eV electrons, 1.5 µA, for 1 minute.

When the surface was bombarded with the same electron fluence and energy for the second time, the overall onset shift was -0.25 eV, i.e. ~0.1 eV more than after the first bombardment. It is proposed that this larger shift is due to the additional presence of O_{ad} species on the surface during the second bombardment, which should have a higher ESD cross section than BO species, and a similar contribution to the average work function (see section 5.3.2). Exposing the surface to O_2 for a second time caused an onset shift of 0.1 eV, i.e. 0.06 eV less than with the first exposure. The smaller shift can be due to fewer BOV sites being produced relative to the first bombardment, and that some amount of O_{ad} species may still be present on the surface.

The reason for the creation of fewer BOV sites is that the surface is already defective before the second bombardment, since only half of BOVs are healed during O_2 exposure, as mentioned in section 5.2.2. Consequently, the presence of Ti^{3+} in the surface region decreases the ESD cross section for oxygen species, as already discussed in accordance to the Kotani-Toyozawa mechanism of oxygen desorption in section 5.3.2. Since bombardment will now create less BOVs, with some already being saturated from the O_{ad} that were not removed, the second exposure to O_2 results in an overall smaller increase of the work function, as fewer molecules are adsorbed.

The same experiment was performed on the TiO_2(110)-(1×1) surface prepared by annealing in UHV, thus creating a surface with a certain initial amount of BOVs. The onset shift is shown in Figure 6.18. Due to the presence of BOVs prior to electron bombardment, the onset shift caused by ESD is now only -0.1 eV, i.e. 0.06 eV smaller than in the previous experiment. The higher number of BOVs now present on the surface results in more adsorbed oxygen species during O_2 exposure, with a total shift of 0.25 eV. Not only is this shift larger than the one obtained in the first experiment (see Figure 6.17), it is also larger than the previously obtained O_2 adsorption saturation of ~0.2 eV (see Figure 6.15).

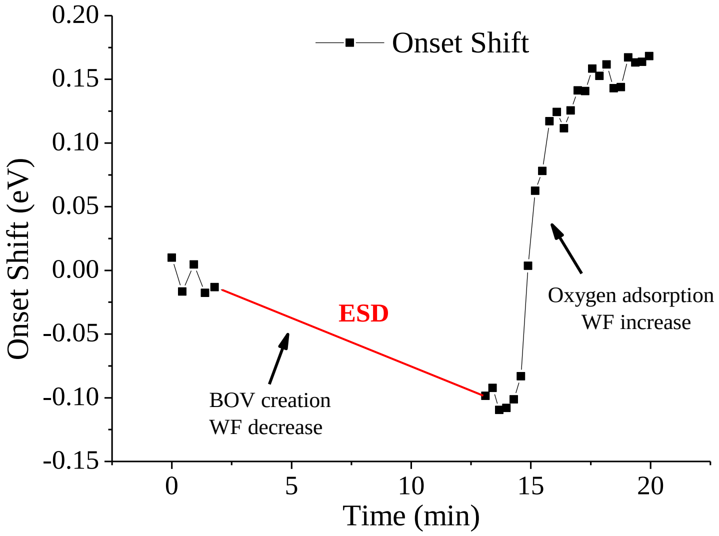

Figure 6.18 - Onset shift during electron bombardment of the TiO_2(110) surface prepared in UHV, followed by exposure to O_2 at 1×10^{-8} mbar. Surface bombarded by 45 eV electrons, 1.5 µA, for 1 minute

From this result it can also be said that the highest concentration of BOVs obtained simply by annealing in UHV is never as high as that of the electron bombarded surface, and ESD can be thus used to create a more defective surface in a controlled manner. This result is also in accordance with STM observations as mentioned in section 5.3.2.

The relatively large onset shifts that were obtained in these experiments, caused by an electron bombardment of moderate intensity, shows that it should be possible to perform this measurement as a function of electron fluence, and obtain ESD cross sections from the work function time/fluence dependency.

6.6.1 ESD Kinetics of Oxygen Species

The removal rate of bridging oxygen species from the $TiO_2(110)$-(1×1) surface during electron bombardment, i.e. the change of BO species concentration n_{BO} with time, is:

$$\frac{dn_{BO}}{dt} = -\varphi\sigma_{BO}n_{BO} \tag{6.12}$$

where φ(cm^{-2}s^{-1}) is the electron flux and σ_{BO} (cm^2) is the ESD cross section of BO species. The cross section σ_{BO} can be further defined as $\sigma_{BO} = P_{BO}I_{BO}$, where I_{BO} (cm^2) is the cross section for core hole creation (ionization), and P_{BO} is the probability of desorption following the excitation process. For the stoichiometric surface, $n_{BO}(0) = n_0$, where n_0 is the density of the (1×1) unit cell ($n_0 = 5.2\times10^{14}$ cm^{-2}). Solving the above differential equation results in the following expression for $n_{BO}(t)$:

$$n_{BO}(t) = n_O e^{-\varphi\sigma_{BO}t} \tag{6.13}$$

The concentration of BOVs as a function of bombardment time can also be quantified:

$$n_{BOV}(t) = n_0 - n_{BO}(t) = n_0\left(1 - e^{-\varphi\sigma_{BO}t}\right) \tag{6.14}$$

It should be stressed that this simplified model does not consider effects such as the decrease of the cross-section with the concentration of BOVs, or other effects that occur on the surface when the BOV concentration is increased above a certain level, such as surface reconstruction or migration from the sub-surface layers. As such, it should only be valid for very small BOV concentrations.

Assuming that, besides BOVs, no other defects are created during electron bombardment, the time dependence of the average work function is:

$$\Phi_{avg}(t) \;=\; f_{sub}\Phi_{sub} + f_{BO}(t)\Phi_{BO} \;+\; f_{BOV}(t)\Phi_{BOV} \tag{6.15}$$

where Φ_{sub} is the local work function of the substrate (the portion of the surface that is neither BO or BOV), Φ_{BO} and Φ_{BOV} are the local work functions of BO and BOV sites, respectively. The local work function of each site is weighted by the surface fraction occupied by the respective species, with $f_{BO}(t) = A_{BO}n_{BO}(t)$, $f_{BOV}(t) = A_{BO}n_{BOV}(t)$, and $f_{sub} = 1 - (f_{BO} + f_{BOV})$. A_{BO} is the area of a single BO/BOV site. Using the radius of the O^{2-} ion in bulk TiO_2 as a reference ($r_{O2-} = 1.4$ Å [2]), $A_{BO} \approx 6.2\times10^{-16}$ cm^2. Assuming the measurement is always performed in the small patch regime, the onset shift will be equal to the average work function difference, as shown in chapter 4:

$$\begin{gathered}\Delta onset(t) = \Phi_{avg}(t) - \Phi_{avg}(0) = \\ \Delta\Phi_{BO} n_0 A_{BO}\left(e^{-\varphi\sigma_{BO}t} - 1\right) \approx \\ 0.32\Delta\Phi_{BO}\left(e^{-\varphi\sigma_{BO}t} - 1\right)\end{gathered} \tag{6.16}$$

With $\Delta\Phi_{BO} = \Phi_{BO} - \Phi_{BOV}$. Considering electron bombardment of a surface with an initial concentration of BOVs equal to n_{BOV0}, the onset shift is:

$$\Delta onset(t) = \Delta\Phi_{BO} A_{BO}(n_0 - n_{BOV0})\left(e^{-\varphi\sigma_{BO}t} - 1\right) \tag{6.17}$$

In the case of surfaces prepared with BOVs and exposed to O_2 before bombardment, a certain coverage of oxygen adatoms atop 5-fold Ti ions is also expected, equal to θ_{Oad0}. These atoms are removed from the surface following electron bombardment with a cross section σ_{Oad}. Taking the substrate work function as being homogenous, i.e. the removal of O_{ad} species changes the local work function from Φ_{Oad} to Φ_{sub}, the surface average work function is:

$$\Phi_{avg}(t) = f_{sub}(t)\Phi_{sub} + f_{Oad}(t)\Phi_{Oad} + f_{BO}(t)\Phi_{BO} + f_{BOV}(t)\Phi_{BOV} \tag{6.18}$$

where Φ_{Oad} is the local work function of O_{ad} atoms. Assuming that a single O_{ad} species occupies the same surface area as a BO, $f_{Oad}(t) = A_{BO}\theta_{Oad}(t)$, and the substrate surface fraction is $f_{sub}(t) = 1 - A_{BO}\left(\theta_0 + \theta_{Oad}(t)\right)$. With this in mind, the onset shift is thus equal to:

$$\Delta onset = \Delta\Phi_{Oad}\theta_{Oad0}A_{BO}(e^{-\varphi\sigma_{Oad}t} - 1) + \Delta\Phi_{BOV}A_{BO}(\theta_0 - \theta_{BOV0})(e^{-\varphi\sigma_{BO}t} - 1) \tag{6.19}$$

With $\Delta\Phi_{Oad} = \Phi_{Oad} - \Phi_{sub}$.

6.6.2 Improved Model for Oxygen ESD Kinetics Based on Monte-Carlo Simulations

The model presented in the previous section is a basic simplification. The value of σ_{BO} is not constant, and should decrease when θ_{BOV} increases. As previously mentioned, the coverage of BOVs saturates at 10-12% ML, at which point the value of σ_{BO} should be zero. To improve this model, a Monte-Carlo simulation was designed, similar to the one introduced by Dulub and co-authors [145].

In this new model, the surface is simulated as a matrix of BO sites, each one having a probability *P* for desorption due to electron impact. Bombardment is then simulated by randomly choosing individual sites for impact. If desorption takes place (with a probability *P*), the chosen site is turned into a BOV, and a number of neighbouring sites in the same oxygen row have their ESD probability affected, as shown in Figure 6.19 a). The number of affected BO sites and the probability distribution was adjusted so that the coverage of BOVs saturated at the reported value of 10-12% ML, and the time dependence of the BOV coverage matches the experimental results presented below in Figure 6.20.

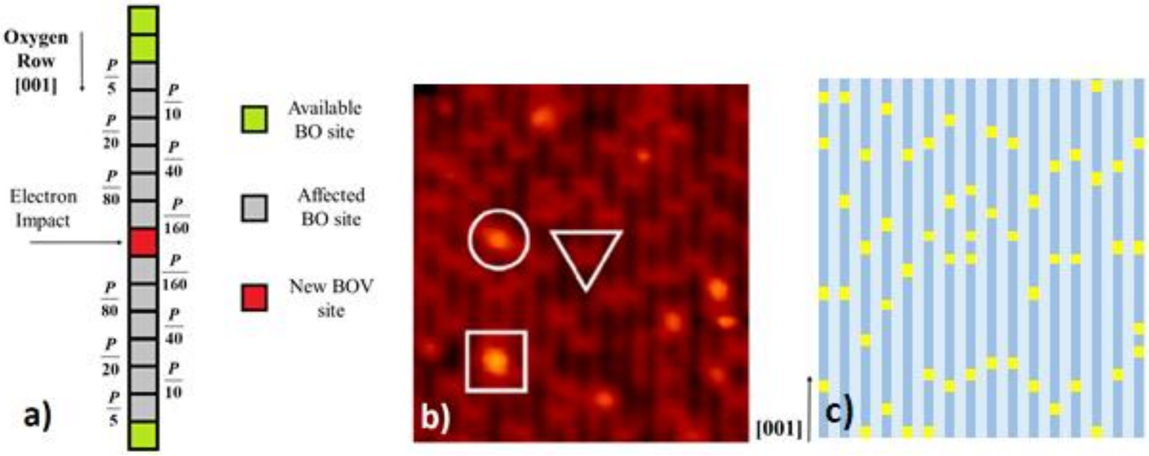

Figure 6.19 – a) Configuration of a single bridging oxygen row in the Monte-Carlo simulation following electron impact, and the affected probabilities of surrounding BO sites. b) STM picture of the electron bombarded $TiO_2(110)$-(1×1) rutile surface, taken from [119], with defects being indicated by the symbols - BOVs (triangle), OH (circle), and OH pair (square) c) Distribution of BOV sites (yellow squares) on the surface obtained in the Monte-Carlo simulation.

An analysis of the STM pictures from the available literature shows that this appears to be a fair approximation, as it is very rare to observe BOV sites in close proximity along the same row, while apparently having very little effect on the adjacent rows. A comparison between an STM example and a portion of the surface obtained in the Monte-Carlo simulation is presented in Figure 6.19 b) and c), showing a similar spatial distribution of BOV sites. The experimental cross section for ESD of oxygen species can be obtained by tuning the value of *P* in the Monte-Carlo model, so that the simulated BOV coverage and the measured onset shift have the same time dependence.

A set of experiments has been performed to test the proposed models. The $TiO_2(110)$-(1×1) defect-free surface was exposed to electron bombardment at 20, 40 and 80 eV, and the onset position was measured as a function of electron fluence, shown in Figure 6.20 a). The background change/drop of the work function was measured before the experiment (not shown), and its contribution was subtracted from the original results. Therefore, only the onset shift caused by electron bombardment is considered. Each point in the measurement corresponds to the average of 4 values measured consecutively, performed between each electron bombardment stage. The results were fitted to equation (6.16).

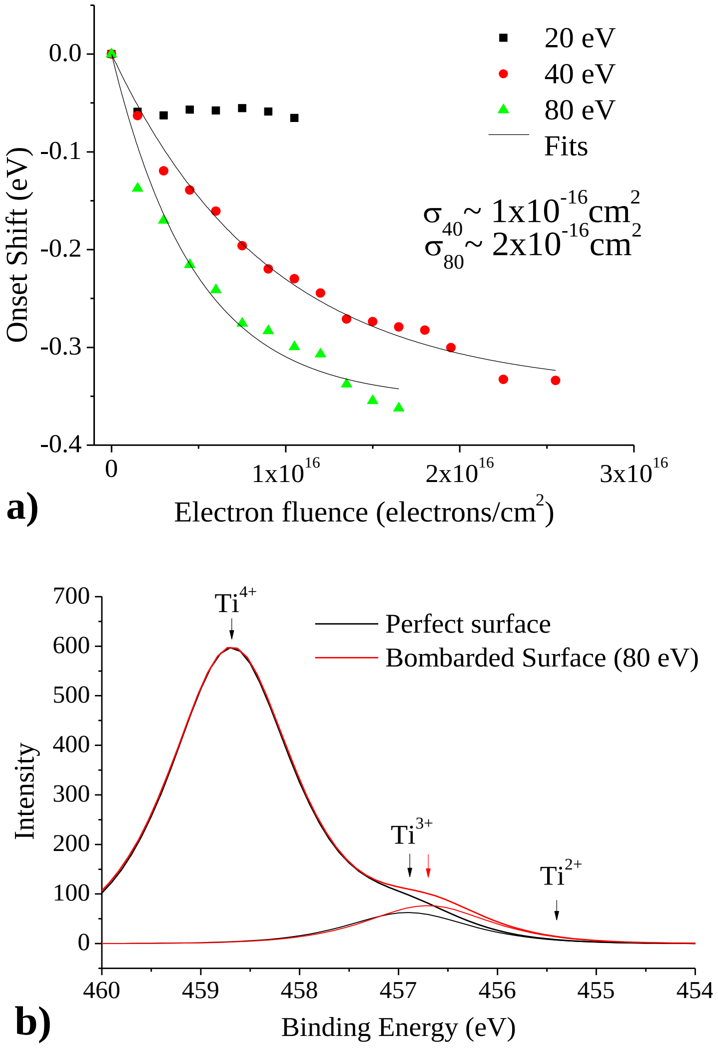

Figure 6.20 – a) Onset shift during electron bombardment of the TiO_2 surface for electron energies of 20, 40 and 80 eV, as a function of electron fluence. b) Detail of the Ti $2p_{3/2}$ peak showing an area increase and small energy shift of the Ti^{3+} contribution.

It is clear from the bombardment at 20 eV that, at this energy, which is below the expected threshold for oxygen desorption (~34 eV), electron bombardment does not induce a work function change, as no surface BOVs are created. The -0.05 eV onset shift between the first and seconds points is possibly due to the initial release of gas contaminants when the filament for electron bombardment was turned on, or due to a problem in the measurement of the first point (e.g. different bias voltage, bad sample position, etc.). It is believed that this initial point should be disregarded, since it is clear from the rest of the experiment that no consistent onset shift is being induced by the electron bombardment.

Although the results were expected to deviate from the model as the concentration of BOVs is increased, it was still possible to fit a single exponential contribution to bombardments at 40 and 80 eV, with both fits resulting in a saturated shift of ~0.35eV. Nevertheless, associating this value with the $0.32\Delta\Phi_{BO}$ term of the original model (see equation (6.16)) implies that, at saturation, all BO sites are converted to BOVs, which cannot be the case. Consequently, not much information can be drawn from this magnitude. Still, the fact that both results show a comparable threshold for the onset shift indicates that the surfaces are being altered in a similar way by the two energies, but at different rates. The ESD cross sections of 40 eV and 80 eV electrons obtained from the fit are 1×10^{-16} cm^2 and 2×10^{-16} cm^2, respectively, which, although not directly comparable (different surface facets, preparations, electron energy, and surface temperature), appears to be higher than those reported in other studies. A value of 5×10^{-19} cm^2 is reported for bombardment with 180 eV electrons at 80 K [148], and a value of 9×10^{-17} cm^2 is reported for the TiO_2(011) surface, for 300 eV electrons [145]. The high cross section value obtained is somewhat expected, as this model is based on the highly inaccurate assumption of a complete removal of BO species. A more accurate and lower value should be obtained from the Monte Carlo simulation.

For additional confirmation that the decrease of the work function is due to the creation of defects, XPS analysis was performed on the 80 eV bombarded surface, before and after electron bombardment. The comparison of the Ti $2p_{3/2}$ peak is presented in Figure 6.20 b), showing a clear increase of the Ti^{3+} contribution for the electron bombarded surface. The relative contribution of Ti^{3+} increased by ~2%, and its position was shifted by 0.2 eV towards lower binding energies. Furthermore, the XPS analysis shows no signs of increase of the Ti^{2+} contribution following the electron bombardment, which is also an indication that only BOVs are created, and that the surface was not significantly reduced/damaged by the bombardment (see Figure 6.2).

In order to calculate the ESD cross section using the Monte Carlo model, a simulated surface consisting of 200 × 200 sites (representing BOs) was used, with a total number of electrons hitting this surface being 40-50 times the amount of sites (i.e. $1.6\text{-}2.0\times10^{6}$). The number of BOVs created by the bombardment was followed as a function of the total fluence (measured in monolayers, with 1 ML=5×10^{14} cm^{-2}), and the onset shift shown on Figure 6.20 a) was converted to BOV coverage, resulting in a BOV saturation matching that of the simulation. As previously stated, the probability distribution for the different sites, shown in Figure 6.19 a), was tuned so that the saturated BOV coverage was in the 10-12% ML range, the distribution of created BOV sites matches STM observations, and the BOV time dependence follows the shape of the experimental results. A geometric progression dependence, starting at $P/160$ for BOV neighbouring sites, and increasing by a factor of two for each subsequent neighbour, up to $P/5$, was chosen. The electron fluence was converted to monolayer units, so that both fluences could be directly comparable. The value of P, as well as its change for neighbouring sites, was then adjusted in the simulation until the two curves displayed the same time dependence. The probability distribution of neighbouring sites that was used is shown above in Figure 6.19 a), and Figure 6.21 a) shows the compared results obtained for $P_{40eV} = 0.0085$ and $P_{80eV} = 0.0165$. The ESD cross section can then be calculated by multiplying this probability with the area of the unit cell, from which $\sigma_{40eV} = 1.6 \times 10^{-17}$ cm^2 and $\sigma_{80eV} = 3.2 \times 10^{-17}$ cm^2 are obtained, which is about one order of magnitude smaller than those obtained from the analytical model, and more consistent with the data from the literature. A statistical analysis of the model, performed on 500 simulations, showed a statistical noise lower around 0.5% of the calculated BOV percentage, i.e., for a concentration of 10% ML, a standard deviation of 0.05% ML was observed. It should be stated that there is some fitting margin in these results, especially considering the distribution of probabilities shown in Figure 6.19 a). One manner in which to improve the reliance of the model would be to perform a statistical analysis of the distribution of BOV sites by STM imaging, as performed by Dulub and co-authors for the TiO_2 (011)-(2×1) surface [145]. In their work, a probability for ESD of sites neighbouring BOVs following a geometric progression was also used, with a factor of ten for each subsequent neighbouring site. Nonetheless, since a variety of fitting criteria were considered, such as the BOV distribution, saturated concentration, and time dependence with total electron fluence, the results should still be considered as reasonably reliable.

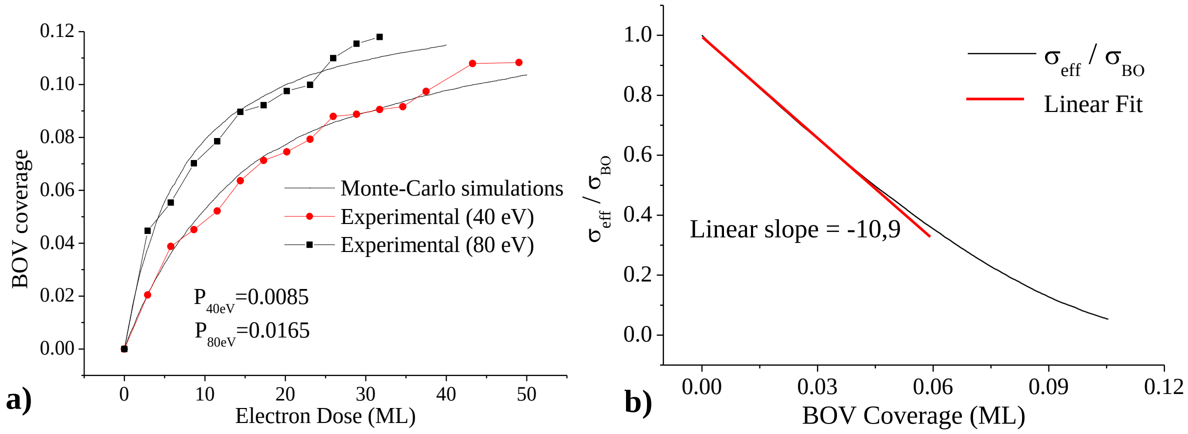

Figure 6.21 a) – Comparison of the coverage of BOVs vs electron dose obtained experimentally with that of the Monte-Carlo simulations. b) Change of the effective cross section with BOV coverage.

The cross-sections obtained correspond to the initial ESD cross section of oxygen species, valid only for the perfect surface. As the concentration of BOVs increases, the cross sections of neighbouring sites is significantly decreased, thus affecting the experimental ESD cross section. The concept of an effective cross section, corresponding to the average cross section of all BO species in the surface for a given coverage, can thus be introduced. This magnitude can be calculated by averaging the distribution of probabilities in the simulated matrix. Since the BOV coverage is rather low at any moment of the experiment, it is concluded that the saturation of the work function change is exclusively due to the change of the effective cross section. The ratio between σ_{eff} and σ_{BO} (cross section of the perfect surface) is presented in Figure 6.21 b), as a function of BOV coverage. Knowing how the value of σ_{eff} is changing with the concentration of BOVs, it is possible to apply an analytical model based on the differential equation (6.12), which could then be solved numerically.

Further attempts were made to perform the same analysis of the electron energy dependence, but for the ESD cross section of O_{ad} species, and compare it to the one obtained for BO species. Having a surface covered with O_{ad} requires its preparation with an initial concentration of BOVs, by annealing in UHV, followed by exposure to O_2. However, this could not be performed in an acceptably reproducible way, as the cumulative effect of electron bombardment creates a very defective surface that could not be recovered to its initial state by annealing in UHV, and required an O_2 atmosphere for a proper recovery. For this reason, the results obtained for bombardment at different energies were not comparable, as the surface's initial concentration of BOVs was different for each experiment.

6.7 Hydrogen ESD

A similar experiment was performed to show that desorption of hydrogen species from the TiO_2(110)-(1×1) surface by ESD can also be followed by measuring the onset shift during the electron bombardment. The TiO_2 sample was annealed in UHV in order to create a surface with oxygen defects, and was subsequently exposed to 1×10^{-8} mbar of water vapour for 40 minutes. After the water flow is turned off, the sample was left for 20 minutes to allow the complete desorption of water molecules weakly bonded to 5f Ti rows. With this procedure, a surface with isolated OH pairs on bridging oxygen rows is expected. As already discussed, one OH pair is formed per each water molecule due to its dissociative adsorption on a BOV sites. It is known from the STM and DFT analyses that the components of an OH pair repel each other and are separated over time, with the presence of water on 5f Ti rows further increasing the separation rate [13].

This surface was then bombarded with 30 eV electrons, with the bombardment being periodically interrupted to measure the onset position. The onset shift during the water exposure and electron bombardment is shown in Figure 6.22 a).

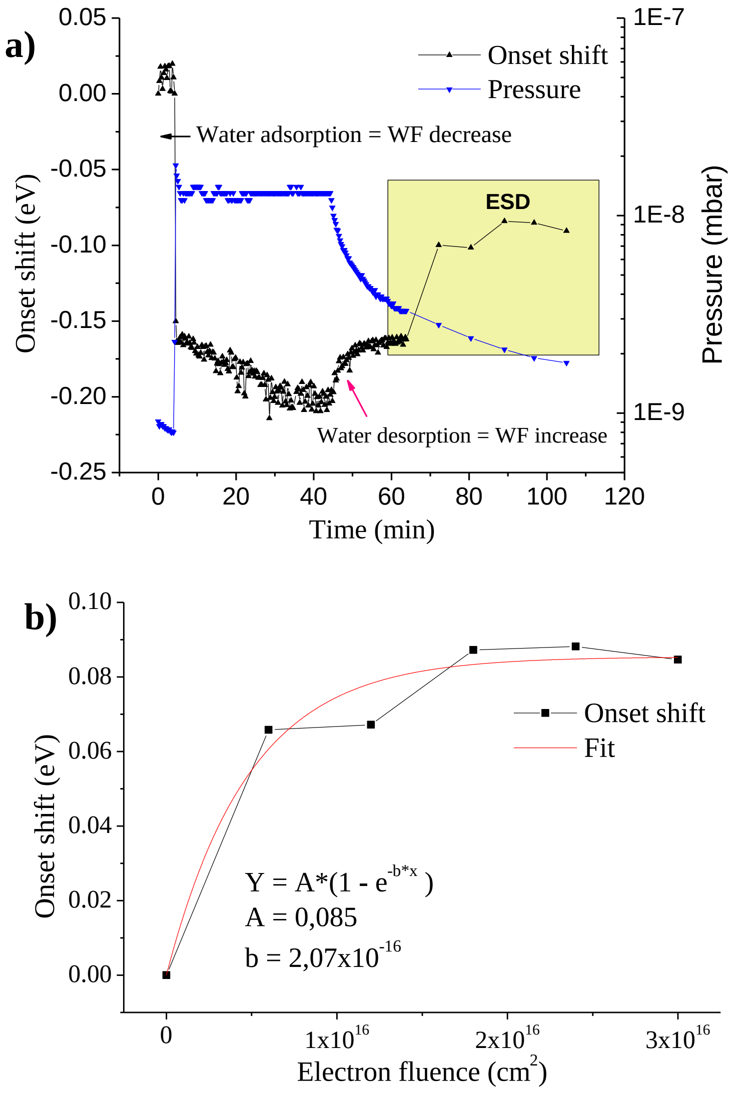

Figure 6.22 – a) Onset shift of the $TiO_2(110)$ during water exposure at 1×10^{-8} mbar, followed by electron bombardment at 30 eV. b) Onset shift during electron bombardment at 30 eV, as a function of electron fluence.

The initial fast drop of the work function is due to water adsorption, later followed by a comparatively smaller and slower increase, when the water gas flow is finally turned off. As discussed in section 6.3.1, the slow background drop of the work function, here at a rate of ~0.01 eV per 10 minutes, is most likely due to the adsorption of hydrocarbon contaminants present in the system. The positive onset shift when the water partial pressure is decreased, starting at around 45 minutes , is due to the desorption of water from 5f Ti rows, as discussed in section 6.3. Before the electron bombardment is initiated, the surface should be covered with separated hydroxyl pairs. During the ESD stage, the work function increases as expected, due to the removal of hydrogen species from the surface. Figure 6.22 b) shows the onset shift during the electron bombardment, as a function of electron fluence. As performed in section 6.3.2, the background drop was fitted to a slow exponential decay and its contribution was removed. The results were fit to a model similar to the one presented in section 6.6.1. Here, the onset shift due to hydrogen removal is equal to:

$$\Delta onset\left(t\right)=\Delta\Phi_{OH}n_{OH,0}A_{BO}\left(1-e^{-\varphi\sigma_{H}t}\right)$$

where σ_H is the cross section for hydrogen desorption from the adsorbed OH groups, $n_{OH,0}$ is the concentration of OH groups prior to bombardment, and $\Delta\Phi_{OH}=\Phi_{OH}-\Phi_{BO}$.

From the obtained fit, the value of σ_H for the 30 eV energy was calculated as $\sim 2\times10^{-16}$ cm^2, which is an extremely high value when compared to the one obtained by Suzuki and co-authors [149] (10^{-19} cm^2 range). It is possible that the STM results obtained in their work were not correctly interpreted, since at the time the work was performed (1999), the identification of BOV/OH sites on STM pictures of the TiO_2(110)-(1×1) rutile surface was still highly debated, as reported in the paper itself. The more likely reason for the cross-section difference is in the lower energy used in their study of only 20 eV, which corresponds to the threshold energy for hydrogen desorption (binding energy of the O 2s level). For this energy the cross section for H desorption should still be extremely low. An improved setup is required to perform the analysis of the ESD cross section for different energies in an acceptable way and compare cross section results directly. Since the overall onset shift is rather small, a higher density of points is essential for a correct comparison to be made.

6.8 Overview of ESD monitoring with the onset method

It has been shown from these results that the onset measurement can be a useful tool to follow changes induced by electron bombardment on the rutile TiO_2(110) surface. The desorption of BO, O_{ad} and H species was successfully identified with this method, clearly suggesting that the same approach can be also adopted for other adsorbed species that induce a measurable onset shift. Moreover, it has been shown that by bombarding the TiO_2 surface with electrons of a certain energy, and following its WF change, it is also possible to prepare a surface with a desired concentration of defects/adsorbed species.

The experimental setup should however be improved, particularly by using a low energy electron gun to irradiate the surface area of the TiO_2 crystal. This change would introduce a higher precision of both the electron bombardment energy and current. With the current method being used, where the sample is directly bombarded by electrons emitted from a filament placed close to the surface, the electron energy ranges between the voltage difference of the filament, which is around 4V. It is also possible that part of the measured current comes from electrons hitting the sample holder, and that the surface is not homogenously bombarded. Furthermore, because the work function is very sensitive to first layer changes, degassing from the filament close to the surface presents another problem for the measurement. Using an electron gun would possibly solve all these issues, while also allowing the onset measurement to be performed during the bombardment, significantly increasing the density of points. The increased precision of energy and current, together with real time measurement, would allow for a more comprehensive analysis of the ESD processes here studied.

7

7 Summary and Conclusions

The work here presented was performed with the overall goal of studying the presence of defects on the TiO_2(110)-(1×1) surface, and their influence on the adsorption of H_2O and O_2 gases, mainly using the surface analysis technique of work function measurement based on the onset position, supported by XPS analysis. With this goal, the work was segmented into three distinct parts:

- Upgrade of the surface analysis system Kratos XSAM 800,
- Revision of the work function measurement technique,
- Work function based study of the TiO_2(110) surface defects and H_2O/O_2 adsorption, and ESD of oxygen and hydrogen species.

Each of these objectives was divided in a series of tasks summarized ahead.

7.1 Upgrade of Kratos XSAM 800 System

The Kratos XSAM 800 system was upgraded and adapted for the work plan with the TiO_2(110)-(1×1) surface. The vacuum system was improved with better-quality pumping of the gas line and the sample insertion chamber, and higher precision pressure measurement. A series of overdue maintenance tasks were performed (filament and electron multiplier replacement, cleaning of filters and water cooling system, etc.) and faulty/damaged instrumentation was repaired. A setup for the annealing, electron/ion bombardment, and analysis of the TiO_2(110) single crystal was mounted, as well as that for gas introduction in low pressure ranges (10^{-9} to 10^{-8} mbar).

The replacement of the original control system was realized by making adaptations to its electronics, and connecting to a National Instruments data acquisition board (NI PCIe-6323). Digital signals originally used for the power supply control of the spectrometer were replaced by analogue voltages produced by the new data acquisition board. The board is also controlling different relays for turning on/off the voltage supplies and selecting the spectrometer operation regime. Furthermore, it performs counting of the detected pulses, control of different voltages in the charged particle detection system (electron-optics column, energy analyser and detector), and the raster scanning of the ion beam. The control software was also developed, in LabVIEW environment, for XPS and electron spectroscopy analysis, and for sample imaging based on ion bombardment.

Following the change of the control electronics, the energy spectrometer and the detector system were properly characterized. This was performed by evaluating the non-linearity of the electron multipliers (measured counts vs real counts), and determining the spectrometer’s transmission function. Knowledge of both is essential for accurate XPS analysis quantification, and, since it is not constant throughout the system’s life-time, requires periodical measurement. The transmission function was measured using two distinct approaches. In addition to the well-established first-principles method, a novel, here denoted as sample-biasing method, was developed. The results of the novel approach are identical to the former, but with much higher signal to noise ratio and a shorter measurement time. The latter is caused by the usage of a single sample (here we propose clean gold sample), while several previously cleaned samples had to be used in the first-principles method. These results both validated the physical background of the proposed method and proved its relative advantage.

To finalize the upgrade of the Kratos XSAM 800 system, the transmission of the electron-optical column was optimized. This was accomplished by individually modifying the voltages of its electrodes, with the goal of maximizing the number of detected counts for a given electron kinetic energy and analyser pass energy. Since it takes too long to map the complete set of possible voltage combinations, a sub-category of genetic search procedures, denoted as differential evolution algorithm, was employed to perform this search in a timely manner. Software was written in LabVIEW to automatically perform this task, applying the search algorithm to the control voltages of the system. The system was optimized in the kinetic energy range of 200-1200 eV, for the pass energies of 20, 40 and 80 eV, with optimization factors ranging from 10% to 110%. Following this optimization, the transmission function for the new voltage set was determined again, which was later used for the quantification of XPS spectra.

7.2 Revision of the Work Function Measurement Method

With its fast acquisition time and high sensitivity, the technique of work function measurement based on the onset position of the secondary electron energy distribution has proved to be a useful tool for the analysis of adsorption and desorption processes on the TiO_2 surface [23–25]. With the goal of further improving the capabilities of this technique, a variety of raw data treatment procedures was evaluated, with different smoothing and fitting methods being tested, so that the onset position is more accurately determined. This allows the detection of very small onset shifts, typically down to about 10 meV.

The physical model behind the onset position was revised under the light of the patch field theory [107,108]. The presence of surface regions with distinct work function values creates an additional potential barrier above the surface of the lower work function patches (due to the contact potential difference), which ultimately increases the cut-off energy of the secondary electron distribution, i.e., the onset position. In the absence of external electric fields, the onset position will thus be related to the averaged surface work function, and not the minimum local work function of the analysed area.

The charged particle simulator SIMION was used to model a variety of different surface patch distributions. For the case where a surface substrate is covered with identically shaped patches of equal work function, a semi-empirical law was reached for the potential energy distribution above the surface, as a function of patch size, shape, total surface coverage, and local work function difference between the substrate and the patch. Additionally, when work function measurements are performed with the sample biased to a certain voltage, there is an external field which will affect the potential energy above the surface. The influence of this field on the onset position was also considered. In short, depending on the relation between the magnitude of the external field and the size of the patches, the onset position measurement may be performed in three different regimes. It may correspond to the surface averaged work function (small patch/ weak external field), to the minimum local work function of the analysed area (big patches/strong external field), or to a value in between.

An experiment was conducted to validate the new interpretation of the onset position. A sample was prepared, consisting of a nickel substrate (higher work function) with a single indium patch (lower work function). The onset position was separately measured on the two materials as a function of the external field’s intensity. As expected, when measured on the indium patch, it shifted from the surface averaged work function to the local work function of indium, while it stayed constant when measured uniquely on the nickel substrate. Moreover, the change of the onset shift from the indium patch vs. the external field follows the analytical dependence derived by the model that was introduced.

7.3 Work function Based Study of TiO_2 Surface Defects and O_2/H_2O Adsorption

With the improved and more sensitive XPS system, and the revised physical model for the work function measurement based on the onset position, these two techniques were combined to study the $TiO_2(110)$-(1×1) surface.

The initial concentration of surface defects was manipulated by adjusting different parameters for the preparation of a fresh surface layer (sputtering intensity, annealing time and temperature, and relative O_2 pressure in the chamber during the annealing). Preparation procedures were then correlated with the relative work function of the surface. Having established the range of work function values between low and high surface concentration of defects, the reduction level of the surface can now be roughly estimated by performing this measurement. This approach appeared to be useful in the experiments that followed.

7.3.1 Adsorption of H_2O and O_2 on the $TiO_2(110)$-(1×1) Surface with Different Reduction Levels

From the previous work performed by our group with the adsorption of H_2O on the $TiO_2(110)$ surface, some doubts have remained concerning the nature of the slow exponential decrease of the work function, and the work function recovery when the water flow is turned off (associated with desorption of water molecules from surface Ti rows).

A series of tests was conducted in which the fresh surface was exposed to different gases in a controlled way, as well as to potentially surface damaging processes. The goal was to understand if any of the gases present in UHV, or if the measurement process itself were altering the surface, and consequentially its work function. It was concluded that the slow drop of the work function is related to the adsorption of hydrocarbon species, which are accumulated in the vacuum system over time and slowly contaminate the surface. The level of contamination accumulated during the experiment is typically below the detection limit of the XPS system.

These hydrocarbons can be temporarily eliminated from the vacuum system with a standard baking procedure, but will accumulate again with the system's regular usage, even if there is no significant change of the measured base pressure.

As has been shown in previous works [23–25], when the water vapour flow is turned off, the work function of the TiO_2(110)-(1×1) surface increases. A portion of the adsorbed water on this surface is weakly bound on Ti rows, with a surface concentration related to the adsorption/desorption equilibrium, which should depend on water pressure. The work function recovery when the water pressure starts to decrease (flow turned off) is thus associated with a decrease of this equilibrium concentration. In order to cement this assumption, the same experiment was conducted at 80ºC, a temperature at which the concentration of H_2O on Ti rows should be very low, according to TPD results [131]. Indeed, the dissociative adsorption of water on BOVs was still observed at 80ºC at the start of exposure (fast work function decrease), but there was no measurable work function recovery when the water flow was turned off. The contaminating hydrocarbon species have also been shown to interact with H_2O molecules present on the surface, preventing desorption. The magnitude of the work function recovery was measured for different contamination levels, and found to be inversely proportional to the amount of carbon adsorbed species. Based on the time evolution of the work function recovery when water flow is turned off, the sticking coefficient and desorption rate of water were determined, for the clean surface, and for different amounts of carbon contamination. Additionally, based on the Topping model, the concentration of surface BOVs on the surfaces used in these experiments was estimated (~7%). The obtained value is perfectly within the range reported in the literature.

The adsorption of O_2 on the TiO_2(110)-(1×1) surface was studied using both work function and XPS analysis. As opposed to the water adsorption, oxygen adsorption has been found to affect the shape of the main Ti XPS peak, decreasing the intensity of the Ti^{3+} contribution, which can thus be used to quantify oxygen adsorption. The electronegative oxygen species are mainly dissociated on BOV sites, with one oxygen atom filling/healing the BOV and the other being adsorbed on top of the adjacent Ti row (typically named oxygen adatom). This process creates surface dipoles oriented towards the bulk, which will increase the surface averaged work function. Since the main adsorption sites for the O_2 molecule are surface BOVs, the magnitude of the work function change due to oxygen adsorption should be closely related to the concentration of these surface defects. The TiO_2(110)-(1×1) surface has been prepared with a wide range of BOV concentrations, and subsequently exposed to oxygen gas. The work function change was monitored in real time during the adsorption process, and the area of the

Ti^{3+} 2p XPS peak was measured before and after oxygen exposure. The magnitude of the total work function change was correlated with the amount of surface defects (controlled by the sample preparation procedure), as well as with the change of the Ti^{3+} 2p XPS peak area. Additionally, the adsorption cross-section for oxygen species was calculated and found to increase with the surface reduction level.

The interaction between H_2O and O_2 on the TiO_2(110)-(1×1) surface was also studied, by alternately exposing the surface to these gases, and monitoring the work function change during exposure. It is known that adsorbed H_2O and OH groups will react with oxygen adatom species, creating a variety of surface sub-species in the reaction process, which can be new reactive adsorption sites for both H_2O and O_2. This was supported by the alternate exposure to these gases. The surface was first saturated with water (work function decrease), and then with oxygen (causing work function increase in part due to proton removal from the OH groups). With the subsequent water exposure, the work function decreased a second time, indicating the creation of new adsorption sites after the oxygen exposure, as the original BOV sites were already filled. The same situation occurred on the second exposure to oxygen. This result indicates that the surface interaction between adsorbed species and either gas will introduce new adsorption sites, which are associated with the different sub-species originated in the reaction. After approximately three cycles of exposure to both gases, the surface reaches a saturated state where neither is adsorbed (no work function change), indicating that possibly all surface defects and reactive sub-species have been neutralized and no more adsorption sites remain, i.e., a stoichiometric, non-reactive surface is produced in the process.

7.3.2 Using Electron Stimulated Desorption for Creation and Neutralization of Surface Defects

With a bombardment energy above a certain threshold, ESD can be used to create BOV defects on the TiO_2(110)-(1×1) surface, by triggering desorption of surface oxygen species. It can also be used to create a stoichiometric surface by causing desorption of hydrogen atoms/ions from adsorbed OH groups [118,148,149]. With this in mind, the work function change of the TiO_2(110)-(1×1) surface was monitored during exposure to electron bombardment at different energies, as the creation of BOVs and neutralization of OH dipoles should be work function changing processes, as has been previously established.

The physical process behind the electron-induced desorption of oxygen species is such that the presence of surface Ti^{3+} ions, which are associated with oxygen vacancies, inhibits their desorption [141]. This was qualitatively confirmed by comparing the work function change due to electron bombardment for the stoichiometric and defective surfaces (same exposure to both), with the former suffering a larger work function shift, which is associated with the creation of more defects. In order to correctly quantify the work function change as a function of electron fluence, a Monte Carlo simulation was conducted in which the electron bombardment of the $TiO_2(110)$-(1×1) surface was replicated, with the creation of a BOV site affecting the probability of oxygen desorption from adjacent sites (by ESD). By adjusting the parameters of this model in order to achieve an agreement with the experimental results (work function change vs electron fluence), the distribution of desorption probabilities for bridging oxygen species adjacent to BOVs was determined, and the initial cross section for oxygen ESD was calculated for bombardment at 40 and 80 eV, and found to be 1.6×10^{-17} cm^2 and 3.2×10^{-17} cm^2, respectively.

The ESD of hydrogen species was performed by producing a surface covered with OH groups, which was then bombarded with 30 eV electrons, with its work function being monitored as a function of electron fluence. A work function increase was observed as this surface is bombarded, due to the removal of protons from adsorbed OH groups i.e. removal of surface dipoles oriented towards the vacuum. Since the probability for hydrogen desorption from OH groups upon electron impact is not affected during the bombardment (as opposed to ESD of oxygen species), a simpler desorption kinetics model was used to describe this process. Based on this model, the ESD cross section for hydrogen with 30 eV electrons was calculated, using the time-dependence of the work function change during bombardment, and found to be equal to $\sim 2\times10^{-16}$ cm^2.

7.4 Final Remarks

The work here presented was performed with great focus on its physics engineering side, thus encompassing the characterization and improvement of instrumentation required to perform XPS and onset techniques, and understanding the fundamentals of the physical processes behind these measurements.

With the work performed on TiO_2, it has been shown that, despite its apparent simplicity, the work function measurement technique based on the onset position can still be used to gather important information on the $TiO_2(110)$-(1×1) surface, due to its high sensitivity to minor surface changes, and the short acquisition time which allows real time monitoring of dynamical processes in the time scale from a few seconds to few hours. Together with XPS analysis (the same instrumentation can be used for both measurements), it was shown that this technique can be used to probe the reduction level of the surface, and estimate the concentration of first-layer defects. Additionally, important information concerning the adsorption of H_2O and O_2 gases, as well as the interaction between the two, was also collected. It should finally be stressed that the study of the surface using these techniques, as opposed to modern STM studies, provides a somehow more complete picture of the adsorption phenomena occurring in the surface, as the information that is gathered is not confined to the small, near-perfect wide terrace areas, which are in a way more typical of these studies.

7.5 Future Work

The KRATOS XSAM 800 system was left in an operative state following its upgrade, and most of the system's hardware is in good condition. However, some of its parts have malfunctioned numerous times, due to the age and wear of the system, which have led to undesired interruptions of the experimental work. It is therefore advisable to continue the system's upgrade by further replacing some of its parts, in particular the high-voltage electronics, which controls the spectrometer, and the detector electronics which amplifies the electron multiplier signal. Both are essential to the correct functioning of the system, and suffered multiple malfunctions. Replacing these with modern electronics parts would also improve the system's capabilities, reducing the base noise level, and increasing the sensitivity of the control voltages. The latter is of particular use for the type of work being performed with work function analysis, which requires monitoring of very small energy shifts. Additionally, the optimization procedure, which produced excellent results on the spectrometer's low magnification mode, can be extended to the high magnification mode, through the addition of two analogue output voltage controls.

The influence of the patch field on the work function measurement should be dependent on the position within the patch from which the electrons originate. It should be possible to measure this dependence by scanning a narrow electron beam across a low work function patch while performing the work function measurement. This experiment was conducted, although with the Ar^+ ion beam generated by the ion gun of the *Multitécnica* system, which produced uncertain results. It should therefore be repeated with a narrower beam, and a radiation source which does not damage the surface.

Considering the work performed with the TiO_2 surface, a number of topics could be further explored. The same type of experiments can be performed with other molecules of relevance in catalysis. It should be noted that adsorption of CO was also performed during this work, showing a very small work function change, likely due to very low dipole moment of the molecule. Nevertheless, from the sign of the work function change with the exposure, it was found that CO molecule is oriented with oxygen facing the vacuum (most probably adsorption on BOVs). Concerning the influence of hydrocarbon contamination on the adsorption process of water molecules, it would be interesting to expose the surface to these contaminants in a more controlled way, and try to establish a correlation between the adsorption/desorption rates of water and the contamination levels. Moreover, the effects of hydrocarbon contamination on the adsorption of other species, besides water could also be explored. While some temperature-dependent experiments were performed, the temperature range for these was highly limited by the experimental setup, as the sample's heating system affects the measurement process (heating above certain temperatures requires electron bombardment, which introduces noise to the detector). An alternative solution would allow heating the sample to higher temperatures while performing XPS/work function measurements, and allow the study of other processes such as desorption of OH species. The ESD processes here studied have been somewhat limited by the electron bombardment setup, which requires sample re-positioning, interferes with the work function measurement, and may contaminate the surface. Upgrading the current setup to include an electron-gun capable of performing this task would open a number of possibilities for measurements, in particular a higher density of points and variety of bombardment energies, thus producing more reliable and extensive results. Finally, the capabilities of XPS and work function measurements to monitor the dynamics of different process on the $TiO_2(110)$ rutile surface can be continued by exploring how the adsorption of different metals, previously studied by Marques [1], is affected by the presence of surface defects and/or contaminants such as hydrocarbons, water, or oxygen.

8

8 References

[1] H.E.P. Marques, Caracterização do crescimento de filmes ultra-finos e nano-estruturas em superfícies, PhD Thesis, Fac. Ciências e Tecnol. Da Univesidade Nov. Lisboa, Lisboa. (2009).

[2] U. Diebold, The surface science of titanium dioxide, Surf. Sci. Rep. 48 (2003) 53–229. https://doi.org/10.1016/S0167-5729(02)00100-0.

[3] I. Fechete, Y. Wang, J.C. Védrine, The past , present and future of heterogeneous catalysis, Catal. Today. 189 (2012) 2–27. https://doi.org/10.1016/j.cattod.2012.04.003.

[4] S. Dang, H. Yang, P. Gao, H. Wang, X. Li, W. Wei, Y. Sun, A review of research progress on heterogeneous catalysts for methanol synthesis from carbon dioxide hydrogenation, Catal. Today. (2019) 61–75. https://doi.org/10.1016/j.cattod.2018.04.021.

[5] H. Zhao, F. Pan, Y. Li, A review on the effects of TiO2 surface point defects on CO2 photoreduction with H2O, J. Mater. 3 (2017) 17–32. https://doi.org/10.1016/j.jmat.2016.12.001.

[6] T. Jafari, E. Moharreri, A. Amin, R. Miao, W. Song, S. Suib, Photocatalytic Water Splitting—The Untamed Dream: A Review of Recent Advances, Molecules. 21 (2016) 900. https://doi.org/10.3390/molecules21070900.

[7] Y.-J. (Eds. . Colmenares, Juan Carlos, Xu, Heterogeneous Photocatalysis, Springer Berlin Heidelberg, Berlin, Heidelberg, 2016. https://doi.org/10.1007/978-3-662-48719-8.

[8] K. (1972). Fujishima, A., Honda, Electrochemical Photolysis of Water at a Semiconductor Electrode, Nature. 238 (1972) 37–38. https://doi.org/10.1038/238038a0.

[9] O. Carp, Photoinduced reactivity of titanium dioxide, Prog. Solid State Chem. 32 (2004) 33–177. https://doi.org/10.1016/j.progsolidstchem.2004.08.001.

[10] A. Mehonic, A.J. Kenyon, Defects at Oxide Surfaces, Springer, Cham, 2015.

https://doi.org/10.1007/978-3-319-14367-5.

[11] S. Wendt, P.T. Sprunger, E. Lira, G.K.H. Madsen, Z. Li, J. Hansen, J. Matthiesen, A. Blekinge-Rasmussen, E. Lægsgaard, B. Hammer, F. Besenbacher, The role of interstitial sites in the Ti3d defect state in the band gap of titania, Science (80-.). 320 (2008) 1755–1759. https://doi.org/10.1126/science.1159846.

[12] E. Lira, P. Huo, J.Ø. Hansen, F. Rieboldt, R. Bechstein, Y. Wei, R. Streber, S. Porsgaard, Z. Li, E. Lægsgaard, S. Wendt, F. Besenbacher, Effects of the crystal reduction state on the interaction of oxygen with rutile TiO2(110), Catal. Today. 182 (2012) 25–38. https://doi.org/10.1016/j.cattod.2011.09.038.

[13] B. Hammer, S. Wendt, F. Besenbacher, Water adsorption on TiO2, in: Top. Catal., 2010: pp. 423–430. https://doi.org/10.1007/s11244-010-9454-3.

[14] E. Lira, J.Ø. Hansen, P. Huo, R. Bechstein, P. Galliker, E. Lægsgaard, B. Hammer, S. Wendt, F. Besenbacher, Dissociative and molecular oxygen chemisorption channels on reduced rutile TiO2(110): An STM and TPD study, Surf. Sci. 604 (2010) 1945–1960. https://doi.org/10.1016/j.susc.2010.08.004.

[15] C.M. Yim, C.L. Pang, G. Thornton, Oxygen vacancy origin of the surface band-gap state of TiO2(110), Phys. Rev. Lett. 104 (2010) 2–5. https://doi.org/10.1103/PhysRevLett.104.036806.

[16] C. Lun Pang, R. Lindsay, G. Thornton, Chemical reactions on rutile TiO2(110)., Chem. Soc. Rev. 37 (2008) 2328–2353. https://doi.org/10.1039/b719085a.

[17] L.-M. Liu, P. Crawford, P. Hu, The interaction between adsorbed OH and O2 on TiO2 surfaces, Prog. Surf. Sci. 84 (2009) 155–176. https://doi.org/10.1016/j.progsurf.2009.01.002.

[18] S. Wendt, R. Schaub, J. Matthiesen, E.K. Vestergaard, E. Wahlström, M.D. Rasmussen, P. Thostrup, L.M. Molina, E. Lægsgaard, I. Stensgaard, B. Hammer, F. Besenbacher, Oxygen vacancies on TiO2(110) and their interaction with H2O and O2: A combined high-resolution STM and DFT study, Surf. Sci. 598 (2005) 226–245. https://doi.org/10.1016/j.susc.2005.08.041.

[19] S.I. Tanaka, K. Mase, S.I. Nagaoka, Photostimulated ion desorption from the TiO2(110) and ZnO($10\bar{1}0$) surfaces, Surf. Sci. 572 (2004) 43–58. https://doi.org/10.1016/j.susc.2004.08.020.

[20] A. Fujishima, X. Zhang, D.A. Tryk, TiO2 photocatalysis and related surface phenomena, Surf. Sci. Rep. 63 (2008) 515–582. https://doi.org/10.1016/j.surfrep.2008.10.001.

[21] U. Diebold, Perspective: A controversial benchmark system for water-oxide interfaces: H2O/TiO2(110), J. Chem. Phys. 147 (2017). https://doi.org/10.1063/1.4996116.

[22] H.P. Marques, a. R. Canário, a. M.C. Moutinho, O.M.N.D. Teodoro, Tracking hydroxyl adsorption on TiO2 (110) through secondary emission changes, Appl. Surf. Sci. 255 (2009) 7389–7393. https://doi.org/10.1016/j.apsusc.2009.04.006.

[23] N. Bundaleski, A.G. Silva, U. Schröder, A.M.C. Moutinho, O.M.N.D. Teodoro, Adsorption dynamics of water on the surface of TiO2 (110), J. Phys. Conf. Ser. 257 (2010) 012008. https://doi.org/10.1088/1742-6596/257/1/012008.

[24] A.G. Silva, N. Bundaleski, A.M.C. Moutinho, O.M.N.D. Teodoro, Dynamics of water adsorption on TiO 2 monitored by work function spectroscopy, Appl. Surf. Sci. 258 (2012) 2006–2009. https://doi.org/10.1016/j.apsusc.2011.05.063.

[25] N. Bundaleski, A.G. Silva, B. Jean-Shaw, O. Teodoro, A. Moutinho, Water on TiO2 studied by work function change: Adsorption in cycles, J. Phys. Conf. Ser. 417 (2013). https://doi.org/10.1088/1742-6596/417/1/012024.

[26] O.M.N.D. Teodoro, J.A.M.C. Silva, A.M.C. Moutinho, Multitechnique description surface analysis system, Vacuum. 46 (1995) 1205–1209.

[27] A.A. Oura, K., Katayama, M., Zotov, A. V., Lifshits, V. G., & Saranin, Surface Science – An Introduction., Adv. Texts Physics. Springer Berlin Heidelb. (2003). https://doi.org/10.1016/j.susc.2009.03.005.

[28] D.P. Woodruff, T.A. Delchar, Modern Techniques of Surface Science, Cambridge University Press, 1994. https://doi.org/10.1017/CBO9780511623172.

[29] A. Zangwill, Physics at Surfaces, Cambridge University Press, 1988. https://doi.org/10.1017/CBO9780511622564.

[30] R.A. van Santen, Modern Heterogeneous Catalysis, Wiley-VCH Verlag GmbH & Co. KGaA, Weinheim, Germany, 2017. https://doi.org/10.1002/9783527810253.

[31] D.L. Auciello, O., Gras-Martí, A., Valles-Abarca, J.A., Flamm, Plasma-Surface Interactions and Processing of Materials, Springer Netherlands, Dordrecht, 1990. https://doi.org/10.1007/978-94-009-1946-4.

[32] J. Wei, R. Macek, Electron-cloud Effects in High-intensity Proton Accelerators, Mini Work. Electron Cloud Simulations Prot. Positron Beams. (2002) 1–30.

[33] J. Ladislas Wiza, Microchannel plate detectors, Nucl. Instruments Methods. 162 (1979) 587–601. https://doi.org/10.1016/0029-554X(79)90734-1.

[34] K. Jousten, Handbook of Vacuum Technology, Wiley-VCH Verlag GmbH & Co. KGaA, Weinheim, Germany, 2016. https://doi.org/10.1002/9783527688265.

[35] J.T. Yates, Experimental Innovations in Surface Science, Springer International Publishing, Cham, 2015. https://doi.org/10.1007/978-3-319-17668-0.

[36] P. Rousseau, H. Khemliche, N. Bundaleski, P. Soulisse, A. Momeni, P. Roncin, Surface analysis with grazing incidence fast atom diffraction (GIFAD), J. Phys. Conf. Ser. 133 (2008) 012013. https://doi.org/10.1088/1742-6596/133/1/012013.

[37] Y.R. Shen, Nonlinear optical studies of surfaces, Appl. Phys. A Solids Surfaces. 59 (1994) 541–543. https://doi.org/10.1007/BF00348272.

[38] J.F. Moulder, W.F. Stickle, P.E. Sobol, K.D. Bomben, Handbook of Photoelectron Spectroscopy, Phys. Electron. Inc., Eden Prairie, Minnesota. (1992). https://doi.org/10.1002/sia.740030412.

[39] M.C. Biesinger, L.W.M. Lau, A.R. Gerson, R.S.C. Smart, Resolving surface chemical states in XPS analysis of first row transition metals, oxides and hydroxides: Sc, Ti, V, Cu and Zn, Appl. Surf. Sci. 257 (2010) 887–898. https://doi.org/10.1016/j.apsusc.2010.07.086.

[40] A.M. Ferraria, A.P. Carapeto, A.M. Botelho Do Rego, X-ray photoelectron spectroscopy: Silver salts revisited, Vacuum. 86 (2012) 1988–1991. https://doi.org/10.1016/j.vacuum.2012.05.031.

[41] S. Tougaard, Surface nanostructure determination by x-ray photoemission spectroscopy peak shape analysis, J. Vac. Sci. Technol. A Vacuum, Surfaces, Film. 14 (1996) 1415–1423. https://doi.org/10.1116/1.579963.

[42] D.R. Vij, Handbook of Applied Solid State Spectroscopy, Springer US, Boston, MA, 2006. https://doi.org/10.1007/0-387-37590-2.

[43] G. Greczynski, L. Hultman, Reliable determination of chemical state in x-ray photoelectron spectroscopy based on sample-work-function referencing to adventitious carbon: Resolving the myth of apparent constant binding energy of the C 1s peak, Appl. Surf. Sci. 451 (2018) 99–103. https://doi.org/10.1016/j.apsusc.2018.04.226.

[44] V.M. Dwyer, J.M. Richards, The depth distribution function in Auger/XPS analysis, Surf. Interface Anal. 18 (1992) 555–560. https://doi.org/10.1002/sia.740180717.

[45] A. Jablonski, C.. Powell, Relationships between electron inelastic mean free paths, effective attenuation lengths, and mean escape depths, J. Electron Spectros. Relat. Phenomena. 100 (1999) 137–160. https://doi.org/10.1016/S0368-2048(99)00044-4.

[46] C.D. Wagner, Sensitivity factors for XPS analysis of surface atoms, J. Electron Spectros. Relat. Phenomena. 32 (1983) 99–102. https://doi.org/10.1016/0368-2048(83)85087-7.

[47] X. Zhang, Synchrotron Radiation Applications, WORLD SCIENTIFIC, 2018.

https://doi.org/10.1142/10643.

[48] J.H. Moore, C.C. Davis, M.A. Coplan, S.C. Greer, Building Scientific Apparatus, Cambridge University Press, 2009.

[49] AG Jacobs, (n.d.). https://jacobs.physik.uni-saarland.de/home/index.php?page=forschung/UHV-Lab-1.

[50] Microchannel Plates, (n.d.). http://www.dmphotonics.com/MCP_MCPImageIntensifiers/microchannel_plates.htm.

[51] J. Trigueiro, W. Lima, N. Bundaleski, O.M.N.D. Teodoro, XPS spectrometer transmission function optimization by the differential evolution algorithm, J. Electron Spectros. Relat. Phenomena. 222 (2018) 122–132. https://doi.org/10.1016/j.elspec.2017.07.004.

[52] W.F. Lima, Requalificação de um espectrómetro Kratos XSAM 800 para Espectroscopia de Fotoelectrões de Raios-X, Faculdade de Ciências e Tecnologia da Universidade Nova de Lisboa, 2015.

[53] A. V Phelps, Z.L. Petrovic, Cold-cathode discharges and breakdown in argon: surface and gas phase production of secondary electrons, Plasma Sources Sci. Technol. 8 (1999) R21–R44. https://doi.org/10.1088/0963-0252/8/3/201.

[54] M. Seah, The quantitative analysis of surfaces by XPS: a review, Surf. Interface Anal. 2 (1980) 222–239. https://doi.org/10.1002/sia.740020607.

[55] N. Mannella, S. Marchesini, A.W. Kay, A. Nambu, T. Gresch, S.H. Yang, B.S. Mun, J.M. Bussat, A. Rosenhahn, C.S. Fadley, Correction of non-linearity effects in detectors for electron spectroscopy, J. Electron Spectros. Relat. Phenomena. 141 (2004) 45–59. https://doi.org/10.1016/j.elspec.2004.03.009.

[56] R.D. Evans, The atomic nucleus, Tata McGraw-Hill Publishing Company Ltd., 1955. http://link.springer.com/10.3103/S0027134912010092.

[57] M.P. Seah, Effective dead time in pulse counting systems, Surf. Interface Anal. 23 (1995) 729–732. https://doi.org/10.1002/sia.740231013.

[58] R.C. Wicks, N.J.C. Ingle, Characterizing the detection system nonlinearity, internal inelastic background, and transmission function of an electron spectrometer for use in x-ray photoelectron spectroscopy, Rev. Sci. Instrum. 80 (2009). https://doi.org/10.1063/1.3131631.

[59] L.T. Weng, G. Vereecke, M.J. Genet, P. Bertrand, W.E.E. Stone, Quantitative XPS. Part I: Experimental determination of the relative analyser transmission function of two different spectrometers — a critical assessment of various methods, parameters involved

and errors introduced, Surf. Interface Anal. 20 (1993) 179–192. https://doi.org/10.1002/sia.740200302.

[60] H. Ebel, G. Zuba, M.F. Ebel, A modified bias-method for the determination of spectrometer functions, J. Electron Spectros. Relat. Phenomena. 31 (1983) 123–130. https://doi.org/10.1016/0368-2048(83)80015-2.

[61] M.P. Seah, XPS reference procedure for the accurate intensity calibration of electron spectrometers— results of a BCR intercomparison co-sponsored by the VAMAS SCA TWA, Surf. Interface Anal. 20 (1993) 243–266. https://doi.org/10.1002/sia.740200309.

[62] J.H. Scofield, Hartree-Slater subshell photoionization cross-sections at 1254 and 1487 eV, J. Electron Spectros. Relat. Phenomena. 8 (1976) 129–137. https://doi.org/10.1016/0368-2048(76)80015-1.

[63] J.J. Yeh, I. Lindau, Atomic subshell photoionization cross sections and asymmetry parameters: $1 \leqslant Z \leqslant 103$, At. Data Nucl. Data Tables. 32 (1985) 1–155. https://doi.org/10.1016/0092-640X(85)90016-6.

[64] C.J. Powell, A. Jablonski, The NIST Electron Effective-Attenuation-Length Database, J. Surf. Anal. 9 (2002) 322–325. https://doi.org/10.1384/jsa.9.322.

[65] N. Farley, Copyright © 2005 Casa Software Ltd, (n.d.). http://www.casaxps.com/.

[66] L. Zommer, Determination of the spectrometer transmission function for XPS quantitative analysis, Vacuum. 46 (1995) 617–620. https://doi.org/10.1016/0042-207X(94)00143-X.

[67] M.P. Seah, A system for the intensity calibration of electron spectrometers, J. Electron Spectros. Relat. Phenomena. 71 (1995) 191–204. https://doi.org/10.1016/0368-2048(94)02275-5.

[68] E.J.N. Wilson, Charged particle beams, Nature. 270 (1977) 764–764. https://doi.org/10.1038/270764b0.

[69] M.P. Seah, G.C. Smith, Quantitative AES and XPS: Determination of the electron spectrometer transmission function and the detector sensitivity energy dependencies for the production of true electron emission spectra in AES and XPS, Surf. Interface Anal. 15 (1990) 751–766. https://doi.org/10.1002/sia.740151208.

[70] O. Sise, T.J.M. Zouros, M. Ulu, M. Dogan, Comparison of fringing field correction schemes for the 180° hemispherical deflector analyzer, Phys. Procedia. 1 (2008) 473–477. https://doi.org/10.1016/j.phpro.2008.07.129.

[71] O. Sise, G. Martínez, I. Madesis, A. Laoutaris, A. Dimitriou, M. Fernández-Martín, T.J.M. Zouros, The voltage optimization of a four-element lens used on a hemispherical

spectrograph with virtual entry for highest energy resolution, J. Electron Spectros. Relat. Phenomena. 211 (2016) 19–31. https://doi.org/10.1016/j.elspec.2016.05.004.

[72] E.D. Goodman, Introduction to genetic algorithms, Proc. GECCO 2007 Genet. Evol. Comput. Conf. Companion Mater. (2007) 3205–3224. https://doi.org/10.1145/1274000.1274111.

[73] R. Storn, K. Price, Differential Evolution – A Simple and Efficient Heuristic for global Optimization over Continuous Spaces, J. Glob. Optim. 11 (1997) 341–359. https://doi.org/10.1023/A:1008202821328.

[74] S. Das, P.N. Suganthan, Differential evolution: A survey of the state-of-the-art, IEEE Trans. Evol. Comput. 15 (2011) 4–31. https://doi.org/10.1109/TEVC.2010.2059031.

[75] S. Das, S.S. Mullick, P.N. Suganthan, Recent advances in differential evolution-An updated survey, Swarm Evol. Comput. 27 (2016) 1–30. https://doi.org/10.1016/j.swevo.2016.01.004.

[76] M. Pedersen, Good Parameters for Differential Evolution, 2010. http://www.hvass-labs.org/people/magnus/publications/pedersen10good-de.pdf.

[77] L.-E. Cheran, S. Johnstone, S. Sadeghi, M. Thompson, Work-function measurement by high-resolution scanning Kelvin nanoprobe, Meas. Sci. Technol. 18 (2007) 567–578. https://doi.org/10.1088/0957-0233/18/3/005.

[78] J. Hölzl, F.K. Schulte, Work function of metals, in: Solid Surf. Physics, Springer Tracts Mod. Phys., Springer-Verlag, 1979: pp. 1–150. https://doi.org/10.1007/BFb0048919.

[79] Y. Park, V. Choong, Y. Gao, B.R. Hsieh, C.W. Tang, Work function of indium tin oxide transparent conductor measured by photoelectron spectroscopy, Appl. Phys. Lett. 68 (1996) 2699. https://doi.org/10.1063/1.116313.

[80] H. Lüth, Surfaces and Interfaces of Solids, Springer Berlin Heidelberg, Berlin, Heidelberg, 1993. https://doi.org/10.1007/978-3-662-10159-9.

[81] S. Evans, Work function measurements by X-Pe spectroscopy, and their relevance to the calibration of X-Pe spectra, Chem. Phys. Lett. 23 (1973) 134–138. https://doi.org/10.1016/0009-2614(73)89582-X.

[82] G. Bachmann, W. Berthold, H. Oechsner, Work function spectroscopy as a tool for thin film analysis, Thin Solid Films. 174 (1989) 149–154. https://doi.org/10.1016/0040-6090(89)90883-3.

[83] J. -M. Pan, B.L. Maschhoff, U. Diebold, T.E. Madey, Interaction of water, oxygen, and hydrogen with TiO $_2$ (110) surfaces having different defect densities, J. Vac. Sci. Technol. A Vacuum, Surfaces, Film. 10 (1992) 2470–2476.

https://doi.org/10.1116/1.577986.

[84] J.L. Larue, J.D. White, N.H. Nahler, Z. Liu, Y. Sun, P.A. Pianetta, D.J. Auerbach, A.M. Wodtke, The work function of submonolayer cesium-covered gold: A photoelectron spectroscopy study, J. Chem. Phys. 129 (2008) 1–7. https://doi.org/10.1063/1.2953712.

[85] W. Song, M. Yoshitake, A work function study of ultra-thin alumina formation on NiAl(l10) surface, Appl. Surf. Sci. 251 (2005) 14–18. https://doi.org/10.1016/j.apsusc.2005.03.116.

[86] G. Zha, W. Jie, X. Bai, T. Wang, L. Fu, W. Zhang, J. Zhu, F. Xu, The study on the work function of CdZnTe with different surface states by synchrotron radiation photoemission spectroscopy, J. Appl. Phys. 106 (2009) 1–6. https://doi.org/10.1063/1.3211325.

[87] N.D. Orf, I.D. Baikie, O. Shapira, Y. Fink, Work function engineering in low-temperature metals, Appl. Phys. Lett. 94 (2009) 0–3. https://doi.org/10.1063/1.3089677.

[88] M. Pivetta, F. Patthey, W.D. Schneider, B. Delley, Surface distribution of Cu adatoms deduced from work function measurements, Phys. Rev. B - Condens. Matter Mater. Phys. 65 (2002) 454171–454175. https://doi.org/10.1103/PhysRevB.65.045417.

[89] K. Ozawa, K. Edamoto, Photoelectron spectroscopy study of K adsorption on ZnO(1 0 $\bar{1}$0), Surf. Sci. 524 (2003) 78–88. https://doi.org/10.1016/S0039-6028(02)02480-9.

[90] K. Onda, B. Li, H. Petek, Two-photon photoemission spectroscopy of TiO2(110) surfaces modified by defects and O2 or H2O adsorbates, Phys. Rev. B. 70 (2004) 045415. https://doi.org/10.1103/PhysRevB.70.045415.

[91] H. Fukagawa, H. Yamane, S. Kera, K.K. Okudaira, N. Ueno, Experimental estimation of the electric dipole moment and polarizability of titanyl phthalocyanine using ultraviolet photoelectron spectroscopy, Phys. Rev. B - Condens. Matter Mater. Phys. 73 (2006) 2–5. https://doi.org/10.1103/PhysRevB.73.041302.

[92] Y. Sun, Z. Liu, P. Pianetta, Surface dipole formation and lowering of the work function by Cs adsorption on InP(100) surface, J. Vac. Sci. Technol. A Vacuum, Surfaces, Film. 25 (2007) 1351. https://doi.org/10.1116/1.2753845.

[93] H. Fukagawa, S. Hosoumi, H. Yamane, S. Kera, N. Ueno, Dielectric properties of polar-phthalocyanine monolayer systems with repulsive dipole interaction, Phys. Rev. B - Condens. Matter Mater. Phys. 83 (2011) 1–8. https://doi.org/10.1103/PhysRevB.83.085304.

[94] G. Eng, H.K.A. Kan, Scanning Auger and work-function measurements applied to dispenser cathodes, Appl. Surf. Sci. 8 (1981) 81–94. https://doi.org/10.1016/0378-5963(81)90008-8.

[95] G. Bachmann, H. Oechsner, J. Scholtes, Surface analysis by work function measurements in a Scanning Auger Microprobe, Fresenius' Zeitschrift Für Anal. Chemie. 329 (1987) 195–200. https://doi.org/10.1007/BF00469136.

[96] H. Oechsner, Scanning work function microscopy, Fresenius. J. Anal. Chem. 355 (1996) 419–424. https://doi.org/10.1007/s0021663550419.

[97] O.M.N.D. Teodoro, A.M.C. Moutinho, Work function microscopy as a tool for materials analysis, Key Eng. Mater. 230–232 (2002) 165–168. https://doi.org/10.4028/www.scientific.net/kem.230-232.165.

[98] A. Imanishi, E. Tsuji, Y. Nakato, Dependence of the work function of TiO2 (Rutile) on crystal faces, studied by a scanning auger microprobe, J. Phys. Chem. C. 111 (2007) 2128–2132. https://doi.org/10.1021/jp0668403.

[99] H.P. Marques, A.R. Canário, A.M.C. Moutinho, O.M.N.D. Teodoro, Work function changes in the Ag deposition on TiO2 (110), Vacuum. 82 (2008) 1425–1427. https://doi.org/10.1016/j.vacuum.2008.03.016.

[100] H. Nonaka, T. Shimizu, K. Arai, A. Kurokawa, S. Ichimura, In-situ Work Function Measurement of Molecular Beam Epitaxy Film Surface Using RHEED-Beam Excited Secondary Electron Peaks, J. Surf. Anal. 9 (2002) 344–347. https://doi.org/10.1384/jsa.9.344.

[101] H. Lüth, Solid Surfaces, Interfaces and Thin Films, Springer Berlin Heidelberg, Berlin, Heidelberg, 2010. https://doi.org/10.1007/978-3-642-13592-7.

[102] J. Topping, P.R.S.L. A, On the mutual potential energy of a plane network of doublets, Proc. R. Soc. London. Ser. A, Contain. Pap. a Math. Phys. Character. 114 (1927) 67–72. https://doi.org/10.1098/rspa.1927.0025.

[103] D.C. Gleason-rohrer, MEASUREMENT OF THE BAND BENDING AND SURFACE DIPOLE AT CHEMICALLY FUNCTIONALIZED SI (111)/ VACUUM INTERFACES, California Institute of Technology, 2014.

[104] H. Brune, Microscopic view of epitaxial metal growth: nucleation and aggregation, Surf. Sci. Rep. 31 (1998) 125–229. https://doi.org/10.1016/S0167-5729(99)80001-6.

[105] S. Surnev, M. Kiskinova, Formation of patchy surface overlayers: Alkali adsorption and alkali carbon monoxide and oxygen coadsorption on Ru(0001) and Ru(10-10), Appl. Phys. A Solids Surfaces. 46 (1988) 323–329. https://doi.org/10.1007/BF01141599.

[106] V.T. Binh, R. Mouton, C. Adessi, V. Semet, M. Cahay, S. Fairchild, Nanopatchwork cathodes: Patch-fields and field emission of nanosize parallel e-beams, J. Appl. Phys. 108 (2010). https://doi.org/10.1063/1.3475343.

[107] N. Bundaleski, J. Trigueiro, a. G. Silva, a. M.C. Moutinho, O.M.N.D. Teodoro, Influence of the patch field on work function measurements based on the secondary electron emission, J. Appl. Phys. 113 (2013) 183720. https://doi.org/10.1063/1.4804663.

[108] J. Trigueiro, N. Bundaleski, A.G. Silva, O.M.N.D. Teodoro, Influence of the patch field on work function study using the onset method, Vacuum. 98 (2013) 41–44. https://doi.org/10.1016/j.vacuum.2013.04.007.

[109] C. Herring, M.H. Nichols, Thermionic emission, Rev. Mod. Phys. 21 (1949) 185–270. https://doi.org/10.1103/RevModPhys.21.185.

[110] J.D. Jackson, Classical Electrodynamics, Wiley, 1962. https://doi.org/10.1023/a:1018821305089.

[111] D.A. Dahl, SIMION for the personal computer in reflection, Int. J. Mass Spectrom. 200 (2000) 3–25. https://doi.org/10.1016/S1387-3806(00)00305-5.

[112] S.L. McArthur, Thin films of Vanadium Oxide Grown on Vanadium metal, Surf. Interface Anal. 38 (2006) 1380–1385. https://doi.org/10.1002/sia.

[113] L.F. Zagonel, M. Bäurer, A. Bailly, O. Renault, M. Hoffmann, S.J. Shih, D. Cockayne, N. Barrett, Orientation-dependent work function of insitu annealed strontium titanate, J. Phys. Condens. Matter. 21 (2009). https://doi.org/10.1088/0953-8984/21/31/314013.

[114] W. Melitz, J. Shen, A.C. Kummel, S. Lee, Kelvin probe force microscopy and its application, Surf. Sci. Rep. 66 (2011) 1–27. https://doi.org/10.1016/j.surfrep.2010.10.001.

[115] S. Bagheri, N. Muhd Julkapli, S. Bee Abd Hamid, Titanium dioxide as a catalyst support in heterogeneous catalysis, ScientificWorldJournal. 2014 (2014) 727496. https://doi.org/10.1155/2014/727496.

[116] Y. Li, X. Xu, Y. Li, C. Ding, J. Wu, A. Lu, H. Ding, S. Qin, C. Wang, Absolute band structure determination on naturally occurring rutile with complex chemistry: Implications for mineral photocatalysis on both Earth and Mars, Appl. Surf. Sci. 439 (2018) 660–671. https://doi.org/10.1016/j.apsusc.2017.12.195.

[117] W. Busayaporn, TiO2 (110) Surface Structure, University of Manchester, 2010.

[118] C.L. Pang, O. Bikondoa, D.S. Humphrey, A.C. Papageorgiou, G. Cabailh, R. Ithnin, Q. Chen, C.A. Muryn, H. Onishi, G. Thornton, Tailored TiO2(110) surfaces and their reactivity, Nanotechnology. 17 (2006) 5397–5405. https://doi.org/10.1088/0957-4484/17/21/019.

[119] C.M. Yim, C.L. Pang, G. Thornton, Oxygen vacancy origin of the surface band-gap state

of TiO2(110), Phys. Rev. Lett. 104 (2010) 2–5. https://doi.org/10.1103/PhysRevLett.104.036806.

[120] W.S. Epling, C.H.F. Peden, M.A. Henderson, U. Diebold, Evidence for oxygen adatoms on TiO2(110) resulting from O2dissociation at vacancy sites, Surf. Sci. 412–413 (1998) 333–343. https://doi.org/10.1016/S0039-6028(98)00446-4.

[121] B. V. Yakshinskiy, M.N. Hedhili, S. Zalkind, M. Chandhok, T.E. Madey, Radiation-induced defect formation and reactivity of model TiO 2 capping layers with MMA: a comparison with Ru, Emerg. Lithogr. Technol. XII. 6921 (2008) 692114. https://doi.org/10.1117/12.772798.

[122] C.L. Pang, R. Lindsay, G. Thornton, Structure of clean and adsorbate-covered single-crystal rutile TiO2 surfaces., Chem. Rev. 113 (2013) 3887–948. https://doi.org/10.1021/cr300409r.

[123] Y. Du, N.A. Deskins, Z. Zhang, Z. Dohnalek, M. Dupuis, I. Lyubinetsky, Formation of O adatom pairs and charge transfer upon O2 dissociation on reduced TiO2(110), Phys. Chem. Chem. Phys. 12 (2010) 6337–6344. https://doi.org/10.1039/c002146f.

[124] Z. Dohnálek, I. Lyubinetsky, R. Rousseau, Thermally-driven processes on rutile TiO2(110)-(1×1): A direct view at the atomic scale, Prog. Surf. Sci. 85 (2010) 161–205. https://doi.org/10.1016/j.progsurf.2010.03.001.

[125] Q. Guo, C. Zhou, Z. Ma, Z. Ren, H. Fan, X. Yang, Elementary photocatalytic chemistry on TiO2surfaces, Chem. Soc. Rev. 45 (2016) 3701–3730. https://doi.org/10.1039/c5cs00448a.

[126] A. Borodin, M. Reichling, Characterizing TiO2(110) surface states by their work function, Phys. Chem. Chem. Phys. 13 (2011) 15442. https://doi.org/10.1039/c0cp02835e.

[127] N. Bundaleski, A.G. Silva, U. Schröder, A.M.C. Moutinho, O.M.N.D. Teodoro, Adsorption dynamics of water on the surface of TiO2 (110), J. Phys. Conf. Ser. 257 (2010) 012008. https://doi.org/10.1088/1742-6596/257/1/012008.

[128] N. Bundaleski, A.G. Silva, B. Jean-Shaw, O. Teodoro, A. Moutinho, Water on TiO2studied by work function change: Adsorption in cycles, J. Phys. Conf. Ser. 417 (2013). https://doi.org/10.1088/1742-6596/417/1/012024.

[129] S. Wendt, J. Matthiesen, R. Schaub, E.K. Vestergaard, E. Laegsgaard, F. Besenbacher, B. Hammer, Formation and splitting of paired hydroxyl groups on reduced TiO2(110)., Phys. Rev. Lett. 96 (2006) 066107. https://doi.org/10.1103/PhysRevLett.96.066107.

[130] J. Matthiesen, J.O. Hansen, S. Wendt, E. Lira, R. Schaub, E. Laegsgaard, F.

Besenbacher, B. Hammer, Formation and diffusion of water dimers on rutile TiO2(110)., Phys. Rev. Lett. 102 (2009) 226101. https://doi.org/10.1103/PhysRevLett.102.226101.

[131] M.A. Henderson, W.S. Epling, C.H.F. Peden, C.L. Perkins, Insights into photoexcited electron scavenging processes on TiO2 obtained from studies of the reaction of O2 with OH groups adsorbed at electronic defects on TiO2(110), J. Phys. Chem. B. 107 (2003) 534–545. https://doi.org/10.1021/jp0262113.

[132] Z. Zhang, O. Bondarchuk, B.D. Kay, J.M. White, Z. Dohnalek, Imaging water dissociation on TiO2(110): Evidence for inequivalent geminate OH groups., J. Phys. Chem. B. 110 (2006) 21840–21845. https://doi.org/10.1021/jp063619h.

[133] T. Minato, Y. Sainoo, Y. Kim, H.S. Kato, K. Aika, M. Kawai, J. Zhao, H. Petek, T. Huang, W. He, B. Wang, Z. Wang, Y. Zhao, J. Yang, J.G. Hou, The electronic structure of oxygen atom vacancy and hydroxyl impurity defects on titanium dioxide (110) surface., J. Chem. Phys. 130 (2009) 124502. https://doi.org/10.1063/1.3082408.

[134] G. Ketteler, S. Yamamoto, H. Bluhm, K. Andersson, D.E. Starr, D.F. Ogletree, H. Ogasawara, A. Nilsson, M. Salmeron, L. Berkeley, M. Sciences, V. Di, S.H. Road, M. Park, The nature of water nucleation sites on TiO2(110) surfaces revealed by ambient pressure X-ray photoelectron spectroscopy, J. Phys. Chem. C. 111 (2007) 8278–8282. https://doi.org/10.1021/jp068606i.

[135] Y. Du, Z. Dohnálek, I. Lyubinetsky, Transient Mobility of Oxygen Adatoms upon O2 Dissociation on Reduced TiO2 (110), J. Phys. Chem. C. 112 (2008) 2649–2653. https://doi.org/10.1021/jp077677u.

[136] Z. Zhang, Y. Du, N.G. Petrik, G.A. Kimmel, I. Lyubinetsky, Z. Dohna, Water as a Catalyst : Imaging Reactions of O 2 with Partially and Fully Hydroxylated TiO 2 (110) Surfaces, 2 (2009) 1908–1916.

[137] Y. Du, N.A. Deskins, Z. Zhang, Z. Dohnálek, M. Dupuis, I. Lyubinetsky, Imaging Consecutive Steps of O2 Reaction with Hydroxylated TiO2 (110): Identification of HO2 and Terminal OH Intermediates, J. Phys. Chem. C. 113 (2009) 666–671. https://doi.org/10.1021/jp807030n.

[138] H.D. Hagstrum, Theory of Auger Ejection of Electrons from Metals by Ions, Phys. Rev. 96 (1954) 336–365. https://doi.org/10.1103/PhysRev.96.336.

[139] P.A. Redhead, Ion Desorption by Electron Bombardment; Relation to Total and Partial Pressure Measurement, J. Vac. Sci. Technol. 7 (1970) 182–187. https://doi.org/10.1116/1.1315789.

[140] T.E. Madey, History of desorption induced by electronic transitions, Surf. Sci. 299–300 (1994) 824–836. https://doi.org/10.1016/0039-6028(94)90700-5.

[141] M.L. Knotek, P.J. Feibelman, Ion desorption by core-hole Auger decay, Phys. Rev. Lett. 40 (1978) 964–967. https://doi.org/10.1103/PhysRevLett.40.964.

[142] S. Tanaka, K. Mase, M. Nagasono, S. Nagaoka, M. Kamada, Electron-ion coincidence study for the TiO2(110) surface, Surf. Sci. 451 (2000) 182–187. https://doi.org/10.1016/S0039-6028(00)00025-X.

[143] A. Kotani, Y. Toyozawa, Photoelectron Spectra of Core Electrons in Metals with an Incomplete Shell, J. Phys. Soc. Japan. 37 (1974) 912–919. https://doi.org/10.1143/JPSJ.37.912.

[144] R.L. Kurtz, R. Stock-Bauer, T.E. Msdey, E. Román, J.L. De Segovia, Synchrotron radiation studies of H2O adsorption on TiO2(110), Surf. Sci. 218 (1989) 178–200. https://doi.org/10.1016/0039-6028(89)90626-2.

[145] O. Dulub, M. Batzill, S. Solovev, E. Loginova, A. Alchagirov, T.E. Madey, U. Diebold, Electron-induced oxygen desorption from the TiO2(011)-2x1 surface leads to self-organized vacancies, Science (80-.). 317 (2007) 1052–1056. https://doi.org/10.1126/science.1144787.

[146] M.L. Knotek, Characterization of hydrogen species on metal-oxide surfaces by electron-stimulated desorption: TiO2and SrTiO3, Surf. Sci. 101 (1980) 334–340. https://doi.org/10.1016/0039-6028(80)90627-5.

[147] Z. Zhang, J.T. Yates, Effect of adsorbed donor and acceptor molecules on electron stimulated desorption: O2/TiO2(110), J. Phys. Chem. Lett. 1 (2010) 2185–2188. https://doi.org/10.1021/jz1007559.

[148] J. Lee, Z. Zhang, J.T. Yates, Electron-stimulated positive-ion desorption caused by charge transfer from adsorbate to substrate: Oxygen adsorbed on TiO2(110), Phys. Rev. B. 79 (2009) 081408. https://doi.org/10.1103/PhysRevB.79.081408.

[149] S. Suzuki, K. Fukui, H. Onishi, Y. Iwasawa, Hydrogen adatoms on TiO2(110)-(1x1) characterized by scanning tunneling microscopy and electron stimulated desorption, Phys. Rev. Lett. 84 (2000) 2156–2159. https://doi.org/10.1103/PhysRevLett.84.2156.

[150] K. Cao, Surface Science Study of Water and Hydrogen Adsorbed on Rutile TiO2(110)-(1x1), University of Virginia, 2014. https://doi.org/10.18130/V3VT0B.

[151] R. Souda, Resonant ion stimulated desorption of O+ from the TiO2(110) surface: Effects of oxygenation and ion bombardment, Nucl. Instruments Methods Phys. Res. Sect. B Beam Interact. with Mater. Atoms. 160 (2000) 453–459. https://doi.org/10.1016/S0168-

583X(99)00620-5.

[152] U. Diebold, T.E. Madey, Adsorption and electron stimulated desorption of NH 3 /TiO 2 (110), J. Vac. Sci. Technol. A Vacuum, Surfaces, Film. 10 (1992) 2327–2335. https://doi.org/10.1116/1.577939.

[153] J.L. De Segovia, M.C. Torquemada, E. Roman, Electron-stimulated desorption of O+ from SO2 and CO adsorbed on TiO2(110), J. Phys. Condens. Matter. 5 (1993). https://doi.org/10.1088/0953-8984/5/33A/031.

[154] J. Lee, Z. Zhang, X. Deng, D.C. Sorescu, C. Matranga, J.T. Yates, Interaction of CO with Oxygen Adatoms on TiO2 (110), J. Phys. Chem. C. 115 (2011) 4163–4167. https://doi.org/10.1021/jp1112697.

[155] V.N. Ageev, S.M. Solovev, Investigation of lithium adsorption on the surface of TiO2 by electron-stimulated desorption, Surf. Sci. 480 (2001) 1–10. https://doi.org/10.1016/S0039-6028(01)01011-1.

[156] D. Menzel, R. Gomer, Desorption from Metal Surfaces by Low-Energy Electrons, J. Chem. Phys. 41 (1964) 3311–3328. https://doi.org/10.1063/1.1725730.

[157] D. Menzel, R. Gomer, Electron-Impact Desorption of Carbon Monoxide from Tungsten, J. Chem. Phys. 41 (1964) 3329–3351. https://doi.org/10.1063/1.1725731.

[158] R.D. Ramsier, J.T. Yates, Electron-stimulated desorption: Principles and applications, Surf. Sci. Rep. 12 (1991) 246–378. https://doi.org/10.1016/0167-5729(91)90013-N.

[159] J. Trigueiro, N. Bundaleski, O.M.N.D. Teodoro, Monitoring dynamics of different processes on rutile TiO 2 (110) surface by following work function change, Vaccum. 152 (2018) 327–329. https://doi.org/10.1016/j.vacuum.2018.03.049.

[160] A.R. Burns, E.B. Stechel, D.R. Jennison, Desorption Induced by Electronic Transitions DIET V, Springer Berlin Heidelberg, Berlin, Heidelberg, 1993. https://doi.org/10.1007/978-3-642-78080-6.

[161] G. Antczak, G. Ehrlich, Jump processes in surface diffusion, Surf. Sci. Rep. 62 (2007) 39–61. https://doi.org/10.1016/j.surfrep.2006.12.001.

[162] D. Halliday, Resnick Robert, J. Walker, Fundamentals of physics, Wiley, 2011.

[163] V.N. Cherepanov, Electric Dipole Moment Function of the OH Molecule, Russ. Phys. J. 46 (2003) 637–640. https://doi.org/10.1023/B:RUPJ.0000008191.01497.d1.

[164] T. Pluta, A.J. Sadlej, R.J. Bartlett, Polarizability of OH-, Chem. Phys. Lett. 143 (1988) 91–96. https://doi.org/10.1016/0009-2614(88)87017-9.

[165] T. Zheng, C. Wu, M. Chen, Y. Zhang, P.T. Cummings, A DFT study of water adsorption on rutile TiO2(110) surface: The effects of surface steps, J. Chem. Phys. 145 (2016)

044702. https://doi.org/10.1063/1.4958969.

[166] H.H. Kristoffersen, J.Ø. Hansen, U. Martinez, Y.Y. Wei, J. Matthiesen, R. Streber, R. Bechstein, E. Lægsgaard, F. Besenbacher, B. Hammer, S. Wendt, Role of Steps in the Dissociative Adsorption of Water on Rutile TiO2(110), Phys. Rev. Lett. 110 (2013) 146101. https://doi.org/10.1103/PhysRevLett.110.146101.

MONITORING ADSORPTION DYNAMICS ON THE RUTILE TIO$_2$(110)-(1×1) SURFACE
WITH WFS AND XPS: SURFACE DEFECTS, WATER AND OXYGEN ADSORPTION

JOÃO TRIGUEIRO SANTOS

2021